

AD_____

Award Number: DAMD17-01-1-0443

TITLE: Improved Ultrasonic Imaging of the Breast

PRINCIPAL INVESTIGATOR: William F. Walker, Ph.D.

CONTRACTING ORGANIZATION: University of Virginia
Charlottesville, VA 22904-4195

REPORT DATE: August 2005

TYPE OF REPORT: Annual Summary

PREPARED FOR: U.S. Army Medical Research and Materiel Command
Fort Detrick, Maryland 21702-5012

DISTRIBUTION STATEMENT: Approved for Public Release;
Distribution Unlimited

The views, opinions and/or findings contained in this report are those of the author(s) and should not be construed as an official Department of the Army position, policy or decision unless so designated by other documentation.

REPORT DOCUMENTATION PAGE				Form Approved OMB No. 0704-0188	
Public reporting burden for this collection of information is estimated to average 1 hour per response, including the time for reviewing instructions, searching existing data sources, gathering and maintaining the data needed, and completing and reviewing this collection of information. Send comments regarding this burden estimate or any other aspect of this collection of information, including suggestions for reducing this burden to Department of Defense, Washington Headquarters Services, Directorate for Information Operations and Reports (0704-0188), 1215 Jefferson Davis Highway, Suite 1204, Arlington, VA 22202-4302. Respondents should be aware that notwithstanding any other provision of law, no person shall be subject to any penalty for failing to comply with a collection of information if it does not display a currently valid OMB control number. PLEASE DO NOT RETURN YOUR FORM TO THE ABOVE ADDRESS.					
1. REPORT DATE (DD-MM-YYYY) 01-08-2005		2. REPORT TYPE Annual Summary		3. DATES COVERED (From - To) 1 Aug 2001 – 31 Jul 2005	
4. TITLE AND SUBTITLE Improved Ultrasonic Imaging of the Breast				5a. CONTRACT NUMBER	
				5b. GRANT NUMBER DAMD17-01-1-0443	
				5c. PROGRAM ELEMENT NUMBER	
6. AUTHOR(S) William F. Walker, Ph.D. E-mail: bwalker@virginia.edu				5d. PROJECT NUMBER	
				5e. TASK NUMBER	
				5f. WORK UNIT NUMBER	
7. PERFORMING ORGANIZATION NAME(S) AND ADDRESS(ES) University of Virginia Charlottesville, VA 22904-4195				8. PERFORMING ORGANIZATION REPORT NUMBER	
9. SPONSORING / MONITORING AGENCY NAME(S) AND ADDRESS(ES) U.S. Army Medical Research and Materiel Command Fort Detrick, Maryland 21702-5012				10. SPONSOR/MONITOR'S ACRONYM(S)	
				11. SPONSOR/MONITOR'S REPORT NUMBER(S)	
12. DISTRIBUTION / AVAILABILITY STATEMENT Approved for Public Release; Distribution Unlimited					
13. SUPPLEMENTARY NOTES					
14. ABSTRACT Ultrasonic imaging is currently used in the breast to distinguish between fluid filled cysts and solid masses, and more rarely, to differentiate between malignant and benign lesions. The utility of ultrasound is limited because microcalcifications (MCs) are not typically visible and because benign and malignant masses often exhibit only subtle image differences. We have invented a new technique that uses modified ultrasound equipment to form images of ultrasonic angular scatter. This method provides a new source of image contrast and should enhance the detectability of MCs and improve the differentiation of benign and malignant lesions. This method yields high resolution images with minimal statistical variability. We have formed images in tissue mimicking phantoms and found that angular scatter offers a new and useful source of image contrast. We have also initiated clinical studies and found that normal soft tissues exhibit significant variations in angular scatter. We have made significant technical advances in image acquisition and signal processing. In the past year we have implemented a new Synthetic Aperture approach to angular scatter imaging that yields significantly better resolution and contrast than earlier approaches. Improved visualization of MCs and benign/malignant differentiation would improve patient care by enhancing diagnosis and improving the localization of needle and core biopsy procedures. These advances may in turn reduce unneeded biopsies and improve biopsy accuracy.					
15. SUBJECT TERMS ultrasound, imaging, microcalcification, acoustic scattering					
16. SECURITY CLASSIFICATION OF:			17. LIMITATION OF ABSTRACT UU	18. NUMBER OF PAGES 176	19a. NAME OF RESPONSIBLE PERSON USAMRMC
a. REPORT U	b. ABSTRACT U	c. THIS PAGE U			19b. TELEPHONE NUMBER (include area code)

Table of Contents

Cover	1
SF 298	2
Table of Contents	3
Proposal Technical Abstract	4
Narrative	6
Key Research Accomplishments	9
Reportable Outcomes	12
Conclusions	15
Appendix 1: Paper: "A Novel Beamformer Design Method for Medical Ultrasound: Part I: Theory"	
Appendix 2: Paper: "A Novel Beamformer Design Method for Medical Ultrasound: Part II: Simulation Results"	
Appendix 3: Paper: "A General Cystic Resolution Metric for Medical Ultrasound"	
Appendix 4: Paper: "A Spline Based Approach for Computing Spatial Impulse Responses"	
Appendix 5: Conf. Paper: "Eval. Trans. Apertures Based Angular Scatter Imaging on a Clin. Imaging System"	
Appendix 6: Conf. Paper: "Novel Aperture Design Method for Improved Depth of Field in Ultrasound Imag."	
Appendix 7: Conf. Paper: "A Novel Aperture Design Method in Ultrasound Imaging"	
Appendix 8: Conf. Paper: "Minimum Sum Squared Error (MSSE) Beamformer Design Techn.: Initial Results"	
Appendix 9: Conf. Paper: "A Constrained Adaptive Beamformer for Medical Ultrasound: Initial Results"	
Appendix 10: Conf. Paper: "Angular Scatter Imaging: Clinical Results and Novel Processing Methods"	
Appendix 11: Conf. Paper: "Angular Scatter Imaging in Medical Ultrasound"	
Appendix 12: Conf. Paper: "Constrained Adaptive Beamforming: Point and Contrast Resolution"	
Appendix 13: Conf. Paper: "Synthetic Aperture Methods for Angular Scatter Imaging"	
Appendix 14: Conf. Paper: "Synthetic Aperture Angular Scatter Imaging: System Refinement"	
Appendix 15: Conf. Paper: "Ultrasonic Synthetic Aperture Angular Scatter Imaging,"	
Appendix 16: Conf. Paper: "A New Performance Analysis Metric for Medical Ultrasound"	
Appendix 17: Conf. Paper: "Design of Apodization Profiles Using a Cystic Resolution for Ultrasound"	
Appendix 18: Conf. Paper: "Adaptive Signal Processing in Medical Ultrasound Beamforming"	

Improved Ultrasonic Imaging of the Breast

William F. Walker, Ph.D.

Technical Abstract:

Ultrasonic imaging has become an increasingly important tool for the diagnosis of breast cancer. While x ray mammography remains the standard for screening, ultrasound is widely used to differentiate fluid filled cysts from solid masses, to guide invasive biopsy procedures, and even to differentiate between benign and malignant lesions. Ultrasound is an attractive choice for these applications because it exposes the patient to no ionizing radiation, requires no uncomfortable breast compression, produces images in real-time, and can successfully image young women with radiographically dense breasts. Although it offers many advantages, ultrasound is limited by the fact that certain soft tissues may appear only subtly different and that microcalcifications (MCs) are not reliably visualized. The inability to reliably image MCs is particularly troublesome because these small calcium crystals are an important mammographic indicator of breast cancer.

This grant would support career development by reducing teaching load to provide time for expanded research efforts and clinical training. If funded, my teaching load would fall from three courses per academic year to one course per academic year. I have been supported by the University of Virginia by provision of excellent laboratory space within the Biomedical Engineering Department, Medical Research Building 4, and occasionally in the Department of Radiology. This laboratory space is well equipped with test equipment, an ophthalmic ultrasound system, a custom ultrasound system, and a GE Logiq 700 ultrasonic imaging system with research interface. The custom system has precise timing control, making it an excellent platform for development of new imaging and flow estimation algorithms. The GE system is coupled to an extended research interface which allows acquisition of up to 32 MB of raw ultrasound echo data. This system is also supported by custom research software, allowing control of aperture geometry and a variety of other system parameters.

The main goals of this grant are:

- (1) Research in angular scatter imaging using the translating apertures algorithm.
- (2) Clinical training in breast cancer imaging and treatment.

The first aim will apply the Translating Apertures Algorithm (TAA) to form images of the angular scatter parameters of tissue. Since the TAA observes the same speckle pattern with angle of interrogation (for omnidirectional scatterers), it eliminates the statistical variability which plagued earlier techniques. This property makes it possible for the TAA to acquire independent, statistically reliable angular scatter profiles at every location in tissue. The specific aims of this research are:

1. Determine bias and variance of angular scatter measurements performed with the TAA.
2. Form novel images using angular scatter data from multiple angles.
3. Implement angular scatter imaging in combination with spatial compounding.

Each of these aims will be performed using experimental phantom data, experimental human tissue data, and computer simulations. All experiments will be performed on a GE Logiq 700 imaging system with a special research interface. The images obtained in aims 2 and 3 will be formed offline using experimental data obtained from the GE Logic 700 system described above.

The techniques developed under this grant will likely improve the visibility of MCs and should also enhance the contrast of soft tissue lesions. Since tumors are known to have different concentrations of extracellular matrix proteins they would be expected to exhibit angular scatter responses different from that of normal tissue. Since MCs have a much higher mass density than their surrounding tissue, they would be expected to exhibit a much greater angular scatter variation than soft tissues.

We have already begun development of one method of angular scatter imaging. In this method we form two separate images of tissue; one which highlights the component of scattering which is uniform with angle (c-weighted image), and a second which highlights the scattering component which varies with angle (d-weighted image). Simulation results indicate that c- and d-weighted images may offer significant new information about soft tissue, and that they will almost certainly improve the detectability of MCs with ultrasound.

The techniques developed here should allow detection of previously invisible tumors, especially in women with radiodense breasts. Furthermore they should improve the accuracy of image guided biopsy procedures by enhancing the visibility of MCs.

I believe that it is my job to develop new technologies which can be implemented to improve patient care. While my knowledge of engineering continues to evolve, I have become increasingly aware of limitations in my knowledge of clinical medicine. If this proposal is funded I will invest a significant amount of time to educate myself in the clinical methods of breast cancer diagnosis and treatment. I will observe breast imaging, biopsy, and surgical procedures to gain first hand knowledge of the strengths and weaknesses of existing methods. I believe that these observations will illuminate new directions of research.

Narrative:

The main goal of this project is the validation of angular scatter ultrasonic imaging as a useful method for improving the detection of microcalcifications and the differentiation of benign and malignant breast tissues. We have successfully implemented angular scatter imaging using two different algorithms on the GE Logiq 700MR imaging system located in the PI's laboratory. The first algorithm uses focused apertures and applies the Translating Apertures Algorithm to obtain angular scatter information with high electronic SNR, but limited depth of field and relatively poor angular resolution. The second method applied Synthetic Aperture (SA) methods to obtain angular scatter information with a somewhat lower SNR, but with excellent depth of field and high angular resolution. We have showed that angular scatter imaging obtains information about both phantoms and human tissues that is not available through existing methods. In phantom experiments we showed that angular scatter imaging improved the contrast of microcalcification mimicking phantom materials by as much as a factor of 5. At this stage of development we are confident that angular scatter offers new and valuable information about tissue microstructure.

As this grant has progressed, we have concentrated our research efforts on the use of SA methods for angular scatter imaging. Although potentially subject to motion artifacts and poor electronic signal to noise ratio, these SA imaging methods have the potential to achieve both high spatial resolution and high angular resolution; a combination which is not possible with conventional imaging schemes. From a first order analysis, the angular resolution of SA methods should be limited only by the physical dimensions of the transducer array elements. Thus an array with finer elements should be able to achieve better angular resolution and therefore gather higher quality information about the tissue structure.

In the early stages of our SA research efforts we rediscovered a well known property of SA imaging, specifically that if one transmits and receives on each element only once, as we desire to optimize angular resolution, the sampling requirements needed to avoid spatial aliasing will not be met. Specifically, this acquisition strategy will lead, with typical array spatial sampling intervals, to the formation of grating lobes. If present, these grating lobes will fundamentally degrade image quality to the point where most diagnostic capabilities are lost. To circumvent this problem we realized that by receiving on each element twice, with different adjacent transmit elements, echo data can be combined to eliminate grating lobes. While this approach slightly reduces angular resolution, the improvements it yields in image quality make this approach well worthwhile.

With grating lobes eliminated, the next challenge for high quality imaging is the formation of a system response with minimal sidelobe levels. While this has been achieved historically by applying well-known signal processing methods such as the Hann and Nuttall apodization, these windows are not optimal for the broad-band, near-field environment of medical ultrasound. In the past two years we have derived new analytical and numerical methods to design the optimal apodization windowing functions for ultrasound imaging. These techniques are generally formulated as a linearly constrained quadratic minimization problem, so that the optimal weights are determined when the point spread function energy is minimized but the mainlobe amplitude is held constant. This Linearly Constrained Least Squares (LCLS) method has been described in a series of conference papers and our team is now preparing a full manuscript describing this approach. One advantage to this method is that it can take into account a variety of non-ideal transducer and system effects such as a poor bandwidth and limited element angular response.

With the system response at a given angle optimized using the LCLS method described above, the next challenge for high quality angular scatter imaging is to maximize the correlation between system responses at

different scattering angles. We will perform this task by utilizing the optimal backscatter point spread function designed using the LCLS method as a goal and then applying the Minimum Sum Squared Error (MSSE) beamformer design technique developed under this grant to minimize the differences between point spread functions at different scattering angles. The advantage of this approach is that by following a mathematically rigorous approach it is guaranteed to minimize system response variations across angles. In the coming months we will combine the MSSE and LCLS methods to obtain optimal angular scatter imaging data experimentally.

One of the original goals of this proposal was to develop methods to quantify performance of angular scatter imaging systems. In the process of working towards this goal it became increasingly clear that existing methods for characterizing general ultrasound imaging system performance were ad hoc and did not adequately convey the subtleties of system performance which are critically important in clinical practice. In order to remedy this problem we invested a significant effort in the development of a general resolution metric for medical ultrasound. Unlike existing methods, which consider the appearance of point targets, which are exceedingly rare *in vivo*, our method considers the contrast of an ideal anechoic cyst placed within a speckle generating background. Although also idealized, this approach considers the very low-level side lobes and grating lobes which tend to dominate real-world performance. We have described this method in a series of conference publications and also in a full paper that is currently under review. We believe that this method provides an elegant approach for guiding the design of ultrasound imaging systems.

The MSSE and LCLS beamformer design methods and the general resolution metric all require high quality models of system performance to achieve meaningful results. While the FIELD II program written by Jørgen Jensen has become a standard for ultrasound simulation, this tool produces time-space system responses, while the design methods and resolution metric developed under this proposal utilize space-space system responses. While FIELD can be used to generate space-space responses, the computational complexity of this approach is daunting and is not practical for most systems of interest. Further, computational artifacts which are insignificant for time-space responses tend to grow to significant levels when space-space responses are extracted. In order to circumvent these limitations we have developed a new simulation tool, named DELFI, which inherently computes space-space responses. This code uses a spline-based signal model to analytically compute transmit-receive system responses. We have extensively tested this code and when a peer-reviewed publication currently in review is accepted for publication we will place the source code for this tool on the web for public use.

As we have shifted our emphasis from focused data acquisition to SA acquisition we have begun to face significant experimental hurdles. While modern ultrasound systems do acquire the single channel data needed for SA image formation, they do not store this data, but rather process it continuously as it is acquired. Furthermore, traditional systems cannot be readily programmed with the transmit pulse sequences needed for full SA data acquisition. We are working through these limitations by developing rapid serial acquisition tools for the GE Logiq 700MR system. These software modifications should allow us to acquire SA angular scatter data at reasonable frame rates with existing hardware. Although we have made good progress on this goal, the development work is significant and the age of this platform makes available support from GE quite limited. While this effort continues, we are working in parallel to complete an ongoing modification of a Philips SONOS 5500 system in the PI's laboratory. Once complete, this system will acquire nearly two seconds worth of single channel data in parallel for off-line analysis. Although progress on this project is continuous, the challenges of custom hardware design in an academic setting are daunting. Finally, we have recently initiated a collaboration with Innervision, a Canadian ultrasound startup, which should have intrinsic SA acquisition capabilities in its platform. We are confident that one of these strategies will yield a workable experimental system in the next year.

Our extensive efforts in SA imaging have led us to explore the broad range of adaptive imaging techniques utilized on SA data acquired in the domains of RADAR and SONAR. With support from the current grant and a second Army grant, we have tested a number of adaptive imaging methods on both simulated and experimental ultrasound data. Our initial results from this work, described in a series of conference papers and in an nearly complete refereed paper, indicate that conventional wisdom regarding ultrasound system resolution is far from a hard limit, but rather represents a first step in a continuum of possible image contrast and resolution limits. As we refine these methods and move them towards clinical implementation we anticipate applications to angular scatter imaging.

As I reach the end of this career development grant I cannot help but be disappointed at some level that we have not yet achieved significant clinical results. We have however gained a fundamental understanding of the potential of angular scatter imaging and defined a rigorous approach for implementation. In the coming year we will draw upon the results of this grant to move to clinical implementation and work to develop partnerships with commercial entities who could carry these concepts to the widespread clinical application.

Key Research Accomplishments:

a) Determine bias and variance of angular scatter measurements performed with the TAA.

Simulate bias and variance

Months 1-18

Complete, results described in the following publications:

Appendix 2: Paper: "A Novel Beamformer Design Method for Medical Ultrasound: Part II: Simulation Results"

Appendix 5: Conf. Paper: "Eval. Trans. Apertures Based Angular Scatter Imaging on a Clin. Imaging System"

Appendix 6: Conf. Paper: "Novel Aperture Design Method for Improved Depth of Field in Ultrasound Imag."

Appendix 7: Conf. Paper: "A Novel Aperture Design Method in Ultrasound Imaging"

Appendix 8: Conf. Paper: "Minimum Sum Squared Error (MSSE) Beamformer Design Techn.: Initial Results"

Appendix 10: Conf. Paper: "Angular Scatter Imaging: Clinical Results and Novel Processing Methods"

Appendix 13: Conf. Paper: "Synthetic Aperture Methods for Angular Scatter Imaging"

Appendix 14: Conf. Paper: "Synthetic Aperture Angular Scatter Imaging: System Refinement"

Appendix 15: Conf. Paper: "Ultrasonic Synthetic Aperture Angular Scatter Imaging,"

Measure bias and variance in phantoms

Months 7-18

Complete, results described in the following publications:

Appendix 5: Conf. Paper: "Eval. Trans. Apertures Based Angular Scatter Imaging on a Clin. Imaging System"

Appendix 10: Conf. Paper: "Angular Scatter Imaging: Clinical Results and Novel Processing Methods"

Appendix 11: Conf. Paper: "Angular Scatter Imaging in Medical Ultrasound"

Appendix 13: Conf. Paper: "Synthetic Aperture Methods for Angular Scatter Imaging"

Appendix 14: Conf. Paper: "Synthetic Aperture Angular Scatter Imaging: System Refinement"

Appendix 15: Conf. Paper: "Ultrasonic Synthetic Aperture Angular Scatter Imaging,"

Develop and test methods for angle dependent weightings

to compensate for limited element angular response

Months 13-24

Complete, results described in the following publications:

Appendix 1: Paper: "A Novel Beamformer Design Method for Medical Ultrasound: Part I: Theory"

Appendix 2: Paper: "A Novel Beamformer Design Method for Medical Ultrasound: Part II: Simulation Results"

Appendix 5: Conf. Paper: "Eval. Trans. Apertures Based Angular Scatter Imaging on a Clin. Imaging System"

Appendix 6: Conf. Paper: "Novel Aperture Design Method for Improved Depth of Field in Ultrasound Imag."

Appendix 7: Conf. Paper: "A Novel Aperture Design Method in Ultrasound Imaging"

Appendix 8: Conf. Paper: "Minimum Sum Squared Error (MSSE) Beamformer Design Techn.: Initial Results"

Appendix 10: Conf. Paper: "Angular Scatter Imaging: Clinical Results and Novel Processing Methods"

Appendix 15: Conf. Paper: "Ultrasonic Synthetic Aperture Angular Scatter Imaging,"

Appendix 17: Conf. Paper: "Design of Apodization Profiles Using a Cystic Resolution for Ultrasound"

Develop and test apodization schemes to compensate for

apparent apodization due to element angular response

Months 19-36

Complete, results described in the following publications:

Appendix 1: Paper: "A Novel Beamformer Design Method for Medical Ultrasound: Part I: Theory"

Appendix 2: Paper: "A Novel Beamformer Design Method for Medical Ultrasound: Part II: Simulation Results"

Appendix 6: Conf. Paper: "Novel Aperture Design Method for Improved Depth of Field in Ultrasound Imag."

Appendix 7: Conf. Paper: "A Novel Aperture Design Method in Ultrasound Imaging"

Appendix 8: Conf. Paper: "Minimum Sum Squared Error (MSSE) Beamformer Design Techn.: Initial Results"

Appendix 10: Conf. Paper: “Angular Scatter Imaging: Clinical Results and Novel Processing Methods”
Appendix 15: Conf. Paper: “Ultrasonic Synthetic Aperture Angular Scatter Imaging,”
Appendix 17: Conf. Paper: “Design of Apodization Profiles Using a Cystic Resolution for Ultrasound”

Develop expressions relating correlation to variance Months 1-12

We are no longer working towards this original goal. Rather than comparing correlation and variance we have focused the relationship between correlation and sum squared error. Sum squared error provides a more useful metric as it can form the basis of algorithms to improve system performance and contains the effects of both bias and variance. In the following papers we have considered the impact of sum squared error on correlation:

Appendix 2: Paper: “A Novel Beamformer Design Method for Medical Ultrasound: Part II: Simulation Results”
Appendix 5: Conf. Paper: “Eval. Trans. Apertures Based Angular Scatter Imaging on a Clin. Imaging System”
Appendix 6: Conf. Paper: “Novel Aperture Design Method for Improved Depth of Field in Ultrasound Imag.”
Appendix 7: Conf. Paper: “A Novel Aperture Design Method in Ultrasound Imaging”
Appendix 8: Conf. Paper: “Minimum Sum Squared Error (MSSE) Beamformer Design Techn.: Initial Results”
Appendix 10: Conf. Paper: “Angular Scatter Imaging: Clinical Results and Novel Processing Methods”
Appendix 15: Conf. Paper: “Ultrasonic Synthetic Aperture Angular Scatter Imaging,”

b) Form novel images using angular scatter data from multiple angles.

Simulate angular scatter data

(using Rayleigh, Faran, and other models)

Months 13-48

Ongoing, no results to report at this time.

Acquire data from tissue mimicking phantoms

Months 7-30

Ongoing, results described in the following publications:

Appendix 5: Conf. Paper: “Eval. Trans. Apertures Based Angular Scatter Imaging on a Clin. Imaging System”
Appendix 10: Conf. Paper: “Angular Scatter Imaging: Clinical Results and Novel Processing Methods”
Appendix 11: Conf. Paper: “Angular Scatter Imaging in Medical Ultrasound”
Appendix 13: Conf. Paper: “Synthetic Aperture Methods for Angular Scatter Imaging”
Appendix 14: Conf. Paper: “Synthetic Aperture Angular Scatter Imaging: System Refinement”
Appendix 15: Conf. Paper: “Ultrasonic Synthetic Aperture Angular Scatter Imaging,”

Acquire data from human breast tissue

Months 13-36

Experimental system development underway.

Form parametric images using polynomial fits

Months 16-39

Ongoing, no results to report at this time.

Adapt Haider’s method to angular scatter imaging

Months 19-42

No results to report at this time.

Image variance of angular scatter

Months 16-39

Ongoing, no results to report at this time.

Develop other imaging methods

Months 22-48

Ongoing, no results to report at this time.

Test methods to improve depth of field

Months 13-48

Ongoing, results described in the following publications:

Appendix 1: Paper: "A Novel Beamformer Design Method for Medical Ultrasound: Part I: Theory"

Appendix 2: Paper: "A Novel Beamformer Design Method for Medical Ultrasound: Part II: Simulation Results"

Appendix 5: Conf. Paper: "Eval. Trans. Apertures Based Angular Scatter Imaging on a Clin. Imaging System"

Appendix 6: Conf. Paper: "Novel Aperture Design Method for Improved Depth of Field in Ultrasound Imag."

Appendix 7: Conf. Paper: "A Novel Aperture Design Method in Ultrasound Imaging"

Appendix 8: Conf. Paper: "Minimum Sum Squared Error (MSSE) Beamformer Design Techn.: Initial Results"

Appendix 10: Conf. Paper: "Angular Scatter Imaging: Clinical Results and Novel Processing Methods"

Appendix 13: Conf. Paper: "Synthetic Aperture Methods for Angular Scatter Imaging"

Appendix 14: Conf. Paper: "Synthetic Aperture Angular Scatter Imaging: System Refinement"

Appendix 15: Conf. Paper: "Ultrasonic Synthetic Aperture Angular Scatter Imaging,"

Appendix 17: Conf. Paper: "Design of Apodization Profiles Using a Cystic Resolution for Ultrasound"

Develop and test methods to detect specular reflectors

Months 1-24

No results to report at this time.

c) Implement angular scatter imaging in combination with spatial compounding.

Implement TAA and spatial compounding on the GE

Months 25-36

No results to report at this time.

Develop methods to reduce the impact of limited element
angular response

Months 31-48

Underway, initial results described in the following publications:

Appendix 1: Paper: "A Novel Beamformer Design Method for Medical Ultrasound: Part I: Theory"

Appendix 2: Paper: "A Novel Beamformer Design Method for Medical Ultrasound: Part II: Simulation Results"

Appendix 6: Conf. Paper: "Novel Aperture Design Method for Improved Depth of Field in Ultrasound Imag."

Appendix 7: Conf. Paper: "A Novel Aperture Design Method in Ultrasound Imaging"

Appendix 8: Conf. Paper: "Minimum Sum Squared Error (MSSE) Beamformer Design Techn.: Initial Results"

Appendix 10: Conf. Paper: "Angular Scatter Imaging: Clinical Results and Novel Processing Methods"

Appendix 15: Conf. Paper: "Ultrasonic Synthetic Aperture Angular Scatter Imaging,"

Appendix 17: Conf. Paper: "Design of Apodization Profiles Using a Cystic Resolution for Ultrasound"

Test compounding with the TAA on phantoms

Months 31-48

No results to report at this time.

Test compounding with the TAA on tissues

Months 37-48

No results to report at this time.

Reportable Outcomes:

(Note that student authors are underlined.)

Refereed Publications:

Ranganathan, K. and W. F. Walker, "A Novel Beamformer Design Method for Medical Ultrasound: Part I: Theory," IEEE Trans. Ultrason. Ferroelec. Freq. Contr., IEEE Trans. Ultrason. Ferroelec. Freq. Contr, vol. 50, no. 1, pp. 15-24, 2003.

Ranganathan, K. and W. F. Walker, "A Novel Beamformer Design Method for Medical Ultrasound: Part II: Simulation Results," IEEE Trans. Ultrason. Ferroelec. Freq. Contr., vol. 50, no. 1, pp. 25-39, 2003.

Ranganathan, K. and W.F. Walker, "A General Cystic Resolution Metric for Medical Ultrasound," submitted to IEEE Trans. Ultrason. Ferroelec. Freq. Contr., Apr., 2005.

Walker, W.F., "A Spline Based Approach for Computing Spatial Impulse Responses," submitted to IEEE Trans. Ultrason. Ferroelec. Freq. Contr., Feb., 2005.

Conference Presentations with Paper:

Viola, F. and W.F. Walker, "Adaptive Signal Processing in Medical Ultrasound Beamforming," 2005 IEEE Ultrasonics Symposium, in press.

D.A. Guenther, Ranganathan, K. and W.F. Walker, "Design of Apodization Profiles Using a Cystic Resolution Metric for Ultrasound," 2005 IEEE Ultrasonics Symposium, in press.

Guenther , D.A., M.J. McAllister, K.W. Rigby, and W.F. Walker, "Ultrasonic Synthetic Aperture Angular Scatter Imaging," presented at the 2004 Asilomar Conference on Signals, Systems, and Computers.

Ranganathan, K. and W.F. Walker, "A New Performance Analysis Metric for Medical Ultrasound," presented at the 2004 IEEE Ultrasonics Symposium.

Guenther , D.A., K. Ranganathan, M.J. McAllister, K.W. Rigby, and W.F. Walker, "Synthetic Aperture Angular Scatter Imaging: System Refinement," presented at the 2004 IEEE Ultrasonics Symposium.

Guenther, D.A., K. Ranganathan, M.J. McAllister, K.W. Rigby, and W.F. Walker, "Synthetic Aperture Methods for Angular Scatter Imaging," SPIE Medical Imaging 2004, Proc. SPIE 5373, pp. 52-60, 2004.

Mann, J. A. and W. F. Walker, "Constrained Adaptive Beamforming: Point and Contrast Resolution," 2003 SPIE Medical Imaging Symposium.

Walker, W. F. and M. J. McAllister, "Angular Scatter Imaging in Medical Ultrasound," presented at the 36th Asilomar Conference on Signals, Systems, and Computers.

McAllister, M. J. and W. F. Walker, "Angular Scatter Imaging: Clinical Results and Novel Processing Methods," Proc. IEEE Ultrason. Symp., pp. ***-***, 2002.

Mann, J. A. and W. F. Walker, "A Constrained Adaptive Beamformer for Medical Ultrasound: Initial

Results,” Proc. IEEE Ultrason. Symp., pp. ***-***, 2002.

Ranganathan, K., and W. F. Walker, “The Minimum Sum Squared Error (MSSE) Beamformer Design Technique: Initial Results,” Proc. IEEE Ultrason. Symp., pp. ***-***, 2002.

Ranganathan, K. and W. F. Walker, “A Novel Aperture Design Method in Ultrasonic Imaging,” Proc. SPIE vol. 4687, pp. 13-24, Medical Imaging 2002: Ultrasonic Imaging and Signal Processing, 2002.

McAllister, M. J., K. W. Rigby and W. F. Walker, “Evaluation of Translating Apertures Based Angular Scatter Imaging on a Clinical Imaging System,” Proc. IEEE Ultrason. Symp., pp. 1555-8, 2001.

Ranganathan, K. and W. F. Walker, “A Novel Aperture Design Method for Improved Depth of Field in Ultrasound Imaging,” Proc. IEEE Ultrason. Symp., pp. 1543-6, 2001.

Conference Presentations with Abstract:

Viola, F., and W.F. Walker, “Adaptive Beamforming for Medical Ultrasound Imaging,” U.S. Dept. of Defense Breast Cancer Research Program Era of Hope 2005 Meeting, June 2005.

Walker, W.F., M.J. McAllister, K.W. Rigby, “In Vivo Imaging of Ultrasonic Angular Scatter,” U.S. Dept. of Defense Breast Cancer Research Program Era of Hope 2002 Meeting, September 2002.

Presentations:

Nov., 2004	Senior Physics Seminar, Bridgewater College, Bridgewater, VA “Ultrasound Research at UVA”
Oct. 2003	Parent’s Weekend, UVA SEAS, Charlottesville, VA “Ultrasound: The Basics and the Future”
June, 2003	Alumni Weekend, UVA SEAS, Charlottesville, VA “Ultrasound: The Basics and the Future”
Oct., 2002	Philips Research Center, Paris France “Medical Ultrasound Research at UVA”
Mar., 2002	Phillips Medical Sys., Bothell, WA “Radiation Force, Angular Scatter, & Novel Beamforming”
Feb., 2002	IBM Watson Research Center, White Plains, NY “Compute & Storage Intensive Ultrasound Research”

Patents:

“Angular Scatter Imaging Using Translating Apertures and Method Thereof,” W.F. Walker, G.E. Trahey, and M.J. McAllister, United States Patent 6,692,439 issued February 17, 2004.

“System and Method for Application of a Resolution Metric and Design for Apodization Profiles for Optimal Cystic Contrast,” D.A. Guenther and W.F. Walker, patent disclosure filed September, 2005.

“A Synthetic Aperture Method for Angular Scatter Imaging,” D.A. Guenther and W.F. Walker, Provisional Patent Application filed February 17, 2004.

“Method, System, and Computer Program Product for Constrained Adaptive Beamforming: Point and Contrast Resolution,” J.A. Mann and W.F. Walker, Provisional Patent Application filed October 7, 2003. (abandoned)

“Related Method and System for Constrained Adaptive Beamforming: Point and Contrast Resolution,” J.A. Mann and W.F. Walker, Provisional Patent Application filed March 12, 2003. (superceded by later provisional)

“An Improved Beamforming Method and System for Ultrasonic Imaging,” K. Ranganathan and W.F. Walker, Provisional Patent Application filed October 5, 2001. (abandoned)

New Funding Applications:

“Transmit Beam Design for Extended Focal Depth Ultrasound,” the National Institutes of Health, \$294,294, PI Yibin Zheng, co-PIs William F. Walker and Seth D. Silverstein, funding requested from December 1, 2005 to November 30, 2006 (10% effort) (pending).

“IGERT: Biomedical Ultrasound from Transducer to Image,” The National Science Foundation, \$2,600,000, PI Travis N. Blalock, co-PIs Scott T. Acton, John A. Hossack, Michael Reed, and William F. Walker, funding requested from September 1, 2006 to September 1, 2011 (8% effort) (not funded).

“Breast Ultrasound Imaging with Reduced Speckle and Enhanced Resolution,” The Army Breast Cancer Congressionally Directed Medical Research Program, \$104,268, PI Scott T. Acton, co-PI William F. Walker, funding requested from September 1, 2005 to August 31, 2006 (5% effort) (not funded).

“Compound Imaging for Low Cost C-Scan Ultrasonic Imaging,” the National Institutes of Health, \$145,827, funding requested from January 1, 2006 to June 30, 2006, PI Karen E. Morgan, co-PIs W.F. Walker, T.N. Blalock, and J.A. Hossack (5% Effort) (pending).

“Portable C-Scan Ultrasound for Rapid Vascular Access.” the National Institutes of Health, \$149,970, funding requested from January 1, 2006 to June 30, 2006, PI Karen E. Morgan, co-PIs W.F. Walker, T.N. Blalock, and J.A. Hossack (5% Effort) (pending).

“Acoustic Radiation Force for the Assessment of Thrombogenicity,” the National Institutes of Health, \$121,096, funding requested from July 1, 2005 to June 30, 2006, PI Francesco Viola, co-PIs W.F. Walker and M.B. Lawrence (10% Effort) (pending).

“Sonorheometry for In Vitro Assessment of Viscoelastic Properties,” The National Institutes of Health, \$1,750,000, funding requested July 2005 to June 2010, PI W.F. Walker (25% effort) (pending).

“Radiation Force Imaging in the Eye”, The Whitaker Foundation, \$80,000, transitional funding requested from January 1, 2005 to December 31, 2005, PI W.F. Walker (18% effort) (funded).

Conclusions:

Angular scatter imaging with ultrasound shows tremendous promise for improving the visualization of microcalcifications and improving the differentiation of various soft tissue types. While our original concept of applying fully focused apertures with the Translating Apertures Algorithm now appears to be limited, the Synthetic Aperture methods developed under this grant appear to be fundamentally well suited to clinical imaging. Our experimental results indicate that angular scatter variations are significant in both phantoms and human tissues, and that they offer a source of contrast that is distinct from traditional backscatter. The greatest immediate challenge to implementing SA angular scatter imaging clinically is the real-time acquisition of full SA data sets. We are exploring collaborations with a number of companies and also pursuing the development of our own custom hardware to implement SA angular scatter imaging with follow on funding.

A Novel Beamformer Design Method for Medical Ultrasound. Part I: Theory

Karthik Ranganathan and William F. Walker, *Member, IEEE*

Abstract—The design of transmit and receive aperture weightings is a critical step in the development of ultrasound imaging systems. Current design methods are generally iterative, and consequently time consuming and inexact. We describe a new and general ultrasound beamformer design method, the minimum sum squared error (MSSE) technique. The MSSE technique enables aperture design for arbitrary beam patterns (within fundamental limitations imposed by diffraction). It uses a linear algebra formulation to describe the system point spread function (psf) as a function of the aperture weightings. The sum squared error (SSE) between the system psf and the desired or goal psf is minimized, yielding the optimal aperture weightings. We present detailed analysis for continuous wave (CW) and broadband systems. We also discuss several possible applications of the technique, such as the design of aperture weightings that improve the system depth of field, generate limited diffraction transmit beams, and improve the correlation depth of field in translated aperture system geometries. Simulation results are presented in an accompanying paper.

I. INTRODUCTION

ULTRASONIC imaging is an important medical diagnostic tool that entails four critical steps. An ultrasound waveform is first generated and transmitted by exciting a piezoelectric transducer with a suitable electric signal; usually a finite duration pulse. This transmitted ultrasound beam propagates through tissue, undergoing diffraction and attenuation as well as scattering and reflection at tissue interfaces. Next, the reflected or scattered echoes propagate back to the transducer where they are received and converted to electric signals. These received echoes are then processed and mapped to form an image. Simple ultrasound systems use a single large piezoelectric transducer to generate and receive ultrasound. However, state of the art systems use phased array technology similar to that used in contemporary radar and sonar. These systems use transducer arrays comprising a multitude of small transducer elements. Subsets of these elements form the active transducer aperture that is used for transmission and reception. The prime reason for the use of arrays is the fact that the independent operation of each element

enables more control over the transmission and reception processes. On transmit, the application of distinct time delays [1] to the pulses used to excite each element focuses the transmitted ultrasound beam to a specific point. These delays are calculated using elementary geometry to compensate for differences between the path lengths from each element to the point of interest. In addition to these time delays, magnitude weights [1] may be applied to the elements (apodization) to control the shape of the ultrasonic beam. These weights are usually determined iteratively or adapted from windowing functions described in signal processing literature. These magnitude and phase weights play a critical role in determining system resolution and contrast. More advanced medical ultrasound systems enable not only transmit focusing and apodization, but also the generation of arbitrary transmit waveforms for each element.

On the receive side, state of the art systems change their focus dynamically as a function of time after transmit [1]. This means that the system is ideally focused at the point of origin of the echoes received at any time. In addition to dynamic focusing, these systems also implement dynamic apodization [1] to maintain a constant system f-number within the physical constraints of the transducer. The f-number is the ratio of the range being interrogated to the aperture size. Keeping the f-number constant throughout acquisition results in a more spatially invariant system response with range. Some systems have Finite Impulse Response (FIR) filters on each receive channel to apply focal time delay increments that are smaller than the system sampling interval. These filters usually have few taps and fixed coefficients. Among other topics, this paper considers what might be possible if flexible dynamic FIR filters were placed on each channel. As we will show, such an alteration would enable tremendous control over the system response.

Ultrasound beam characteristics fundamentally affect image quality and the quality of data acquired for signal processing. Because of this significance, much of system design is dedicated to optimizing beam parameters. The two most important beam parameters are mainlobe width and sidelobe levels. Mainlobe width determines the system point resolution, and sidelobe levels determine the system contrast. As mentioned previously, these and other beam parameters can be adjusted by changing the magnitude and phase (or time delay) of the weightings applied to the active elements. These parameters are also influenced by the size of the active aperture (the number of active elements) and the frequency of the ultrasound pulse.

Manuscript received May 16, 2002; accepted August 28, 2002. This work was supported by Susan G. Komen Breast Cancer Foundation Imaging Grant No. 99-3021 and United States Army Congressionally Directed Medical Research Program Grant No. DAMD 17-01-10443. Inspiration from this work stems from National Science Foundation Major Research Instrumentation Grant 0079639.

The authors are with the Department of Biomedical Engineering, University of Virginia, Charlottesville, VA (e-mail: kr6u@virginia.edu).

Magnitude weightings, phase weightings, aperture size, and operating frequency can each be adjusted to manipulate beam parameters. Unfortunately, these beamforming parameters do not act independently; altering one changes the impact of each of the others. Thus, beamformer design is a complicated multiparameter optimization problem. Because of this complexity, beamformer parameters are typically determined using a combination of ad hoc methods, simplified theory, and iterative simulation and experimentation. Although these methods are effective, they are time consuming and provide no guarantee that the optimal solution has been found. Therefore, there is a fundamental need to develop a design method that simultaneously considers the impact of all the controllable beamformer parameters in a straightforward and rigorous way.

We propose a general aperture design method, supported by rigorous theory, that can be applied in arbitrary system geometries to design apertures that optimize beam parameters. Our technique utilizes a linear algebra formulation of the sum squared error (SSE) between the system point spread function (psf) and the desired or goal psf. Minimization of this error yields unique aperture weightings that maximize the system psf's resemblance to the desired psf. A strength of our approach is that it utilizes system characteristics that may be obtained through theory, simulation, or experiments. Simulation results are presented in another paper [2].

Our method is similar to the technique used by Ebbini and Cain [3] to generate specialized beam patterns for hyperthermia, and by Li *et al.* [4] for the compensation of blocked elements. However, there are significant differences between these methods and the technique we describe. Chief among these is the fact that our technique is more general. It describes a method for the design of optimized apertures for any application, and enables the design of arbitrary beam patterns. Such patterns are, of course, fundamentally constrained by wavelength and aperture size. The designed beam simply will be that which most closely approximates the desired beam given the limitations of the physics. The differences between the MSSE technique and the techniques described in [3] and [4] are discussed in more detail later in this manuscript. This paper outlines the theoretical description of the MSSE technique for narrowband and broadband systems, describes a modified technique for reduced computational cost, and discusses a few examples of applications. Simulation results for these examples are described in [2].

II. THEORY

We present one-way and two-way continuous wave (CW) and broadband formulations of the MSSE technique. Please note that all operators and variables in the CW formulations are complex valued, and operators and variables in the broadband formulations are real valued.

A. Continuous Wave Formulation

1. *One-Way Analysis:* The phase and magnitude of the ultrasonic field at a point in space generated by an ultrasound transducer element depend upon several factors. These include the Euclidean distance between the point and the element, the orientation of the element relative to the point, the frequency of the emitted wave, and frequency-dependent attenuation of the medium. Assuming linear propagation, the complex ultrasonic field $p(x_i)$ at a point in space x_i can be expressed as:

$$p(x_i) = \int_{-\infty}^{\infty} S(\chi, x_i) W(\chi) d\chi, \quad (1)$$

where χ represents position in the aperture plane, $W(\chi)$ is the complex aperture weighting function, and $S(\chi, x_i)$ is a propagation function that incorporates any or all of the factors mentioned above. $S(\chi, x_i)$ determines the complex field at x_i due to the aperture weighting at χ . This propagation function may be determined through theory, simulations, or experiments. A simple propagation function can be formulated based on the Rayleigh-Sommerfeld diffraction equation, which is derived in ([5, pp. 46–50]). The propagation function may also include limited element angular response using the formulation derived in [6], as well as other such complicating factors.

The formulation for the ultrasonic field can readily be discretized because the transducer aperture comprises a finite number of elements. Therefore, the field p_j at a point j due to an aperture of N elements can be expressed as:

$$p_j = \sum_{i=1}^N s_{i,j} w_i, \quad (2)$$

where $s_{i,j}$ is the propagation function that determines the field at the point j due to the i^{th} element, and w_i is the weighting applied to the i^{th} element. Therefore, p_j is the sum of the contribution of each element to the field at j . Note that this formalism makes no assumptions about the geometry or other characteristics of the transducer elements. Eq. (2) can be expressed in a matrix formulation as follows:

$$p_j = [s_{1,j} \ s_{2,j} \ s_{3,j} \ \cdots \ s_{N,j}] \begin{bmatrix} w_1 \\ w_2 \\ w_3 \\ \vdots \\ w_N \end{bmatrix}. \quad (3)$$

Therefore, the one-way M -point lateral psf at the range z can be represented as:

$$P_z = \begin{bmatrix} s_{1,1} & s_{2,1} & \cdots & s_{N,1} \\ s_{1,2} & s_{2,2} & \cdots & \cdot \\ \cdot & \cdot & \cdots & \cdot \\ \cdot & \cdot & \cdots & \cdot \\ s_{1,M} & \cdot & \cdots & s_{N,M} \end{bmatrix} \begin{bmatrix} w_1 \\ w_2 \\ \cdot \\ \cdot \\ w_N \end{bmatrix} = S_z W, \quad (4)$$

where S_z is an $M \times N$ matrix of propagation functions with $s_{i,j}$ denoting the propagation function that determines the field at the point j due to the i^{th} element, W is an $N \times 1$ vector of aperture weightings, and the resulting psf P_z is an $M \times 1$ vector. Note that our field point/element notation differs from the conventional row/column ordering. We have chosen this ordering for purposes of clarity and consistency within the manuscript, as will become more clear in the broadband formulation below. As mentioned previously, this formulation permits analysis with complicated propagation functions that may include limited element angular response, frequency dependent attenuation, and other factors that are difficult to model. Using the formulation in (4), the transmit and receive psfs at the range z can be expressed as:

$$P_{Tz} = S_z T \quad (5)$$

and

$$P_{Rz} = S_z R, \quad (6)$$

respectively, where T and R are the transmit and receive aperture weightings, respectively.

Let \tilde{P}_{Tz} represent the desired one-way psf for the application of interest. We can then characterize the degree of similarity of the desired psf, \tilde{P}_{Tz} , and the actual system psf, P_{Tz} , by the sum squared error between them. Minimizing this SSE would yield a system psf optimally similar to the goal psf. Therefore, beamformer design is simply the selection of transmit aperture weightings such that the SSE between the desired and actual system psfs is minimized. Using (5), the SSE can be expressed as follows:

$$\begin{aligned} SSE &= (P_{Tz} - \tilde{P}_{Tz})^H (P_{Tz} - \tilde{P}_{Tz}) \\ &= (S_z T - \tilde{P}_{Tz})^H (S_z T - \tilde{P}_{Tz}), \end{aligned} \quad (7)$$

where the superscript H denotes a conjugate transpose operation.

The formulation in (7) is common in signal processing, and substantial literature is devoted to the solution to (7) with the minimum SSE (least squares solution). Drawing upon [7], the optimal transmit aperture weightings are given by:

$$T = (S_z^H S_z)^{-1} S_z^H \tilde{P}_{Tz} = S_z^\# \tilde{P}_{Tz}, \quad (8)$$

where the superscripts $^{-1}$ and $^\#$ denote a matrix inverse and a pseudoinverse operation, respectively. Therefore, $S_z^\#$ is the pseudoinverse of S_z .

Eq. (8) provides a simple method for the calculation of the transmit weightings that yield the system psf at the range z that is optimally similar to the goal or desired psf.

2. One-Way Analysis with Weighting Function: In certain applications, the psf characteristics at some lateral positions may be more critical than at others because the width of the mainlobe of the psf determines system point resolution and the magnitudes of the side-lobes determine the system contrast. In a given application, it may be more

important to enforce low sidelobe levels than to precisely control the mainlobe. In such cases, we can incorporate a weighting function, F , that emphasizes or de-emphasizes selected features in the psf during the MSSE design process. The SSE (7) can be rewritten with the weighting function as:

$$SSE = (F_d S_z T - F_d \tilde{P}_{Tz})^H (F_d S_z T - F_d \tilde{P}_{Tz}), \quad (9)$$

where F_d is a diagonalized $M \times M$ matrix with the elements of F along its 0th diagonal. These elements should have a large value where a close match between the goal and designed psf is required. Smaller values can be used in regions where a close match is less critical. The solution for the receive weightings, as drawn from [7] is:

$$\begin{aligned} T &= ((F_d S_z)^H F_d S_z)^{-1} (F_d S_z)^H F_d \tilde{P}_{Tz} \\ &= (S_z^H F_d^H F_d S_z)^{-1} S_z^H F_d^H F_d \tilde{P}_{Tz} \\ &= (F_d S_z)^\# F_d \tilde{P}_{Tz}, \end{aligned} \quad (10)$$

where $(F_d S_z)^\#$ is the pseudoinverse of $F_d S_z$.

3. Two-Way Analysis: In most ultrasonic imaging applications, the two-way impulse response is of greater interest than the one-way response. The two-way response can be readily determined by applying the radar equation [8]. It states that, for continuous wave applications, the two-way response is simply the product of the transmit and receive responses. Applying this knowledge to our linear algebra formulation yields the following two-way response:

$$P_{TRz} = P_{Tz} \cdot P_{Rz} = (S_z T) \cdot (S_z R), \quad (11)$$

where \cdot indicates point-by-point multiplication. Eq. (11) can be rewritten as:

$$P_{TRz} = P_{Tzd} P_{Rz} = P_{Tzd} S_z R = P_{TzdS} R, \quad (12)$$

where P_{Tzd} is a diagonal $M \times M$ matrix with the elements of P_{Tz} along its 0th diagonal, and $P_{TzdS} = P_{Tzd} S_z$. This changes the point multiplication operation to a regular matrix multiplication operation.

Similar to the one-way analysis, if the goal two-way psf for the application of interest is \tilde{P}_{TRz} , the SSE can be expressed as:

$$SSE = (P_{TRz} - \tilde{P}_{TRz})^H (P_{TRz} - \tilde{P}_{TRz}). \quad (13)$$

Applying (12), (13) can be rewritten and solved using [7] as shown below, yielding the optimum receive weightings:

$$SSE = (P_{TzdS} R - \tilde{P}_{TRz})^H (P_{TzdS} R - \tilde{P}_{TRz}), \quad (14)$$

$$R = (P_{TzdS}^H P_{TzdS})^{-1} P_{TzdS}^H \tilde{P}_{TRz} = P_{TzdS}^\# \tilde{P}_{TRz}, \quad (15)$$

where $P_{TzdS}^\#$ is the pseudoinverse of P_{TzdS} .

Eq. (15) specifies the complex weightings to be applied to the transducer elements constituting the receive aperture to obtain a system psf, P_{TRz} , at the range z , that optimally resembles the desired or goal psf, \tilde{P}_{TRz} .

4. Two-Way Analysis with Weighting Function: As with the one-way analysis, a weighting function F can be incorporated in the SSE formulation to selectively emphasize or de-emphasize features in the psf during the minimization operation. Rewriting the SSE (14) after including the weightings matrix, the resulting receive weightings can be solved for in a manner similar to that used in (9) and (10).

$$\begin{aligned} R &= \left((F_d P_{TzdS})^H F_d P_{TzdS} \right)^{-1} (F_d P_{TzdS})^H F_d \tilde{P}_{TRz} \\ &= (P_{TzdS}^H F_d^H F_d P_{TzdS})^{-1} P_{TzdS}^H F_d^H F_d \tilde{P}_{TRz} \\ &= (F_d P_{TzdS})^\# F_d \tilde{P}_{TRz}, \end{aligned} \quad (16)$$

where F_d is again a diagonalized $M \times M$ matrix with the elements of F along its 0th diagonal, and $(F_d P_{TzdS})^\#$ is the pseudoinverse of $F_d P_{TzdS}$.

B. Broadband Formulation

1. One-Way Analysis: The formulations described in the previous section are CW formulations. Medical ultrasound systems use monochromatic (CW) excitation only for specific modalities such as CW Doppler. For the majority of applications, an ultrasound pulse with some finite bandwidth is used. The previously described CW formulation will have limited accuracy in this broadband scenario.

The one-way psf at a specific range z can be represented as a function of time and lateral position as follows:

$$P_z = \begin{bmatrix} p_{1,1} & p_{2,1} & \cdots & p_{n_p,1} \\ p_{1,2} & p_{2,2} & \cdots & \cdot \\ \cdot & \cdot & \cdot & \cdot \\ \cdot & \cdot & \cdot & \cdot \\ p_{1,n_{tp}} & \cdot & \cdots & p_{n_p,n_{tp}} \end{bmatrix}, \quad (17)$$

where P_z is an $n_{tp} \times n_p$ matrix that is a two-dimensional function of position and time. It consists of the field at each of n_p lateral points in space, at each of n_{tp} points in time. It comprises elements of the form $p_{i,j}$, which is the field at lateral point i at time sample j . Eq. (17) can be rewritten by reshaping the matrix as follows:

$$P_z = \begin{bmatrix} p_{1,1} \\ p_{1,2} \\ \cdot \\ \cdot \\ p_{1,n_{tp}} \\ p_{2,1} \\ p_{2,2} \\ \cdot \\ \cdot \\ p_{n_p,n_{tp}} \end{bmatrix}, \quad (18)$$

where the first n_{tp} elements represent the field at lateral point 1 at each of n_{tp} time samples, the next n_{tp} elements represent the field at lateral point 2 for the same n_{tp} time samples, and so on until the last n_{tp} time samples for the n_p^{th} lateral point.

The field at a point in space over n_{tp} time samples can be expressed as a function of a propagation matrix, A , and a set of aperture weightings, T . The propagation matrix depends upon the excitation pulse and the element impulse responses of the transmit aperture. It is a function of time and the spatial positions of the element and field point under consideration. It describes the contribution of each element at each field point as a function of time. The aperture weightings are also two-dimensional, being a function of the element number and time, and can be expressed for each of n_a elements over each of n_{ta} time samples as:

$$T = \begin{bmatrix} t_{1,1} & t_{2,1} & \cdots & t_{n_a,1} \\ t_{1,2} & t_{2,2} & \cdots & \cdot \\ \cdot & \cdot & \cdot & \cdot \\ \cdot & \cdot & \cdot & \cdot \\ t_{1,n_{ta}} & \cdot & \cdots & t_{n_a,n_{ta}} \end{bmatrix}, \quad (19)$$

where $t_{i,j}$ is the aperture weighting for element i at time j . These weightings essentially form the coefficients of a FIR filter. Eq. (19) also can be reshaped as follows:

$$T = \begin{bmatrix} t_{1,1} \\ t_{1,2} \\ \cdot \\ \cdot \\ t_{1,n_{ta}} \\ t_{2,1} \\ t_{2,2} \\ \cdot \\ \cdot \\ t_{n_a,n_{ta}} \end{bmatrix}, \quad (20)$$

where the first n_{ta} elements are the aperture weightings for element 1 at each of n_{ta} time samples, the next n_{ta} elements are the weightings for element 2 for the same n_{ta} time samples, and so on until the last n_{ta} elements for the n_a^{th} element. Using (18) and (20), we can now write the complete one-way system psf P_z as (21) (see next page) or

$$P_z = A_z T, \quad (22)$$

where A_z is an $(n_p \cdot n_{tp}) \times (n_a \cdot n_{ta})$ propagation matrix. Each element $a_{i,j,k,l}$ determines the field due to the weighting at time sample j applied to element i , at time sample l at lateral field point k . The transmit and receive psfs at the range z , therefore, can be expressed as follows:

$$P_{Tz} = A_z T, \quad (23)$$

$$P_{Rz} = A_z R, \quad (24)$$

respectively, where T and R are the $(n_a \cdot n_{ta}) \times 1$ transmit and receive aperture weightings, respectively.

$$\begin{bmatrix} p_{1,1} \\ p_{1,2} \\ \vdots \\ p_{1,n_{tp}} \\ p_{2,1} \\ p_{2,2} \\ \vdots \\ p_{n_p,n_{tp}} \end{bmatrix} = \begin{bmatrix} a_{1,1,1,1} & a_{1,2,1,1} & \cdots & a_{1,n_{ta},1,1} & a_{2,1,1,1} & a_{2,2,1,1} & \cdots & a_{n_a,n_{ta},1,1} \\ a_{1,1,1,2} & a_{1,2,1,2} & \cdots & a_{1,n_{ta},1,2} & a_{2,1,1,2} & a_{2,2,1,2} & \cdots & a_{n_a,n_{ta},1,2} \\ \vdots & \vdots & \ddots & \vdots & \vdots & \vdots & \ddots & \vdots \\ a_{1,1,1,n_{tp}} & a_{1,2,1,n_{tp}} & \cdots & a_{1,n_{ta},1,n_{tp}} & a_{2,1,1,n_{tp}} & a_{2,2,1,n_{tp}} & \cdots & a_{n_a,n_{ta},1,n_{tp}} \\ a_{1,1,2,1} & a_{1,2,2,1} & \cdots & a_{1,n_{ta},2,1} & a_{2,1,2,1} & a_{2,2,2,1} & \cdots & a_{n_a,n_{ta},2,1} \\ a_{1,1,2,2} & a_{1,2,2,2} & \cdots & a_{1,n_{ta},2,2} & a_{2,1,2,2} & a_{2,2,2,2} & \cdots & a_{n_a,n_{ta},2,2} \\ \vdots & \vdots & \ddots & \vdots & \vdots & \vdots & \ddots & \vdots \\ a_{1,1,n_p,n_{tp}} & a_{1,2,n_p,n_{tp}} & \cdots & a_{1,n_{ta},n_p,n_{tp}} & a_{2,1,n_p,n_{tp}} & a_{2,2,n_p,n_{tp}} & \cdots & a_{n_a,n_{ta},n_p,n_{tp}} \end{bmatrix} \begin{bmatrix} t_{1,1} \\ t_{1,2} \\ \vdots \\ t_{1,n_{ta}} \\ t_{2,1} \\ t_{2,2} \\ \vdots \\ t_{n_a,n_{ta}} \end{bmatrix}, \quad (21)$$

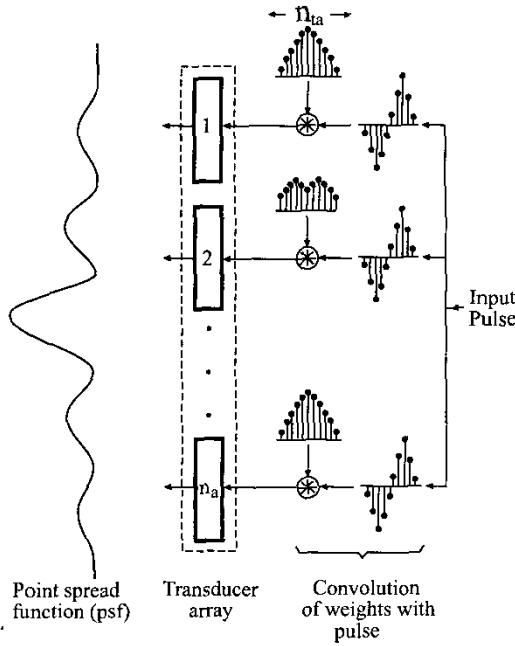


Fig. 1. Broadband formulation. The pulse applied to each element is convolved with a set of weights that is distinct for each element. This operation is analogous to applying an FIR filter to each element/channel.

The generation of a one-way psf is shown in Fig. 1. The transmit pulse applied to each element is first convolved with a set of weights that is unique for each element. The results of these convolutions then are convolved with the respective element spatial impulse responses and finally summed in space to generate the beam pattern. Note that the broadband formulation in (22) describes the psf at a single range. Therefore, the formulation does not perform a convolution to determine the ultrasonic field at multiple range points. However, there is a convolution that describes the response at each lateral point of interest as a function of time in the formulation. The transmit weights that are calculated using the formulation are eventually convolved with the pulse (and the element response) to form the resultant beam pattern. This operation would impact the field at multiple ranges.

We can now derive the transmit weightings that force the one-way system psf to optimally resemble a specified goal psf, \tilde{P}_{Tz} . The SSE between the goal and system one-way psfs at range z can be expressed as:

$$SSE = (P_{Tz} - \tilde{P}_{Tz})^T (P_{Tz} - \tilde{P}_{Tz}), \quad (25)$$

where the superscript T indicates a transpose operation. A conjugate operation is unnecessary because the weights are real valued. Substituting (23) in (25) yields:

$$SSE = (A_z T - \tilde{P}_{Tz})^T (A_z T - \tilde{P}_{Tz}). \quad (26)$$

As in the CW formulations, the transmit weightings that minimize the SSE can be determined using [7] and are given by:

$$T = (A_z^T A_z)^{-1} A_z^T \tilde{P}_{Tz} = A_z^\# \tilde{P}_{Tz}, \quad (27)$$

where $A_z^\#$ is the pseudoinverse of A_z .

2. One-Way Analysis with Weighting Function: As in the CW analysis, we can incorporate a weighting function F in the analysis. In the broadband case, however, F is an $(n_p \cdot n_{tp}) \times 1$ element weighting vector as shown below.

$$F = \begin{bmatrix} f_{1,1} \\ f_{1,2} \\ \vdots \\ f_{1,n_{tp}} \\ f_{2,1} \\ f_{2,2} \\ \vdots \\ f_{n_p,n_{tp}} \end{bmatrix}, \quad (28)$$

where F consists of the weighting to be applied to the field at each of n_p points in space, at each of n_{tp} points in time. It comprises elements of the form $f_{i,j}$, which is the weighting applied to the field at point i at time sample j . The SSE (26) can be rewritten with the weighting function as:

$$SSE = (F_d A_z T - F_d \tilde{P}_{Tz})^T (F_d A_z T - F_d \tilde{P}_{Tz}), \quad (29)$$

where F_d is a diagonalized $(n_p \cdot n_{tp}) \times (n_p \cdot n_{tp})$ matrix with the elements of F along its 0th diagonal. The solution for the transmit weightings, therefore, is:

$$\begin{aligned} T &= \left((F_d A_z)^T F_d A_z \right)^{-1} (F_d A_z)^T F_d \tilde{P}_{Tz} \\ &= (A_z^T F_d^T F_d A_z)^{-1} A_z^T F_d^T F_d \tilde{P}_{Tz} \\ &= (F_d A_z)^\# F_d \tilde{P}_{Tz}, \end{aligned} \quad (30)$$

where $(F_d A_z)^\#$ is the pseudoinverse of $F_d A_z$.

3. Two-Way Analysis: The two-way pulse-echo psf can also be expressed as a linear algebra formulation in a similar fashion to the one-way psf:

$$P_{TRz} = A_{zz} R, \quad (31)$$

where A_{zz} is the propagation function, and R is the $(n_a \cdot n_{ta}) \times 1$ weighting vector with weights for each of n_a receive elements at each of n_{ta} time samples. A_{zz} is a function of the transmit aperture weights, the excitation pulse, and the element impulse responses of the transmit and receive apertures. The SSE between the goal and system pulse-echo psfs at range z is:

$$SSE = \left(P_{TRz} - \tilde{P}_{TRz} \right)^T \left(P_{TRz} - \tilde{P}_{TRz} \right), \quad (32)$$

where \tilde{P}_{TRz} is the goal or desired pulse-echo psf at range z . We can substitute (31) in (32) and solve for the receive weightings to be applied using [7]:

$$SSE = \left(A_{zz} R - \tilde{P}_{TRz} \right)^T \left(A_{zz} R - \tilde{P}_{TRz} \right), \quad (33)$$

$$R = \left(A_{zz}^T A_{zz} \right)^{-1} A_{zz}^T \tilde{P}_{TRz} = A_{zz}^\# \tilde{P}_{TRz}, \quad (34)$$

where $A_{zz}^\#$ is the pseudoinverse of A_{zz} .

4. Two-Way Analysis with Weighting Function: We again can include a weighting function F , which is an $(n_p \cdot n_{tp}) \times 1$ element weighting vector. Solving after application of the weighting function yields the following receive weightings:

$$\begin{aligned} R &= \left((F_d A_{zz})^T F_d A_{zz} \right)^{-1} (F_d A_{zz})^T F_d \tilde{P}_{TRz} \\ &= (A_{zz}^T F_d^T F_d A_{zz})^{-1} A_{zz}^T F_d^T F_d \tilde{P}_{TRz} \\ &= (F_d A_{zz})^\# F_d \tilde{P}_{TRz}, \end{aligned} \quad (35)$$

where F_d is again a diagonalized $(n_p \cdot n_{tp}) \times (n_p \cdot n_{tp})$ matrix with the elements of F along its 0th diagonal, and $(F_d A_{zz})^\#$ is the pseudoinverse of $F_d A_{zz}$.

5. Reduced Computational Cost Through Symmetry Relations: The computation of aperture weights in the MSSE

technique requires significant resources, due to the pseudoinverse operation and the large propagation matrices required. Note that the application of the weights has a much lower computational cost than the design of the weights. In order to reduce the computational complexity of our broadband formulation, we take advantage of the symmetry present in the system. We first use the lateral symmetry of the psf. This symmetry means that we can, if we choose, use just half of both the goal and system psfs for the calculation of the optimal weightings. The one-way psf is then:

$$P_z = \begin{bmatrix} p_{1,1} & p_{2,1} & \cdots & p_{n_p/2,1} \\ p_{1,2} & p_{2,2} & \cdots & \cdot \\ \cdot & \cdot & \cdots & \cdot \\ \cdot & \cdot & \cdots & \cdot \\ p_{1,n_{tp}} & \cdot & \cdots & p_{n_p/2,n_{tp}} \end{bmatrix}, \quad (36)$$

where P_z is an $(n_p/2) \times (n_{tp})$ matrix, consisting of the field at each of only $n_p/2$ points in space at each of n_{tp} points in time. Eq. (36) can be rewritten as:

$$P_z = \begin{bmatrix} p_{1,1} \\ p_{1,2} \\ \cdot \\ p_{1,n_{tp}} \\ p_{2,1} \\ p_{2,2} \\ \cdot \\ p_{n_p/2,n_{tp}} \end{bmatrix}, \quad (37)$$

where P_z is an $(n_p/2 \cdot n_{tp}) \times 1$ vector. The goal psf also must be rewritten in a similar fashion.

The symmetry of the transmit and receive apertures is another property that can be exploited to reduce computational cost. As shown in Fig. 2, pairs of elements can be generated by grouping elements on either side that are at the same distance from the center axis, because these elements will have the same weightings, assuming no beamsteering. Assuming that the aperture comprises an even number of elements, the transmit weightings then can be expressed as:

$$T = \begin{bmatrix} t_{1,n_a,1} & t_{2,n_a-1,1} & \cdots & t_{n_a/2,n_a/2+1,1} \\ t_{1,n_a,2} & t_{2,n_a-1,2} & \cdots & \cdot \\ \cdot & \cdot & \cdots & \cdot \\ \cdot & \cdot & \cdots & \cdot \\ t_{1,n_a,n_{ta}} & \cdot & \cdots & t_{n_a/2,n_a/2+1,n_{ta}} \end{bmatrix}, \quad (38)$$

where $t_{i,j,k}$ is the aperture weighting for elements i and j

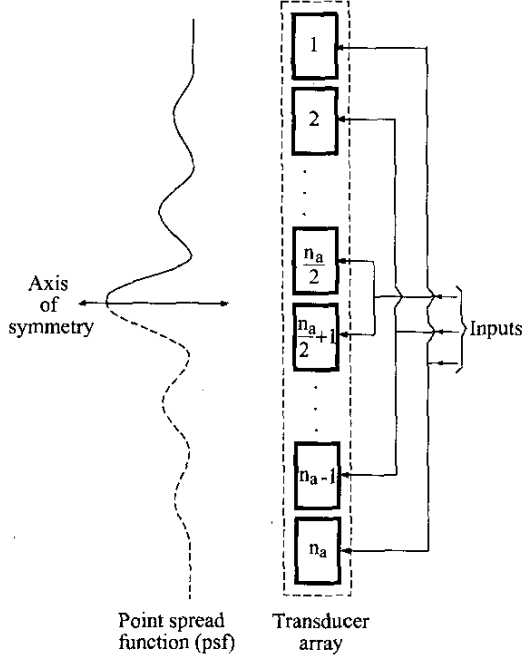


Fig. 2. Exploitation of symmetry for reduced computational cost. Because the aperture is symmetric about the center elements, pairs of elements that would have the same weights are grouped together. Also, the lateral symmetry of the psf about the center axis permits analysis with just one half of the psf.

at time k . Eq. (38) also can be reshaped as follows:

$$T = \begin{bmatrix} t_{1,n_a,1} \\ t_{1,n_a,2} \\ \vdots \\ t_{1,n_a,n_{ta}} \\ t_{2,n_a-1,1} \\ t_{2,n_a-1,2} \\ \vdots \\ t_{n_a/2,n_a/2+1,n_{ta}} \end{bmatrix}, \quad (39)$$

where the first n_{ta} elements are the aperture weightings for elements 1 and n_a at each of n_{ta} time samples, the next n_{ta} elements are the weightings for elements 2 and $n_a - 1$ at the same n_{ta} time samples, and so on until the last n_{ta} weightings for elements $n_a/2$ and $n_a/2 - 1$.

The derivation is now analogous to the analysis in (23) and (25)–(27) yielding the transmit weightings:

$$T = (A_z^T A_z)^{-1} A_z^T \tilde{P}_{Tz} = A_z^\# \tilde{P}_{Tz}. \quad (40)$$

This use of symmetry reduces the size of the matrix subject to the pseudoinverse operation by a factor of 2 in each dimension; therefore, it also reduces the required memory. The same technique can be applied in the two-way pulse-echo scenario to reduce computational cost.

III. APPLICATIONS

The MSSE technique described above is extremely general and can be applied in wide-ranging scenarios. A few possible applications are described.

A. Enhanced Depth of Field

The DOF of an ultrasound imaging system is generally defined as the axial region over which the system is in focus, or more rigorously, the axial region over which the system response satisfies some chosen criterion. It is generally desired that the system psf remains similar to the psf at the focus for as large an axial span as possible.

Current techniques to improve DOF include transmit apodization, dynamic receive apodization, and dynamic receive focusing [1]. However effective the above techniques are, their implementation is typically ad hoc and lacks formal theory describing their effectiveness in improving DOF. If the MSSE technique is implemented for every range under consideration, with the goal psf being the psf obtained at the focus, we can derive formally the receive apodization weightings that force the psf at each specific range of interrogation to be maximally similar by minimizing the SSE. These weightings can then be used to implement dynamic apodization and maximize the DOF.

As demonstrated in (11) and (12), we can express the pulse-echo two-way psf at a range z as the point-by-point multiplication of the one-way transmit and receive psfs at range z :

$$P_{TRz} = P_{Tz} \cdot P_{Rz} = (S_z T) \cdot (S_z R) \quad (41)$$

$$P_{TRz} = P_{Tzd} P_{Rz} = P_{Tzd} S_z R = P_{TzdS} R. \quad (42)$$

The transmit psf, P_{Tz} , is fixed at each range of interrogation because we consider each transmit focus separately. From (15), the receive weightings at a range z that minimize the SSE between the psf at the focus and the psf at z , and therefore maximize the DOF are:

$$R = (P_{TzdS}^H P_{TzdS})^{-1} P_{TzdS}^H \tilde{P}_{TRz} = P_{TzdS}^\# \tilde{P}_{TRz}, \quad (43)$$

where \tilde{P}_{TRz} is the psf at the focus.

B. Limited Diffraction Transmit Beams

Modern ultrasound systems use dynamic receive focusing and dynamic apodization to expand their useful DOF. Ultimately, however, the DOF is limited by the use of a fixed transmit focus. Thus, multiple transmissions with different focal ranges must be performed along each image line in order to obtain a high quality image. This slows image acquisition significantly.

Limited diffraction beams [9] have been suggested as a way to enhance DOF without requiring multiple transmissions. The MSSE technique described here can be readily

applied to design such beams. We present CW analysis to generate limited diffraction beams through the application of appropriate transmit weights.

If $P_1, P_2, P_3, \dots, P_Q$ are CW transmit (one-way) psfs at Q different ranges of interest, and we are interested in maintaining the transmit beam profile through these ranges, the objective is to derive a set of transmit aperture weightings that would minimize the SSE between the system and goal psfs at each of these ranges. We can express the one-way psfs at all ranges of interest as follows:

$$\begin{bmatrix} P_1 \\ P_2 \\ P_3 \\ \vdots \\ P_Q \end{bmatrix} = P_{TQ} = \begin{bmatrix} S_1 \\ S_2 \\ S_3 \\ \vdots \\ S_Q \end{bmatrix} [T] = S_Q T, \quad (44)$$

where P_{TQ} is a $(M \cdot Q) \times 1$ vector made up of Q vertically tiled M -point psfs at the Q ranges of interest, S_Q is an $(M \cdot Q) \times N$ matrix made up of Q vertically tiled $M \times N$ propagation matrices, one for each of the Q ranges of interest, and T is the $N \times 1$ vector of transmit aperture weightings. The SSE then can be expressed as follows:

$$SSE = (P_{TQ} - \tilde{P}_{TQ})^H (P_{TQ} - \tilde{P}_{TQ}), \quad (45)$$

$$\text{where } \tilde{P}_{TQ} = \begin{bmatrix} \tilde{P}_1 \\ \tilde{P}_2 \\ \tilde{P}_3 \\ \vdots \\ \tilde{P}_Q \end{bmatrix},$$

is an $(M \cdot Q) \times 1$ vector consisting of Q vertically tiled $M \times 1$ goal or desired psfs, one for each range. Note that \tilde{P}_{TQ} cannot be constructed by simply replicating the same psf Q times, because constructing one-way psfs with the same phase at each range is impossible. In CW implementation, an appropriate phase term that accounts for propagation must be applied to the goal psf at each range. This phase term is a function of the range under consideration and the wave propagation speed. In broadband implementation, appropriate time delays need to be applied. Using (44), (45) can be rewritten and solved to obtain the transmit weightings that minimize the SSE:

$$SSE = (S_Q T - \tilde{P}_{TQ})^H (S_Q T - \tilde{P}_{TQ}), \quad (46)$$

$$T = (S_Q^H S_Q)^{-1} S_Q^H \tilde{P}_{TQ} = S_Q^\# \tilde{P}_{TQ}, \quad (47)$$

where $S_Q^\#$ is the pseudoinverse of S_Q .

Eq. (47) specifies the complex weightings to be applied to the transmit aperture to obtain one-way transmit psfs at the specified ranges that optimally resemble the goal psfs. Therefore, these transmit weightings will result in a limited diffraction transmit beam, which will have a beneficial impact on DOF.

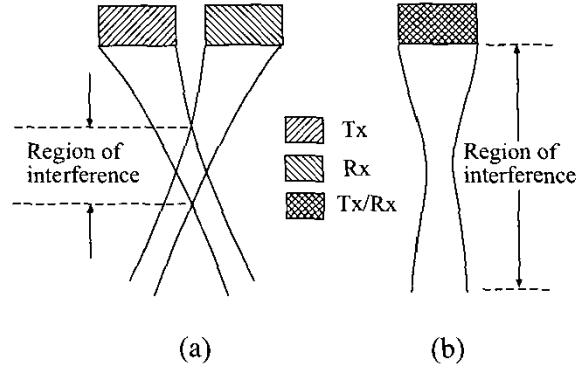


Fig. 3. Reduced DOF in translated aperture geometries. (a) depicts the angular scatter geometry, and (b) shows the backscatter geometry. The reduced depth of field is due to the limited region of overlap of the transmit and receive beams in (a), as compared to the completely coincident transmit and receive beams in (b).

C. Increased Correlation Depth of Field in Translated Aperture Geometries

Biological tissues are known to exhibit variations in angular scattering [10]–[12]. That is, the scattered echo magnitude and phase depend upon the angle between the propagation vectors of the incident and observing waves. It has long been hypothesized that this parameter might offer valuable diagnostic information. We have proposed using the translating apertures algorithm (TAA), as the foundation of angular scatter imaging methods [13]. Previous methods that were used to make angular scatter measurements [14], [15] have entailed the use of pistons that were mechanically rotated to measure the average angular scatter over some area at a single frequency. Imaging systems also have been developed to make images at a single scattering angle other than 180° [16], [17]. However, in all these methods the speckle pattern that was obtained varied with angle, and images obtained at different angles could not be processed coherently to obtain accurate complex angular scatter information. The reason for the change in the speckle pattern was a rotation of the system psf with a change in the relative position of the transmit and receive apertures. In the TAA, the transmit and receive apertures are translated by an equal distance in opposite directions. This enables the acquisition of accurate angular scatter data without the confounding influence of system psf rotation.

Although offering several advantages, the TAA results in a significantly reduced DOF as the transmit and receive apertures are translated. This is due to the crossing of the transmit and receive beams, which results in interference over a reduced area as the apertures are translated. This is shown in Fig. 3. Our technique of optimizing dynamic receive aperture weightings can be applied to improve the correlation DOF between the backscatter (nontranslated) and angular scatter (translated) geometry psfs at a specific range. Note that the previously described symmetry technique for the broadband formulation cannot be completely

utilized in translated aperture geometries. This is due to a loss of symmetry that is caused by the translation of the apertures, which results in unique element weightings for each element. We can write the two-way CW psf for the backscatter geometry at range z as follows:

$$P_{TRz0} = P_{Tz0} \cdot P_{Rz0} = (S_{Tz0} T_0) \cdot (S_{Rz0} R_0), \quad (48)$$

where P_{Tz0} and P_{Rz0} are the $M \times 1$ transmit and receive psfs, respectively; S_{Tz0} and S_{Rz0} are the $M \times N$ transmit and receive propagation functions, respectively, at range z ; and T_0 and R_0 are the $N \times 1$ transmit and receive aperture weightings, respectively. The subscript '0' denotes no translation (zero shift), or the backscatter geometry. Similarly, the two-way CW psf for the angular scatter geometry at the same range z is:

$$P_{TRz1} = P_{Tz1} \cdot P_{Rz1} = (S_{Tz1} T_1) \cdot (S_{Rz1} R_1), \quad (49)$$

where P_{Tz1} and P_{Rz1} are the $M \times 1$ transmit and receive psfs, respectively; S_{Tz1} and S_{Rz1} are the $M \times N$ transmit and receive propagation functions, respectively, at range z ; T_1 and R_1 are the $N \times 1$ transmit and receive aperture weightings, respectively; and the subscript '1' denotes the translated angular scatter geometry. Because the apertures are translated, the propagation functions are no longer the same for the transmit and receive apertures. Eq. (49) can be rewritten as:

$$P_{TRz1} = P_{Tz1d} P_{Rz1} = P_{Tz1d} S_{Rz1} R_1 = P_{Tz1dS} R_1, \quad (50)$$

where P_{Tz1d} is a diagonalized $M \times M$ matrix with the elements of P_{Tz1} along its 0th diagonal, and

$$P_{Tz1dS} = P_{Tz1d} S_{Rz1}. \quad (51)$$

Our objective is to maintain a constant system response as the apertures are translated. Again, this means maximizing the correlation between the system responses of the backscatter and angular scatter geometries, or minimizing the SSE between the two psfs. The SSE can be expressed as follows:

$$SSE = (P_{TRz1} - P_{TRz0})^H (P_{TRz1} - P_{TRz0}). \quad (52)$$

Using (50), (52) can be modified and solved to obtain the receive weightings that minimize the SSE as:

$$SSE = (P_{Tz1dS} R_1 - P_{TRz0})^H (P_{Tz1dS} R_1 - P_{TRz0}), \quad (53)$$

$$R_1 = (P_{Tz1dS}^H P_{Tz1dS})^{-1} P_{Tz1dS}^H P_{TRz0} = P_{Tz1dS}^\# P_{TRz0}. \quad (54)$$

where $P_{Tz1dS}^\#$ is the pseudoinverse of P_{Tz1dS} .

Eq. (54) specifies the complex weightings to be applied to the transducer elements that comprise the receive aperture after translating the apertures. Application of these

weightings would generate a system psf P_{TRz1} at the range z that optimally resembles the goal psf P_{TRz0} , or the psf with no translation.

D. Optimal Receive Weighting for Harmonic Imaging

The previously described MSSE technique is not limited to aperture design assuming linear propagation. Conventional ultrasound imaging assumes linear propagation of the ultrasound pulse, and the receive process assumes that the received echoes have the same frequency content as that of the transmitted pulse. However, the propagation process is nonlinear and shifts some of the signal energy to harmonics of the fundamental frequency. Current state-of-the-art ultrasound systems have the capability of imaging echoes received at these higher harmonics (harmonic imaging), for improved image contrast and resolution [18]. Our technique of dynamic weighting can be adapted to design receive apertures for harmonic imaging. The transmit beam profile resulting from nonlinear processes can be determined analytically, experimentally, or through simulations, and be substituted into our formulation. The algorithm assumes linear propagation during the receive process. Eq. (15), which is rewritten below, describes the relationship between the optimum weightings and the analytically or experimentally determined goal psf.

$$R = (P_{Tzds}^H P_{Tzds})^{-1} P_{Tzds}^H \tilde{P}_{TRz} = P_{Tzds}^\# \tilde{P}_{TRz}.$$

IV. DISCUSSION

The MSSE technique is a generalized technique for the design of arbitrary system responses, through the use of aperture weights. Analysis that illustrates the theory underlying the technique has been presented for both CW and broadband systems. The propagation functions that have been described can be determined through experiments and simulations or derived from theory.

The real-time implementation of the beamformer is conceptually simple. In the CW case, complex apodization would be used to implement the technique. The weights either can be stored and retrieved in a look-up table or calculated as required. For the broadband case, implementation is analogous to using an FIR filter on each channel. In the one-way design implementation, conventional FIR filters would be used; in the two-way design implementation, dynamic shift-variant FIR filters would be used. There are no restrictions on filter length; the algorithm uses the specified length to optimize performance. However, as in conventional FIR filters, performance depends upon the filter length, and it is advisable to have the maximum possible length that can be practically implemented. Some current ultrasound systems already have a crude FIR filter on each channel, and they conceivably could be extended to apply the MSSE technique by modifying them to be shift variant. Again, the weights can either be stored and retrieved in a look-up table system or calculated as required.

The design method described here is different and superior to the pseudoinverse based methods described in [3] and [4] for several reasons. The methods in [3] and [4] are limited to CW systems. We present analysis for CW as well as broadband systems. Our method is also more general as we describe a general method for the design of apertures for any application. Another important distinction is that the methods in [3] and [4] are limited to one-way analysis (i.e., either transmit or receive). Our technique is adaptable for one-way or two-way analysis. Another distinction is that in [3] and [4], a few control points were used in order to ensure an underdetermined system of equations and obtain an exact beam pattern at those few points; in our technique, the entire goal psf is used to obtain the least squares solution of an overdetermined system of equations. This method enables excellent control of the system psf, and has a significant impact on aperture design for several applications such as improved DOF. Simulation results for these and other examples are described in an accompanying paper [2].

V. CONCLUSIONS

The MSSE technique is a general beamforming method that can be used to design apertures for specific applications. It enables the design of arbitrary beam profiles by calculating the appropriate optimum aperture weightings. The system performance is optimized because the calculated weightings minimize the SSE between the desired and achieved system responses. The algorithm can be implemented readily in both CW and broadband systems. In CW systems, the receive weights can be implemented through apodization and time delays or complex weights. In broadband systems, implementation is analogous to having a dynamic FIR filter on each channel.

REFERENCES

- [1] K. Thomenius, "Evolution of ultrasound beamformers," in *Proc. IEEE Ultrason. Symp.*, 1996, pp. 1615–1622.
- [2] K. Ranganathan and W. F. Walker, "A novel beamformer design method for medical ultrasound. Part II: Simulation results," *IEEE Trans. Ultrason., Ferroelect., Freq. Contr.*, vol. 50, no. 1, pp. 25–39, 2003.
- [3] E. S. Ebbini and C. Cain, "Multiple-focus ultrasound phased-array pattern synthesis: Optimal driving-signal distributions for hyperthermia," *IEEE Trans. Ultrason., Ferroelect., Freq. Contr.*, vol. 36, no. 5, pp. 540–548, 1989.
- [4] P.-C. Li, S. W. Flax, E. S. Ebbini, and M. O'Donnell, "Blocked element compensation in phased array imaging," *IEEE Trans. Ultrason., Ferroelect., Freq. Contr.*, vol. 40, no. 4, pp. 283–292, 1993.
- [5] J. W. Goodman, *Introduction to Fourier Optics*, 2nd ed. New York: McGraw-Hill, 1988.
- [6] A. R. Selfridge, G. S. Kino, and B. T. Khuri-Yakub, "A theory for the radiation pattern of a narrow-strip acoustic transducer," *Appl. Phys. Lett.*, vol. 37, no. 1, pp. 35–36, 1980.
- [7] L. L. Scharf, *Statistical Signal Processing: Detection, Estimation, and Time Series Analysis*. Reading, MA: Addison-Wesley, 1991.
- [8] B. D. Steinberg, *Principles of Aperture and Array System Design: Including Random and Adaptive Arrays*. New York: Wiley, 1976.
- [9] J.-Y. Lu, "Experimental study of high frame rate imaging with limited diffraction beams," *IEEE Trans. Ultrason., Ferroelect., Freq. Contr.*, vol. 45, no. 1, pp. 84–97, 1998.
- [10] R. C. Chivers and C. R. Hill, "A spectral approach to ultrasonic scattering from human tissue: Methods, objectives and backscattering measurements," *Phys. Med. Biol.*, vol. 20, no. 5, pp. 799–815, 1975.
- [11] D. K. Nassiri and C. R. Hill, "The use of acoustical angular scattering measurements to estimate structural parameters of human and animal tissues," *J. Acoust. Soc. Amer.*, vol. 79, no. 6, pp. 2048–2054, 1986.
- [12] J. A. Campbell and R. C. Waag, "Ultrasonic scattering properties of three random scattering media," *J. Acoust. Soc. Amer.*, vol. 75, pp. 1879–1886, 1984.
- [13] W. F. Walker, "C- and d-weighted ultrasonic imaging using the translating apertures algorithm," *IEEE Trans. Ultrason., Ferroelect., Freq. Contr.*, vol. 48, no. 2, pp. 452–461, 2001.
- [14] W. J. Davros, J. A. Zagzebski, and E. L. Madsen, "Frequency-dependent angular scattering of ultrasound by tissue-mimicking materials and excised tissue," *J. Acoust. Soc. Amer.*, vol. 80, pp. 229–237, 1986.
- [15] J. A. Campbell and R. C. Waag, "Measurements of calf liver ultrasonic differential and total scattering cross sections," *J. Acoust. Soc. Amer.*, vol. 75, pp. 603–611, 1984.
- [16] M. T. Robinson and O. T. Von Ramm, "Real-time angular scatter imaging system for improved tissue contrast in diagnostic ultrasound images," *IEEE Trans. Ultrason., Ferroelect., Freq. Contr.*, vol. 41, no. 1, pp. 44–52, 1994.
- [17] J. C. Lacefield, "Angular scatter ultrasound imaging using separated arrays," Ph.D. dissertation, Durham, NC: Duke University, 1999.
- [18] F. Tranquart, N. Grenier, V. Eder, and L. Pourcelot, "Clinical use of ultrasound tissue harmonic imaging," *Ultrasound Med. Biol.*, vol. 25, no. 6, pp. 889–894, 1999.



Karthik Ranganathan received his B.E. in Biomedical Engineering from the University of Bombay, Bombay, India in 1999.

After completing his B.E., he joined the Department of Biomedical Engineering at the University of Virginia, Charlottesville, VA where he is currently a Ph.D. candidate. His research interests include ultrasound beamforming, signal processing and angular scatter measurement techniques.



William F. Walker (S'95-M'96) received the B.S.E. and Ph.D. degrees in 1990 and 1995 from Duke University, Durham, NC. His dissertation explored fundamental limits on the accuracy of adaptive imaging.

After completing his doctoral work, he stayed on at Duke as an Assistant Research Professor in the Department of Biomedical Engineering. At the same time he served as a Senior Scientist and President of NovaSon Corporation located in Durham, NC. In 1997 he joined the faculty of the Department of Biomedical Engineering at the University of Virginia, Charlottesville, VA as an Assistant Professor. His research interests include aperture domain processing, beamforming, angular scatter imaging, and tissue elasticity imaging.

A Novel Beamformer Design Method for Medical Ultrasound. Part II: Simulation Results

Karthik Ranganathan and William F. Walker, *Member, IEEE*

Abstract—In the first part of this work, we introduced the minimum sum squared error (MSSE) technique of ultrasound beamformer design. This technique enables the optimal design of apertures to achieve arbitrary system responses. In the MSSE technique, aperture weights are calculated and applied to minimize the sum squared error (SSE) between the desired and actual system responses. In this paper, we present the results of simulations performed to illustrate the implementation and validity of the MSSE technique. Continuous wave (CW) and broadband simulations are presented to demonstrate the application of the MSSE method to obtain arbitrary system responses (within fundamental physical limitations of the system). We also describe CW and broadband simulations that implement the MSSE method for improved conventional depth of field (DOF) and for improved correlation DOF in translated aperture geometries. Using the MSSE technique, we improved the conventional DOF by more than 200% in CW simulations and more than 100% in broadband simulations. The correlation DOF in translated aperture geometries was improved by more than 700% in both CW and broadband simulations.

I. INTRODUCTION

IN an accompanying paper [1], we described the minimum sum squared error (MSSE) technique of aperture design. This technique enables the design of ultrasound systems for arbitrary system responses and beam profiles. This is done by calculating and applying the aperture weightings that optimally produce these profiles within fundamental limits imposed by wavelength. In the MSSE design technique, the system point spread function (psf) is expressed in a linear algebra formulation as a function of aperture weights and a propagation function. This propagation function may be derived theoretically or determined by simulations or experiments. The sum squared error (SSE) between the desired (goal) psf and the realized psf is then minimized. A brief review of the major results derived in [1] for both continuous wave (CW) and broadband systems is provided below.

Manuscript received May 16, 2002; accepted August 28, 2002. This work was supported by Susan G. Komen Breast Cancer Foundation Imaging Grant No. 99-3021 and United States Army Congressionally Directed Medical Research Program Grant No. DAMD 17-01-10443. Inspiration from this work stems from National Science Foundation Major Research Instrumentation Grant 0079639.

The authors are with the Department of Biomedical Engineering, University of Virginia, Charlottesville, VA (e-mail: kr6u@virginia.edu).

A. One-Way Continuous Wave Formulation

We can express the one-way transmit psf at some range z as a function of a propagation matrix S_z and the transmit aperture weightings T . S_z may include factors such as limited element angular response [2] and frequency dependent attenuation. This relationship is expressed in a linear algebra formulation as a matrix multiplication. Using [3], we can then derive the least squares solution for the transmit weightings that minimize the sum squared error (SSE) between the system psf and the desired or goal psf. Because the SSE is minimized, application of these transmit weightings results in the generation of a one-way psf that is optimally similar to the goal psf. The transmit weightings that minimize the SSE between the system psf and goal psf are given by:

$$T = (S_z^H S_z)^{-1} S_z^H \tilde{P}_{Tz} = S_z^\# \tilde{P}_{Tz}, \quad (1)$$

where the superscripts H , -1 , and $\#$ denote the conjugate transpose, matrix inverse and pseudoinverse operations, respectively, and \tilde{P}_{Tz} represents the goal psf. $S_z^\#$ is the pseudoinverse of S_z .

B. Two-Way Continuous Wave Formulation

We also can derive the receive aperture weights that would minimize the SSE between the two-way system psf and a two-way desired or goal psf. The two-way psf can be expressed using the well-known radar equation [4]. The radar equation states that the two-way psf is the product of the one-way transmit and receive psfs. The receive psf is expressed as a function of a set of receive weights and a receive propagation matrix in a similar fashion to the transmit psf described in the previous section. The transmit psf is diagonalized to eliminate the point-by-point multiplication operation, and then combined with the receive propagation matrix. This process yields an expression that formulates the two-way psf in a linear algebra formulation as a function of the receive weights and the secondary function derived from the one-way transmit psf and the receive propagation matrix. The SSE between the two-way psf and the goal psf is minimized by the following receive weights:

$$R = (P_{Tzds}^H P_{Tzds})^{-1} P_{Tzds}^H \tilde{P}_{TRz} = P_{Tzds}^\# \tilde{P}_{TRz}, \quad (2)$$

where P_{Tzds} is the secondary function described above and is constructed by diagonalizing P_{Tz} with its elements

along the 0th diagonal, and then multiplying the resulting matrix with the propagation function S_z . $P_{Tz}^\#$ is the pseudoinverse of $P_{Tz}S$.

C. One-Way Broadband Formulation

The above CW formulations are of limited use in broadband ultrasound systems that utilize finite bandwidth pulses. Because CW ultrasound is used only for limited applications such as CW Doppler, we also derived one-way and two-way formulations that adapt the MSSE technique for broadband systems. The one-way psf can be expressed as the product of a propagation matrix A_z with the transmit aperture weights T . The psf is a function of lateral position and time, and the aperture weights are a function of the element number and time. The propagation matrix depends upon the excitation pulse and the impulse responses of the elements that comprise the transmit aperture. Using [3], the transmit weights that minimize the SSE between the system psf and the goal psf can be solved for and are given by:

$$T = (A_z^T A_z)^{-1} A_z^T \tilde{P}_{Tz} = A_z^\# \tilde{P}_{Tz}, \quad (3)$$

where \tilde{P}_{Tz} is the goal or desired psf, and $A_z^\#$ is the pseudoinverse of A_z . Implementation of these weights is analogous to applying a dynamic Finite Impulse Response (FIR) filter to every channel and summing their outputs.

D. Two-Way Broadband Formulation

The two-way pulse-echo psf can be expressed as the product of a two-way propagation matrix A_{zz} with the receive aperture weights R . A_{zz} depends upon the excitation pulse, the transmit and receive aperture element impulse responses, and the transmit aperture weightings. The receive weightings that optimize the system psf are given by:

$$R = (A_{zz}^T A_{zz})^{-1} A_{zz}^T \tilde{P}_{TRz} = A_{zz}^\# \tilde{P}_{TRz}, \quad (4)$$

where \tilde{P}_{TRz} is the goal two-way psf and $A_{zz}^\#$ is the pseudoinverse of A_{zz} .

E. Reduced Computational Cost Through Symmetry Relations

The design of weights via the MSSE technique is computationally expensive because of the need to compute the pseudoinverse of the large propagation matrix during the calculation of the aperture weights. In order to reduce computational complexity, we exploit the lateral symmetry of the transducer apertures and the psfs [1]. Due to this symmetry, it is sufficient to compute only half of the weights, using just half of the psf. This results in the reduction of the computational complexity and enables more efficient computation of the aperture weights. Note that the application of the weights has a relatively low computational cost when compared to the design of the weights.

TABLE I
PARAMETERS USED IN CONTINUOUS WAVE (CW) SIMULATIONS,
UNLESS OTHERWISE MENTIONED.

Parameter	Value
Number of elements	32
Element pitch	135 μm
Focus	1.3 cm
Lateral window over which the psf was calculated	180°
psf window sampling interval	0.01°
Ultrasonic wave propagation speed	1540 m/s
Frequency	10 MHz

TABLE II
PARAMETERS USED IN BROADBAND SIMULATIONS, UNLESS
OTHERWISE MENTIONED.

Parameter	Value
Number of elements	32
Element pitch	135 μm
Focus	1.3 cm
Lateral window over which the psf was calculated	70 mm
psf window sampling interval	50 μm
Ultrasonic wave propagation speed	1540 m/s
Center frequency	10 MHz
-6 dB Bandwidth	75%
Temporal sampling of psf	120 MHz
Temporal spacing of weights for each element	25 ns

The weights can either be computed and stored in a look-up table system or calculated as required. They can then be applied as conventional FIR filters in the one-way design case, or as dynamic shift variant filters in the two-way design case.

All the formulas presented above are comprehensively derived in [1]. This paper describes the results of simulations that were implemented to demonstrate the validity and flexibility of the MSSE design technique.

II. SIMULATIONS

We performed two sets of simulations to investigate the performance of the MSSE technique. The first set was intended to illustrate the implementation of the MSSE technique to obtain a predetermined system psf in CW and broadband systems. The second set was designed to implement the technique in some of the examples of application described in [1]. The default CW system parameters are described in Table I, and the default broadband system parameters are described in Table II. Unless stated otherwise, these parameters were used in all simulations. All simulations were performed in Matlab (The Mathworks, Inc., Natick, MA). We used Field II, an ultrasound simulation package developed by Jensen [5], in all the broadband simulations.

A. Single Range Design Examples

1. *CW One-Way Design Example (Transmit only)*: For all CW simulations, the propagation function was derived from the Rayleigh-Sommerfeld equation ([6, pp. 46–50]). The elements were treated as point sources. The propagation function for the field at an arbitrary point p due to element e is:

$$s_{e,p} = \frac{\exp(jkr_{ep})}{r_{ep}}, \quad (5)$$

where r_{ep} is the length of the vector pointing from element e to field point p , and $k = \frac{2\pi}{\lambda}$ is the wave number, with λ being the acoustic wavelength.

We used the parameters described in Table I in the simulations. We chose the goal psf to be a Hann window [7, pp. 170–172] of width 32° and calculated the optimum transmit weights using (1). No transmit apodization other than the calculated weights was used. The window of analysis was $\pm 90^\circ$. Due to the large angles of interrogation, we included the obliquity factor in these simulations. The obliquity factor accounts for limited element angular response and was included in the propagation function as follows:

$$s_{e,p} = \frac{\exp(jkr_{ep})}{r_{ep}} \cos(\theta_{ep}), \quad (6)$$

where $\cos(\theta_{ep})$ is the obliquity factor, and θ_{ep} is the angle between the vector pointing from element e to field point p , and the vector normal to the plane of the transducer. Because elements were modeled as point sources, the sinc directivity pattern expected for elements of finite extent was not used.

We calculated the system psf after applying the MSSE designed transmit weightings. Figs. 1(a) and 1(b) show the goal psf and the designed system psf, respectively. Figs. 1(c) and 1(d) display the magnitude and phase of the calculated transmit aperture weights.

Performance of the MSSE technique. In an effort to explore the performance of the algorithm, we made the Hann window goal psf increasingly narrower. We progressively reduced the goal psf width to 16° , 8° , and 4° . The Rayleigh resolution limit for the geometry that was used is around 2.04° . Figs. 1(e) and 1(f) show the goal and generated system psfs, respectively, when the goal psf was 16° wide. Figs. 1(g) and 1(h) show the magnitude and phase of the calculated weights, respectively, for the 16° goal psf. Figs. 1(i)–1(l) display the same information for a goal psf of width 8° , and Figs. 1(m)–1(p) depict the results obtained when the goal psf had a width of 4° .

Effects of the size of the window of analysis. The MSSE algorithm optimizes the system psf only within the window of analysis. Effects that occur outside this window are ignored, thereby introducing potential artifacts in the ultrasonic field generated outside the analysis window. We performed simulations to investigate the effects of varying this window's size on the ultrasonic field outside the window. The goal psf was a Hann window that was 6° wide.

The MSSE technique was implemented for analysis window sizes of $\pm 15^\circ$, $\pm 30^\circ$, $\pm 45^\circ$, $\pm 60^\circ$, $\pm 75^\circ$, and $\pm 90^\circ$, sampled every 0.01° . The system psf was then computed over a $\pm 90^\circ$ window using the calculated transmit weights.

Fig. 2(a) depicts the ideal psf used for a $\pm 15^\circ$ window of analysis. Fig. 2(b) illustrates the psf obtained after implementation of the MSSE algorithm, and Fig. 2(c) shows the obtained psf on a logarithmic scale after being normalized to the peak mainlobe level. Figs. 2(d)–2(f), 2(g)–2(i), 2(j)–2(l), 2(m)–2(o), and 2(p)–2(r) depict the same information for window analysis sizes of $\pm 30^\circ$, $\pm 45^\circ$, $\pm 60^\circ$, $\pm 75^\circ$, and $\pm 90^\circ$, respectively. The extent of the window of analysis is shown by dotted lines in each plot.

Effect of errors in the assumed ultrasonic wave propagation speed. The adverse effects of errors in the assumed wave propagation speed on the response of an ultrasound system are well-known [8]. Because the MSSE technique uses dynamic shift-variant aperture weights, errors in the assumed wave speed are an important concern. Therefore, we implemented simulations in which the actual wave speed was underestimated by 25 m/s, 50 m/s, and 75 m/s, and then overestimated by 25 m/s, 50 m/s, and 75 m/s. The goal psf was a 6° wide Hann window. The window of analysis was $\pm 90^\circ$, and it was sampled every 0.01° . We compared the psfs obtained in these simulations to the psf obtained when the assumed speed was correct, which is shown in Fig. 3(a). Figs. 3(c), 3(g), and 3(k) depict the psfs obtained when the assumed sound speed was underestimated by 25 m/s, 50 m/s, and 75 m/s, respectively. Figs. 3(e), 3(i), and 3(m) display the psfs obtained when the assumed speed was overestimated by 25 m/s, 50 m/s, and 75 m/s, respectively. Fig. 3(b) depicts the obtained psf error magnitude when the assumed speed was correct. Figs. 3(d), 3(h), and 3(l) show the psf error magnitude when the speed was underestimated, and Figs. 3(f), 3(j), and 3(n) display the psf error magnitude when the speed was overestimated. The presented psfs were computed at the intended transmit foci, not the shifted foci. The objective of these simulations was to investigate the degradation in the performance of the MSSE algorithm that is produced by an incorrect, assumed propagation speed at a particular location of interest. Simulations were also performed at the shifted focus. Although the results are not presented here, they were qualitatively similar.

2. CW Two-Way Design Example (Transmit-Receive):

A Hann window of width 4° was chosen to be the goal two-way psf. We implemented the MSSE technique by calculating and applying optimum receive aperture weights using (2). No apodization was used on the transmit aperture. Table I lists the parameters used in the simulation. We then computed the two-way system psf using the calculated receive weights. Figs. 4(a) and 4(b) depict the goal psf and the achieved system psf. Fig. 4(c) displays the magnitude of the error between the goal and system psfs. Figs. 4(d) and 4(e) display the magnitude and phase of the calculated receive aperture weights, respectively.

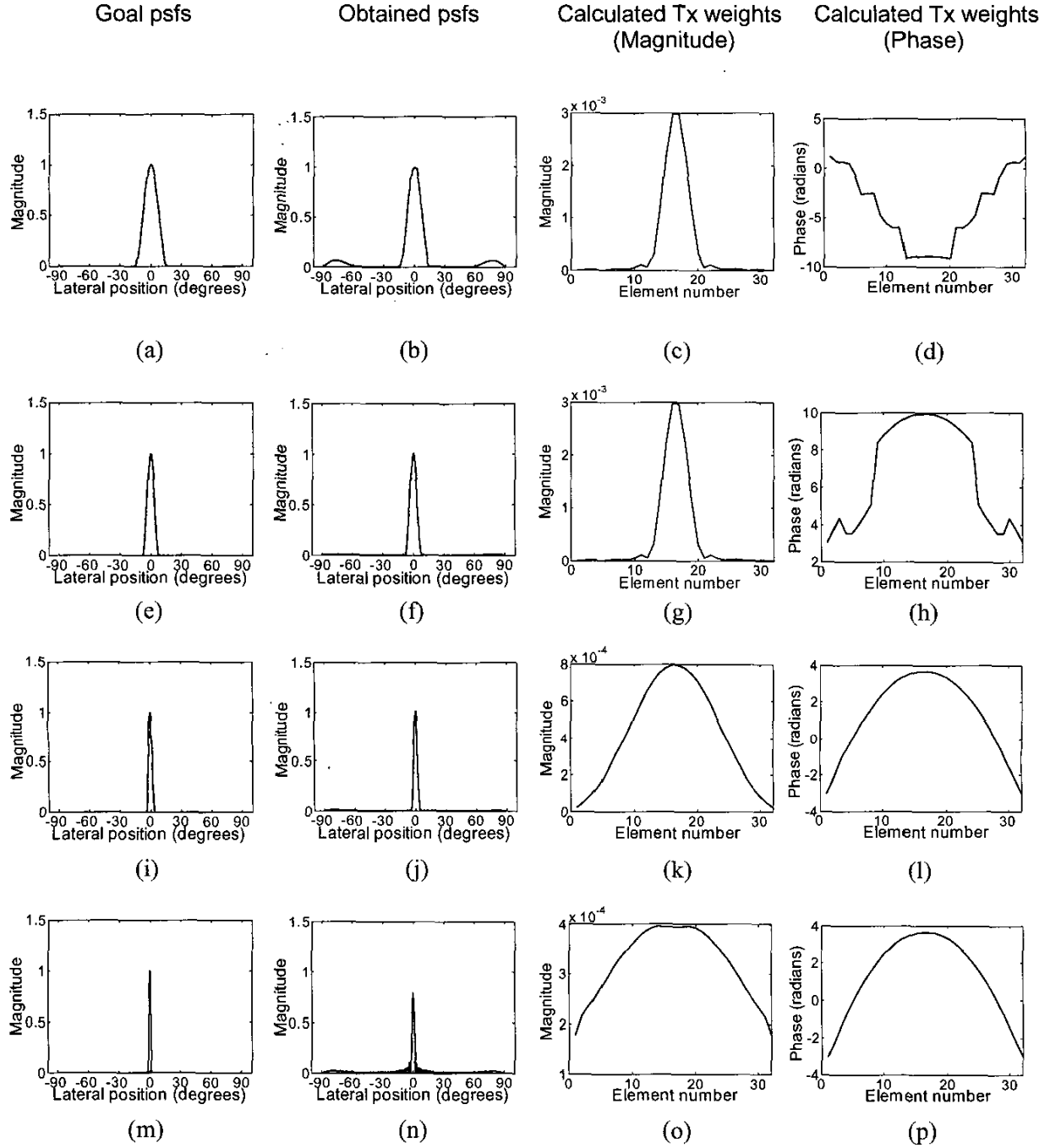


Fig. 1. One-way CW design example for goal psfs of width 32°, 16°, 8°, and 4°. The first column depicts the goal psfs; the second column shows the obtained psfs, both as a function of lateral position. Results for goal psf widths of 32°, 16°, 8°, and 4°, respectively, are shown from top to bottom. The third and fourth columns illustrate the magnitude and phase of the calculated transmit weights, respectively, as a function of element number. It can be seen that the obtained psfs are qualitatively similar to the goal psfs in all the simulations. The profile of the magnitude of the calculated weights shown in (c), (g), (k), and (o) expectedly becomes wider as the goal psf becomes narrower.

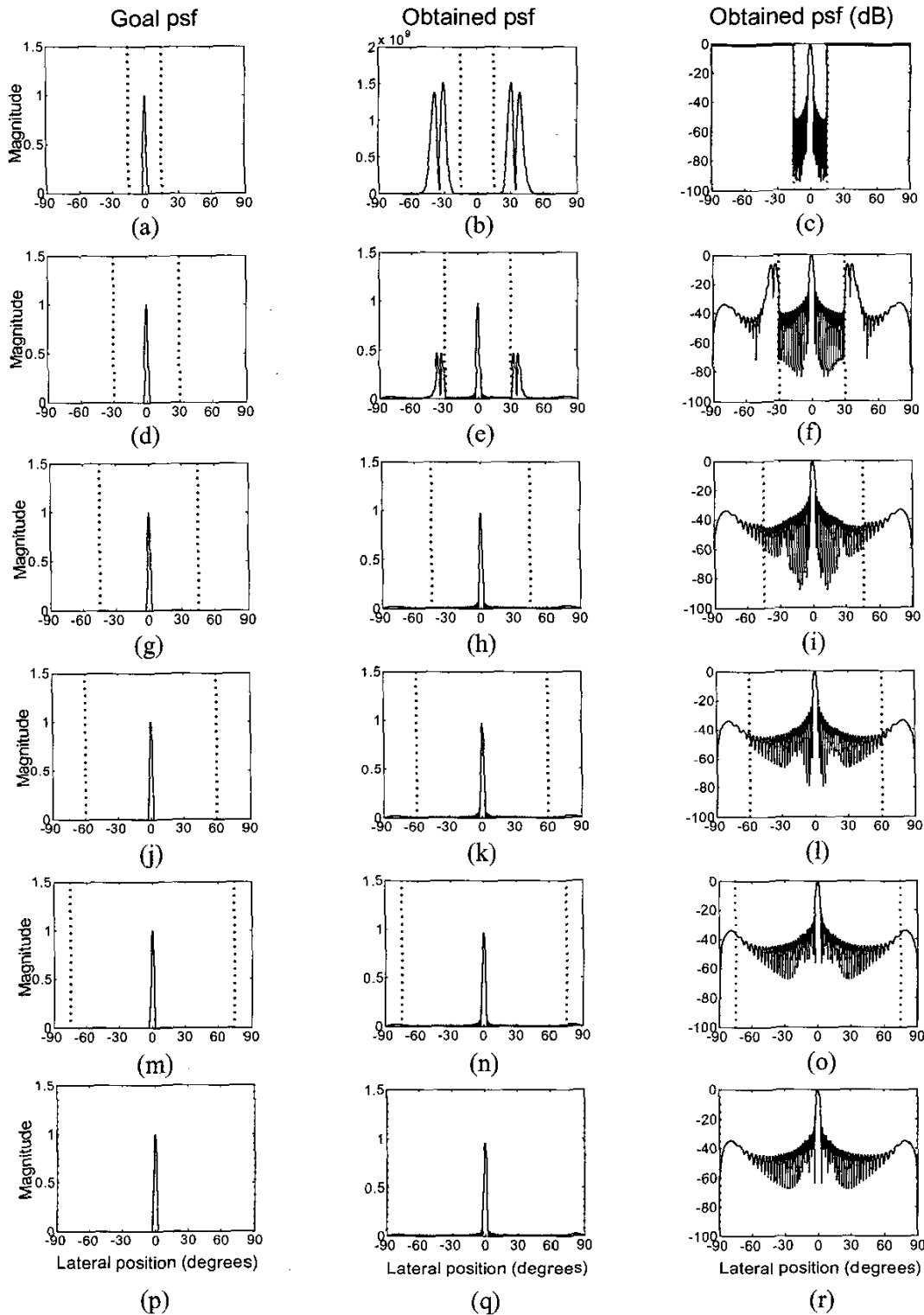


Fig. 2. Effects of the size of the window of analysis. The first column depicts the goal psfs while the second column shows the obtained psfs, respectively, both as a function of lateral position, for different analysis window sizes. Results for analysis window sizes of $\pm 15^\circ$, $\pm 30^\circ$, $\pm 45^\circ$, $\pm 60^\circ$, $\pm 75^\circ$, and $\pm 90^\circ$ are shown from top to bottom. The third column shows the obtained psfs on a logarithmic scale after being normalized to the peak mainlobe level. The edges of the window of analysis are indicated by the dotted lines in each plot. It can be seen clearly that the size of the analysis window plays a critical role in the performance of the MSSE algorithm. As can be seen from plots (b), (c), (e), and (f), the obtained psf has large grating lobes outside the analysis window if it is too small. An analysis window of at least $\pm 45^\circ$ is required.

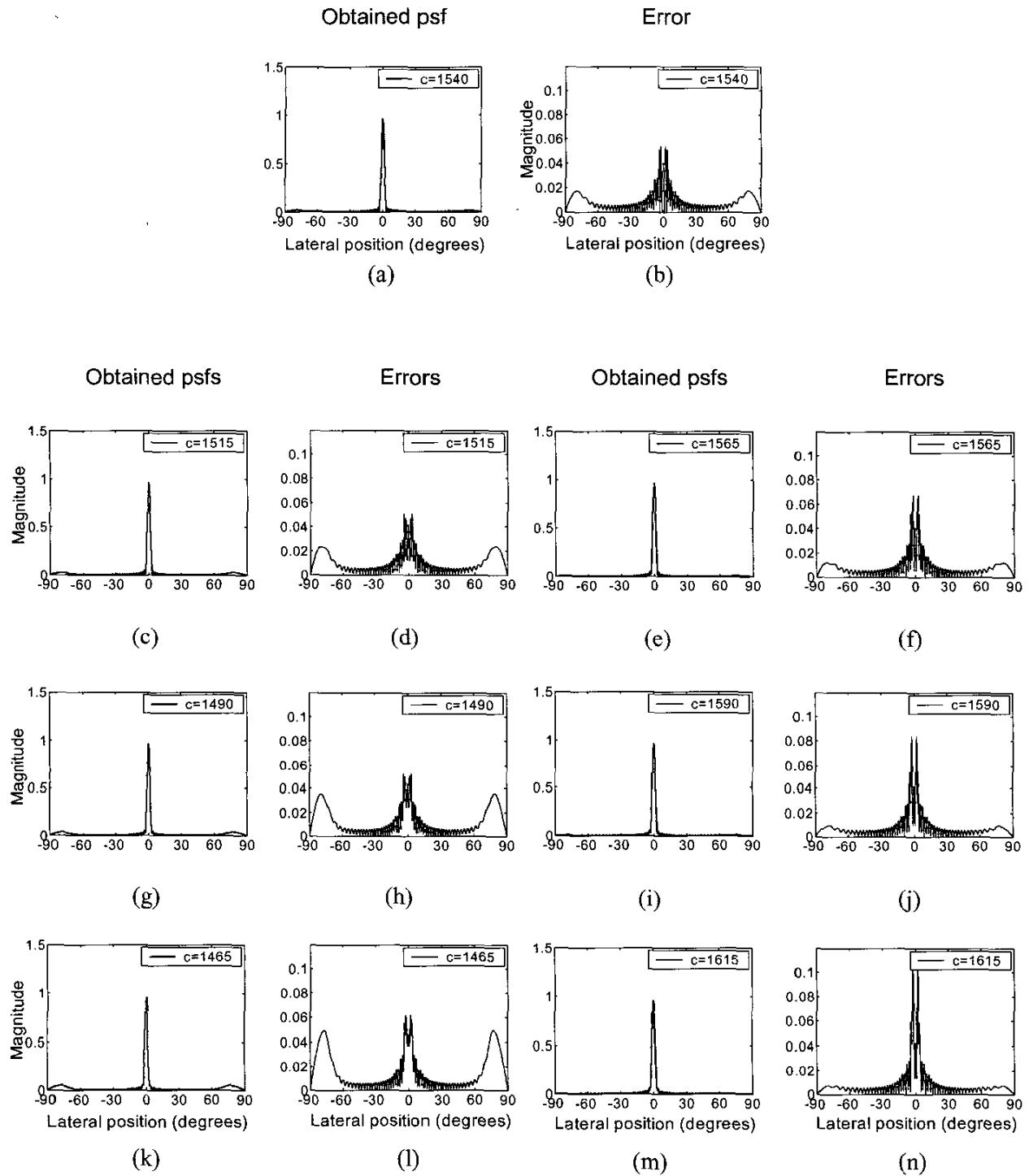


Fig. 3. Effect of errors in the assumed wave propagation speed. The plots show the obtained psfs and psf errors when the assumed wave speed is correct, underestimated by 25 m/s, 50 m/s, and 75 m/s, and overestimated by 25 m/s, 50 m/s, and 75 m/s. (a) depicts the obtained psf with the correct wave speed, and (b) illustrates the obtained psf error. Below, the first and second columns depict the obtained psfs and psf error magnitudes as a function of angle when the speed was underestimated by 25 m/s, 50 m/s, and 75 m/s, respectively. The third and fourth columns depict the obtained psfs and psf error magnitudes as a function of angle when the speed was overestimated by 25 m/s, 50 m/s, and 75 m/s respectively. The performance of the MSSE technique was slightly degraded when the assumed wave propagation speed was incorrect, but the overall errors were reasonable, showing that the MSSE technique is stable.

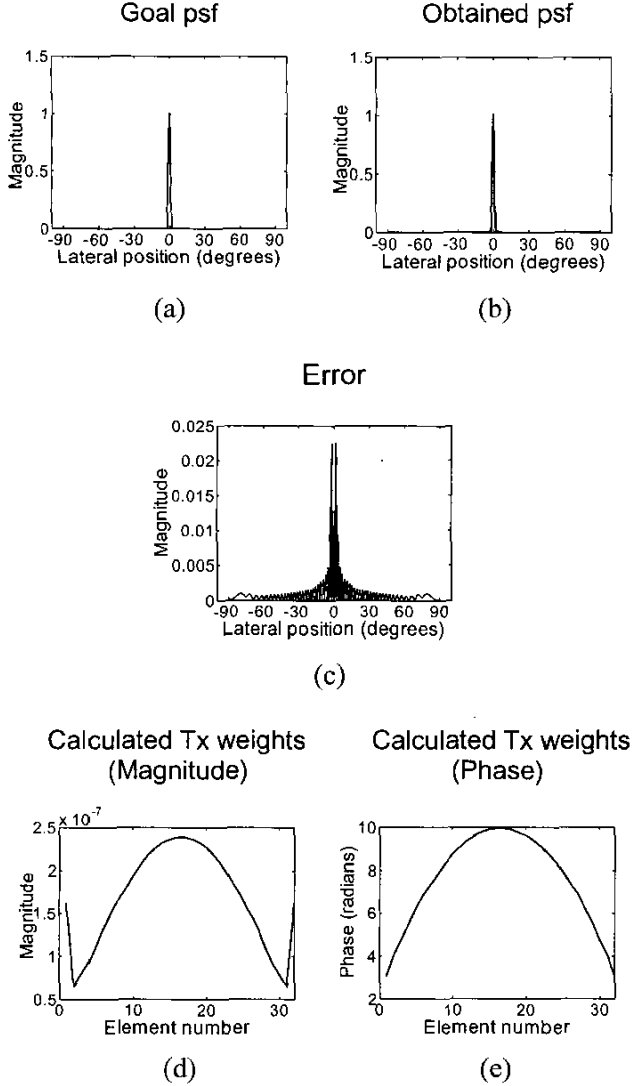


Fig. 4. Two-way CW design example. (a) depicts the goal psf as a function of lateral position, and (b) depicts the obtained psf as a function of lateral position. (c) illustrates the error between the goal and the obtained psfs as a function of lateral position. (d) shows the magnitude and (e) shows the phase of the calculated receive weights, respectively, as a function of element number.

3. Broadband One-Way Example (Transmit only): We used the ultrasound simulation package Field II, developed by Jensen [5], for all broadband simulations. All broadband simulations took advantage of system symmetry to reduce computational complexity [1], as previously described. The propagation matrix, A_z , was a four-dimensional function. For an aperture of N elements, every term of A_z was of the form $a_{i,N-i,j,k,l}$. It determined the field due to the weighting at time sample j applied to elements i and $N-i$, at time sample l at lateral field point k . It was constructed using dual element spatial impulse responses that described the contributions of a selected pair of elements at each field point at each sampled time point. The dual element responses were determined by transmitting only on selected pairs of elements. These were then used to construct the

propagation function. The goal psf was generated by axially weighting a sinusoidal signal by a Hann window, and multiplying the result by a lateral Hann window. Note that this goal psf is quite challenging because it lacks the wavefront curvature that would normally be expected.

In all broadband simulations, we downsampled the propagation matrix by a factor of 3. This had the effect of reducing the upper cut-off frequency in the frequency response of the FIR filter formed by the calculated weights. The temporal sampling rate of the psf was 120 MHz. The upper cut-off frequency, therefore, was reduced from half the temporal sampling rate of the psf (60 MHz) to 20 MHz. This rate still provided adequate sampling given an input pulse with a center frequency of 10 MHz and a -6 dB relative bandwidth of 75%. Table II lists the parameters used in the simulation.

We then calculated the optimum transmit weights using the goal psf and the downsampled propagation matrix. Figs. 5(a) and 5(b) show the goal and the achieved system psfs, respectively, both as a function of lateral position and time. We also envelope-detected the psfs using the Hilbert transform ([9, pp. 359–367]), and then peak-detected them in the time dimension to generate beam profiles. Figs. 5(c) and 5(d) show these goal and achieved system psf profiles as a function of lateral position. Figs. 5(e) and 5(f) display the calculated transmit weights as a function of the element number and time, and the magnitude of the error as a function of lateral position and time, respectively. The error was calculated by computing the difference between the goal and system psfs. Note that the weights do not include geometric focal delays. The delays were applied separately prior to the application of the weights. The result obtained by convolution of the calculated weights with the transmit pulse is presented in Fig. 5(g).

4. Broadband Two-Way Example (Transmit-Receive):

The goal psf was constructed in a similar manner to the one-way example, except for a scaling factor that accounted for the reduction in magnitude due to two-way propagation. The propagation matrix A_{zz} , however, was different from the one-way case. We constructed the propagation functions by using the entire transmit aperture and receiving only on selected pairs of elements. Transmit focal delays were applied, but no transmit apodization was used. All the other parameters are listed in Table II. We then downsampled the resulting propagation matrix by a factor of 3 and used it to calculate the receive weights that minimize the SSE. Figs. 6(a) and 6(b) display the goal and achieved system psfs, respectively. As in the one-way case, we envelope-detected and peak-detected the psfs. The goal and achieved system psf profiles are displayed in Figs. 6(c) and 6(d), respectively. Figs. 6(e) and 6(f) show the calculated receive weights and the psf error magnitude respectively.

B. Applications

1. Enhanced Depth of Field: The DOF of an ultrasound system is the axial region within which the system is said

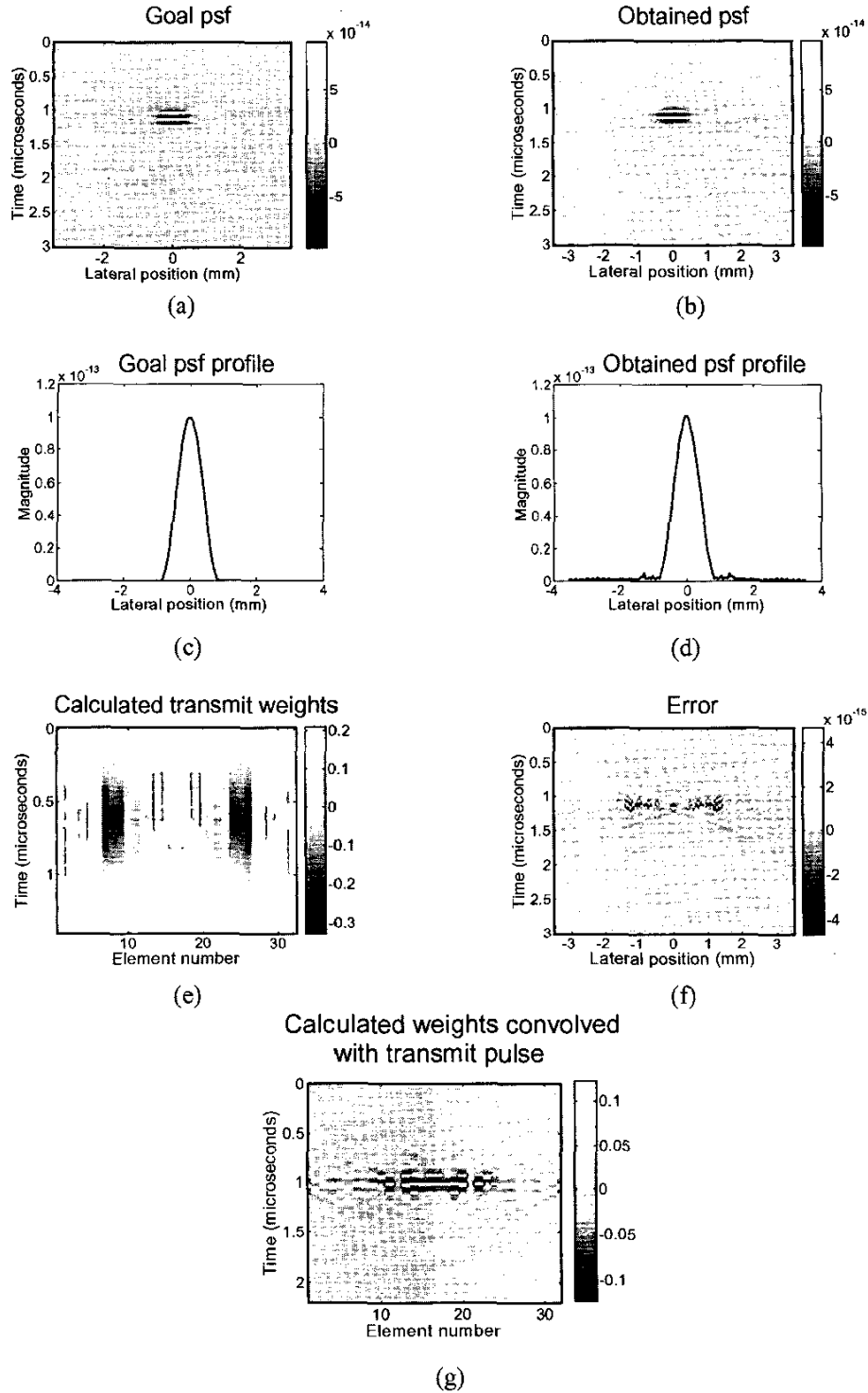


Fig. 5. One-way broadband design example. (a) depicts the goal psf as a function of lateral position and time, and (b) depicts the obtained psf as a function of lateral position and time. (c) shows the goal psf beam profile as a function of lateral position, and (d) shows the obtained psf beam profile as a function of lateral position. These profiles were obtained by envelope detection using the Hilbert transform [9, pp. 359–367], followed by peak detection of the psf along the time dimension. (e) shows the calculated receive weights as a function of element number and time, and (f) illustrates the error between the goal and the obtained psfs as a function of lateral position and time. (g) depicts the results obtained by convolving the calculated transmit weights with the transmit pulse. It can be seen from (a) and (b) that the goal and obtained psfs are very similar. The beam profile of the obtained psf in (d) shows high frequency errors, which are also noticeable in the error image in (f). These errors are caused by the inadequately low temporal sampling rate used in our simulations in Field II due to computational limitations, and should be eliminated with a higher sampling rate.

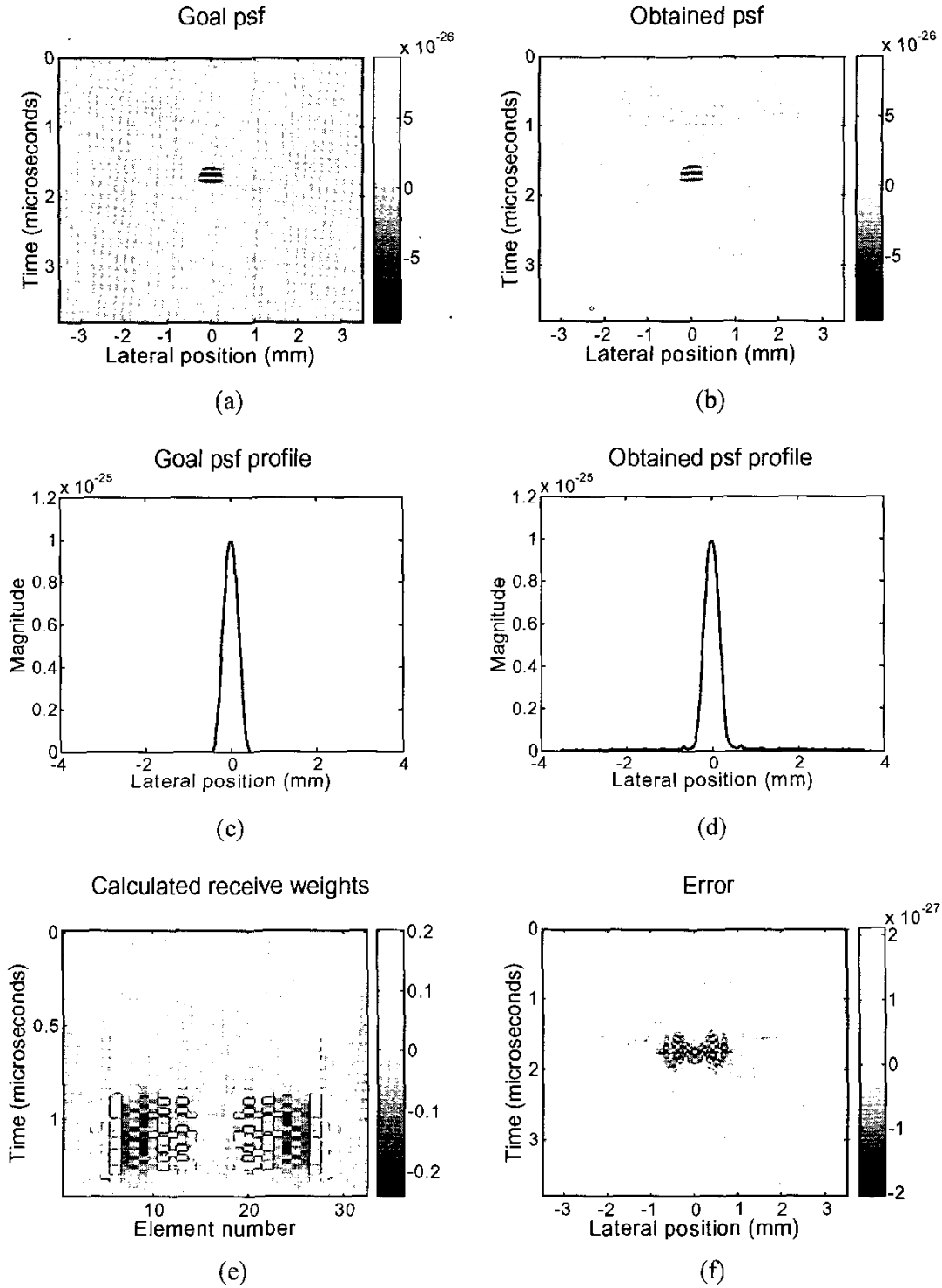


Fig. 6. Two-way broadband design example. (a) depicts the goal psf as a function of lateral position and time, and (b) depicts the obtained psf as a function of lateral position and time. (c) shows the goal psf beam profile as a function of lateral position, and (d) shows the obtained psf beam profile as a function of lateral position. These profiles were obtained by envelope detection using the Hilbert transform [9, pp. 359–367], followed by peak detection of the psf along the time dimension. (e) shows the calculated receive weights as a function of element number and time, and (f) illustrates the error between the goal and the obtained psfs as a function of lateral position and time. It can be seen from (a) and (b) that the goal and obtained psfs are very similar. As in the one-way simulations, the beam profile of the obtained psf in (d) shows high frequency errors, which are also noticeable in the error image in (f). These errors are caused by the inadequately low temporal sampling rate used in our simulations in Field II due to computational limitations, and should be eliminated with a higher sampling rate.

to be in focus, or the axial region within which the system psf satisfies a chosen criterion. The system psf should ideally remain similar to the psf at the focus for as large an axial range as possible. Application of the MSSE technique using the psf at the focus as the goal psf at each range should theoretically yield weights that minimize the SSE between the goal psf and the psf at the range of interest. This, in turn, should maximize the DOF. With this rationale, we applied the two-way MSSE technique in both CW and broadband simulations in an attempt to improve the DOF of the system. The technique was applied at every sampled axial range point. The goal or desired psf at each range point was the psf computed at the focus.

In both CW and broadband simulations, we generated the goal psf using 16-element transmit and receive apertures, while we used a 16-element transmit and 32-element receive aperture for the actual system psf. i.e. weights were calculated for 32 receive elements. The system was focused at 6.5 mm. A Hann window was used as a transmit apodization function in all simulations, and as receive apodization during the generation of the goal psf. We performed CW simulations to maximize the DOF over an axial window from 0.1 mm to 50 mm that was sampled every 0.1 mm. The lateral window over which the CW psf was calculated was sampled at 5 μm to enable accurate estimation of the full width at half maximum (FWHM) of the mainlobe. We also implemented broadband simulations over an axial window from 0.5 mm to 32.5 mm that was sampled every 2 mm. All other parameters are listed in Tables I and II.

Current ultrasound systems attempt to improve the DOF by using dynamic apodization and dynamic receive focusing [10], and we used these in control simulations to establish a basis for comparison with the results obtained using the MSSE technique. We allowed the apodization profile to grow as a function of range assuming an infinitely large aperture, and used the central portion of the profile to implement dynamic apodization on the 32 receive elements.

In broadband simulations, the temporal sampling was 120 MHz, and the propagation matrix was downsampled by a factor of 3 to limit the frequency response of the calculated weights. In order to perform accurate analysis, we interpolated the broadband psfs by a factor of 10 in both the temporal and lateral spatial dimensions using cubic spline interpolation.

We calculated correlation coefficients to compare the psf at each range of interrogation with the psf at the focus. The correlation coefficients were computed for complex data in CW simulations and for real data in broadband simulations. We also calculated the FWHM of the mainlobe for each psf. Figs. 7(a) and 7(b) depict the correlation coefficients and the mainlobe FWHM obtained in CW simulations. The dotted lines indicate the transmit focus. These were obtained at each range of interrogation for the control case and the case when the MSSE technique was applied. Figs. 7(c) and 7(d) display the correlation coefficients and the mainlobe FWHM for broadband simulations

of the control and the MSSE technique cases. A more qualitative assessment of the efficacy of the MSSE technique can be made using Figs. 7(c) and 7(f). Both these images were constructed by superimposing CW psfs at multiple ranges that were normalized to their peak mainlobe levels. The images are shown on a logarithmic scale and are a function of range and lateral position. Fig. 7(e) was constructed using psfs obtained in the control simulation. Fig. 7(f) was generated using psfs from the simulation involving the MSSE technique.

2. Increased Correlation Depth of Field in Translated Aperture Geometries: The translating apertures algorithm (TAA) is a technique that is used in phase aberration correction [11], [12] and to obtain accurate angular scatter data [13]. Data are acquired using two system geometries, the backscatter geometry in which the transmit and receive apertures are coincident, and the angular scatter geometry in which the apertures are translated by equal distances in opposite directions. Despite its many advantages, use of the TAA results in a dramatically reduced DOF. This is due to the separation of the transmit and receive apertures, which causes only a limited interference of the transmit and receive beams. In order to fully utilize the TAA, a high correlation between the psfs of the translated and the nontranslated geometries is required over an extended axial region.

We performed CW and broadband simulations in an effort to investigate the ability of the MSSE technique to improve the correlation DOF in the TAA. We applied the MSSE technique to a translated apertures system with the goal psf being that generated by the same system without any translation of the apertures at the same range. Both transmit and receive apertures comprised 16 elements. In the translated geometry case, the apertures were translated by 8 elements in opposite directions. The system was focused at 6.5 mm. As in the enhanced conventional DOF case, we performed CW simulations over an axial window from 0.1 mm to 50 mm that was sampled every 0.1 mm. We also implemented broadband simulations over an axial window from 0.5 mm to 32.5 mm that was sampled every 2 mm. A Hann window was used as apodization on the transmit apertures and on the receive aperture during the generation of the goal psf. The temporal sampling in broadband simulations was 120 MHz. We downsampled the broadband propagation matrix by a factor of 3, and interpolated the system psfs by a factor of 10 in both the time and lateral space dimensions prior to analysis. Other parameters were consistent with Tables I and II.

Correlation coefficients were calculated at each range by correlating the psf obtained after application of the MSSE technique in the translated geometry with the psf obtained using the nontranslated geometry. As a comparison, we also performed a control simulation in which we calculated correlation coefficients by correlating the translated and nontranslated geometry psfs, without the application of the MSSE technique. Figs. 8(a) and 8(b) show the correlation curves obtained in CW and broadband simulations, respectively. The dotted lines indicate the transmit focus.

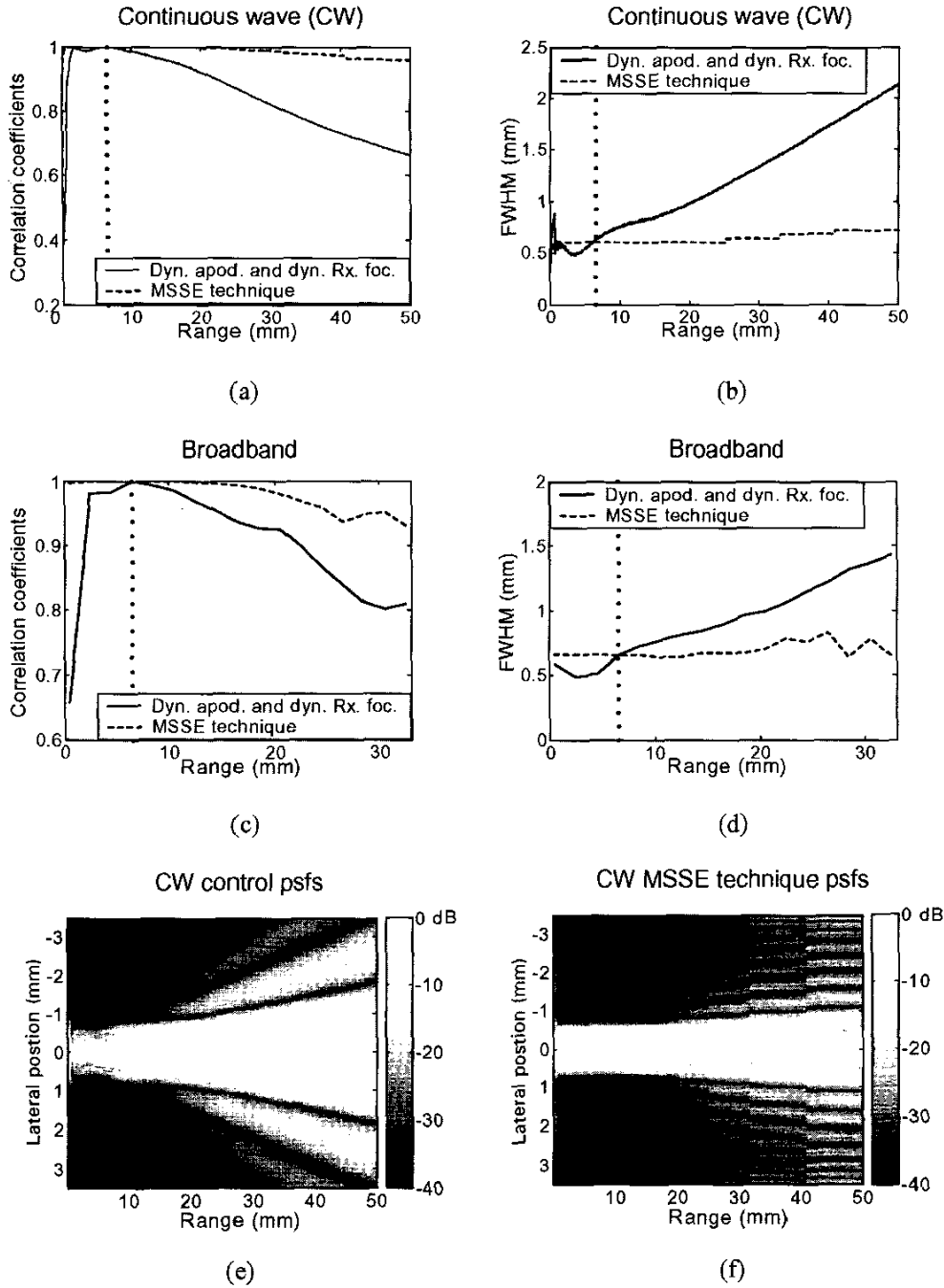


Fig. 7. Application of the MSSE technique for enhanced depth of field (DOF). (a) shows CW correlation coefficients, calculated by correlating the psf at each range of interrogation with the psf at the focus, as a function of range. (b) shows the FWHM of the mainlobe obtained in CW simulations as a function of range. (c) shows broadband correlation coefficients, and (d) shows the FWHM of the mainlobe obtained in broadband simulations, both as a function of range. Dynamic apodization and dynamic receive focusing were used in the control simulations. The dotted lines indicate the transmit focus. (e) depicts CW psf images generated using control psfs, and (f) shows psfs obtained by applying the MSSE technique. Both images were formed from normalized and logarithmically compressed lateral psfs at multiple ranges. Each column in the images consists of the psf at a single range. In both CW and broadband simulations, use of the MSSE technique resulted in an increased DOF. This is apparent from the correlation coefficients in (a) and (c), in which the coefficients obtained from the MSSE simulations are higher than those obtained from control simulations. It also can be seen from (b) and (d) that the mainlobe width over the span of interrogated axial ranges is maintained much better in MSSE simulations than in control simulations. A qualitative comparison between the MSSE technique and control simulations can be made from (e) and (f).

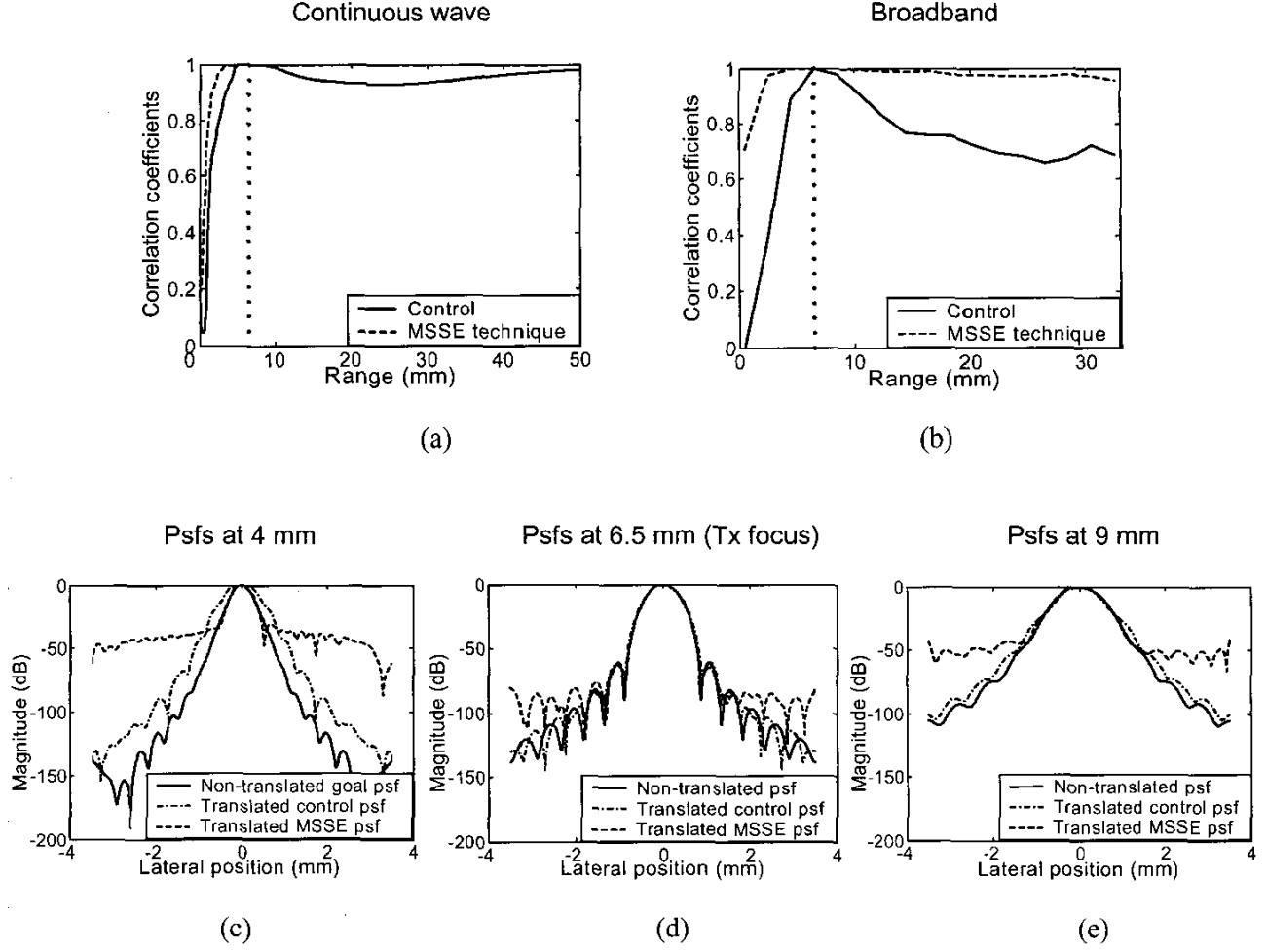


Fig. 8. Results of simulations for increased correlation depth of field (DOF) in translated aperture geometries. (a) depicts the correlation coefficients obtained in CW simulations, calculated by correlating the non-translated geometry psf at each range with the translated geometry psf at the same range, as a function of range. (b) shows the correlation coefficients obtained in broadband simulations as a function of range. The dotted lines indicate the transmit focus. At each range, the MSSE technique was applied in the translated geometry case with the non-translated geometry psf as the goal psf. In control simulations, the translated and non-translated geometry psfs were obtained without application of the MSSE technique. (c) depicts the goal psf (which is the psf obtained with the nontranslated geometry), the translated geometry control psf, and the translated geometry psf obtained using the MSSE technique at an axial range of 4 mm. The same information at the transmit focus (6.5 mm) and at 9 mm is depicted in (d) and (e), respectively. It is apparent that the correlation coefficients obtained from the MSSE simulations are higher than those obtained from control simulations, and the MSSE technique significantly improves the DOF. It can be seen from (c), (d), and (e) that the MSSE algorithm preferentially optimizes the mainlobe at the cost of increased sidelobe levels. If it is important to maintain low sidelobe levels, the weighted MSSE technique described in [1] can be used to achieve a compromise between optimizing the mainlobe and controlling sidelobe levels.

Fig. 8(c) depicts the goal psf (the psf obtained with the nontranslated geometry), the translated geometry control psf, and the translated geometry psf obtained using the MSSE technique at an axial range of 4 mm. Figs. 8(d) and 8(e) depict the same information at the transmit focus (6.5 mm), and at 9 mm.

III. DISCUSSION

Figs. 1(a)–1(d) demonstrate the use of the MSSE technique in the most basic system configuration that was simulated, i.e., the one-way CW system. The goal psf was a 32°-wide Hann window as shown in Fig. 1(a). It can be

seen from Fig. 1(b) that the designed system psf closely approximates it. The magnitude and phase of the calculated transmit weights can be seen in Figs. 1(c) and 1(d). We use two error metrics throughout this section. We use the ratio of the root mean square (rms) error between the psfs to the peak magnitude of the goal psf as a metric of the error in our desired psf, and refer to it as the relative rms error. We also use the ratio of the peak error magnitude to the peak magnitude of the goal psf, and refer to it as the relative peak error. The relative rms error in the one-way CW simulation was 0.029, and the relative peak error was 0.066.

Figs. 1(a)–1(p) illustrate the flexibility of the MSSE technique. In these simulations, the goal psf width was pro-

gressively reduced to 16° , 8° , and 4° in order to investigate the performance of the technique. The relative rms errors obtained in the three simulations were 0.005, 0.0052, and 0.0295, and the relative peak errors were 0.012, 0.023, and 0.214, respectively. The error in obtaining the 16° and 8° wide goal psfs is much lower than the error for the 32° and 4° wide goal psfs. However, it can be seen from Fig. 1 that the goal and obtained psfs are qualitatively quite similar. An examination of the magnitude of the calculated weights in Figs. 1(c), 1(g), 1(k), and 1(o) shows that the apodization profile expectedly becomes wider as the goal psf becomes narrower.

The effects of varying the size of the window of analysis are shown in Fig. 2. It can be seen from Figs. 2(b) and 2(c) that, when a $\pm 15^\circ$ analysis window was used, the ultrasonic field outside the window was unstable and undesirable, exhibiting erratic behavior with very large grating lobes. The dotted lines indicate the extent of the window of analysis, and it can be seen that the grating lobes occur just outside the window. Results improved when the window size was progressively increased in steps of $\pm 15^\circ$ to $\pm 90^\circ$, as can be seen from Figs. 2(d)–2(r). The grating lobe magnitudes were progressively reduced as the window size was increased. Beyond a window size of $\pm 45^\circ$, however, the improvement outside the analysis window was negligible. In the $\pm 15^\circ$ and $\pm 30^\circ$ window cases, it can be seen that the grating lobes occur immediately outside the window. These grating lobes, caused by inadequate analysis window size, disappear for a $\pm 45^\circ$ window of analysis. Therefore, it can be seen that the size of the window of analysis significantly impacts the obtained ultrasonic field, and it must be carefully chosen to suit the application. Ideally it would always cover $\pm 90^\circ$, although computational and memory requirements may limit the practical range.

We also investigated the effect of errors in the assumed speed of sound. Simulation results are displayed in Fig. 3. Fig. 3(b) shows the psf error when the assumed speed of sound was correct. In this case, the relative rms error was 0.012 and the relative peak error was 0.054. As the wave speed was underestimated by 25 m/s, 50 m/s, and 75 m/s, the relative rms and peak errors rose to 0.022 and 0.062, respectively. This is shown in Figs. 3(d), 3(h) and 3(l). When the wave speed was overestimated by 25 m/s, 50 m/s, and 75 m/s, the relative rms and peak errors rose to 0.015 and 0.102, respectively, as can be seen in Figs. 3(f), 3(j) and 3(n). The observed errors were reasonable, despite the extremely wide range considered. Therefore, the MSSE algorithm is stable in the sense that small errors in the assumed wave propagation speed do not appear to result in a significant degradation of performance.

Fig. 4 demonstrates the use of the MSSE technique in the design of two-way system responses. It can be seen from Figs. 4(a) and 4(b) that the system psf obtained by the MSSE technique is very similar to the goal psf. The resulting relative rms error was 0.002, and the relative peak error was 0.022. Note that the errors obtained in the one-way and two-way simulations cannot be compared directly because the transmit psf was predetermined in the two-

way simulations, and the two-way psf was optimized using only the receive weights. Therefore, there is inherently less flexibility available to the algorithm than in the one-way design procedure, and it generally performs more poorly than the one-way algorithm, except in a limited range of goal psf widths. The goal psf width for the two-way simulation presented in Fig. 4 falls within this range.

Fig. 5 depicts the results obtained when the MSSE algorithm was implemented in one-way broadband simulations. It can be seen from Figs. 5(a) and 5(b) that the goal and system psfs are qualitatively quite similar. The relative rms error was 0.003, and the relative peak error was 0.05.

Results from the two-way broadband simulation are shown in Fig. 6. The relative rms error was 0.001, and the relative peak error was 0.022.

The results obtained in the one- and two-way broadband design simulations (Figs. 5 and 6) must be interpreted with caution because the goal psfs used are difficult to realize using spherical waves, as can be seen in Figs. 5(a) and 6(a). The goal psfs had flat wavefronts and would have been easy to generate using plane waves, but plane waves are an unrealistic model of the ultrasonic field emitted by transducer elements. Medical ultrasonic imaging is typically performed in the near field of the transducer. Because of this, both transmitted and received wavefronts should properly be considered as spherical wavefronts. In spite of the challenging goal psfs used here, there is a very good qualitative agreement between the goal and system psfs. Unlike in the CW simulations, the relative errors in the two-way broadband simulation are smaller than that obtained in the one-way simulation. We believe that this is due to the more realistic broadband simulations performed using Field II. Field II uses elements of finite spatial extent, as opposed to the ideal point sources used in the CW simulations. The use of such elements simulates the effects of nonuniform element angular response, which we hypothesize to be partly responsible for the lower two-way relative errors. The size of the window of analysis and the choice of spatial and temporal sampling rates also may play a significant role. However, in both one-way and two-way simulations, we were able to approximate a very challenging goal psf.

The ability of the MSSE technique to improve the DOF is illustrated in Fig. 7. The DOF was defined in terms of correlation coefficient as the axial region over which the coefficient remained above 0.99. In the CW case, the DOF in control simulations was 7.8 mm, and it increased by 249% to 27.2 mm when the MSSE technique was applied. In the broadband simulations, the DOF increased from 4.1 mm for control to 17.4 mm upon the application of the MSSE technique, an increase of 325%. The improvement in the DOF in CW simulations can be clearly seen in Fig. 7(a), and in broadband simulations in Fig. 7(c).

The DOF also was defined in terms of the FWHM of the mainlobe. Here we considered the DOF to be the region within which the FWHM stayed within $\pm 25\%$ of its value at the focus. The DOF calculated using the FWHM

criterion increased from 11 mm in control simulations to almost the entire range of interrogation, i.e., 50 mm. This represents a 355% increase in the DOF when the MSSE technique was applied. The CW control and MSSE technique FWHM results can be seen in Fig. 7(b). Fig. 7(d) displays the FWHM results for broadband simulations. In the broadband case, the DOF evaluated using the FWHM increased from 12 mm to about 25.4 mm upon application of the MSSE technique, an increase of about 112%. It can be seen clearly in Figs. 7(b) and 7(d) that the mainlobe FWHM at the focus was identical for the control and MSSE technique cases, but it varied more slowly away from the focus when the MSSE method was applied. Therefore, a significant improvement in the DOF was obtained in both CW and broadband simulations.

A more qualitative assessment of the efficacy of the MSSE technique can be made using Figs. 7(e) and 7(f). Fig. 7(e) shows the CW psfs obtained in control simulations and simulations that implemented the MSSE technique. The psfs are displayed as a function of range and lateral position. It can be seen that there is significant broadening of the psf mainlobe with range in the control simulation. Fig. 7(f) clearly demonstrates the dramatic improvement in the DOF obtained using the MSSE beamforming technique. This improvement, though, comes at the cost of slightly increased sidelobe levels. This is due to the fact that the MSSE algorithm minimizes the energy in the difference between the goal and system psfs. Because most of the energy is contained in the mainlobe, the algorithm preferentially optimizes mainlobe width at the cost of higher sidelobe levels. However, as described in [1], we can apply a weighting function to selectively emphasize sidelobes during the MSSE design process. The procedure involves the selection of an appropriate function that weights the sidelobes of the psf more than the mainlobe during the SSE minimization operation. Implementing the MSSE technique then would yield aperture weightings that preferentially maintain low sidelobe levels, at the expense of mainlobe width. This would enable a compromise between the overall performance of the algorithm and sidelobe levels. However, as can be seen from Fig. 7, the MSSE technique performs much better overall than the conventional techniques of dynamic apodization and dynamic receive focusing, and greatly enhances the depth of field.

Fig. 8 illustrates the use of the MSSE design method in the TAA. Fig. 8(a) shows the correlation coefficients obtained by correlating the nontranslated geometry psf with the translated geometry psf in CW simulations. As previously described, the correlation DOF was defined as the axial region within which the correlation coefficient remained over 0.99. The correlation DOF increased from 5.2 mm in control simulations to 46.9 mm upon the application of the MSSE technique. This represents an 802% increase in the DOF. Fig. 8(b) displays the correlation coefficients obtained in broadband simulations. The DOF increased from 1.0 mm to 8.8 mm in broadband simulations, an increase of 780%.

The goal, control, and MSSE technique psfs at axial ranges of 4 mm, 6.5 mm, and 9 mm are depicted in Figs. 8(c), 8(d), and 8(e), respectively. It can be seen clearly that the MSSE technique preferentially optimizes the mainlobe of the obtained psf, at the cost of higher sidelobes. If sidelobe levels are too high, the weighted MSSE technique described in [1] can be used to achieve a compromise between optimizing the mainlobe and controlling sidelobe levels.

The MSSE design method worked exceedingly well over the range of conditions considered in this paper, but we must exercise some caution in interpreting these results. The results shown in Fig. 2 clearly demonstrate that use of an appropriately large window of analysis is critical. Another concern is the effect of assuming an incorrect propagation model in the derivation of the optimum aperture weights. Errors such as a mismatch in the assumed and actual wave propagation speeds have been shown to have an adverse effect on the design method, although observed errors were small. Phase aberration will also adversely impact the performance of the MSSE algorithm, because it is unaccounted for in the propagation models used. Blocked or dead elements will also have an effect, because any assumed propagation functions for these elements will cause an undesired contribution to the ultrasound field. These effects remain to be investigated in detail, but the initial simulation results that have been presented suggest that the MSSE technique is a robust beamformer design tool.

The calculated weights do not lend themselves to intuition, but the MSSE algorithm may be considered to be analogous to the discrete Fourier transform [9] or wavelet transform ([9, pp. 500–502]). The discrete Fourier transform expresses a signal in terms of multiple narrowband signals with unique frequencies. We can process (weight) these narrowband signals, then use the inverse discrete Fourier transform to sum them and construct a new signal that we desire. Similarly, the wavelet transform decomposes a signal into a set of weighted wavelets that can be summed to construct a new desired signal. The MSSE algorithm is analogous because it decomposes the system response into the contributions of the individual elements. These individual element responses then are weighted and summed to construct the desired system response. The individual element responses are not necessarily orthogonal such as the kernel functions used in Fourier and wavelet decompositions, but the MSSE algorithm operates under the same principle.

Simulations have shown the MSSE beamformer design technique to be able to design apertures for applications that require arbitrary system responses. One such application is multidimensional blood velocity estimation as described in [14] and [15]. The specialized psfs required for the methods in [14] and [15] can be optimally generated using the MSSE technique. Because the MSSE technique derives aperture weights that minimize the SSE between the goal and system psfs, the calculated weights generate a system response that is optimally similar to the goal response. This eliminates the usual need for iteration to

obtain an adequate response. The technique has also been shown to be successful in developing apertures for common beamformer design problems such as limited depth of field. Overall, the MSSE technique has the potential to improve beamforming in general, with much better control of beam parameters than is possible with current beamforming techniques. The direct solutions provided by this approach also have the potential to save a great deal of time by obviating iterative design.

IV. CONCLUSIONS

The MSSE technique has been shown to be effective in designing ultrasound systems that generate arbitrary desired system responses. Simulation results in one-way and two-way CW and broadband systems demonstrate that it is straightforward to implement and can be applied to a wide range of potential applications. Simulation results obtained by implementing the beamforming method in examples of application demonstrate the success of the technique in solving common problems that are encountered in ultrasound imaging, such as a restricted depth of field.

Therefore, the MSSE technique has been shown to have significant potential to improve ultrasound beamforming and can be applied in any ultrasound application in which better control of beam parameters is desired. Specifically, applications that require specialized psfs are well suited for the technique. There is no iteration involved; therefore, design time is considerably reduced. Further investigation is required to examine the effects of phase aberration, blocked elements, and imposing constraints on the calculated aperture weights. But our simulations indicate that the MSSE technique consistently outperforms current beamforming techniques.

REFERENCES

- [1] K. Ranganathan and W. F. Walker, "A novel beamformer design method for medical ultrasound. Part I: Theory," *IEEE Trans. Ultrason., Ferroelect., Freq. Contr.*, vol. 50, no. 1, pp. 15–24, 2003.
- [2] A. R. Selfridge, G. S. Kino, and B. T. Khuri-Yakub, "A theory for the radiation pattern of a narrow-strip acoustic transducer," *Appl. Phys. Lett.*, vol. 37, no. 1, pp. 35–36, 1980.
- [3] L. L. Scharf, *Statistical Signal Processing: Detection, Estimation, and Time Series Analysis*. Reading, MA: Addison-Wesley, 1991.
- [4] B. D. Steinberg, *Principles of Aperture and Array System Design: Including Random and Adaptive Arrays*. New York: Wiley, 1976.
- [5] J. A. Jensen and N. B. Svendsen, "Calculation of pressure fields from arbitrarily shaped apodized and excited ultrasound transducers," *IEEE Trans. Ultrason., Ferroelect., Freq. Contr.*, vol. 39, no. 2, pp. 262–267, 1992.
- [6] J. W. Goodman, *Introduction to Fourier Optics*, 2nd ed. New York: McGraw-Hill, 1988.
- [7] B. Porat, *A Course in Digital Signal Processing*. New York: Wiley, 1997.
- [8] M. E. Anderson, "The impact of sound speed errors on medical ultrasound imaging," *J. Acoust. Soc. Amer.*, vol. 107, no. 6, pp. 3540–3548, 1997.
- [9] R. N. Bracewell, *The Fourier Transform and Its Applications*, 3rd ed. New York: McGraw-Hill, 2000.
- [10] K. Thomenius, "Evolution of ultrasound beamformers," *Proc. IEEE*, 1996, pp. 1615–1622.
- [11] G. C. Ng, "A speckle target adaptive imaging technique in the presence of distributed aberrations," *IEEE Trans. Ultrason., Ferroelect., Freq. Contr.*, vol. 44, no. 1, pp. 140–151, 1997.
- [12] W. F. Walker and G. E. Trahey, "Speckle coherence and implications for adaptive imaging," *J. Acoust. Soc. Amer.*, vol. 101, no. 4, pp. 1847–1858, 1997.
- [13] W. F. Walker, "C- and d-weighted ultrasonic imaging using the translating apertures algorithm," *IEEE Trans. Ultrason., Ferroelect., Freq. Contr.*, vol. 48, no. 2, pp. 452–461, 2001.
- [14] J. A. Jensen and P. Munk, "A new method for estimation of velocity vectors," *IEEE Trans. Ultrason., Ferroelect., Freq. Contr.*, vol. 45, no. 3, pp. 837–851, 1998.
- [15] M. E. Anderson, "Multi-dimensional velocity estimation with ultrasound using spatial quadrature," *IEEE Trans. Ultrason., Ferroelect., Freq. Contr.*, vol. 45, no. 3, pp. 852–861, 1998.



Karthik Ranganathan received his B.E. in Biomedical Engineering from the University of Bombay, Bombay, India in 1999.

After completing his B.E., he joined the Department of Biomedical Engineering at the University of Virginia, Charlottesville, VA where he is currently a Ph.D. candidate. His research interests include ultrasound beamforming, signal processing and angular scatter measurement techniques.



William F. Walker (S'95-M'96) received the B.S.E. and Ph.D. degrees in 1990 and 1995 from Duke University, Durham, NC. His dissertation explored fundamental limits on the accuracy of adaptive imaging.

After completing his doctoral work, he stayed on at Duke as an Assistant Research Professor in the Department of Biomedical Engineering. At the same time he served as a Senior Scientist and President of NovaSon Corporation located in Durham, NC. In 1997 he joined the faculty of the Department of Biomedical Engineering at the University of Virginia, Charlottesville, VA as an Assistant Professor. His research interests include aperture domain processing, beamforming, angular scatter imaging, and tissue elasticity imaging.

A General Cystic Resolution Metric for Medical Ultrasound

Karthik Ranganathan¹ and William F. Walker^{1, 2}

¹Biomedical Engineering, University of Virginia, Charlottesville, VA 22908

²Electrical and Computer Engineering, University of Virginia, Charlottesville, VA 22904

Abstract:

This paper describes a metric that can be used to characterize the resolution of arbitrary, broadband, coherent imaging systems. The metric is particularly suited to medical ultrasound because it characterizes scanner performance using the contrast obtained by imaging anechoic cysts of various sizes that are embedded in a speckle generating background, accounting for the effect of electronic noise. We present the theoretical derivation of the metric and provide simulation examples that demonstrate its utility. We utilize the metric to compare a low-cost, handheld, C-scan system under development in our laboratory to conventional ultrasound scanners. We also present the results of simulations that were designed to evaluate and optimize various parameters in our system, including the $f/\#$ and apodization windows. We investigate the impact of electronic noise on our system and quantify the tradeoffs associated with quantization in the analog to digital converter. Results indicate that an $f/1$ receive aperture combined with 10 bit precision and an SNR of 0 dB per channel would result in adequate image quality.

I. INTRODUCTION

The evaluation of imaging performance is an essential task in the development of ultrasound systems, both to predict fundamental limits on quality and to optimize parameters for system design. It is possible to estimate the performance of existing systems by imaging phantoms or human subjects, but during system design, it is necessary to be able to determine imaging performance of a proposed system prior to construction. The ability to accurately predict performance enables system optimization and quantitative consideration of engineering tradeoffs early in the design process and significantly reduces the time and cost investment in system development. To support these goals, this paper develops a general resolution metric for comparing arbitrary imaging systems.


The most common metric used to estimate scanner performance is the beamplot, which has been adapted from RADAR. System resolution is usually described using a combination of the full width at half maximum (FWHM) or -6 dB beamwidth of the beamplot and the beamwidth at other levels [1]. Sidelobe and grating lobe levels are used to estimate eventual image contrast. Although widely used, there are disadvantages to using the beamplot to estimate the performance of ultrasound systems. Targets in medical ultrasound are usually weakly reflecting tissues in a scattering medium, unlike RADAR targets that are more often highly reflective and in a non-scattering background. Therefore, there may be scenarios in which the FWHM criterion indicates excellent performance, but actual images of tissue do not reveal important details. Vilkomerson et al [2] demonstrated that the FWHM criterion sometimes provides misleading information about resolution in ultrasound systems. It is, in addition,

difficult to be certain about the best levels at which to characterize and optimize the beamplot. In other words, it is difficult to decide whether to optimize the mainlobe width or sidelobe and grating lobe levels for an overall increase in image quality. As mentioned above, performance may be determined by imaging phantoms; however, this does not provide a way to theoretically assess the performance of different hypothetical imaging systems. While repeated image simulations could be performed to assess a wide variety of system parameters, including resolution, this approach is very computationally challenging. We need a metric that ties together resolution and contrast in a way that is relevant to diagnostic ultrasound imaging.

Vilkomerson et al addressed the limitations of the beamplot and proposed the concept of “cystic resolution” [2] in which performance was quantified as the size of a void that produced a given contrast. The analysis, while novel and useful, was limited to narrowband circular apertures and neglected the axial dimension. Üstüner et al [3] extended cystic resolution to a 3D broadband model that addressed the above problems but did not describe its theoretical foundation or publish the model in an archival journal. The lack of a theoretical background in [3] obscures important details, resulting in a limited understanding of the formulation and its utility and drawbacks. We derive a metric identical to that in [3], extend it to include the effects of electronic noise, and present simulation results that demonstrate its utility.

II. THEORY

Our goal is to derive a metric to quantify the contrast resolution of an arbitrary broadband ultrasound system. Let the point spread function (psf) of the ultrasound system be defined as

], a function of three-dimensional (3D) space (\vec{x}) and time (t). Time in this expression is included for the propagation of the sensitivity function through the tissue and thus typically begins at transmission and ends at the completion of a single echo line. The medium scattering function is modeled as a stochastic process $N(\vec{x})$, undergoing negligible tissue motion during reception of an individual echo line and therefore being constant with time. We assume that the effect of electronic noise during transmit is negligible due to the high signal to noise ratio (SNR) on transmit, and model the electronic noise on receive as another stochastic process $E(t)$. Combining these factors, and assuming that the electronic noise is purely additive, the received signal as a function of time is

$$S_b(t) = \int_{-\infty}^{\infty} P(\vec{x}, t) N(\vec{x}) d\vec{x} + E(t) \quad (1)$$

Consider the mean squared received signal $\langle S_b^2(t) \rangle$ where $\langle \rangle$ is the expected value operator:

$$\langle S_b^2(t) \rangle = \left\langle \left[\int_{-\infty}^{\infty} P(\vec{x}_1, t) N(\vec{x}_1) d\vec{x}_1 + E(t) \right] \left[\int_{-\infty}^{\infty} P(\vec{x}_2, t) N(\vec{x}_2) d\vec{x}_2 + E(t) \right] \right\rangle. \quad (2)$$

$$\begin{aligned} \langle S_b^2(t) \rangle &= \left\langle \int_{-\infty}^{\infty} \int_{-\infty}^{\infty} P(\vec{x}_1, t) P(\vec{x}_2, t) N(\vec{x}_1) N(\vec{x}_2) d\vec{x}_1 d\vec{x}_2 \right\rangle \\ &\quad + \left\langle \int_{-\infty}^{\infty} \int_{-\infty}^{\infty} P(\vec{x}_1, t) N(\vec{x}_1) E(t) d\vec{x}_1 \right\rangle \end{aligned}$$

$$+ \left\langle \int_{-\infty}^{\infty} \int_{-\infty}^{\infty} P(\vec{x}_2, t) N(\vec{x}_2) E(t) d\vec{x}_2 \right\rangle + \langle E^2(t) \rangle \quad (3)$$

Rearranging the expected value operator to account for the fact that the scattering function and electronic noise are stochastic but the psf is deterministic yields:

$$\begin{aligned} \langle S_b^2(t) \rangle &= \int_{-\infty}^{\infty} \int_{-\infty}^{\infty} P(\vec{x}_1, t) P(\vec{x}_2, t) \langle N(\vec{x}_1) N(\vec{x}_2) \rangle d\vec{x}_1 d\vec{x}_2 \\ &+ \int_{-\infty}^{\infty} \int_{-\infty}^{\infty} P(\vec{x}_1, t) \langle N(\vec{x}_1) E(t) \rangle d\vec{x}_1 \\ &+ \int_{-\infty}^{\infty} \int_{-\infty}^{\infty} P(\vec{x}_2, t) \langle N(\vec{x}_2) E(t) \rangle d\vec{x}_2 + \langle E^2(t) \rangle \end{aligned} \quad (4)$$

We assume that the electronic noise $E(t)$ and the scattering function ✗ are uncorrelated and obtain:

$$\langle S_b^2(t) \rangle = \int_{-\infty}^{\infty} \int_{-\infty}^{\infty} P(\vec{x}_1, t) P(\vec{x}_2, t) \langle N(\vec{x}_1) N(\vec{x}_2) \rangle d\vec{x}_1 d\vec{x}_2 + \langle E^2(t) \rangle \quad (5)$$

This expression can be further simplified by assuming that the target scattering function is a stationary, white noise process whose autocorrelation is a delta function. Applying this assumption yields:

$$\langle S_b^2(t) \rangle = \int \int_{-\infty}^{\infty} P(\vec{x}_1, t) P(\vec{x}_2, t) a \delta(\vec{x}_1 - \vec{x}_2, t) d\vec{x}_1 d\vec{x}_2 + \langle E^2(t) \rangle$$

(6)

where a is a scaling factor. Performing the outermost integral in the first term yields:

$$\langle S_b^2(t) \rangle = a \int_{-\infty}^{\infty} P^2(\vec{x}, t) d\vec{x} + \langle E^2(t) \rangle \quad (7)$$

The mean squared received signal is therefore a function of only the 3D psf and the electronic noise. We can now describe a mask that defines the location and size of a spherical anechoic void (cyst):

$$\begin{aligned} M(\vec{x}) &= 0, \quad |\vec{x}| \leq R \\ &= 1, \quad |\vec{x}| > R, \end{aligned} \quad (8)$$

where R is the radius of the cyst and the cyst center is at the origin of the coordinate system.

$M(\vec{x})$ is also independent of time since we assume no tissue motion during the acquisition.

The scattering medium with the void is represented as $N(\vec{x})M(\vec{x})$. The received signal energy is expected to be at a minimum when the beam axis coincides with the center of the void and as much of the psf energy as possible lies in the region defined by the void. The received signal in this circumstance can then be written as:

$$S_c(t) = \int_{-\infty}^{\infty} P(\vec{x}, t) N(\vec{x}) M(\vec{x}) d\vec{x} + E(t) \quad (9)$$

The mean squared received signal $\langle S_c^2(t) \rangle$ is:

$$\begin{aligned} \langle S_c^2(t) \rangle = & \left\langle \left[\int_{-\infty}^{\infty} P(\vec{x}_1, t) N(\vec{x}_1) M(\vec{x}_1) d\vec{x}_1 + E(t) \right] \right. \\ & \cdot \left. \left[\int_{-\infty}^{\infty} P(\vec{x}_2, t) N(\vec{x}_2) M(\vec{x}_2) d\vec{x}_2 + E(t) \right] \right\rangle \end{aligned} \quad (10)$$

$$\begin{aligned} \langle S_c^2(t) \rangle = & \left\langle \int_{-\infty}^{\infty} \int_{-\infty}^{\infty} P(\vec{x}_1, t) P(\vec{x}_2, t) N(\vec{x}_1) N(\vec{x}_2) M(\vec{x}_1) M(\vec{x}_2) d\vec{x}_1 d\vec{x}_2 \right\rangle \\ & + \left\langle \int_{-\infty}^{\infty} \int_{-\infty}^{\infty} P(\vec{x}_1, t) N(\vec{x}_1) M(\vec{x}_1) E(t) d\vec{x}_1 \right\rangle \\ & + \left\langle \int_{-\infty}^{\infty} \int_{-\infty}^{\infty} P(\vec{x}_2, t) N(\vec{x}_2) M(\vec{x}_2) E(t) d\vec{x}_2 \right\rangle + \langle E^2(t) \rangle \end{aligned} \quad (11)$$

Since the psf and the mask are deterministic:

$$\begin{aligned} \langle S_c^2(t) \rangle = & \int \int_{-\infty}^{\infty} P(\vec{x}_1, t) P(\vec{x}_2, t) M(\vec{x}_1) M(\vec{x}_2) \langle N(\vec{x}_1) N(\vec{x}_2) \rangle d\vec{x}_1 d\vec{x}_2 \\ & + \int_{-\infty}^{\infty} \int_{-\infty}^{\infty} P(\vec{x}_1, t) M(\vec{x}_1) \langle N(\vec{x}_1) E(t) \rangle d\vec{x}_1 \end{aligned}$$

$$+ \int_{-\infty}^{\infty} \int_{-\infty}^{\infty} P(\vec{x}_2, t) M(\vec{x}_2) \langle N(\vec{x}_2) E(t) \rangle d\vec{x}_2 + \langle E^2(t) \rangle \quad (12)$$

Once again, assuming $N(\vec{x})$ is a stationary white noise process and uncorrelated to $E(t)$, we get:

$$\langle S_c^2(t) \rangle = \int_{-\infty}^{\infty} \int_{-\infty}^{\infty} P(\vec{x}_1, t) P(\vec{x}_2, t) M(\vec{x}_1) M(\vec{x}_2) \delta(\vec{x}_1 - \vec{x}_2, t) d\vec{x}_1 d\vec{x}_2 + \langle E^2(t) \rangle \quad (13)$$

$$\langle S_c^2(t) \rangle = a \int_{-\infty}^{\infty} P^2(\vec{x}, t) M^2(\vec{x}) d\vec{x} + \langle E^2(t) \rangle \quad (14)$$

The contrast of the cyst can then be defined as:

$$C(t) = \sqrt{\frac{\langle S_c^2(t) \rangle}{\langle S_b^2(t) \rangle}} = \sqrt{\frac{a \int_{-\infty}^{\infty} P^2(\vec{x}, t) M^2(\vec{x}) d\vec{x} + \langle E^2(t) \rangle}{a \int_{\Omega} P^2(\vec{x}, t) d\vec{x} + \langle E^2(t) \rangle}} \quad (15)$$

We define the electronic SNR as a function of time:

$$SNR(t) = \frac{\sigma_{signal}(t)}{\sigma_{noise}(t)} \quad (16)$$

where $\sigma_{signal}(t)$ and $\sigma_{noise}(t)$ are the standard deviations of the signal and noise components respectively. Note that we define the standard deviations over an ensemble of signal and noise realizations and not in time. $\sigma_{signal}(t)$ can be expressed as:

$$\sigma_{signal}(t) = \sqrt{\left\langle \int_{-\infty}^{\infty} P(\bar{x}_1, t) N(\bar{x}_1) d\bar{x}_1 \int_{-\infty}^{\infty} P(\bar{x}_2, t) N(\bar{x}_2) d\bar{x}_2 \right\rangle} \quad (17)$$

$$\sigma_{signal}(t) = \sqrt{a \int_{-\infty}^{\infty} P^2(\bar{x}, t) d\bar{x}} \quad (18)$$

$\sigma_{noise}(t)$ can be expressed as:

$$\sigma_{noise}(t) = \sqrt{\langle E^2(t) \rangle} \quad (19)$$

Applying (18) and (19) to (16) yields:

$$SNR(t) = \frac{\sigma_{signal}(t)}{\sigma_{noise}(t)} = \sqrt{\frac{a \int_{-\infty}^{\infty} P^2(\bar{x}, t) d\bar{x}}{\langle E^2(t) \rangle}} \quad (20)$$

or equivalently

$$\langle E^2(t) \rangle = \frac{a \int_{-\infty}^{\infty} P^2(\vec{x}, t) d\vec{x}}{SNR^2(t)} \quad (21)$$

Applying (21), (15) can now be modified to yield:

$$C(t) = \sqrt{\frac{a \int_{-\infty}^{\infty} P^2(\vec{x}, t) M^2(\vec{x}) d\vec{x} + \frac{a \int_{-\infty}^{\infty} P^2(\vec{x}, t) d\vec{x}}{SNR^2(t)}}{a \int_{-\infty}^{\infty} P^2(\vec{x}, t) d\vec{x} + \frac{a \int_{-\infty}^{\infty} P^2(\vec{x}, t) d\vec{x}}{SNR^2(t)}}} \quad (22)$$

We can simplify the expression in (22) as follows:

$$C(t) = \sqrt{\frac{SNR^2(t) \int_{-\infty}^{\infty} P^2(\vec{x}, t) M^2(\vec{x}) d\vec{x} + \int_{-\infty}^{\infty} P^2(\vec{x}, t) d\vec{x}}{SNR^2(t) \int_{-\infty}^{\infty} P^2(\vec{x}, t) d\vec{x} + \int_{-\infty}^{\infty} P^2(\vec{x}, t) d\vec{x}}} \quad (23)$$

$$= \sqrt{\frac{\int_{-\infty}^{\infty} P^2(\vec{x}, t) M^2(\vec{x}) d\vec{x}}{1 + SNR^2(t)} \frac{\int_{-\infty}^{\infty} P^2(\vec{x}, t) d\vec{x}}{1 + SNR^2(t)}} \quad (24)$$

$$= \sqrt{\frac{1 + SNR^2(t) \frac{E^{out}(t)}{E^{tot}(t)}}{1 + SNR^2(t)}} \quad (25)$$

where $E^{out}(t)$ is the psf energy outside the void as a function of time:

$$E^{out}(t) = \int_{-\infty}^{\infty} P^2(\vec{x}, t) M^2(\vec{x}) d\vec{x} \quad (26)$$

and $E^{tot}(t)$ is the total psf energy as a function of time:

$$E^{tot}(t) = \int_{-\infty}^{\infty} P^2(\vec{x}, t) d\vec{x} \quad (27)$$

Equations (24) and (25) describe the contrast relative to background speckle obtained by an imaging system with the psf $P(\vec{x}, t)$ and electronic SNR defined statistically by $SNR(t)$, when imaging an anechoic cyst whose size and location are described by the mask $M(\vec{x})$. Equation (25) can alternatively be expressed as a function of the psf energy within the cyst, $E^{in}(t)$, given by:

$$E^{in}(t) = E^{tot}(t) - E^{out}(t) \quad (28)$$

Modifying (25):

$$C(t) = \sqrt{\frac{1 + SNR^2(t) \left(1 - \frac{E^{tot}(t) - E^{out}(t)}{E^{tot}(t)} \right)}{1 + SNR^2(t)}} \quad (29)$$

Substituting (28) in (29) yields:

$$C(t) = \sqrt{\frac{1 + SNR^2(t) \left(1 - \frac{E^{in}(t)}{E^{tot}(t)} \right)}{1 + SNR^2(t)}} \quad (30)$$

Note that if the cyst is large enough so that the entire psf energy is contained within the cyst, the contrast depends solely on the electronic noise. While (24), (25), and (30) can individually completely characterize system performance for a given cyst, analysis at the instant in time when the received signal is minimum (i.e. when as much of the psf energy as possible lies within the cyst) is usually sufficient. At this single instant in time t_o , we can express the psf as a function of only 3D space at the time of interest $P_{t_o}(\vec{x})$, and the SNR also at the time of interest SNR_{t_o} . Modifying (24), the contrast at time t_o is:

$$C_{t_o} = \sqrt{\frac{1 + SNR_{t_o}^2 \frac{\int_{-\infty}^{\infty} P_{t_o}^2(\vec{x}) M^2(\vec{x}) d\vec{x}}{\int_{\text{cyst}} P_{t_o}^2(\vec{x}) d\vec{x}}}{1 + SNR_{t_o}^2}} \quad (31)$$

$$= \sqrt{\frac{1 + SNR_{t_o}^2 \frac{E_{t_o}^{out}}{E_{t_o}^{tot}}}{1 + SNR_{t_o}^2}} \quad (32)$$

where $E_{t_o}^{out}$ is the psf energy outside the cyst and $E_{t_o}^{tot}$ is the total psf energy, both at time t_o .

Equation (32) can also be modified to express the contrast as a function of the psf energy within the cyst at time t_o , $E_{t_o}^{in}$.

$$C_{t_o} = \sqrt{\frac{1 + SNR_{t_o}^2 \left(1 - \frac{E_{t_o}^{in}}{E_{t_o}^{tot}}\right)}{1 + SNR_{t_o}^2}} \quad (33)$$

If we neglect electronic noise, SNR_{t_o} becomes infinite and (31) can be modified to the equation for contrast presented in [3]:

$$C_{t_o} = \sqrt{\frac{\int_{-\infty}^{\infty} P_{t_o}^2(\vec{x}) M^2(\vec{x}) d\vec{x}}{\int_{-\infty}^{\infty} P_{t_o}^2(\vec{x}) d\vec{x}}} = \sqrt{\frac{E_{t_o}^{out}}{E_{t_o}^{tot}}} = \sqrt{1 - \frac{E_{t_o}^{in}}{E_{t_o}^{tot}}} \quad (34)$$

We can compute the contrast for cysts of different sizes using one of the above expressions for cystic contrast, and characterize system performance as a function of cyst size as in [2] and [3]. This metric can be used for 4D spatiotemporal analysis of arbitrary broadband

ultrasound systems, but 3D spatial analysis using (31) or (34) is adequate to characterize scanner performance as temporal analysis does not provide critical information. Note that in certain cases, it is valuable to compute the metric for different cyst locations to quantify depth of field, the effect of dynamic focusing, and other factors pertaining to the shift variance of the imaging system. Note also that while (24), (31), and (34) can be used to determine cystic resolution, we can also optimize system parameters by computing contrast as a function of cyst size and determining parameter values that maximize the contrast at the cyst sizes of interest.

III. METHODS

The derived metric is useful for guiding the design and optimization of ultrasound systems. We highlight these applications through a series of examples drawn from our ongoing efforts to develop a low cost, handheld, C-scan ultrasound system for use in routine procedures such as image guided needle/IV line insertion and emergency room/battlefield triage. Our system utilizes a fully sampled 2D array [4] interfaced to a custom integrated circuit with transmit protection, analog conditioning, and sampling and digitizing circuitry [5]. Beamforming is implemented by complex phase rotation of I/Q data that are generated by directly sampling the received radiofrequency (RF) signal [6]. Our beamforming strategy, direct sampled I/Q (DSIQ) beamforming, results in poorer image quality than might be obtained using time delays; however, the use of a fully sampled 2D array enables dynamic focusing in elevation, which may outweigh the performance loss incurred by using DSIQ beamforming. In order to investigate such tradeoffs, we compared our current first generation prototype system to a conventional system with a 1D array that focused in azimuth using time delays and in elevation with a lens.

The conventional system had a 128 element 1D array with a pitch of 135 μm , while default parameters for our prototype system are listed in table 1. Our system does not have the ability to focus or apodize on transmit, so we focused and apodized only on receive in both sets of simulations. Receive apodization was implemented with 1D and 2D Nuttall windows [7]. We simulated our system using DELFI [8], a custom ultrasound simulation package. Spatial pulse-echo responses were computed by transmitting a plane wave on all elements and receiving sequentially on each element. The psfs were computed in the 3D cylindrical volume described in table 1 at two times - the time taken to propagate to the focus and back to the transducer, and a quarter period (at the center frequency) later [6]. We then combined the two psfs computed for each receive element to form a single complex psf [6]. We implemented apodization and focusing by complex phase rotation, and summed across elements to obtain the complete summed and focused response. Note that our first generation system differs significantly from the final system we envision. The final system will have a much larger element count and smaller pitch. We will likely focus using a modified version of DSIQ beamforming to avoid focusing problems due to phase wraparound. The current prototype does not have sampling and digitizing circuitry, and we also intend to improve the analog conditioning circuitry.

We used FIELD II [9] to simulate the conventional system by computing the spatiotemporal response at each point in the 3D spatial window of analysis. We applied the Hilbert transform [10] to form a complex analytic signal whose real part was the original received response and whose imaginary part was the Hilbert transform of that response. The 3D spatial psf was constructed by summing the samples at the two-way propagation time determined by array geometry and the location of the focus. Since the conventional system uses a lens in

elevation and since significant portions of targets are often imaged away from the elevation focus, we computed two psfs to compare to our system, one with the elevation focus coincident with the azimuthal focus at 1 cm, and one with the elevation focus set to 2.8 cm. Figure 1 shows slices of the two psfs obtained with the 1D array and focusing via time delays. Figure 2 shows slices of the psf obtained with the 2D array and DSIQ beamforming. We used (34) to compute the contrast for cysts of different sizes. We ignored the effects of electronic noise because noise estimates for our first generation prototype will be of limited relevance in our final system. Figure 3 depicts the contrast as a function of cyst size for the three geometries examined.

The above application of the metric allows direct comparison between our C-scan system and more conventional linear array based systems; a comparison which would be difficult using only the beamplot or even the psf. We have also applied the metric to quantify the often subtle differences in performance that result from changes in our system configuration. In each of the following examples, application of the metric provides a clear guidance in system design.

Although lower electronic noise is always preferable, practical systems almost always exhibit other limitations, such as limited dynamic range, which render noise reduction beyond some threshold SNR of limited use. To determine this threshold in our system, we varied the electronic SNR per channel, as listed in table 2, computed the psf using DELFI as described above, and used (31) to compute the contrast as a function of cyst size for our prototype system. Figures 4(a) and 4(b) depict the obtained contrast as a function of cyst size when receive apodization was implemented with flat and Nuttall windows, respectively.

It is well known that digitizer quantization affects sidelobe levels [11]. State of the art clinical scanners typically use 10 bits to represent each sample; however, compromises made in fabricating our 2D array transducer and in beamforming might render 10 bits superfluous in our prototype system. We tested this hypothesis by investigating the impact of quantization on cyst contrast in an ideal scanner with no electronic noise. We quantized the single receive element responses, obtained as described above, using different precisions (table 3) and then apodized, focused, and summed the responses. Note that the precisions listed in table 3 correspond to one real sample and therefore a full complex sample would be represented using twice the listed number of bits. The effect of quantization on cyst contrast is illustrated in figure 5.

The choice of receive $f/\#$ is an important design parameter in our system because we focus solely by phase rotation of the received data. While larger apertures improve resolution when conventional time delay focusing is used, larger apertures might degrade image quality in our system because of the limitations of DSIQ beamforming [6]. In addition, our elements are highly directive because of our large pitch (635 μm) and thus large apertures might yield higher grating lobes. We explored the impact of $f/\#$ by computing the contrast as a function of cyst size for the $f/\#$ s listed in table 4. Figure 6 plots contrast as a function of cyst size for each $f/\#$ tested.

Finally, we explored the effect of varying the apodization window on our system. We used six windows, listed in table 5. Figure 7(a) depicts contrast as a function of cyst size for each window in a noise free environment, and figure 7(b) plots the obtained contrast in the presence of electronic noise with an SNR of -10 dB per channel. It is worth noting that selecting apodization windows based solely on the presented metric might not result in the best image

quality. A particular window might reduce grating lobes and sidelobes, but if it also reduces array gain, losses in sensitivity (reduction in SNR) might outweigh the contrast benefits. Table 6 lists the contrasts (when imaging a cyst of radius 2.5 mm) and the associated sensitivities obtained using each window. Contrasts with no electronic channel noise, and noise with an SNR of -10 dB and 0 dB per channel are listed. The sensitivities were calculated from the peak magnitude of the psfs and are normalized to the sensitivity obtained using flat apodization. We use a cyst of radius 2.5 mm because one of the major applications envisioned for our C-scan system is image guided needle/IV line insertion in the arm, where the veins are approximately 5 mm in diameter.

IV. RESULTS AND DISCUSSION

Figure 1 depicts slices of the psf obtained in our control simulation of conventional ultrasound systems, with the elevation focus at the azimuthal focus (1 cm) and at 2.8 cm. We see a similar response for the two geometries in the azimuth-range plane in 1(e) and 1(f), but as expected, the elevation focus plays a role in the azimuth-elevation and elevation-range planes in 1(a)-1(d). We see a significant broadening of the psf in these planes when the elevation focus is moved away from the azimuthal focus.

Figure 2 shows slices of the psf obtained for our C-scan system. The slice in the azimuth-elevation plane in 2(a) shows a broader mainlobe in azimuth than the 1D array in figure 1, due to our use of only phase delays for focusing. The response is also broader in elevation when compared to the 1D array with a coincident focus in azimuth and elevation. The benefit of a

variable elevation focus becomes apparent though when we compare results from our system to those from the 1D array geometry with the elevation focus at 2.8 cm. The beam is broader in elevation in the 1D case, as can be seen in 1(b) and 1(d). However, a slice of the psf obtained with the 2D array in the azimuth-range plane reveals not only a broad mainlobe but also significant grating lobes.

Figure 3 depicts a comparison of the three geometries described above. It can be seen that the contrast obtained with the 2D array is much worse than with the 1D array with a coincident azimuth and elevation foci. Recall that the metric computes the ratio of the psf energy outside the cyst to the total psf energy. Therefore, when considering the contrast curve for our system, the rightmost portion of the contrast curve (for cysts with radii greater than 4 mm) is affected only by the grating lobes. However, as the size of the cyst decreases, the effects of the sidelobes (cyst radii from 1.5 to 4 mm), and eventually the mainlobe (cyst radii less than 2 mm), come into consideration. The effects of a larger mainlobe and grating lobes combine to limit contrast in our prototype system across cysts of all sizes. However, when we compare our system to the 1D case with different foci in azimuth and elevation, we see that the mainlobe broadening in elevation in the 1D case greatly reduces contrast for that geometry. Since one of the primary applications for our system is image guided needle/IV line insertion, we are particularly interested in cysts of radii between 1.5 to 2.5 mm. In this range, we see that our system performs reasonably; an impressive conclusion considering the reductions in hardware complexity and cost of our approach.

Note that the flat region of the contrast curve ($\text{radii} > 4 \text{ mm}$) for our system depends on the level of the grating lobes and is therefore mostly dependent on the array pitch. The array pitch in our current prototype is large ($635 \text{ }\mu\text{m}$) due to printed circuit board (PCB) fabrication limitations [4]. We will reduce array pitch significantly in our next prototype, which should in turn yield an overall improvement in contrast. Under these conditions, our low cost strategies may outperform conventional 1D arrays.


Figure 4 illustrates the effect of electronic noise on receive. It can be seen, as expected, that the contrast increases with increasing SNR. The plots suggest that improving the electronic SNR much beyond 0 dB per channel will yield no noticeable improvement in image quality. While an SNR greater than 0 dB results in better contrast for large cysts, our focus on imaging cysts having a radius less than 2.5 mm makes this result of limited relevance. As we improve our element pitch and thus reduce grating lobes, the flat region of the curves will change and we will most certainly need to reconsider the effect of SNR.

The effect of quantization can be seen in figure 5. Quantization noise significantly degrades the obtained contrast when less than 10 bits are used per real sample. While these simulations did not include the effect of electronic noise, an electronic SNR as low as 0 dB per channel should still render these results valid.

Figure 6 shows the effect of varying the $f/\#$. We see that contrast increases with increasing $f/\#$ for large cysts. This is due to the 2D array pitch, which results in highly directive elements and thus large grating lobes when large apertures are used. Large $f/\#$ s ($>f/1.5$),

however, result in a very broad mainlobe and reduce contrast when imaging small cysts. Figure 6 suggests that an $f/1$ system would be a good compromise for imaging cysts of all sizes. While this analysis ignores the effect of aperture size on system sensitivity, sensitivity would increase with increasing aperture size. For poor SNR environments, it may be necessary to consider the impact of SNR and $f/\#$ simultaneously.

Finally, figure 7 shows the contrasts obtained using different apodization windows in the presence and absence of electronic noise. Contrasts obtained using each tested apodization window for a cyst of radius 2.5 mm are listed in table 6 for various SNR values, along with the effect of the windows on system sensitivity. There is generally an inverse relationship between contrast and sensitivity. The Nuttall window maximizes contrast for all simulated noise levels, but it is also the window most affected by electronic noise. The contrast trends seen in table 6 when the noise level is varied indicate that the Hann or Tukey windows are least affected by noise, because of comparatively high array gain. Note, however, that the Gaussian window would be a poor choice for all conditions because it yields a poorer contrast for the same sensitivity as the Hann window.

As demonstrated by the above examples, application of the proposed metric eases parameter optimization easier because any system can be characterized by a single scalar quantity. The goal of system design is then to simply maximize the cystic contrast, leaving no room for ambiguity. This is in stark contrast to use of the beamplot, in which optimization is not necessarily clear. The proposed metric is also very flexible because the mask  can be changed to match the target of interest. We could also introduce scatterers in the region defined

by the mask, as described in [2], to predict performance when imaging hypoechoic or hyperechoic lesions. Note, however, that the expressions derived in this paper for the psf energy outside and within the cyst are valid only if the mask represents an anechoic region. The major drawback of the proposed metric is that it neglects the effect of speckle statistics and size on target detectability [15]. Despite this drawback, the above metric is much better suited to characterize medical ultrasound systems than current approaches.

VI. CONCLUSIONS

Existing methods to characterize ultrasound systems are limited in their utility. The beamplot is usually of limited use unless the goal is to image a bright point target. It is, in addition, difficult to decide how to optimize the beamplot to improve overall imaging performance. Contrast detail phantoms cannot be used to assess hypothetical systems without excessive computational costs. We built upon [2-3] to derive a metric to characterize arbitrary 3D broadband ultrasound systems including the effects of electronic noise. We presented simulation results that demonstrated the use of the metric in designing ultrasound systems, and showed that it enables the straightforward optimization of any parameter that affects image quality.

VII. ACKNOWLEDGEMENTS

This work was supported by NIH grant EB002348 and by award DAMD17-01-1-0443 from the US Army Congressionally Directed Medical Research Program.

VIII. REFERENCES

- [1] B. D. Steinberg, *Principles of Aperture and Array System Design*, John Wiley & Sons, 1976, pp. 40-52.
- [2] D. Vilkomerson, J. Greenleaf, and V. Dutt, "Towards a resolution metric for medical ultrasonic imaging," *Proc. IEEE Ultrason. Symp.*, vol. 2, pp. 1405-1410, 1995.
- [3] K. F. Üstüner and G. L. Holley, "Ultrasound Imaging System Performance Assessment," presented at the 2003 AAPM Annual Meeting.
- [4] E. Girard, S. Zhou, W. Walker, T. Blalock, and J. Hossack, "High element count two dimensional transducer array," *Proc. IEEE Ultrason. Symp.*, vol. 1, pp. 964-967, 2003.
- [5] M. I. Fuller, T. N. Blalock, J. A. Hossack and W. F. Walker, "A portable, low-cost, highly integrated, 3D medical ultrasound system," *Proc. IEEE Ultrason. Symp.*, vol. 1, pp. 38-41, 2003.
- [6] K. Ranganathan, M. K. Santy, T. N. Blalock, J. A. Hossack., and W. F. Walker, "Direct Sampled I/Q Beamforming for Compact and Very Low Cost Ultrasound Imaging," *IEEE Trans. Ultrason. Ferroelectr., Freq. Contr.*, vol. 51, no. 9, pp. 1082-1094, 2004.

- [7] A. H. Nuttall, "Some Windows with Very Good Sidelobe Behavior." *IEEE Trans. Acoust. Speech Signal Process.*, vol. 29, no. 1, pp. 84-91.
- [8] W. F. Walker, "A Spline Based Approach for Computing Spatial Impulse Responses," submitted to the IEEE Transactions on Ultrasonics, Ferroelectrics, and Frequency Control.
- [9] J. A. Jensen and N. B. Svendsen, "Calculation of pressure fields from arbitrarily shaped apodized and excited ultrasound transducers," *IEEE Trans. Ultrason. Ferroelectr., Freq. Contr.*, vol. 39, no. 2, pp. 262-267, 1992.
- [10] R. N. Bracewell, *The Fourier Transform and its Applications*, 3rd ed., McGraw-Hill, 2000, pp. 359-367.
- [11] B. D. Steinberg, "Digital Beamforming in Ultrasound," *IEEE Trans. Ultrason. Ferroelectr., Freq. Contr.*, vol. 39, no. 6, pp. 716-721, 1992.
- [12] A. V. Oppenheim, A.V., and R.W. Schaffer, *Discrete-Time Signal Processing*, Prentice-Hall, 1989, pp. 447-448.
- [13] F. J. Harris, "On the Use of Windows for Harmonic Analysis with the Discrete Fourier Transform," *Proc. IEEE*, vol. 66, no. 1, pp. 51-83, 1978.

- [14] Digital Signal Processing Committee of IEEE Acoustics, Speech, and Signal Processing Society, ed., *Programs for Digital Signal Processing*, New York: IEEE Press, 1979. Program 5.2.

- [15] S. W. Smith, R. F. Wagner, J. M. Sandrik, and H. Lopez, "Low Contrast Detectability and Contrast/Detail Analysis in Medical Ultrasound," *IEEE Trans. Ultrason. Ferroelectr., Freq. Contr.*, vol. 30, no. 3, pp. 164-173, 1983.

Figure and table captions -

Figure 1:

Slices of the simulated 3D spatial psf obtained for a conventional system with a 1D array and time delay focusing. The system had a 128 element 1D array with a pitch of 135 μm and apodization was implemented on receive with a Nuttall window. We computed two psfs, one with the elevation focus at the azimuthal focus of 1 cm and another with the elevation focus at 2.8 cm. (a), (c), and (e) depict slices in azimuth-elevation, elevation-range, and azimuth-range respectively, for the system with a coincident focus. (b), (d), and (f) depict slices in azimuth-elevation, elevation-range, and azimuth-range respectively, with the elevation focus set to 2.8 cm. The beam broadens significantly in elevation when the elevation focus is moved away from the azimuthal focus.

Figure 2:

Slices of the simulated 3D spatial psf obtained simulating the first generation prototype of our low-cost C-scan system with a 2D array and direct sampled I/Q (DSIQ) beamforming. Relevant parameters are listed in table 1. (a) and (b) depict slices in azimuth-elevation and azimuth-range respectively. Due to symmetry, the elevation-range slice is identical to the azimuth-elevation slice and is therefore not shown. The mainlobe is broader in azimuth than both 1D array cases in figure 1, and broader in elevation than the 1D array case with a coincident focus in azimuth and elevation. However, the use of a 2D array enables a variable elevation focus and therefore results in a narrower mainlobe in elevation when compared to the 1D case with different azimuthal and elevation foci. An important and undesirable result of a large pitch

(635 μm) in our 2D array is large grating lobes as seen in (b).

Figure 3:

Comparison of our prototype C-scan system with a conventional system. Cystic contrast was computed using (34) and is plotted as a function of cyst size. The rightmost portion of the curve (for large cysts) is affected largely by the grating lobes. As the radius of the cyst decreases, the effects of the sidelobes, and eventually the mainlobe, come into consideration. The contrast obtained with the 2D array is poorer than with the 1D array with a coincident focus in azimuth and elevation, due to larger grating lobes and mainlobe in our system. However, our system outperforms the 1D array system focused at 2.8 cm when imaging small cysts (radii < 1.5 mm) because of the poor elevation beamwidth of the 1D array system. Since one of the primary applications for our low-cost system is image guided needle/IV line insertion, we are most interested in cysts of radii between 1.5 to 2.5 mm. In this range, we see that our system is comparable to the conventional system. Note that we will reduce the array pitch significantly in future generations of our system, and thus hope to reduce grating lobes and improve contrast.

Figure 4:

Effect of electronic noise. Contrasts were computed using (31) for the SNRs listed in table 2 and are shown as a function of cyst size when receive apodization was implemented using (a) a flat window and (b) a Nuttall window. Image quality improves with increasing SNR, as can be seen, although improving the electronic SNR much beyond 0 dB per channel seems to offer little advantage.

Figure 5:

Effect of quantization. Single receive element responses were quantized using different precisions (table 3) for each real sample, and then apodized, focused, and summed to yield 3D responses. Contrasts were computed using (34) and are plotted as a function of cyst size. Performance is significantly worse when less than 10 bits per real sample are used. We did not include the effects of electronic noise in these simulations; however, from figure 4, an electronic SNR of 0 dB per channel or better would render these results valid.

Figure 6:

Effect of $f/\#$. Contrasts were computed using (34) and are plotted as a function of cyst size for the $f/\#$ s listed in table 4. Contrast generally improves with increasing $f/\#$, the highly directive array elements of our prototype system increase grating lobes when large apertures are used. Large $f/\#$ s ($>f/1.5$) result in a very broad mainlobe and reduce contrast when imaging small cysts. An $f/1$ system results in good all round performance. Note that sensitivity is ignored in these simulations but increases with decreasing $f/\#$.

Figure 7:

Effect of apodization with (a) no electronic noise, and (b) electronic noise with SNR -10 dB per channel. Contrasts were computed using (34) in the noise-free case and (31) when noise was considered, using psfs obtained with the apodization windows listed in table 5 and are plotted as a function of cyst size. The Nuttall window yields the best contrast for cysts of all sizes. Although the contrast values obtained using the Nuttall window are also the most affected

by noise (better perceived in table 6), it yields the best performance through the range of noise levels that we investigated.

Table 1:

List of default parameters used to simulate our C-scan system.

Table 2:

Single receive channel SNR values used with (31) to estimate the impact of electronic noise.

Table 3:

Number of bits used to represent each real value to determine the minimum precision required in our system.

Table 4:

$F/\#$ s used on receive to determine the optimal $f/\#$ for our system.

Table 5:

Windows used to determine the impact of receive apodization on cyst contrast.

Table 6:

Contrasts obtained for a cyst of radius of 2.5 mm with varying amounts of electronic noise using different apodization windows, and their associated sensitivities or array gain

normalized to the array gain obtained using flat apodization. Contrasts with no electronic channel noise, and noise with an SNR of -10 dB and 0 dB per channel are listed. Contrasts were computed using (34) in the noise-free case and (31) when noise was considered. The Nuttall window maximizes contrast for all simulated noise levels, while the flat and Tukey windows are least affected by electronic noise because of comparatively high array gain. Note that the Gaussian window is a poor choice for this geometry as it yields less contrast for the same sensitivity as the Hann window.

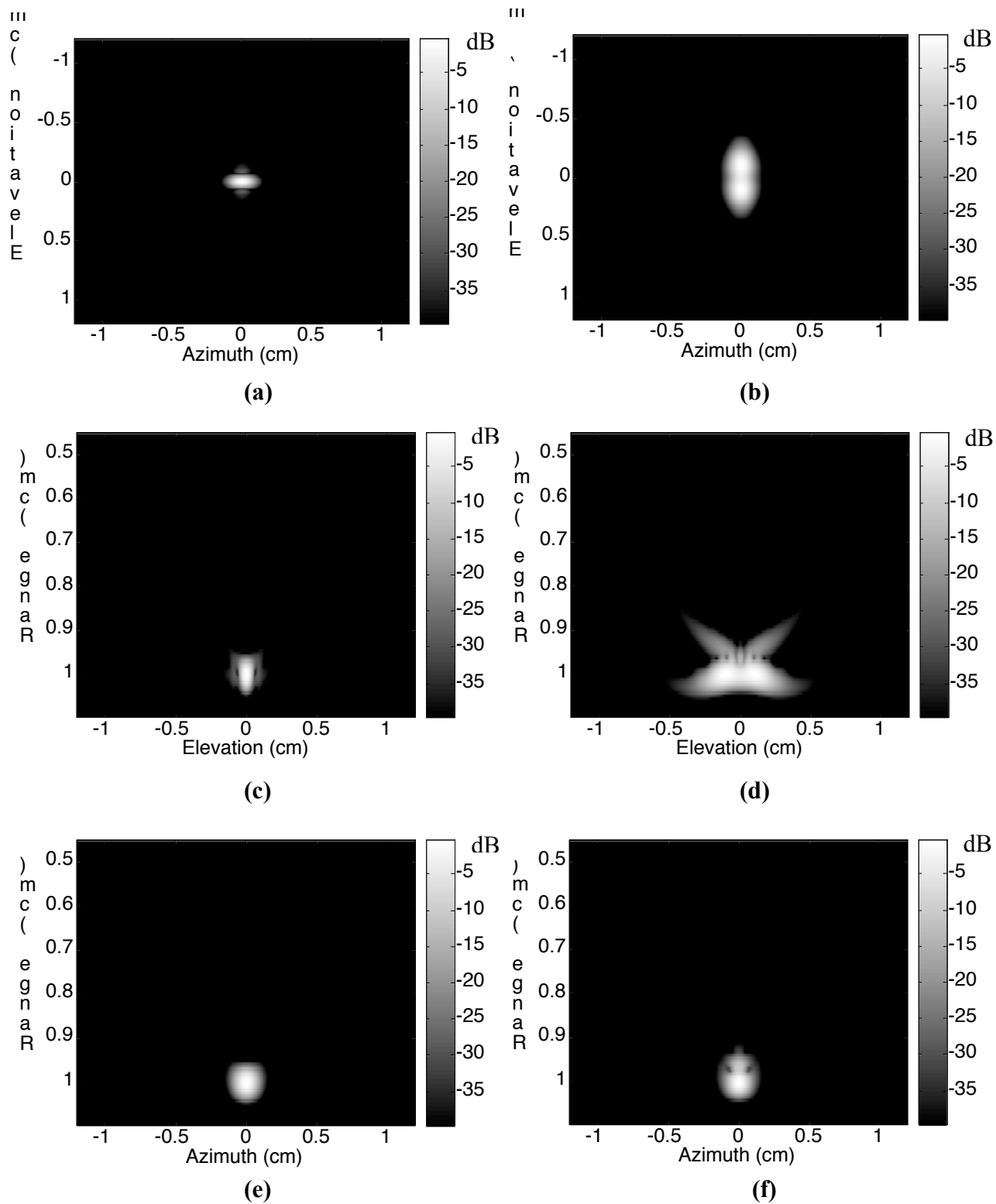


Figure 1

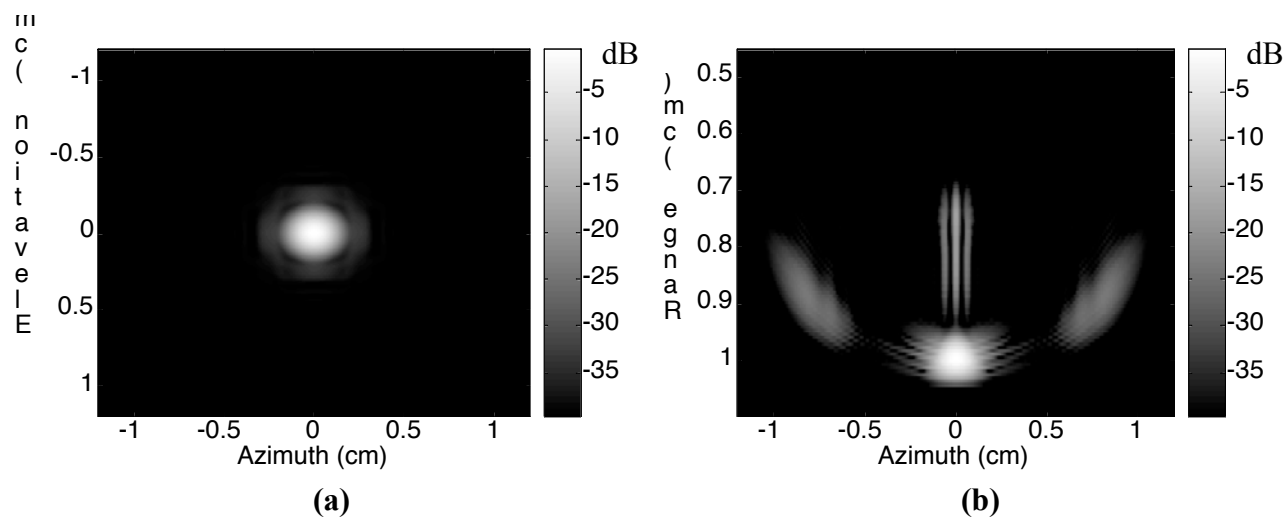


Figure 2

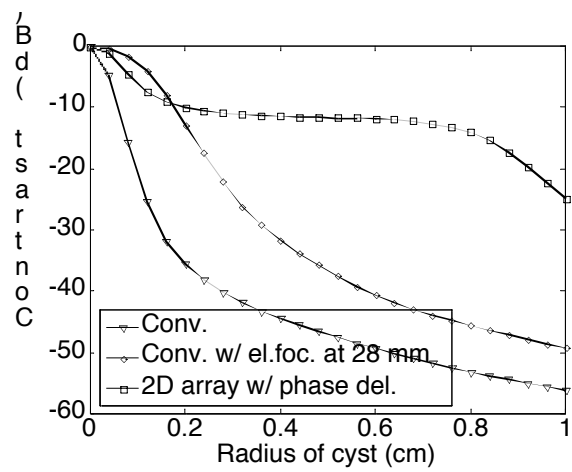
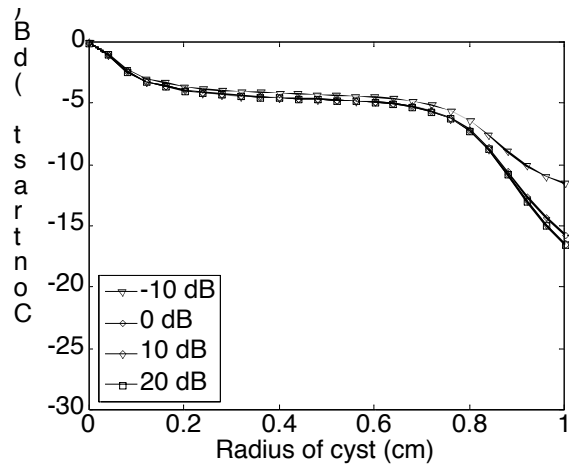
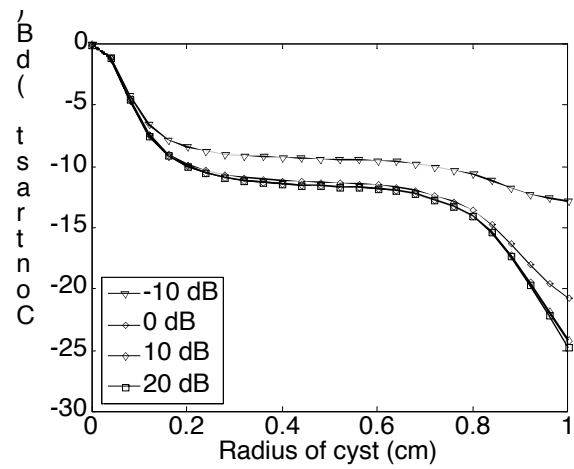


Figure 3



(a)



(b)

Figure 4

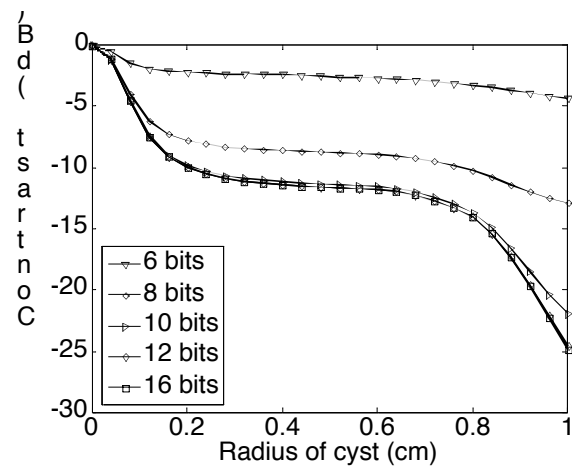


Figure 5

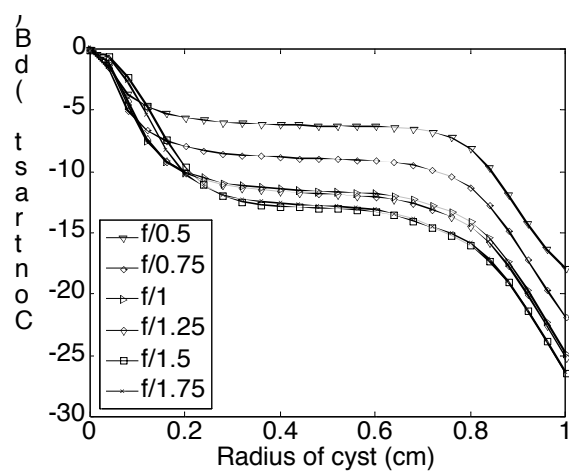
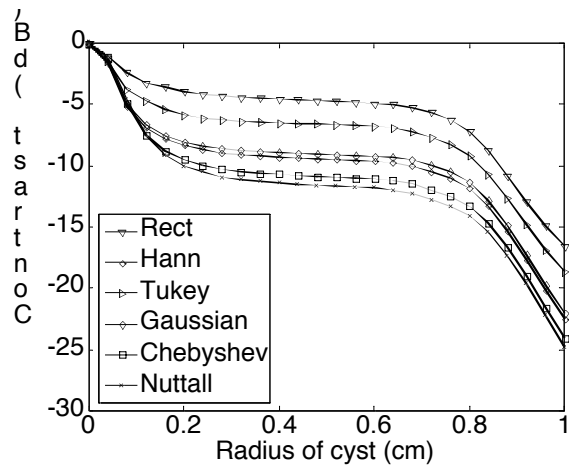
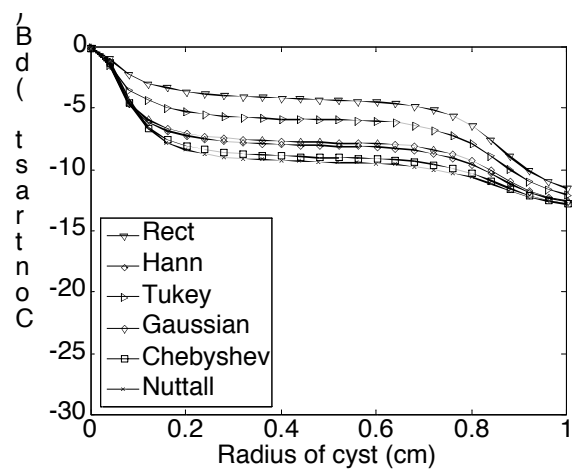


Figure 6



(a)



(b)

Figure 7

2D array layout	32 x 32
Pitch	635 μm
Receive focus	1 cm
f/#	1
Receive apodization	Nuttall window
Transmit pulse center frequency	3.3 MHz
Transmit pulse length	3 cycles weighted by a Nuttall window
Spatial window over which psf was computed	Cylindrical volume with radius 2.4 cm and height 1 cm
Spatial sampling	60 μm radially, 1 degree in angle, and 60 μm in range

Table 1

Electronic SNR per channel (dB)
-10
0
10
20

Table 2

Quantization (# bits)
6
8
10
12
16

Table 3

f/#
0.50
0.75
1
1.25
1.5
1.75

Table 4

Apodization
Flat
Hann [12]
Tukey [13]
Gaussian [13]
Chebyshev (relative sidelobe attenuation of 100 dB) [14]
Nuttall [7]

Table 5

Window	Array gain (dB)	Contrast (dB) with - 10dB electronic SNR	Contrast (dB) with 0 dB electronic SNR	Contrast (dB) with no electronic noise
Rect	0	-4	-4	-4
Hann	-7	-8	-9	-9
Tukey	-2	-6	-6	-6
Gaussian	-7	-7	-8	-8
Chebyshev	-9	-8	-10	-10
Nuttall	-11	-9	-10	-11

Table 6

A Spline Based Approach for Computing Spatial Impulse Responses

William F. Walker, Ph.D.

Department of Biomedical Engineering

Department of Electrical and Computer Engineering

University of Virginia

bwalker@virginia.edu

Abstract:

This paper describes an analytical approach for computing the two-way far-field spatial impulse response from rectangular transducer elements under arbitrary excitation. The described approach determines the response as the sum of polynomial functions, making computational implementation quite straightforward. The proposed algorithm was implemented as a C routine under Matlab and results were compared to theory and to those obtained under similar conditions from the well established FIELD II program. All results were in excellent agreement. The proposed method is quite efficient for computing spatial sensitivity functions at a single instant in time; an application for which FIELD II is not well optimized. Under the specific conditions tested here, the proposed algorithm was approximately 25 times faster than FIELD II for computing spatial sensitivity functions, with no loss in quality.

Introduction:

The design of modern phased array ultrasonic imaging systems relies heavily on the use of computer simulations. This is necessary because the broadband and near-field nature of most clinical imaging environments severely limits the utility of the Fraunhofer approximation [1] and other theoretical methods. Furthermore, the high degree of optimization of modern systems makes even small deviations from theory significant. For example, if the system designer is concerned with the array sensitivity pattern down 80 dB from the main-lobe, then a deviation from theory of only 0.1% (-60dB) will significantly affect performance and make optimization to the desired level impossible. Clearly, highly accurate simulation tools are required to guide the selection of transducer geometry, apodization, operating frequency, and other parameters.

While most researchers and designers would agree upon the need for accurate simulation, the appropriate approach depends upon the specific problem of interest and the parameters that are most significant to that problem. For example, in cases where details of transducer vibration and crosstalk are of interest, a computationally costly finite element analysis may be required to capture the most relevant behavior. For such problems the highly optimized PZFlex (Weidlinger Associates, Inc. New York, NY) package is widely used [2]. In other cases, where the detailed transducer response is of less interest, but the propagation medium is inhomogeneous or multiple scattering occurs, the more computationally efficient Finite Difference Method, such as that implemented in Wave2000 (CyberLogic Inc., New York, NY), may be used.

For the vast majority of situations, where the propagation medium can be considered homogeneous or inhomogeneities can be modeled as a near-field thin phase

screen, Stepanishen's method [3], as implemented in Jørgen Jensen's FIELD II program [4] has become a *de facto* standard. This approach determines the spatial impulse response of each transmit element, convolves this with the spatial impulse response of each receive element, convolves this result with the transmitted pulse, and convolves this with the transmit and receive electromechanical impulse responses to determine the two-way temporal response at a point in space. This technique, as implemented in Jensen's code, has been highly refined over roughly a decade of development so that it is extremely efficient and available in a compiled form on a variety of computer platforms (<http://www.es.oersted.dtu.dk/staff/jaj/field/>). By computing the temporal signals returned from various target locations, FIELD II readily models common experimental situations.

While the temporal response returned by FIELD II provides an excellent parallel to experiment, recent theoretical work by Zemp [5] and Walker [6] highlights the importance of considering the full four or five dimensional system response. In a previous paper [6], this author discussed a general signal model describing the system response as a function of three spatial dimensions and time. While much of this detail is hidden experimentally, the consideration of the full dimensionality of the system response yields insights and offers paths for analysis that are not apparent in the more conventional two dimensional (space, time) view of the system. Zemp [5] carried this concept one step further, including another dimension for image line index, thereby further clarifying system behavior. Our laboratory has recently applied these frameworks to derive a general resolution metric that allows quantitative comparison of system performance, even when the individual impulse responses of those systems are very different in structure [7]. Interestingly, this new resolution metric is based upon the system response throughout space at a single instant in time; a form of the impulse response that is not naturally determined by FIELD II. Although such responses can be computed by sampling the temporal responses generated by FIELD II, this approach is extremely costly in terms of both computation and storage.

In this paper we describe a new approach to computing spatial impulse responses that directly determines the response throughout space at a single instant in time. This approach is complementary to FIELD II, simply yielding responses in a different set of dimensions. Because results from this code are predictive of system performance and are a permutation of the data available from FIELD II, we name this code DELFI. In this paper we describe the theoretical underpinnings of the DELFI code, describe implementation, and validate the code through comparisons with FIELD II and analytical predictions. We discuss the relative computational efficiency of DELFI and discuss future directions for development and refinement.

Theory:

We begin our derivation by considering the general approach employed by Jensen in the FIELD II program [4]. We consider the system response for a specific transmit-receive element pair to be a four dimensional function of space and time:

$$p(x, y, z, t) = e(t) * m_t(t) * m_r(t) * h_t(x, y, z, t) * h_r(x, y, z, t) \quad (1)$$

where x , y , and z are the three spatial dimensions, t is the time for a given line (proportional to range in the beamformed image), $p(x, y, z, t)$ is the system point spread function (psf), $e(t)$ is the electrical excitation of the transmit element, $m_t(t)$ and $m_r(t)$ are the electromechanical transfer functions of the transmit and receive elements respectively, $h_t(x, y, z, t)$ and $h_r(x, y, z, t)$ are the spatial impulse responses of the transmit and receive elements respectively, and $*$ indicates convolution in the time dimension. In typical systems the excitation and the transmit and receive electromechanical transfer functions are assumed constant for all elements of the array. Thus we can convolve these terms together before computing the overall response with little loss in generality. Performing this step we simplify (1) to yield:

$$p(x, y, z, t) = emm_r(t) *_t h_t(x, y, z, t) *_t h_r(x, y, z, t) \quad (2)$$

where $emm_r(t)$ is the combined effect of the excitation and the transmit and receive electromechanical transfer functions and can be represented mathematically as $emm_r(t) = e(t) *_t m_t(t) *_t m_r(t)$. While FIELD II computes expressions (1) or (2) using sampled versions of each of the component signals, we take an alternate approach, instead using analytical expressions for these functions.

The utility of an analytical approach depends upon the choice of expressions used: they must be general enough to include all relevant cases, but they must be constrained in such a way to guarantee the presence of an analytical solution. Since (2) allows for consideration of most practically interesting cases and requires two convolutions (rather than the four convolutions of (1)) we build our algorithm upon this expression. Further simplification can be made by assuming that the point of interest lies in the far-field of both the transmit and receive elements. This is not an onerous assumption since cases where the response would lie in the near-field of a physical element can be readily modeled using a superposition of computational elements for which the far-field assumption is valid. We further simplify the problem by assuming that the elements are rectangular.

Following these assumptions, and once again drawing upon the methodology of Jensen [4], we recognize that the one-way spatial impulse response of an element takes on one of three functions. If the field point lies on a line perpendicular to the element face and passing through its center then the spatial impulse response as a function of time is simply a delta function, as shown in the left panel of figure 1. If the field point does not fulfill the first condition, but instead lies upon one of two planes passing through the element center and perpendicular to the element edges then the spatial impulse response in time is a rectangle function, as depicted in the central panel of figure 1. Finally, if the field point fulfills neither of the above conditions then the spatial impulse response in time is a trapezoid function, as shown in the right panel of figure 1. These possible one-way spatial impulse responses are summarized mathematically below. Note we describe the rectangle and trapezoid functions using sums of unit step and ramp functions.

$$h_0(x, y, z, t) = A_0(x, y, z) \delta(t - t_0) \quad (3)$$

$$h_1(x, y, z, t) = A_1(x, y, z)u(t - t_{1,0}) - A_1(x, y, z)u(t - t_{1,1}) \quad (4)$$

$$h_2(x, y, z, t) = (t - t_{2,0})A_2(x, y, z)u(t - t_{2,0}) - (t - t_{2,1})A_2(x, y, z)u(t - t_{2,1}) \\ - (t - t_{2,2})A_2(x, y, z)u(t - t_{2,2}) + (t - t_{2,3})A_2(x, y, z)u(t - t_{2,3}) \quad (5)$$

where h_0 , h_1 , and h_2 represent the delta, rectangle, and trapezoid spatial impulse responses respectively and $u(t)$ is the unit step function. The scaling functions $A_0(x, y, z)$, $A_1(x, y, z)$, and $A_2(x, y, z)$ are constant at any specific spatial location and include $1/r$ spreading, scaling to account for the element size, and an obliquity factor to account for a soft transducer baffle [8], if desired. The time delay t_0 present in (3) is determined by the speed of sound and the distance from the element center to the field point. Similarly, the delays present in (4) and (5) are determined from the speed of sound and distances between the field point and the element edges and corners, respectively.

To determine the two-way response from an element pair we must convolve the appropriate version of (3)-(5) for the receive element with the appropriate version of (3)-(5) for the transmit element. While superficial analysis suggests that nine permutations are possible, a more careful examination reveals that since the order of convolution is irrelevant, some of these permutations are redundant. Thus, the two-way response must fit one of the following six general expressions.

$$h_{tr} = h_t * h_r = \left\{ h_0 * h_0 \text{ or } h_0 * h_1 \text{ or } h_0 * h_2 \text{ or } h_1 * h_1 \text{ or } h_1 * h_2 \text{ or } h_2 * h_2 \right. \quad (6)$$

where we have dropped space and time references to simplify notation. Note that while the simplified notation of (6) suggests that in some cases (such as $h_0 * h_0$) the transmit and receive responses are identical, this is intended only to state that the transmit and receive responses fit the same function; they may have different delays and scaling. Substituting (3)-(5) into (6) yields a set of six possible two-way impulse responses:

$$h_{0_a} * h_{0_b} = A_{0_a} A_{0_b} \delta(t - t_{0_a} - t_{0_b}) \quad (7)$$

$$h_{0_t} * h_1 = A_0 A_1 \sum_{j=0}^1 (-1)^j u(t - t_0 - t_{1,j}) \quad (8)$$

$$h_{0_t} * h_2 = A_0 A_2 \sum_{j=0}^3 c_j (t - t_0 - t_{2,j}) u(t - t_0 - t_{2,j}) \quad (9)$$

$$h_{1_a} * h_{1_b} = A_{1_a} A_{1_b} \sum_{j=0}^1 \sum_{k=0}^1 (*1)^j (*1)^k (t * t_{1_a,j} * t_{1_b,k}) u(t * t_{1_a,j} * t_{1_b,k}) \quad (10)$$

$$h_{1_t} * h_2 = A_1 A_2 \sum_{j=0}^1 \sum_{k=0}^3 (-1)^j c_k (t - t_{1,j} - t_{2,k})^2 u(t - t_{1,j} - t_{2,k}) \quad (11)$$

$$h_{2_a_t} * h_{2_b_t} = A_{2_a} A_{2_b} \sum_{j=0}^3 \sum_{k=0}^3 c_j c_k (t - t_{2_a,j} - t_{2_b,k})^3 u(t - t_{2_a,j} - t_{2_b,k}) \quad (12)$$

where $c_j = \{1 \text{ for } j = 0 \text{ or } 3 \text{ and } -1 \text{ for } j = 1 \text{ or } 2\}$. With each of the six possible two-way impulse responses in hand we can now consider an appropriate analytical representation of the excitation function (including transmit and receive electromagnetic transfer functions). While a number of possible functions are attractive, we choose to represent $emm_{tr}(t)$ using cubic splines [9]. This representation is attractive because it allows arbitrary function shapes while restricting the form of the function to be no higher order than piecewise cubic polynomial. Writing this spline representation explicitly yields:

$$emm_{tr}(t) = \sum_{j=M_0}^{M_1} (\alpha_j + \beta_j t + \gamma_j t^2 + \delta_j t^3) (u(t - j\partial) \partial u(t \partial (j+1)\partial)) \quad (13)$$

where α_j , β_j , γ_j , and δ_j are the spline coefficients, M_0 and M_1 are the first and last spline indices, and ∂_j is the spline to spline interval. We can now complete an analytical expression for (2) by convolving (13) with the appropriate version of (7)-(12). While such a convolution appears quite tedious, it can be readily performed utilizing Laplace transforms [10]. The resulting expression is a sum of 3rd, 4th, 5th, 6th, or 7th order polynomials (multiplied by unit step functions), with the polynomial order depending upon the combination of element responses employed. We do not present the analytical form of these expressions since they offer little insight and are quite lengthy. Utilizing these final polynomial expressions, the complete two-way response for a given transmit-receive element pair can be computed by simply summing polynomials.

Validation:

The proposed algorithm was implemented in a C routine called as a mex file within Matlab (The Mathworks, Inc. Natick, MA). This approach allowed us to readily generate array geometries and visualize results within Matlab, while taking advantage of the increased computational efficiency of compiled C. All calculations were performed in IEEE Standard double precision floating point arithmetic. All simulations were performed on an Apple Powerbook G4 computer running Matlab 7.0.1 under Mac OS 10.3.7.

The validity of the proposed algorithm was tested by comparing the two-way spatial response of a single 2D array element as predicted by DELFI and FIELD II. For both codes the array element was modeled using a single computational element. Both codes also assumed a combined excitation and transmit/receive electromechanical impulse response equal to a 5.0 MHz sine multiplied by an 8 cycle Nuttall window [11]. The spline representation of the pulse utilized in DELFI was generated at a sampling rate

of 8 times the assumed center frequency (40 MHz). This sampling rate was found empirically to generate a pulse with harmonics approximately 100 dB down from the main signal. FIELD II calculations utilized a sampling rate 5 times higher than this (200 MHz). While this rate is twice the default for FIELD II (100 MHz), our experience suggests that this rate is certainly within an appropriate range for calculations of this type. The system response was determined in radial coordinates over an angle of 0° to 90° (sampled at 0.45°) covering a range from 19.925 cm to 20.075 cm (sampled at 10 μm). For DELFI all points were computed at the time instant that centered the sensitivity function at 20 cm. For FIELD II a complete response in range, azimuth, and time was computed, with the time that centered the sensitivity function at 20 cm selected for analysis.

Typical DELFI and FIELD II sensitivity functions for a $300 \times 300 \mu\text{m}$ element are shown in figure 2. Both responses have been normalized to allow comparison. These responses are quite similar except for a series of artifacts located about the 0° line in the FIELD II response. Although the source of this artifact is not apparent, it may result from the corrections FIELD II employs when sampling the infinite bandwidth spatial impulse responses of the array elements.

Additional simulations were performed to determine computational times and the similarity of responses for square elements ranging in size from 50 to 600 microns. All computational times were estimated using the tic and toc commands in Matlab. Across this set of 12 simulations the computation time for DELFI ranged from approximately 0.21 to 0.29 seconds. Over the same set of conditions FIELD II execution times ranged from 5.33 to 7.61 seconds. Comparing matched sets of simulations, FIELD II took from 18.4 to 33.6 times as long for the computation, with the average time of computation being 27.1 times greater for FIELD II. Note that these times do not include any array definitions or other housekeeping operations. For the sake of comparison we also computed the temporal response at the focus using both codes. FIELD II computations were performed at a sampling rate of 200 MHz and the DELFI code was run repeatedly at different time points to generate a waveform sampled at 40 MHz. Under these conditions the FIELD II response was computed in 1.2 ms and the DELFI response was computed in 7.2 ms, giving FIELD II a factor of 6 advantage in computational time. This difference is surprisingly modest given that DELFI was called 65 times from within a loop in Matlab, a process that engendered significant overhead. Straightforward modifications of DELFI might significantly improve its relative performance when temporal responses are required. While it would be inappropriate to over-generalize from this limited set of simulations, the existing DELFI code is computationally attractive for applications where spatial responses at a single time point are desired.

The accuracy of DELFI was quantified by computing the Full Width at Half Maximum (FWHM) of the two-way single element sensitivity function over a range of element sizes ranging from 50 to 600 microns in 50 micron steps. The same metric was also computed for FIELD II simulations, with both results compared to the iterative theoretical method of [12]. McKeighen's iterative method determines the element's FWHM sensitivity by modeling the response as a sinc squared multiplied by a cosine squared obliquity term (to account for an assumed soft baffle condition). McKeighen's method was implemented using 100 iterations at an assumed center frequency of 5.0 MHz. FIELD II and DELFI used sampling rates and the pulse definitions described

above. The FWHM of the spatial sensitivity function was estimated from the curve formed by taking the maximum of each lateral line, after computing the absolute value of the response. Results comparing FIELD II, DELFI, and McKeighen's theory are shown in figure 3. All three methods are in excellent agreement.

Discussion:

Computing the spatial impulse response of a transmit-receive element pair by convolving (13) with (7)-(12) analytically offers both advantages and disadvantages relative to the established approach using discrete time convolution. On the positive side the analytical approach allows direct computation of the response at a single instant in time. In contrast, the conventional discrete time approach (at least as currently implemented) requires the computation of a full temporal response even if only a single time point is required. An additional advantage of the analytical approach is that it yields an exact solution, at least within the numerical precision of the computer used for the calculation and within the limitations of the far-field approximation. In contrast, the discrete time approach utilizes under-sampled versions of the element responses and thus introduces some error. In addition, the discrete implementation makes it difficult to compute the spatial response at any exact instant in time. A relative weakness of the analytical approach is that significantly more computation is required to determine a temporal response at a single location. A further limitation of the analytical approach, at least as implemented here, is the occasional numerical instability that results from subtracting multiple high-order polynomials.

The DELFI code described here is still in an early stage of development, with many directions apparent for enhancing computational efficiency and improving accuracy. The current code determines the result of the convolution of a single spline segment with two trapezoid functions by summing 16 7th order polynomials. This approach is computationally tedious and prone to numerical instability. One possible direction for simplification would begin with the recognition that the first half of this response (in time) requires only 8 polynomials for synthesis. Next, by considering the response in negative time it is apparent that the second half (again in time) of this response also requires only 8 polynomials. Together this realization could cut computation time in half. Additional computational savings are undoubtedly possible. Algorithmic accuracy could be enhanced by utilizing a more sophisticated model for the element impulse responses. Spline functions might prove particularly suitable for modeling complicated near-field responses [13, 14].

Conclusion:

The DELFI code presented here employs analytical convolution of cubic spline functions with continuous time element responses to compute the spatial impulse response of ultrasound transducers. Comparison with FIELD II and theoretical methods show that the proposed algorithm performs comparably to existing methods. For the computation of impulse responses at a single instant in time, the proposed algorithm is as much as 30 times faster than FIELD II. For computing temporal responses the proposed code is approximately 6 times slower than FIELD II, although further refinement may reduce this mismatch. The proposed algorithm, as implemented by the DELFI code, offers an attractive complement to the well established FIELD II program.

Acknowledgements:

This work was supported in part by NIH Grant EB002348 and the US Army Congressionally Directed Research Program under Grant DAMD17-01-1-0443. The author would like to thank Drake Guenther and Karthik Ranganathan for their valuable feedback on this manuscript.

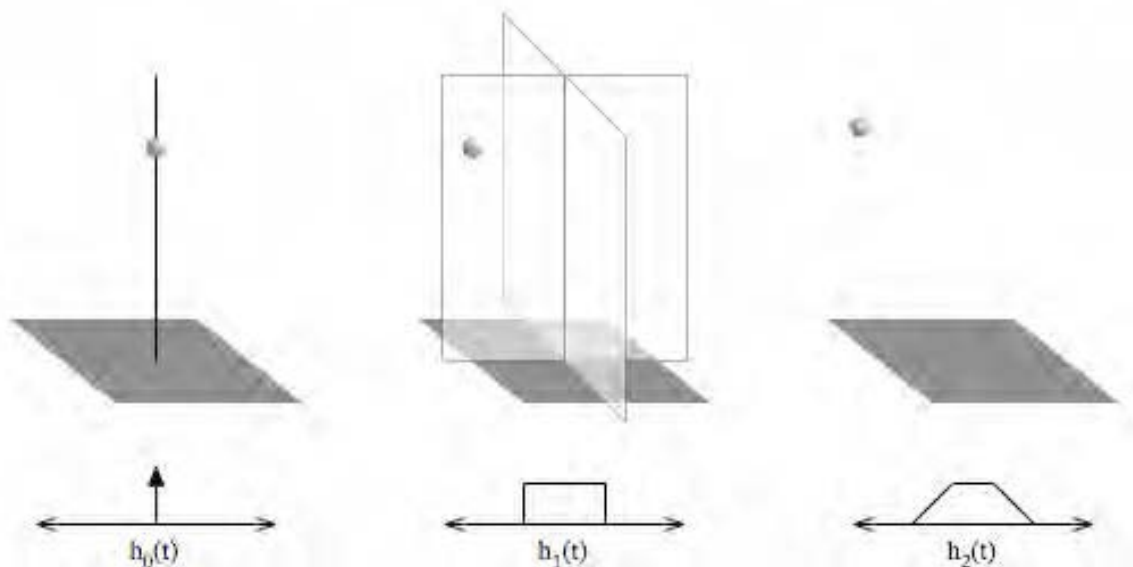


Figure 1:

Geometries for determining the one-way spatial impulse response of an individual array element. In the left panel the field point lies on a line through the element's center and perpendicular to its face. In the center panel the field point does not satisfy the first condition, but lies on a plane that bisects the element and is perpendicular to its face. In the right panel the field point lies at any location not satisfying either of the first two conditions.

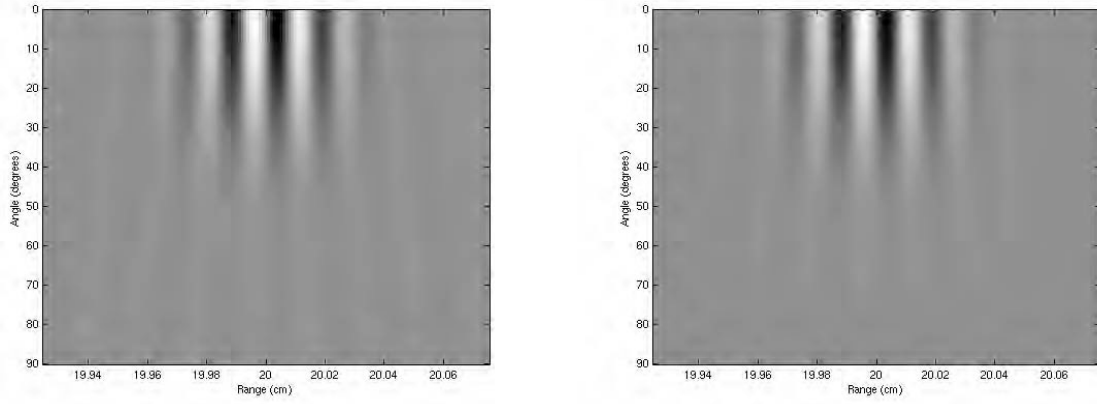


Figure 2:

The spatial impulse response of a 300 μm square array element in a soft baffle for an 8 cycle Nuttall windowed 5.0 MHz transmit pulse. The left panel depicts the output of the proposed algorithm (DELFI) while the right panel indicates the output of FIELD II. Both responses have been normalized to allow easy comparison. The responses are nearly identical with the exception of localized artifacts near the 0° line of the FIELD II response.

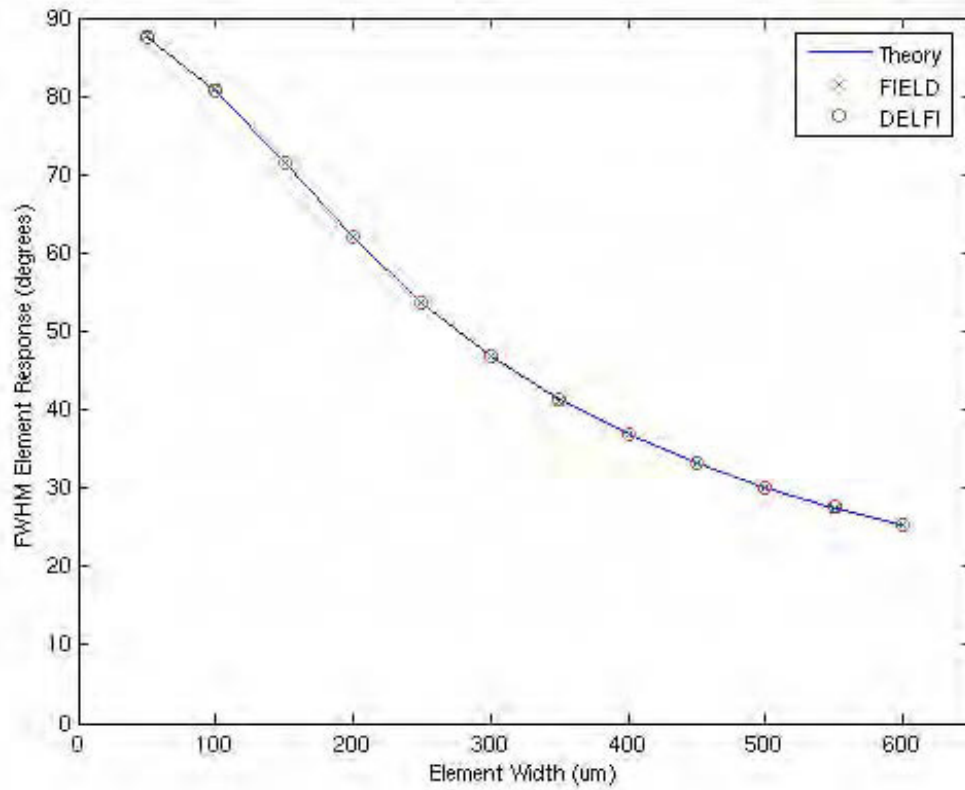


Figure 3:

Full Width at Half Maximum of the spatial sensitivity function of a square 2D array element. All analyses / simulations were performed at a 5.0 MHz center frequency with the soft baffle assumption. All methods are clearly in excellent agreement.

References:

- [1] J. W. Goodman, *Introduction to Fourier Optics*. San Francisco: McGraw-Hill, 1986.
- [2] G. L. Wojcik, D. K. Vaughan, N. Abboud, and J. Mould, "Electromechanical modeling using explicit time-domain finite elements," presented at Proc. 1993 Ultrasonics Symposium, Baltimore, 1993.
- [3] P. R. Stepanishen, "Transient Radiation from Pistons in an Infinite Baffle," *Journal of the Acoustical Society of America*, vol. 49, pp. 1629-1638, 1970.
- [4] J. A. Jensen and N. B. Svendsen, "Calculation of pressure fields from arbitrarily shaped, apodized, and excited ultrasound transducers," *IEEE Transactions on Ultrasonics, Ferroelectrics, and Frequency Control*, vol. 39, pp. 262-267, 1992.
- [5] R. J. Zemp, C. K. Abbey, and M. F. Insana, "Linear system models for ultrasonic imaging: application to signal statistics," *IEEE Transactions on Ultrasonics Ferroelectrics & Frequency Control*, vol. 50, pp. 642-54, 2003.
- [6] W. F. Walker, "The Significance of Correlation in Ultrasound Signal Processing," presented at SPIE International Symposium on Medical Imaging, San Diego, CA, 2001.
- [7] K. Ranganathan and W. F. Walker, "A New Performance Analysis Metric for Medical Ultrasound," presented at IEEE Ultrasonics Symposium, Montreal, Canada, 2004.
- [8] A. R. Selfridge, G. S. Kino, and B. T. Khuri-Yahub, "A theory for the radiation pattern of a narrow strip acoustic transducer," *Applied Physics Letters*, vol. 37, pp. 35-6, 1980.
- [9] C. de Boor, *A Practical Guide to Splines*: Springer-Verlag, 1978.
- [10] S. Haykin and B. Van Veen, *Signals and Systems*, 2 ed: Wiley, 2003.
- [11] A. H. Nuttall, "Some Windows with Very Good Sidelobe Behavior," *IEEE Transactions on Acoustics, Speech, and Signal Processing*, vol. ASSP-29, pp. 84-91, 1981.
- [12] R. E. McKeighen, "Design Guidelines for Medical Ultrasonic Arrays," presented at SPIE Medical Imaging: Ultrasonic Transducer Engineering, San Diego, CA, 1998.
- [13] J. A. Hossack and G. Hayward, "Efficient calculation of the acoustic radiation from transiently excited uniform and apodised rectangular apertures," presented at IEEE Ultrasonics Symposium, 1993.
- [14] J. A. Jensen, "A New Calculation Procedure for Spatial Impulse Responses in Ultrasound," *Journal of the Acoustical Society of America*, vol. 105, pp. 3266-74, 1999.

Evaluation of Translating Apertures Based Angular Scatter Imaging on a Clinical Imaging System

M. J. McAllister¹, K. W. Rigby², W. F. Walker¹

¹Department of Biomedical Engineering, University of Virginia, Charlottesville, VA, U.S.A. 22908

²GE Corporate Research & Development, Schenectady, NY, U.S.A.

Abstract - Traditional ultrasound systems measure backscatter in B-mode, capturing only the acoustic energy that is reflected directly from the target region to the transducer face. These systems fail to utilize the information in the echo field that is scattered in other directions and therefore cannot characterize the angular scattering behavior of the targets being observed. Since target-specific angular scattering has great potential as a source of increased contrast in biological tissues, it is desirable to modify the method of acquisition in order to obtain reliable information about this behavior. However, prior systems used to investigate this information have been clinically unwieldy and statistically inaccurate over small regions. We have implemented a method of acquisition that utilizes the translating apertures algorithm (TAA) to reliably separate target-specific angular scatter information from the effects of changing acquisition geometry. This acquisition method has been implemented in real-time on a clinical linear array system. Seven interrogation angles are acquired for each imaging line, and the TAA is implemented repeatedly across the array to yield per-pixel maps of angular scatter behavior. We present comparisons of per-pixel angular scatter behavior for a variety of target types, including correlation analysis of a Rayleigh-regime wire target phantom and comparative image analysis with phantoms containing targets of varying compressibility and density. It is shown that the TAA maintains a high per-pixel correlation level over a broad range of interrogation angles. Comparative angular scatter imaging is shown to yield relative contrast improvements on the order of 10-15dB in some targets.

I. INTRODUCTION

Traditional clinical ultrasound imaging methods yield information about the echogenicity of targets

within the imaging field by processing only those echoes which are returned directly to the point of transmission (backscatter). Such systems do not consider portions of the returning echo field which are scattered in other directions, and thus cannot provide information about the angular scatter profile of insonified targets. The character of the angular scatter profile has been shown to contain significant information about the type of target being observed [1], so it is desirable to develop an imaging system which can process this type of information in a clinically useful manner.

In general, the amplitude of the echo field emitted by a Rayleigh scattering target will exhibit an angular dependence that is proportional to its background-relative compressibility and density:

$$R = \frac{2\pi f a^3}{3rc} \left[\frac{\kappa_t - \kappa}{\kappa} + \frac{3\rho_t - 3\rho}{2\rho_t - \rho} \cos(\theta_s) \right] \quad (1)$$

where a is the scatterer radius, r is the target range, κ_t and κ are the target and background compressibilities, respectively, ρ_t and ρ are the target and background densities, respectively, and θ_s is the scattering angle relative to backscatter (180°). Generated echoes consist of the summed contributions of an omni-directional wave caused by local compressibility variations and an angle-dependent (dipolar) wave caused by local variations in density, but this information cannot be separated with a conventional imaging geometry.

We have developed an imaging system using the translating apertures algorithm (TAA) [2] which allows for the reliable evaluation of the echo field at multiple interrogation angles. This allows for the omni-directional and angle-dependent components of the echo field to be evaluated separately, which introduces compressibility and density variations as a new source of potential image contrast. This imaging method is implemented in real-time on a GE Logiq 700MR clinical imaging system using a 7.5MHz linear array probe. We present the initial

evaluation of this system's ability to isolate angular scatter information through analysis of a variety of target types.

II. METHODS

The advantage of the translating apertures algorithm over traditional angular scatter acquisition geometries [3] is the reliable isolation of target-specific echo information from other system effects. Moving the transmit and receive apertures in equal and opposite directions to increase interrogation angle provides a stable system point spread function through a broad angular range.

In order to implement the TAA on a linear array in a useful manner that can generate images, it is necessary to modify system behavior during transmission and reception such that a variety of angles can be interrogated for every point in lateral space along the array. Implementation of the TAA on the Logiq 700 system involves extensive modification to allow for precise control of the apertures being utilized for transmission and reception for every set of pulses that the system fires. Since linear array systems are designed to focus at multiple depths and (typically) fire one set of focused pulses per lateral image line per focus, modifications must be made to interrogate a single region in space at multiple angles.

Firstly, identical transmit/receive beamforming is implemented across multiple system focal zones, such that the system interrogates the same spatial region many times (according to the number of interrogation angles desired). It should be emphasized that though the system interprets each of these redundant firings as a different *spatial* focal zone, all the calculated time delays are identical for each zone. Additionally, dynamic receive focusing and transmit/receive apodization (which are depth dependent) are disabled. Aperture translation is achieved through pre-calculated electronic channel maps which can independently turn any array element on or off during transmit and receive operations. By using the same beamforming calculations for every "zone," small angles can be interrogated by turning on transmit/receive elements near the center of the active aperture, and large angles can be interrogated by enabling elements near the edge. All imaging vectors are placed in line with the physical imaging

elements to assure absolute symmetry as TAA is applied to separate the active transmit and receive apertures in equal and opposite directions. The firing order of the system for a four-angle acquisition thus looks like this:

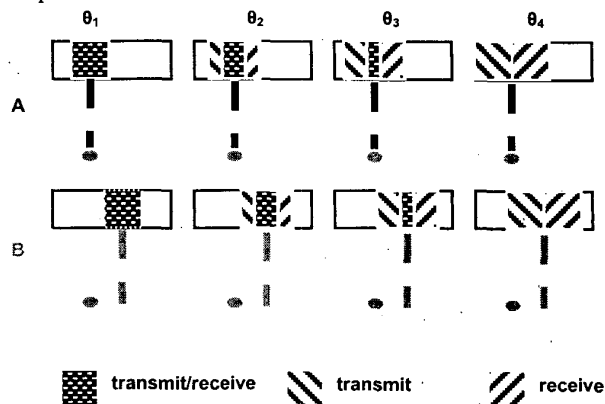


Figure 1: Multi-angle acquisition on a linear array

This example demonstrates acquisition of a backscatter angle (θ_1) and three other interrogation angles for two different imaging lines (A and B). The firing order for the system would be $A\theta_1$, $A\theta_2$, $A\theta_3$, $A\theta_4$, $B\theta_1$, $B\theta_2$, $B\theta_3$, $B\theta_4$. There are approximately 200 lateral spatial vectors per image frame, and up to seven interrogation angles can be interrogated per spatial imaging line.

Complex echo information is obtained in the form of summed IQ data that is offloaded from the Logiq 700 to a pc-based storage system, where it is then unpacked/de-interlaced and processed for the purposes of comparative evaluation.

III. RESULTS

Rayleigh-regime wire target

As it is essential that the TAA acquisition maintain a highly correlated system point spread function across all angles of interrogation, an initial experiment was performed using a $20\mu\text{m}$ diameter stainless steel wire ($< \lambda/10$, approximating a Rayleigh scattering target) in a degassed water bath. Seven acquisition angles were acquired, from backscatter (180°) to 162° in 3-degree increments. Since transmit and receive apodization could not be controlled independently, no apodization was used for any of these experiments. Several parameters were varied to test their effect on psf correlation levels, including the size of the transmit/receive

apertures, the speed of sound used by the system to calculate time delays, and the distance the wire target was placed away from the transducer face. In general, varying the calculated speed of sound produced the same results as moving the transducer axially toward/away from the wire target, and larger transmit/receive apertures provided better correlation values (largely due to increased SNR). Using an 8 element (1.6mm) aperture with the system focused at 12 mm, the following plot was generated to demonstrate correlation depth of field:

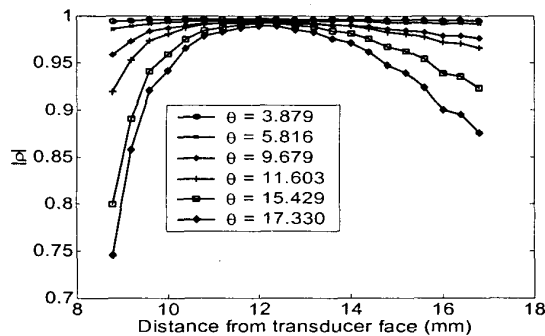


Figure 2. Correlation coefficient vs. distance from transducer face

The complex correlation coefficient ρ was calculated relative to the acquisition at 180° (note that the angle θ on the legend corresponds to $180 - \theta$, it is more intuitive to refer to this angle since increasing θ indicates an increased separation between transmit and receive apertures). Looking at the absolute value of the complex correlation coefficient it is clear that correlation drops when interrogation angle is increased, as well as when the transducer is moved farther from the focus at 12mm. All angles exhibit high correlation levels at/near the focus, and correlation remains above 0.95 for approximately 5 mm for all angles of interrogation.

The simplest method of comparative imaging that can be employed to quantify differences in angular scatter is common- and difference- (c- and d-) weighted subtractive imaging [2]. A difference-weighted image is formed via the subtraction of the complex echoes acquired at an angle of interest from those acquired at the backscatter angle. This eliminates the portion of the echo field common to every acquisition angle and emphasizes those portions of the echo field which change

significantly as the interrogation angle is increased. Subtracting the difference echoes from the echoes acquired at the separation angle of interest yields the common-weighted echo set. Common-weighted images emphasize targets dominated by local variations in compressibility, while difference-weighted images emphasize local variations in density.

To evaluate the potential efficacy of a straightforward subtraction image on the system, the normalized difference energies (DE) of all data sets were calculated as follows:

$$DE = \left| A_0 / \sqrt{A_0 A_0^*} - A_\theta / \sqrt{A_\theta A_\theta^*} \right|^2 \quad (2)$$

Where A_0 is the complex backscatter echo data and A_θ is the complex echo data a higher angle of interrogation. Initial evaluation of this metric is shown in Fig. 3:

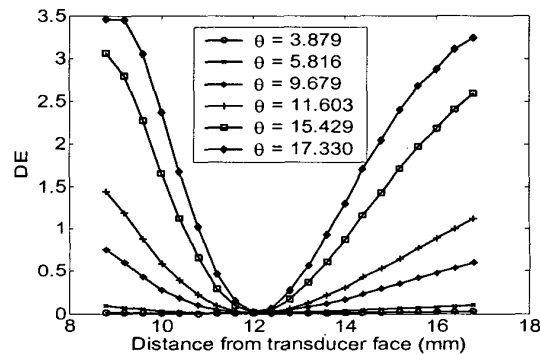


Figure 3. Normalized difference energy vs. distance from focus

Results showed a higher than expected rise in difference energy at high interrogation angles, so in order to improve the depth of field over which C- and D- imaging could be successfully employed, receive time warping (RTW) was applied to align the data acquired at backscatter to the echoes acquired at other angles. RTW compensates for the relative difference in pathlength between the focus and other points in the imaging field when considering angular acquisition vs. backscatter. A complex phase rotation is applied to the angular acquisition data sets to make up for this difference (Fig. 4). RTW greatly enhanced the effective depth of field for C- and D- type image comparisons, offering an order of magnitude improvement at larger interrogation angles.

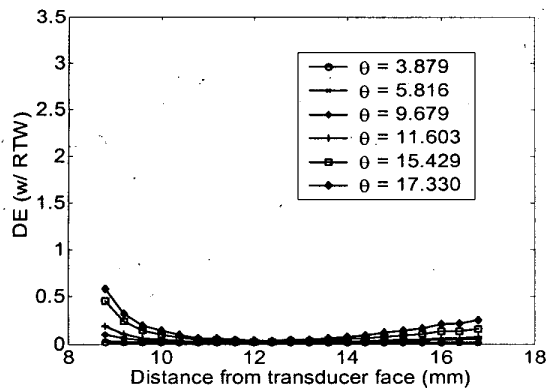


Figure 4. Normalized difference energy vs. distance from transducer face, receive time warping active

To quantify the effectiveness of C- and D-imaging on different target types, a phantom was constructed featuring three different types of 200 μ m diameter wire. The base of the phantom was high-concentration gelatin with 50 μ m diameter Sephadex suspended within to provide background scattering. This gelatin was poured upon a steel wire, nylon monofilament, and cotton/polyester thread placed approximately 1 cm apart, and were set to bisect the imaging plane of the transducer at the focal depth of 12 mm. B-Mode (at $\theta = 0^\circ$) C-, and D-weighted images (from $\theta = 9.679$ degrees) are presented in Fig. 5.

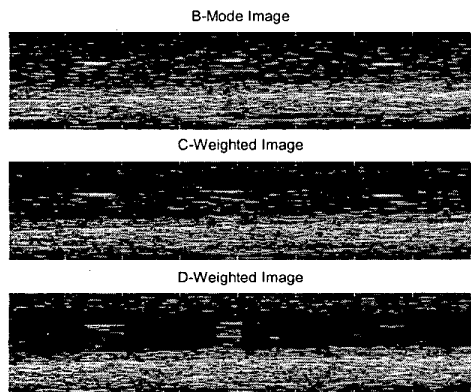


Figure 5. B-Mode, C-weighted, and D-weighted image of steel (left), nylon (center), and cotton (right) wire targets

Average pixel brightness in the three wire regions was compared to that of a neutral background region also at the focus. In the B-Mode images the

contrast between the wires and the background is nearly the same: 21.3dB, 21.9dB, and 23.8dB respectively for the steel, nylon, and cotton wires. Note that they are difficult to differentiate from the B-Mode image alone. In the C-weighted image we see contrast levels of 19.4dB, 20.5dB, and 25.3dB (note the enhanced contrast for the highly compressible cotton thread). In the D-weighted image we see contrast levels of 27.90dB, 22.50dB, and 17.07dB for the steel, nylon, and cotton threads, such that all three wire types are clearly differentiable in the image.

IV. CONCLUSION

Although there are a few considerable limitations currently involved with implementing TAA on a linear array system (most notably, the inability to independently apodize the transmit and receive apertures), it has been shown that there is great potential in this technique for providing new sources of image contrast from previously unobservable target characteristics. Further refinement of the technique should allow for the generation of higher quality overall image data, as well as the potential real-time display of comparative (C/D-type) images.

V. ACKNOWLEDGEMENTS

The author acknowledges the funding of the Susan G. Komen Foundation and the U.S. Army Congressionally Directed Medical Research Program, as well as significant technical support from GE Medical Systems.

VI. REFERENCES

- [1] M. E. Andersen et al., "The detection of breast microcalcifications with medical ultrasound." *JASA.*, vol 101(1), pp. 29-39, 1997.
- [2] W. F. Walker, "C- and D-weighted ultrasonic imaging using the translating apertures algorithm," *IEEE Trans. on UFFC.*, vol. 48, pp. 452-461, 2001.
- [3] J. A. Campbell and R. C. Waag, "Measurements of calf liver ultrasonic differential and total scattering cross sections," *JASA*, vol. 75, pp. 603-611, 1984.

A NOVEL APERTURE DESIGN METHOD FOR IMPROVED DEPTH OF FIELD IN ULTRASOUND IMAGING

Karthik Ranganathan and William F. Walker

Biomedical engineering, University of Virginia, Charlottesville, VA 22903

Abstract – Current aperture design techniques do not allow for the design of apertures that produce a beam pattern optimally similar to the desired pattern. A flexible beamforming technique that enables the optimal design of apertures for a desired system response is presented. This technique involves a linear algebra formulation of the Sum Squared Error (SSE) between the point spread function (psf) of the system, and an ideal or desired psf. Minimization of this SSE yields the optimum aperture weightings. A brief overview of the application of the technique for some common design objectives, along with simulation results is also presented.

I. INTRODUCTION

A common task in ultrasound imaging is the design of apertures for either a specific imaging application, or to improve performance in an existing application. This is usually performed in an iterative and ad-hoc manner. These techniques may result in a system response close to the desired response, but they do not guarantee optimization of ultrasound beam parameters such as main-lobe width and side-lobe levels. Also, given a desired beam pattern, it is not possible to design apertures that produce a beam pattern that optimally resembles the desired beam.

We propose a general aperture design method, with rigorous theory, that can be applied in arbitrary system geometries to design apertures optimizing beam parameters. Our technique involves a linear algebra formulation of the Sum Squared Error (SSE) between the system point spread function (psf) and the desired or ideal psf. Minimization of this error yields unique aperture weightings that force the system psf to resemble the desired psf. It is similar to the technique used by Ebbini [1], and by Ebbini and O'Donnell [2]. Our Minimized Sum Squared Error (MSSE) technique is more general, however, because it enables the use of arbitrary propagation functions.

Another distinction is that in [1] and [2], a few control points were used in order to ensure an underdetermined system of equations and obtain an exact beam pattern at those few points, while we use the entire ideal psf to obtain the least squares solution of an overdetermined system of equations. This method enables excellent control of the system psf, and has a significant impact on aperture design for several applications such as improved depth of field.

II. THEORY

The phase and amplitude of the ultrasonic field at a point in space due to a transducer element depends on several factors. These include the Euclidean distance between the point and the element, the orientation of the element relative to the point, the frequency of the emitted wave, and frequency dependent attenuation of the medium, assuming linear propagation. The complex field at the point under consideration can be written as the product of a propagation function, s , which incorporates any or all of the above mentioned factors, and the weighting (possibly complex) applied to the element, w . i.e. sw . The one-way M-point lateral point spread function (psf) at the range z can be represented as,

$$P_z = \begin{bmatrix} s_{1,1} & s_{1,2} & \cdot & \cdot & \cdot & s_{1,N} \\ s_{2,1} & s_{2,2} & & & & \cdot \\ \cdot & & \cdot & & & \cdot \\ \cdot & & & \cdot & & \cdot \\ s_{M,1} & \cdot & \cdot & \cdot & \cdot & s_{M,N} \end{bmatrix} \begin{bmatrix} w_1 \\ w_2 \\ w_3 \\ \cdot \\ \cdot \\ w_N \end{bmatrix} = S_z W \quad (1)$$

where S_z is an $M \times N$ matrix of propagation functions in which each element $s_{i,j}$ is the propagation function that determines the field at a point i due to element j , W is an $N \times 1$ vector of aperture weightings in which each element w_j is the

weighting applied to the j^{th} element, and P_z is the resulting psf, which is an $M \times 1$ vector. This formulation permits analysis with complicated propagation functions that may include limited element angular response, frequency dependent attenuation, and other difficult to model factors.

Using equation 1 and by applying the well-known Radar Equation, the two-way psf can be written as,

$$P_{TRz} = P_{Tz} \cdot P_{Rz} = (S_z^T) \cdot (S_z R) \quad (2)$$

where P_{Tz} and P_{Rz} are the one-way transmit and receive psfs respectively, T and R are the transmit and receive aperture weightings, and \cdot indicates point by point multiplication. The propagation function is the same on transmit and receive due to acoustic reciprocity. Equation 2 can be rewritten as,

$$P_{TRz} = P_{Tzd} P_{Rz} = P_{Tzd} S_z R = P_{TzdS} R, \quad (3)$$

where P_{Tzd} is a diagonal $M \times M$ matrix with the elements of P_{Tz} along its 0th diagonal, and $P_{TzdS} = P_{Tzd} S_z$. This changes the point multiplication operation to a regular matrix multiplication operation. We can characterize the degree of similarity between the psf at some range z , and some ideal psf by the SSE between them. Using equation 3 the SSE is,

$$\begin{aligned} SSE &= (P_{TRz} - \tilde{P}_{TRzi})^t (P_{TRz} - \tilde{P}_{TRzi}) \\ &= (P_{TzdS} R - \tilde{P}_{TRzi})^t (P_{TzdS} R - \tilde{P}_{TRzi}) \end{aligned} \quad (4)$$

where \tilde{P}_{TRzi} is the ideal psf, and the superscript t denotes a complex conjugate operation.

This is formulation is well-known in signal processing, and using [3], we can obtain a set of receive weightings to be applied so that the SSE between the generated and ideal psfs is minimized.

$$R = (P_{TzdS}^t P_{TzdS})^{-1} P_{TzdS}^t \tilde{P}_{TRzi} = P_{TzdS}^{\#} \tilde{P}_{TRzi} \quad (5)$$

where $P_{TzdS}^{\#}$ is the pseudoinverse of P_{TzdS} .

III. DISCUSSION

Equation 5 specifies the complex weightings to be applied to the transducer elements constituting the

receive aperture to obtain a system psf, P_{TRz} , at the range z , that optimally resembles the desired or ideal psf, \tilde{P}_{TRzi} . This aperture design method guarantees optimal beam patterns. We describe some common design objectives, and the application of our method to design apertures that achieve these objectives, to demonstrate the effectiveness of the MSSE technique.

Objective: Enhanced Depth of field - The depth of field (DOF) of an ultrasound imaging system is generally defined as the axial region over which the system is in focus, or more rigorously, the axial region over which the system response is uniform within some predetermined limit. It is generally desired that the system psf remains similar to the psf at the focus for as large an axial range as possible. Current state of the art techniques to improve depth of field include transmit apodization, dynamic receive apodization and dynamic receive focusing.

However effective the above techniques are, they are ad-hoc and lack formal theory describing the effectiveness in improving depth of field. Our objective is to derive receive weightings that force the psf at each specific range of interrogation to be optimally similar to the psf at the focus, and use these weightings to implement dynamic weighting to maximize depth of field. This can be done easily by setting the ideal psf, \tilde{P}_{TRzi} , in equation 5 to be the psf at the focus. We will obtain receive weightings for the range of interest, z , that will generate a psf that is optimally similar to the psf at the focus.

Objective: Correlation Depth of Field in Translated Aperture Geometries - We have proposed using the Translating Apertures Algorithm (TAA) as the foundation of angular scatter imaging methods [4]. The TAA results in a considerably reduced depth of field as the transmit and receive apertures are translated. Our technique of dynamic receive aperture weightings can be applied to improve the correlation between the backscatter (non-translated) and angular scatter (translated) psfs at each range of interest, and thereby increase the correlation depth of field. We can derive the receive weightings to be applied in the translated apertures geometry to maximize the correlation by minimizing the SSE between the two psfs. We can write the two-way psf for the translated geometry at range z as follows.

$$P_{TRz1} = P_{Tz1} \cdot P_{Rz1} = P_{Tz1} \cdot (S_{Rz1} R_1) \\ = P_{Tz1d} S_{Rz1} R_1 = P_{Tz1dS} R_1 \quad (9)$$

where P_{Tz1d} is a diagonalized $M \times M$ matrix with the elements of P_{Tz1} along the 0th diagonal, the subscript “1” denotes the translated geometry and $P_{Tz1dS} = P_{Tz1d} S_{Rz1}$. The SSE between the psfs for the backscatter and angular scatter geometries is,

$$SSE = (P_{TRz1} - P_{TRz0})^T (P_{TRz1} - P_{TRz0}) \\ = (P_{Tz1dS} R_1 - P_{TRz0})^T (P_{Tz1dS} R_1 - P_{TRz0}) \quad (10)$$

The receive weightings to be applied to the angular scatter geometry that yield the optimum correlation depth of field are therefore [3],

$$R_1 = (P_{Tz1dS}^T P_{Tz1dS})^{-1} P_{Tz1dS}^T P_{TRz0} = P_{Tz1dS}^{\#} P_{TRz0} \quad (11)$$

where $P_{Tz1dS}^{\#}$ is the pseudoinverse of P_{Tz1dS} .

The above design objectives illustrate the flexibility of the MSSE technique. The method, however, is not limited to these examples and can be used to design apertures to obtain any arbitrary system response.

IV. RESULTS AND DISCUSSION

Simulations of the design method were performed by implementing code in Matlab. We used a discretized Rayleigh-Sommerfeld formulation to generate the propagation matrices. The control parameters are described in table 1.

Number of elements	32
Element spacing	200 microns
Apodization	Hann window
Focus	1.2 cm
Frequency of operation	10 MHz
Number of field points	351
Field point spacing	20 microns

Table1. Control parameters.

Enhanced Depth of Field – Figure 1 demonstrates the effectiveness of our technique in improving the depth of field. Every column in each of the three images

corresponds to the lateral psf at a single axial range. This range was varied from 0.31 cm to 5 cm and was sampled every 100 μ m. Figure 1a consists of the lateral psfs corresponding to the control case with no apodization. Figure 1b is made up of the psfs obtained when dynamic apodization and dynamic receive focusing were applied, along with a range dependent gain function. Figure 1c consists of the psfs obtained when our MSSE technique was applied. It can be seen that beam characteristics were maintained over a longer range for our technique, than when conventional beamforming techniques were applied.

Correlation Depth of Field in Translated Aperture Geometries – Figure 2 illustrates the application of the MSSE technique in translated aperture geometries. The correlation coefficients were obtained by correlating the translated aperture (shifted by 10 elements) psf with the non-translated aperture psf at the same range. It can be seen that the application of our technique results in a significantly higher correlation than the control case.

Although results are not shown, it is also possible to design transmit apertures that produce limited diffraction transmit beams and maintain transmit beam characteristics for a significantly larger range. This can be done by tiling the one-way psfs at the specific axial ranges over which the beam characteristics are to be maintained, and tiling the ideal psfs, one for each range of interest. The SSE between the tiled ideal and actual psfs can then be formulated using equation 1. Minimizing this SSE will yield the transmit weightings that produce the optimized limited diffraction transmit beam.

IV. CONCLUSION

The Minimum Sum Squared Error (MSSE) technique provides a general method for the design of aperture weightings that can be applied in arbitrary system geometries to design apertures in order to obtain a beam pattern optimally similar to the desired pattern. By applying the technique to some common design challenges in medical ultrasound, it has been shown to have the potential to significantly improve the performance of imaging systems.

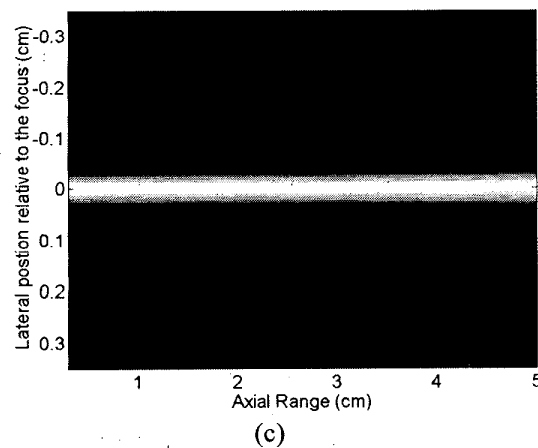
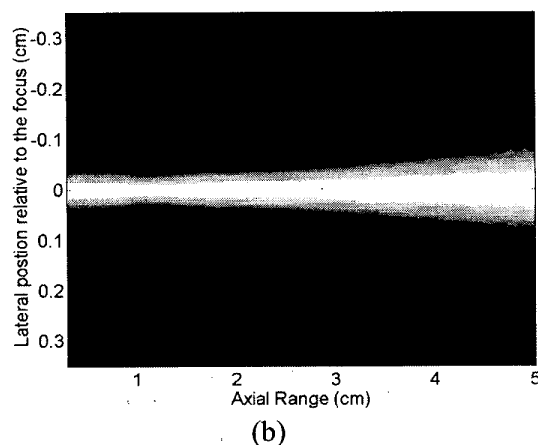
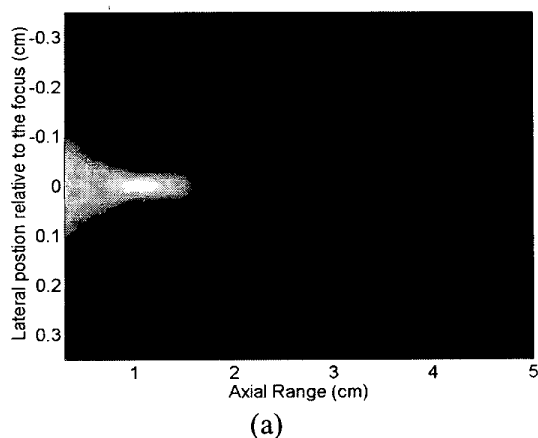


Figure 1. Images obtained from lateral psfs at multiple ranges. Each column consists of the psf at a single range. 1a is the control case, 1b is dynamic apodization and dynamic receive focusing with range dependent gain, and 1c is our MSSE technique.

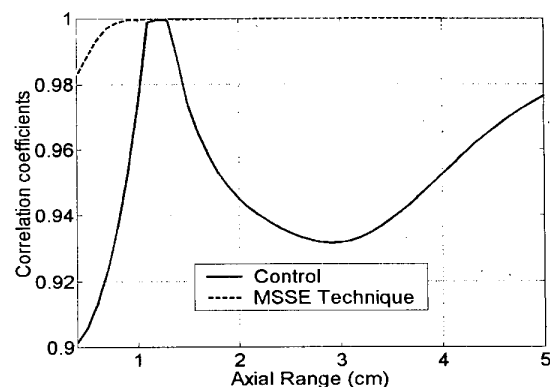


Figure 2. Correlation coefficients obtained by correlating the shifted aperture (10 element shift) psf with the non-shifted aperture psf at the same range.

IV. FUTURE WORK

The technique described above is implemented using a continuous wave (CW) formulation. We have also adapted the technique for broadband systems. We are currently experimenting with broadband simulations, and limited diffraction transmit beams.

V. REFERENCES

- [1] E. S. Ebbini and C. Cain, " Multiple-focus ultrasound phased-array pattern synthesis: Optimal driving signal distributions for hyperthermia," *IEEE Trans. Ultrason. Ferroelectr., Freq. Contr.*, vol. 36, no. 5, pp. 540-548, 1989.
- [2] E. S. Ebbini and M. O'Donnell, " Compensation for missing array elements by direct beam synthesis," *Ultrasonics Symposium, 1991. Proceedings., IEEE 1991*, vol.2, pp. 1343-1346, 1991.
- [3] L. L. Scharf, *Statistical Signal Processing: Detection, Estimation, and Time Series Analysis*, Addison-Wesley Publishing Company, 1991.
- [4] W. F. Walker, "C- and D-Weighted Ultrasonic Imaging Using the Translating Apertures Algorithm," *IEEE Trans. Ultrason., Ferroelectr., Freq. Contr.*, vol. 48, no. 2, pp. 452-461, March 2001.

Author's email – kr6u@virginia.edu

A novel aperture design method in ultrasound imaging

Karthik Ranganathan and William F. Walker
Biomedical Engineering, University of Virginia

ABSTRACT

Conventional techniques used to design transducer apertures for medical ultrasound are generally iterative and ad-hoc. They do not guarantee optimization of parameters such as mainlobe width and sidelobe levels. We propose a dynamic aperture weighting technique, called the Minimum Sum Squared Error (M SSE) technique, that can be applied in arbitrary system geometries to design apertures optimizing these parameters. The M SSE technique utilizes a linear algebra formulation of the Sum Squared Error (SSE) between the point spread function (psf) of the system, and a goal or desired psf. We have developed a closed form expression for the aperture weightings that minimize this error and optimize the psf at any range. We present analysis for Continuous Wave (CW) and broadband systems, and present simulations that illustrate the flexibility of the technique.

Keywords: ultrasound, beam forming, aperture design, minimum sum squared error, SSE, M SSE

1. INTRODUCTION

In ultrasonic imaging, the characteristics of the ultrasound beam fundamentally affect the quality of the data obtained, and therefore need to be carefully adjusted to obtain the desired system response. Beam parameters such as the mainlobe width and sidelobe levels can be adjusted by changing the amplitude and phase (time delay) of the weightings applied to the active elements, and also by controlling the size of the active aperture (the number of active elements) and the frequency of operation.

These beam forming parameters do not act independently; altering one changes the impact of each of the others. Consequently, beam former design is a complicated multiparameter optimization problem. Because of this complexity, beam former parameters are typically determined using a combination of ad hoc methods, simplified theory, and iterative simulation and experimentation. While these methods are effective, they are time consuming and provide no guarantee that an optimized solution has been found.

We propose a general aperture design method that can be applied in arbitrary system geometries to design apertures that optimize beam parameters. Our technique utilizes a linear algebra formulation of the Sum Squared Error (SSE) between the system point spread function (psf) and the desired or goal psf. Minimization of this error yields unique aperture weightings that force the system psf to resemble the desired psf. It is similar to the technique used by Ebbini et al [1] to generate specialized beam patterns for hyperthermia, and by Li et al [2] for the compensation of blocked elements. There are several differences, however, between these methods and the technique we describe. The analysis in [1] and [2] uses only a few control points, while we use the entire system psf to form an overdetermined system of equations that we then solve. Another important distinction is that unlike [1] and [2], we present analysis for both CW and broadband systems. This paper outlines the theoretical description of the M SSE technique for narrowband and broadband systems and discusses a few examples of application. Simulation results for these examples are also described.

2. THEORY

2.1 One-way Continuous Wave (CW) formulation

The phase and amplitude of the ultrasonic field at a point in space due to an ultrasound transducer element depends on several factors. These include the Euclidean distance between the point and the element, the orientation of the element relative to the point, the frequency of the emitted wave, and frequency dependent attenuation of the medium. Assuming linear propagation, the one-way M-point lateral point spread function (psf) at the range z can be represented as follows.

$$P_z = \begin{bmatrix} S_{1,1} & S_{2,1} & \dots & S_{N,1} \\ S_{1,2} & S_{2,2} & \dots & \dots \\ \vdots & \vdots & \ddots & \vdots \\ S_{1,M} & \dots & \dots & S_{N,M} \end{bmatrix} \begin{bmatrix} W_1 \\ W_2 \\ \vdots \\ W_N \end{bmatrix} = S_z W \quad (1)$$

where S_z is an $M \times N$ matrix of complex propagation functions comprising elements of the form $S_{i,j}$, which represents the propagation function that determines the field at a point i due to element j . W is an $N \times 1$ vector of aperture weightings in which each element W_j is the weighting applied to the j^{th} element. P_z is the resulting $M \times 1$ psf. This formulation permits analysis with complicated propagation functions that may include limited element angular response and other such factors. The transmit psf at the range z can therefore be expressed as follows,

$$P_{Tz} = S_z T \quad (2)$$

where T comprises the transmit aperture weightings. Let us suppose that the desired one-way system transmit psf is \tilde{P}_{Tz} for the application of interest. We can then characterize the degree of similarity between the goal psf \tilde{P}_{Tz} and the actual system psf P_{Tz} by the Sum Squared Error (SSE) between them.

$$\begin{aligned} \text{SSE} &= (P_{Tz} - \tilde{P}_{Tz})^t (P_{Tz} - \tilde{P}_{Tz}) \\ &= (S_z T - \tilde{P}_{Tz})^t (S_z T - \tilde{P}_{Tz}) \end{aligned} \quad (3)$$

where the superscript " t " denotes a conjugate transpose operation. Minimizing the SSE yields the transmit weights that produce the system psf that is optimally similar to the goal psf. The formulation in equation 3 is common in signal processing, and significant literature exists on the solution to the equation with the minimum SSE. Using [3] the transmit aperture weightings that minimize the SSE are given by,

$$T = (S_z^t S_z)^{-1} S_z^t \tilde{P}_{Tz} = S_z^\# \tilde{P}_{Tz} \quad (4)$$

where $S_z^\#$ is the pseudoinverse of S_z . Equation 4 describes the calculation of the transmit weightings that yield the system psf at the range z that is optimally similar to the goal psf.

2.2 Two-way Continuous Wave (CW) formulation

Using the analysis in the previous subsection and by applying the well-known RADAR equation [4], the two-way psf is,

$$P_{TRz} = P_{Tz} \cdot P_{Rz} = (S_z T) \cdot (S_z R), \quad (5)$$

where ' \cdot ' indicates pointwise multiplication. Equation 5 can be rewritten as,

$$P_{TRz} = P_{Tzd} P_{Rz} = P_{Tzd} S_z R = P_{TzdS} R, \quad (6)$$

where P_{Tzd} is a diagonal $M \times M$ matrix with the elements of P_{Tz} along its 0th diagonal, and $P_{TzdS} = P_{Tzd} S_z$. If \tilde{P}_{TRz} is the goal psf, the SSE between the system and goal psfs can be expressed in a similar fashion to the one-way formulation in equation 2. The receive aperture weightings that minimize the SSE can then be determined as shown below.

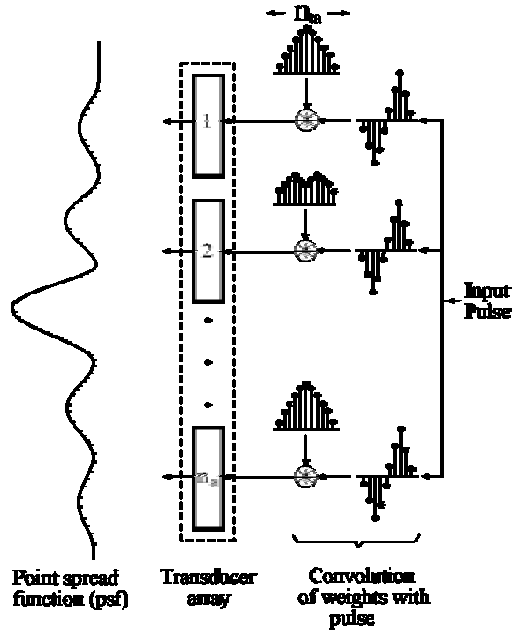


Figure 1. Illustration of broadband formulation. The pulse applied to each element is convolved with a set of weights, which are distinct for each element. This operation is analogous to implementing an FIR filter on each element/channel.

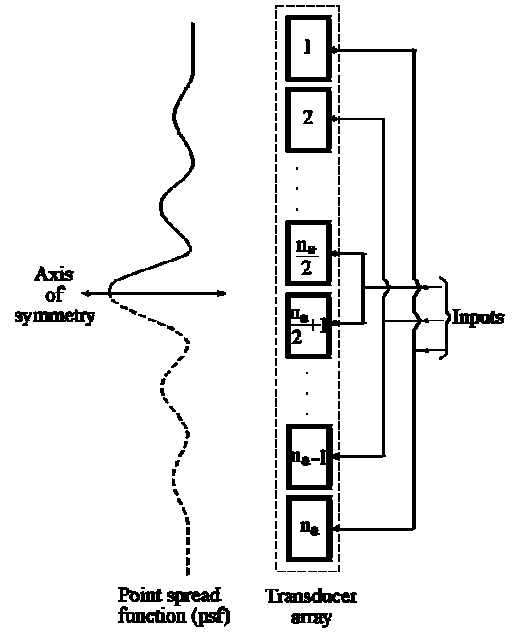


Figure 2. Illustration of the exploitation of symmetry. Since the aperture is symmetric about the center elements, pairs of elements that would have the same weights are grouped together. Also, the lateral symmetry of the psf about the center axis permits analysis with just one half of the psf.

$$\begin{aligned} \text{SSE} &= (\mathbf{P}_{\text{TRZ}} - \tilde{\mathbf{P}}_{\text{TRZ}})^t (\mathbf{P}_{\text{TRZ}} - \tilde{\mathbf{P}}_{\text{TRZ}}) \\ &= (\mathbf{P}_{\text{TzIS}} \mathbf{R} - \tilde{\mathbf{P}}_{\text{TRZ}})^t (\mathbf{P}_{\text{TzIS}} \mathbf{R} - \tilde{\mathbf{P}}_{\text{TRZ}}) \end{aligned} \quad (7)$$

$$\mathbf{R} = (\mathbf{P}_{\text{TzIS}}^t \mathbf{P}_{\text{TzIS}})^{-1} \mathbf{P}_{\text{TzIS}}^t \tilde{\mathbf{P}}_{\text{TRZ}} = \mathbf{P}_{\text{TzIS}}^\# \tilde{\mathbf{P}}_{\text{TRZ}} \quad (8)$$

where $\mathbf{P}_{\text{TzIS}}^\#$ is the pseudoinverse of \mathbf{P}_{TzIS} . Equation 8 specifies the complex weightings to be applied to the transducer elements constituting the receive aperture in order to obtain a two-way system psf \mathbf{P}_{TRZ} at the range z , that optimally resembles the desired or goal psf $\tilde{\mathbf{P}}_{\text{TRZ}}$.

2.3 One-way broadband formulation

The CW formulation described above will have limited accuracy in the analysis of broadband systems. For this case, we have developed a modified formulation. The one-way point spread function (psf) \mathbf{P}_{Tz} at a specific range z is a function of lateral position and time, and can be represented as follows.

$$\mathbf{P}_{\text{Tz}} = \mathbf{A}_z \mathbf{T} \quad (9)$$

where \mathbf{A}_z is a propagation matrix that depends on the excitation pulse and the impulse responses of the elements comprising the transmit aperture. It is a function of time and the spatial positions of the element and field point under consideration. It describes the contribution of each element at each field point as a function of time. The generation of a one-way psf is shown in figure 1. The SSE between the system psf and the desired psf can be expressed as,

$$\text{SSE} = \left(\mathbf{P}_{\text{Tz}} - \tilde{\mathbf{P}}_{\text{Tz}} \right)^T \left(\mathbf{P}_{\text{Tz}} - \tilde{\mathbf{P}}_{\text{Tz}} \right), \quad (10)$$

where the superscript “T” denotes a transpose operation. Using equation 9, we can solve for the transmit weightings that minimize the SSE in equation 10.

$$\mathbf{T} = \left(\mathbf{A}_z^T \mathbf{A}_z \right)^{-1} \mathbf{A}_z^T \tilde{\mathbf{P}}_{\text{Tz}} = \mathbf{A}_z^\# \tilde{\mathbf{P}}_{\text{Tz}} \quad (11)$$

2.4 Two-way broadband formulation

Similar to the one-way psf, the two-way pulse-echo psf can also be expressed in a linear algebra formulation.

$$\mathbf{P}_{\text{TRz}} = \mathbf{A}_{\text{zz}} \mathbf{R}, \quad (12)$$

where \mathbf{A}_{zz} is a function of the transmit aperture weights, the excitation pulse, and the transmit and receive aperture element impulse responses. If $\tilde{\mathbf{P}}_{\text{TRz}}$ is the goal psf at range z , the SSE between the goal and actual pulse-echo psfs can be expressed using equation 12, and minimized to obtain the optimum receive weights as shown below.

$$\text{SSE} = \left(\mathbf{P}_{\text{TRz}} - \tilde{\mathbf{P}}_{\text{TRz}} \right)^T \left(\mathbf{P}_{\text{TRz}} - \tilde{\mathbf{P}}_{\text{TRz}} \right) \quad (13)$$

$$\mathbf{R} = \left(\mathbf{A}_{\text{zz}}^T \mathbf{A}_{\text{zz}} \right)^{-1} \mathbf{A}_{\text{zz}}^T \tilde{\mathbf{P}}_{\text{TRz}} = \mathbf{A}_{\text{zz}}^\# \tilde{\mathbf{P}}_{\text{TRz}} \quad (14)$$

where $\mathbf{A}_{\text{zz}}^\#$ is the pseudo-inverse of \mathbf{A}_{zz} .

2.5 Modified broadband formulation for reduced computational complexity

The calculation of aperture weights in the MSSSE technique requires significant computational resources, due to the pseudo-inverse operation and the large matrices involved. However, the lateral symmetry of the apertures and the psfs can be exploited in order to reduce the computational complexity of the broadband formulation. We can, if we choose, use just half of both the goal and actual psfs for the calculation of the optimal weightings. The symmetry of the transmit and receive apertures can also be used to reduce the size of the matrices involved. Pairs of elements can be considered by grouping elements that are on opposite sides and at the same distance from the center axis. The computational complexity is therefore reduced by a factor of 4. This concept is illustrated in figure 2.

2.6 Application to enhance Depth of Field (DOF)

The Minimum Sum Squared Error (MSSSE) technique that is described above for CW and broadband systems is extremely general and can be applied in wide-ranging design scenarios. As an example, we describe the application of the technique for improved Depth of Field.

The Depth of Field (DOF) of an ultrasound imaging system is generally defined as the axial region over which the system is in focus, or more rigorously, the axial region over which the system response is uniform within some predetermined limit. It is usually desired that the system psf remains similar to the psf at the focus for as large an axial range as possible.

Currently techniques that are used to improve the DOF include apodization and dynamic receive focusing. A static apodization function is generally applied to the transmit aperture, while dynamic apodization is implemented on the receive aperture. If the MSSSE technique is implemented for every range under consideration with the goal psf being the psf obtained at the focus, we can formally derive receive apodization weightings that force the psf at each specific range of interrogation to be maximally similar by minimizing the SSE. These weightings can then be used to implement dynamic apodization and maximize the DOF.

3. SIMULATIONS

We have implemented two sets of simulations in order to illustrate the working of the MSSE technique. The first set was intended to illustrate the implementation of the MSSE technique to obtain predetermined system psfs in CW and broadband systems. The second set was designed to implement the technique to improve the system DOF in CW and broadband simulations. The default system parameters are described in table 1. Unless otherwise mentioned, these parameters were used in all simulations. All simulations were performed in Matlab. Field II, an ultrasound simulation package developed by Jensen [5], was used for all broadband simulations.

Parameter	Value
Number of elements	32
Element pitch	135 μ m
Focus	1.3 cm
Lateral window over which the psf was calculated	70 mm
psf window sampling interval	20 μ m
Ultrasonic wave propagation speed	1540 m/s
Center frequency	10 MHz
Bandwidth (in broadband simulations)	75%
Temporal sampling of psf (in broadband simulations)	84 MHz
Temporal spacing of weights for each element (in broadband simulations)	36 ns

Table 1: List of default parameters used in the simulations, unless otherwise mentioned.

3.1 One-way CW design example

For all CW simulations, we adapted the propagation function from the Rayleigh-Sommerfeld equation described in [6]. The elements were treated as point sources. The parameters that were used are described in table 1. The goal psf was chosen to be a Hann window of width 7 mm. The optimum transmit weights were computed using equation 4, and the system psf was calculated after application of these weights. Figures 3(a) and 3(b) show the goal psf and the resulting system psf respectively. No transmit apodization, other than the calculated weights, was used. Figures 3(c) and 3(d) display the calculated transmit aperture weights, and the magnitude of the error between the goal and resulting psfs respectively. The error is the difference between the goal and the obtained psfs.

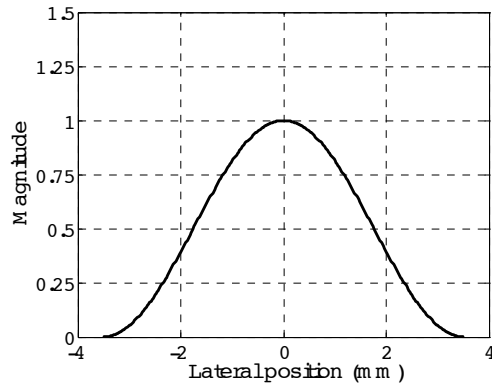
3.2 Two-way CW design example

A Hann window of width 1 mm was chosen to be the goal two-way psf. The MSSE technique was implemented by calculating and applying the receive aperture weights that were obtained using equation 8. No apodization was applied to the transmit aperture. Figures 4(a) and 4(b) depict the goal psf and the psf generated by using the calculated weights respectively. Figures 4(c) and 4(d) display the calculated receive aperture weights, and the magnitude of the error between the goal and resulting psfs respectively.

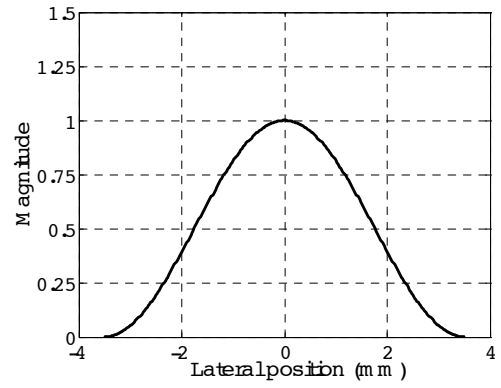
3.3 One-way broadband design example

All broadband simulations took advantage of symmetry to reduce computational complexity, as previously described. The propagation matrix A_z was constructed using dual element impulse responses. We used apodization to transmit only on selected pairs of elements, thus obtaining their contributions at each field point, at each time point under consideration. These were then used to form the propagation function. The ideal psf was generated by axially weighting a sinusoidal signal by a Hann window, and multiplying the result by a lateral Hann window.

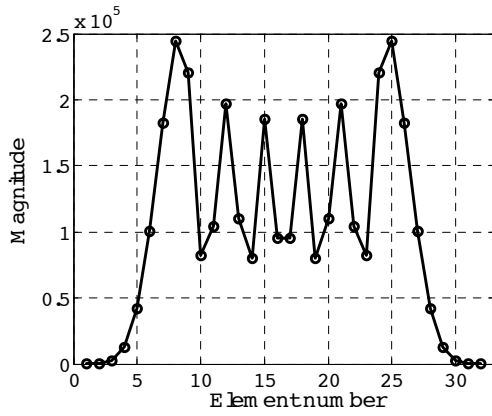
In all broadband simulations, we downsampled the propagation matrix by a factor of 3. This had the effect of reducing the upper cut-off frequency in the frequency response of the FIR filter constructed using the weights from the



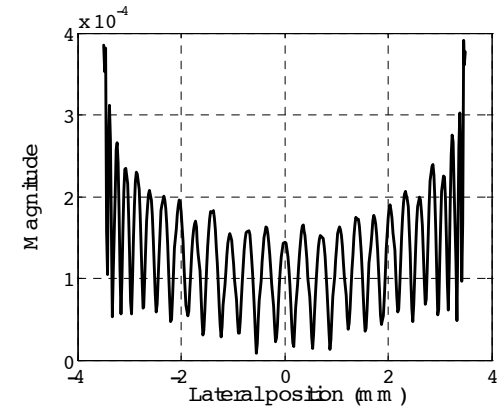
(a)



(b)



(c)



(d)

Figure 3. CW one-way design example showing (a) the goal psf as a function of lateral position, (b) the system psf obtained with the M SSE technique as a function of lateral position, (c) the calculated transmit weights as a function of element number, and (d) the error between the goal and the M SSE technique psfs as a function of lateral position.

temporal sampling rate of the psf (84 MHz) to 28 MHz. This rate still provided adequate sampling since the input pulse had a center frequency of 10 MHz with a bandwidth of 75%.

Using equation 11, we calculated the optimum transmit weights and the resulting system psf. Figures 5(a) and 5(b) show the goal and the M SSE technique psfs respectively, both as a function of lateral position and time. Figures 5(c) and 5(d) depict the calculated transmit weights as a function of the element number and time, and the magnitude of the error as a function of lateral position and time respectively. The error was calculated by computing the difference between the goal and obtained psfs. We also envelope detected and peak detected the psfs to generate beam profiles. Figures 5(e) and 5(f) show the goal and system transmit beam profiles respectively.

3.4 Two-way broadband design example

We used the same goal psf as in the one-way example, except for a scaling factor that accounted for the reduction in magnitude due to two-way propagation. The propagation matrix A_{zz} , however, was different from the one-way case. We generated the propagation functions by using the entire transmit aperture and receiving only on selected pairs of elements. No transmit apodization was used. All other parameters were consistent with table 1.

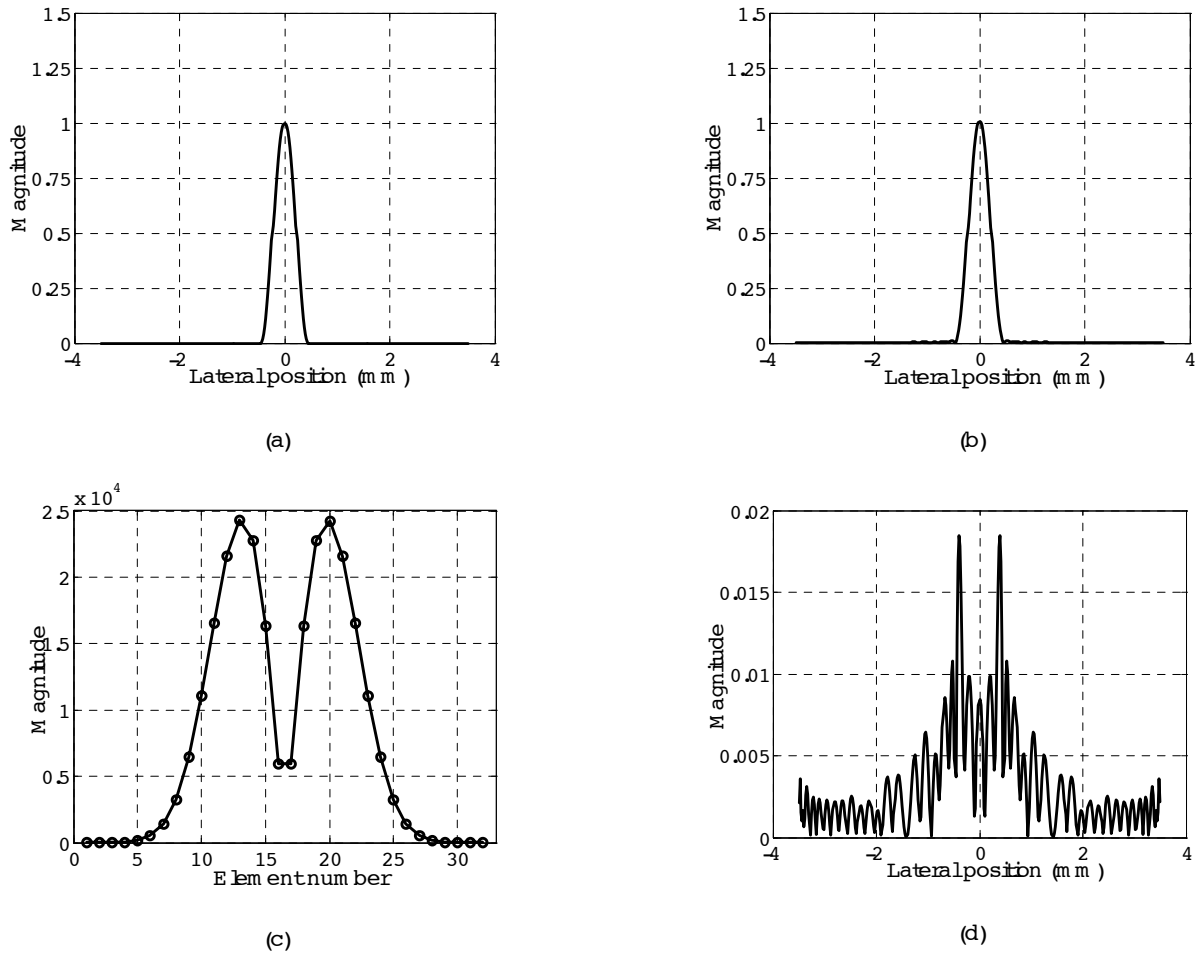
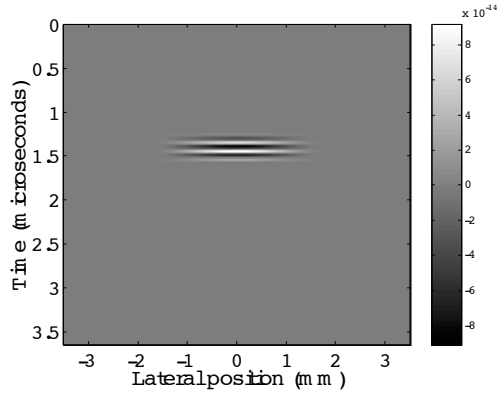


Figure 4. CW two-way design example showing (a) the goal psf as a function of lateral position, (b) the system psf obtained with the M SSE technique as a function of lateral position, (c) the calculated receive weights as a function of element number, and (d) the error between the goal and the M SSE technique psfs as a function of lateral position.

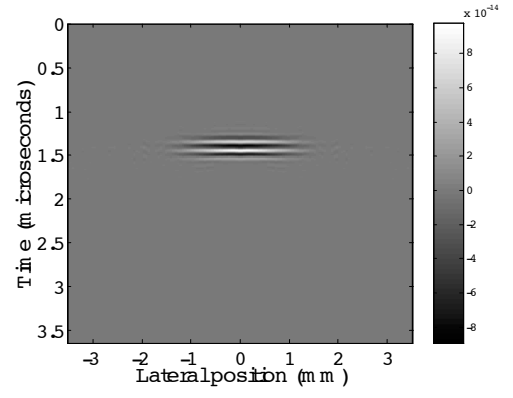
We then downsampled the resulting propagation matrix and used it to calculate the receive weights that minimize the SSE. Figures 6(a) and 6(b) display the goal psf and the system psf obtained with the M SSE technique respectively. Figures 6(c) and 6(d) depict the calculated receive weights and the psf error magnitude respectively. As in the one-way case, we envelope detected and peak detected the psfs. The goal and system psf profiles are displayed in figures 6(e) and 6(f) respectively.

3.5 Enhanced Depth of Field (DOF)

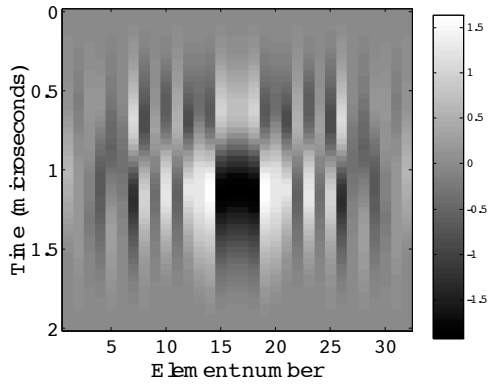
We implemented the M SSE technique to maximize the DOF in both CW and broadband simulations. We generated the goal psf, which was the psf at the focus, using 16 element transmit and receive apertures. We used a 16 element transmit and 32 element receive aperture for the actual system psf. i.e. weights were calculated for 32 receive elements. The system was focused at 6.5 mm. We performed CW simulations to maximize the DOF over an axial window from 0.1 mm to 50 mm that was sampled every 100 μ m. The lateral window over which the CW psf was calculated was sampled at 5 μ m, for more accurate computation of the Full Width Half Maximum (FWHM) of the main lobe. We implemented broadband simulations over an axial window from 0.5 mm to 32.5 mm that was sampled every 2 mm. Current ultrasound systems attempt to improve the DOF by using dynamic apodization and dynamic receive focusing, and we used these in



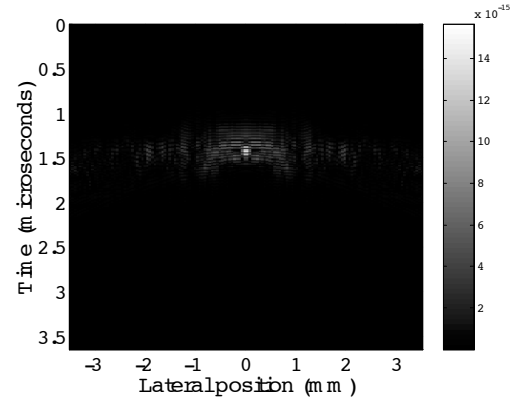
(a)



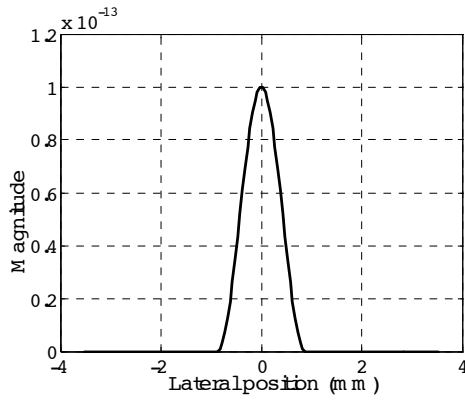
(b)



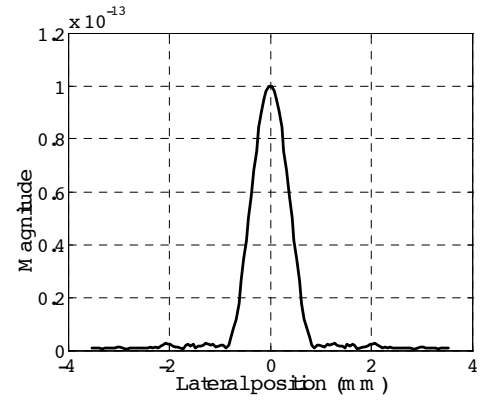
(c)



(d)

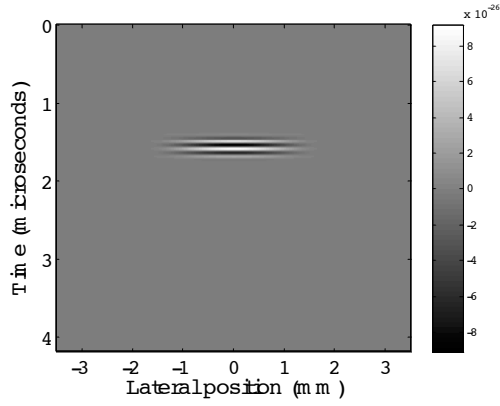


(e)

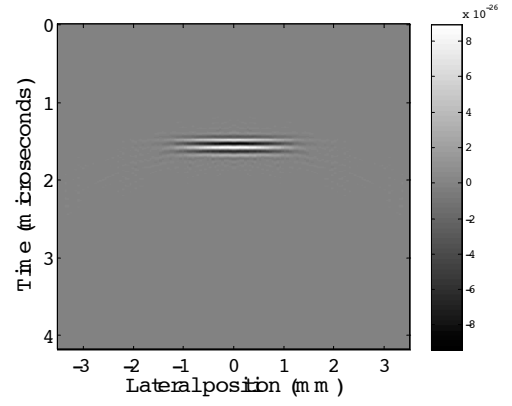


(f)

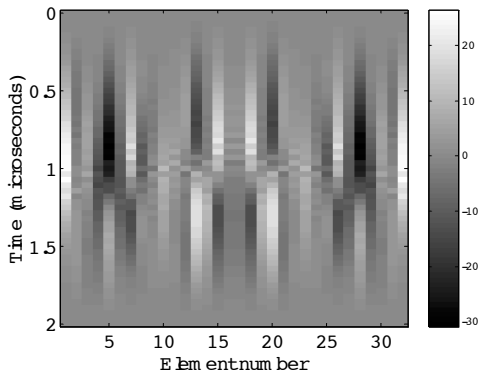
Figure 5: Broadband one-way design example showing (a) the goal psf, and (b) the system psf obtained with the M SSE technique, both as a function of lateral position and time. The calculated transmit aperture weights are displayed in (c) as a function of element number and time, and (d) shows the error between the goal and the M SSE technique psfs as a function of lateral position and time. Subplots (e) and (f) display the envelope and peak detected goal and system psfs respectively, both as a function of lateral position.



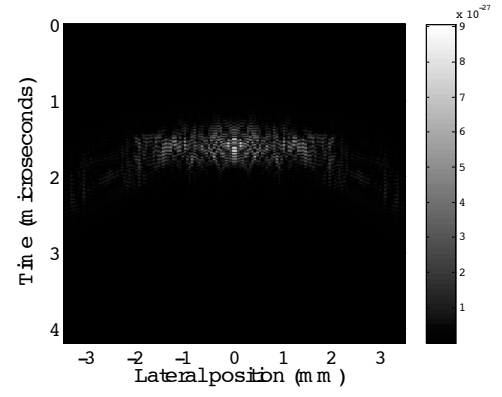
(a)



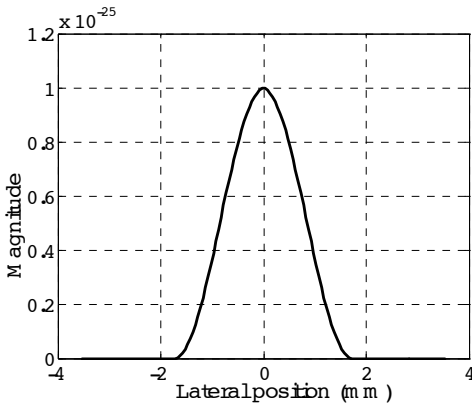
(b)



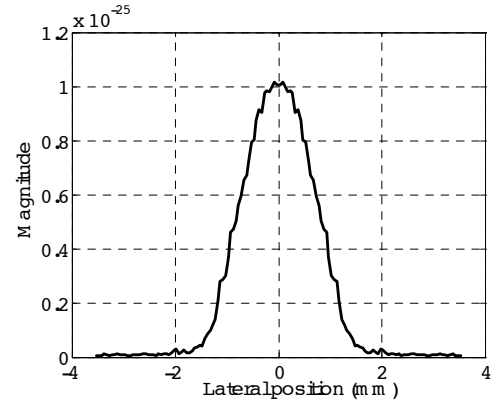
(c)



(d)

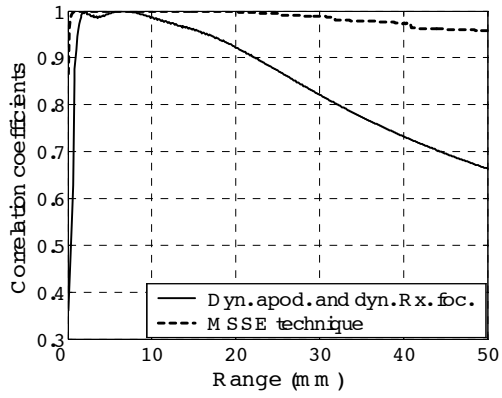


(e)

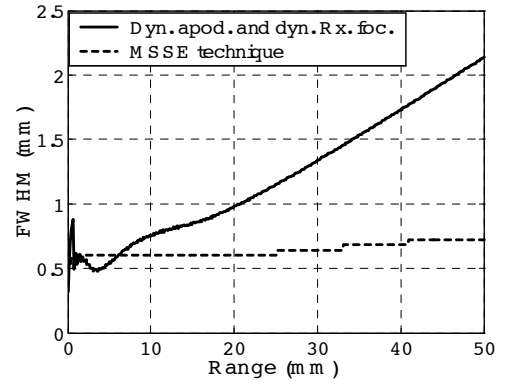


(f)

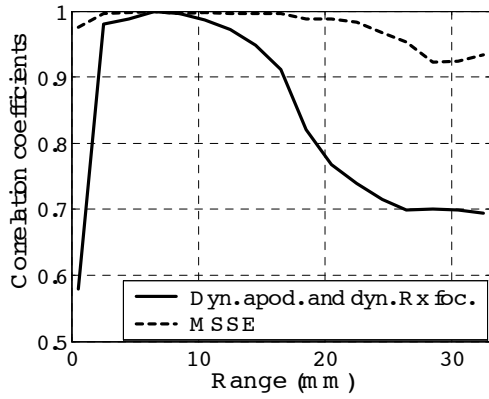
Figure 6: Broadband two-way design example showing (a) the goal psf, and (b) the system psf obtained with the M-SSE technique, both as a function of lateral position and time. The calculated receive aperture weights are displayed in (c) as a function of element number and time, and (d) shows the error between the goal and the M-SSE technique psfs as a function of lateral position and time. Subplots (e) and (f) display the envelope and peak detected goal and system psfs respectively, both as a function of lateral position.



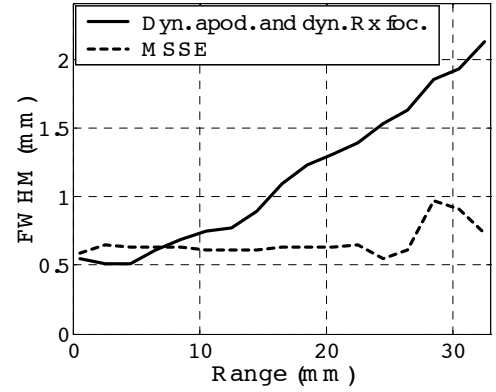
(a)



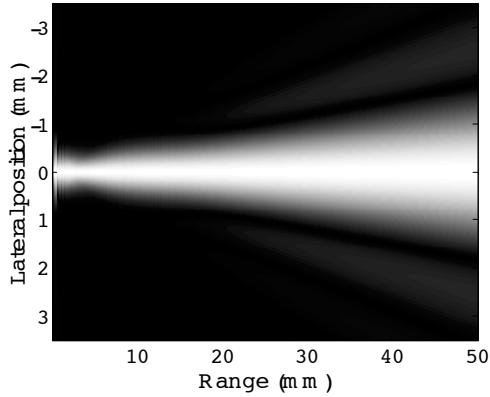
(b)



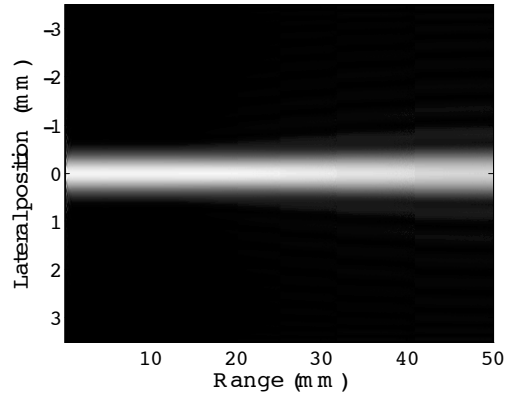
(c)



(d)



(e)



(f)

Figure 7: CW enhanced DOF simulation results showing (a) CW correlation curves, and (b) CW mainlobe FWHM curves in the top panel. The middle panel shows (c) broadband correlation curves, and (d) broadband mainlobe FWHM curves. The lower panel shows (e) the inage obtained using control psfs, and (f) the inage obtained using the psfs generated after application of the M SSE technique. The inages in (e) and (f) were formed from lateral psfs at multiple ranges. Each column consists of the psf at a single range.

control simulations to establish a basis for comparison with the results obtained using the M SSE technique. A Hann window was used as a transmit apodization function in all simulations, and as receive apodization during the generation of the goal psf. The propagation matrix was downsampled to limit the frequency response of the FIR filter constructed using the calculated weights.

5. DISCUSSION

Figure 3 demonstrates the use of the M SSE technique in the most basic ultrasound system configuration that was simulated i.e. the one-way CW system. As shown in figures 3(a) and 3(b), the system psf closely approximates the goal psf. The mean magnitude of the error between the psfs in figure 3(d) was approximately 0.02% of the mean goal psf amplitude.

The results of implementing the M SSE technique in the design of two-way system responses is shown in figure 4. It can be seen that the system psf that was obtained after the application of the M SSE technique and the goal psf are quite similar. The resulting mean error magnitude shown in figure 4(b) was 5.1% of the mean goal psf magnitude. The error was much worse than in the one-way simulation because the goal psf was much narrower and therefore more difficult to generate.

Figure 5 illustrates the results obtained when the M SSE algorithm was implemented in one-way broadband simulations. Observation of figures 5(a), 5(b), 5(e), and 5(f) reveals that the resulting psf has a good qualitative similarity to the goal one-way psf. The mean error magnitude was 17% of the mean psf magnitude.

Results from the two-way broadband simulation are shown in figure 6. The mean error magnitude was 19.8% of the mean goal psf magnitude.

The errors in the broadband simulations are quite large, but it is worth noting from figures 5(a) and 6(a) that the goal psfs used are difficult to realize using spherical waves. They would have been easy to generate using plane waves, but plane waves are an unrealistic model of the ultrasonic field emitted by transducer elements. Field II uses spherical waves to form realistic element responses. In spite of the very challenging goal psf used here, there is a very good qualitative agreement between the goal and system psfs.

The effect of the M SSE technique in improving the Depth of Field (DOF) is illustrated in figure 7. The DOF was defined in terms of correlation coefficients as the axial region over which the coefficients remained over 0.95. In the CW case, the DOF in the control case was 13 mm, while it increased by 285% to almost the entire interrogated range of 50 mm when the M SSE technique was applied. In the broadband simulations, the DOF increased from 8.3 mm in control simulations to 26.7 mm upon the application of the M SSE technique, an increase of 222%. The improvement in the DOF in CW simulations can be clearly seen in figure 7(a), and in broadband simulations in figure 7(c).

The DOF was also defined in terms of the Full Width Half Maximum (FWHM) of the mainlobe. Here we considered the DOF to be the region within which the FWHM stayed within 25% of its value at the focus. The DOF calculated using the FWHM criterion increased from 11 mm in control simulations, to almost the entire range of interrogation i.e. 50 mm. This represents a 355% increase in the DOF when the M SSE technique was applied. The CW control case and M SSE technique case FWHM results can be seen in figure 7(b). Figure 7(d) displays the FWHM information for broadband simulations. In the broadband case, the DOF evaluated using the FWHM increased from 12 mm to around 27 mm upon application of the M SSE technique, an increase of around 125%. Therefore, a significant improvement in the DOF was obtained in both simulations.

A more qualitative assessment of the efficacy of the M SSE technique can be made using figures 7(e) and 7(f). Figure 7(e) shows the CW psfs obtained in control simulations, and 7(f) displays the psfs generated in CW simulations that implemented the M SSE technique. The psfs are displayed as a function of range and lateral position. It can be seen that there is significant broadening of the psf mainlobe with range in the control simulation. Figure 7(f) clearly demonstrates the dramatic improvement in the DOF obtained using the M SSE beam forming technique.

While the M SSE design method worked exceedingly well over the range of conditions considered here, we must exercise some caution in interpreting these results since we only observed the performance of the technique in a limited spatial window. We cannot predict with certainty what will happen outside this design window. Another concern is the effect of assuming a wrong propagation model in the derivation of the optimum aperture weights. Errors such as a mismatch in the assumed and actual wave propagation speeds may have an adverse effect on the design method. We are currently investigating these and other similar concerns.

6. CONCLUSIONS

The Minimum Sum Squared Error (M SSE) technique is a general beam forming method that can be used to design apertures for specific applications. It enables the design of arbitrary beam profiles by calculating the appropriate optimum aperture weightings. The system performance is optimized because the calculated weightings minimize the error between the actual and desired system responses. The algorithm can be readily implemented in both Continuous Wave and broadband systems. In CW systems, the receive weights can be implemented by way of apodization and time delays, or complex weights. In broadband systems, implementation is analogous to applying a dynamic FIR filter to each channel.

The M SSE technique has been shown to be effective in designing ultrasound systems that generate arbitrary desired system responses. Simulation results in one-way and two-way CW and broadband systems demonstrate that it is easy to implement and can be applied in a wide range of potential applications. These simulations indicate that the M SSE technique compares favorably with current techniques used in conventional beam forming, and has the potential to be applied in a variety of ultrasound system design problems.

ACKNOWLEDGEMENTS

We would like to acknowledge the support of the Susan G. Komen Breast Cancer Foundation and the United States Army Congressionally Directed Medical Research Program.

Disclaimer— Significant portions of this manuscript are adapted from papers that are in preparation to be submitted to refereed journals.

REFERENCES

- [1] E. S. Ebbini and C. Cain, "Multiple-focus ultrasound phased-array pattern synthesis: Optimal driving signal distributions for hyperthermia," *IEEE Trans. Ultrason. Ferroelectr., Freq. Contr.*, vol. 36, no. 5, pp. 540-548, 1989.
- [2] P.-C. Li, S. W. Flax, E. S. Ebbini, and M. O'Donnell, "Blocked element compensation in phased array imaging," *IEEE Trans. Ultrason. Ferroelectr., Freq. Contr.*, vol. 40, no. 4, pp. 283-292, 1993.
- [3] L. L. Scharf, *Statistical Signal Processing: Detection, Estimation, and Time Series Analysis*, Addison-Wesley Publishing Company, 1991.
- [4] B. D. Steinberg, *Principles of aperture and array system design: including random and adaptive arrays*, John Wiley Publishing Company, 1976.
- [5] J. A. Jensen and N. B. Svendsen, "Calculation of pressure fields from arbitrarily shaped apodized and excited ultrasound transducers," *IEEE Trans. Ultrason. Ferroelectr., Freq. Contr.*, vol. 39, no. 2, pp. 262-267, 1992.
- [6] J. W. Goodman, *Introduction to Fourier Optics*, pp. 46-50 McGraw-Hill, 1988.

The Minimum Sum Squared Error (M SSE) Beamformer Design Technique: Initial Results

Karthik Ranganathan and William F. Walker

Biom edical Engineering, University of Virginia, Charlottesville, VA 22903

Abstract – The design of transmit and receive aperture weightings is a critical step in the development of ultrasound imaging systems. Current design methods are generally iterative, and consequently time-consuming and inexact. We have previously described a general ultrasound beamformer design method, the minimum sum squared error (M SSE) technique, that addresses these issues. We provide a brief review of the design method, and present results of simulations that investigate the performance of the technique. We also provide an example of application by applying the technique to improve the depth of field in CW and broadband ultrasound systems.

I. INTRODUCTION

We have previously introduced the minimum sum squared error (M SSE) beamforming technique [1], [2]. The M SSE technique can be applied in arbitrary system geometries to design apertures that optimize beam parameters. It utilizes a linear algebra formulation of the sum squared error (SSE) between the system pointspread function (psf) and the desired or goal psf. Minimization of the SSE yields unique aperture weights that maximize the system psf's resemblance to the desired psf. We first provide a brief review of the technique and present a simple broadband design example. We also present the results of simulations that investigate the performance of the technique. Finally, we present an example of application that shows the ease of implementation of the technique to solve common design problems.

II. REVIEW OF THE M SSE TECHNIQUE

The phase and magnitude of the ultrasonic field at a point in space generated by an ultrasound transducer element depend upon several factors including the Euclidean distance between the point and the element, the orientation of the element relative to the point, the frequency of the emitted wave, and frequency dependent attenuation of the

medium. The field can be expressed as a function of the aperture weighting (possibly complex), and a propagation function that includes the effects of the above factors. Therefore, the one-way transmit lateral psf at the range z can be represented as,

$$P_{Tz} = \begin{bmatrix} s_{1,1} & s_{2,1} & \dots & s_{N,1} \\ s_{1,2} & s_{2,2} & \dots & \cdot \\ \cdot & \cdot & \dots & \cdot \\ \cdot & \cdot & \dots & \cdot \\ s_{1,M} & \cdot & \dots & s_{N,M} \end{bmatrix} \begin{bmatrix} t_1 \\ t_2 \\ \cdot \\ \cdot \\ t_N \end{bmatrix} = S_z^T \quad (1)$$

where S_z is an $M \times N$ matrix of propagation functions with $s_{i,j}$ denoting the propagation function that determines the field at the point z due to the i^{th} element, T is an $N \times 1$ vector of aperture weightings, and the psf P_{Tz} is an $M \times 1$ vector.

Let \tilde{P}_{Tz} represent the desired one-way psf for the application of interest. We can then characterize the degree of similarity between \tilde{P}_{Tz} and the actual system psf, P_{Tz} , by the SSE between them. Minimizing this SSE would yield a system psf optimally similar to the goal psf. Therefore, beamformer design is simply the selection of transmit aperture weightings such that the SSE between the desired and actual system psfs is minimized. Using equation 1, the SSE can be expressed as follows.

$$\begin{aligned} \text{SSE} &= (P_{Tz} - \tilde{P}_{Tz})^H (P_{Tz} - \tilde{P}_{Tz}) \\ &= (S_z^T - \tilde{P}_{Tz})^H (S_z^T - \tilde{P}_{Tz}) \end{aligned} \quad (2)$$

where the superscript "H" denotes a conjugate transpose operation. From [3], the least squares solution for the optimal transmit aperture weights is,

$$T = (S_z^H S_z)^{-1} S_z^H \tilde{P}_{Tz} = S_z^\# \tilde{P}_{Tz} \quad (3)$$

Parameter	Value
Number of elements	32
Element pitch	135 μm
Focus	1.3 cm
Lateral window over which the psf was calculated	70 mm / 180°
psf window sampling interval	20 μm / 0.01°
Ultrasonic wave propagation speed	1540 m/s
Center frequency	10 MHz
-6 dB Bandwidth (broadband simulations)	75%
Temporal sampling of psf (in broadband simulations)	120 MHz
Temporal spacing of weights for each element (in broadband simulations)	25 ns

Table 1. Parameters used in simulations. The Cartesian coordinate system was used in the broadband design example and the depth of field simulations. The polar coordinate system was used in the simulations involving the effects of the design window and the wave propagation velocity error simulations.

where the superscripts “ -1 ” and “ $\#$ ” denote a matrix inverse and a pseudoinverse operation respectively.

This formulation can be extended to CW two-way (receive) aperture design, and also to broadband one and two-way beam forming [1], [2].

III. SIMULATIONS

Unless otherwise mentioned, the parameters described in table 1 were used in all simulations described in this paper. In CW simulations, the propagation functions were derived from the Rayleigh-Sommerfeld diffraction equation [4]. Field II, an ultrasound simulation package developed by Jensen [5], was used in all broadband simulations.

We implemented the MSE technique in a simple broadband design example. The goal psf was generated by axially weighting a sinusoidal signal by a Hann window, and multiplying the result by a lateral Hann window. Figures 1(a) and 1(b) show the goal and the generated psfs respectively. Figures 1(c) and 1(d) display the calculated transmit weights and the magnitude of the error respectively. The error is the difference between the goal and system psfs. Note that geometric focal delays are not included in the weights, and must be applied separately.

The MSE algorithm optimizes the system psf only within the design window. Effects occurring outside this window are ignored, introducing artifacts in the ultrasonic field generated outside the window. We performed simulations to investigate the effect of the design window size on the generated field. The goal psf was a 6° wide Hann window. The MSE technique was implemented for design window sizes of $\pm 15^\circ$, $\pm 30^\circ$, and $\pm 45^\circ$. The system psf was computed over a $\pm 90^\circ$ window using the calculated weights. Figure 2 shows the goal and generated psfs. The first column depicts the goal psfs while the second column shows the obtained psfs respectively. The design window edges are shown by dotted lines.

An incorrect estimate of the ultrasound wave propagation speed will degrade the performance of an ultrasound system. Since the MSE technique uses dynamic shift-variant aperture weights, errors in the assumed wave speed are an important concern. Therefore, we implemented simulations in which the actual wave speed (1540 m/s) was underestimated and then overestimated by 25 m/s and 50 m/s. The goal psf was a 6° wide Hann window. The designed psf for each assumed velocity is shown in figure 3.

In order to provide a simple example of the application of the MSE technique in a common design problem, we implemented the two-way MSE technique in both CW and broadband ultrasound systems to improve the depth of field (DOF). The system psf should ideally remain similar to the psf at the focus for as large an axial range as possible for a large DOF. Therefore, the technique was applied at every sampled axial range point with the goal psf at each range point being the psf at the focus. In both CW and broadband simulations, we generated the goal psf using 16 element apertures, while we used a 16 element transmit and a 32 element receive aperture for the actual system psf. The focus was placed at 6.5 mm. A Hann window was used for transmit apodization, and for receive apodization during the generation of the goal psf. We performed control simulations that included dynamic apodization and dynamic receive focusing. Figures 4(a) and 4(b) depict CW and broadband correlation coefficients calculated by correlating the psf at each range with the psf at the focus. The dotted lines show the focus. Figures 4(c) and 4(d) depict images constructed using the control and MSE technique CW psfs.

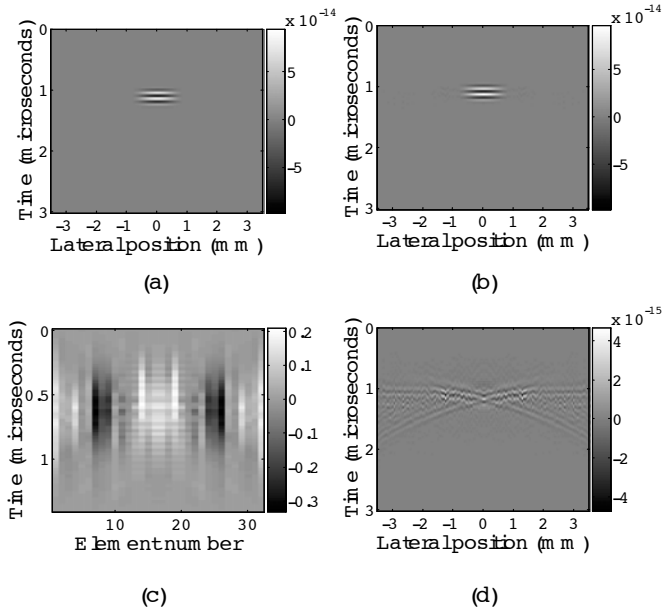


Figure 1. One-way broadband design example: 1(a) and 1(b) depict the goal and obtained psfs 1(c) shows the calculated receive weights as a function of element number and time and 1(d) illustrates the error between the goal and the obtained psfs.

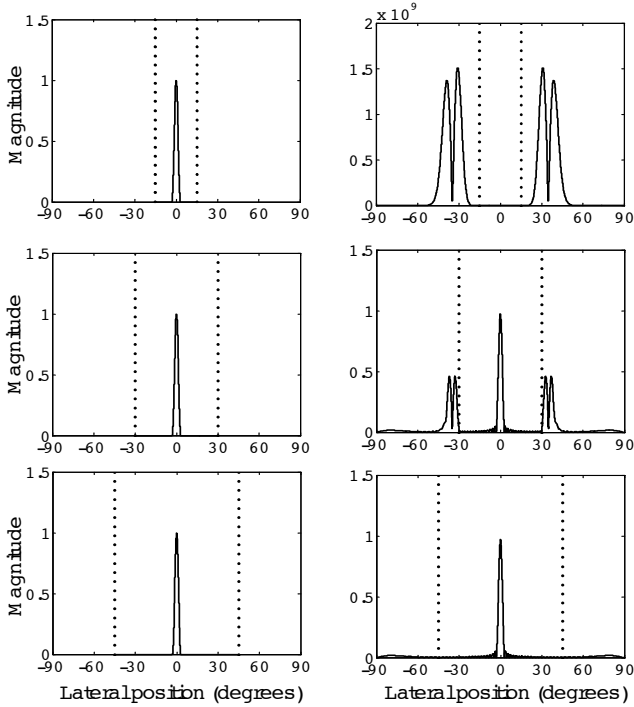


Figure 2. Effects of the size of the design window .The first column depicts the goal psfs while the second column shows the obtained psfs, both as a function of lateral position, for analysis window sizes of $\pm 15^\circ$, $\pm 30^\circ$, and $\pm 45^\circ$ respectively.

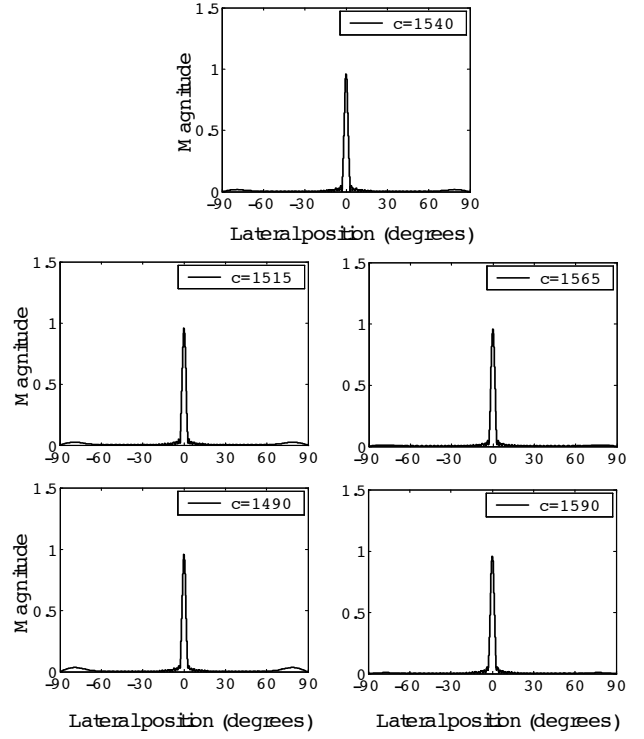


Figure 3. Effect of errors in the assumed wave propagation speed. Figures show the obtained psfs when the assumed wave speed is correct (1540 m/s), underestimated by 25 m/s and 50m/s, and overestimated by 25 m/s and 50 m/s.

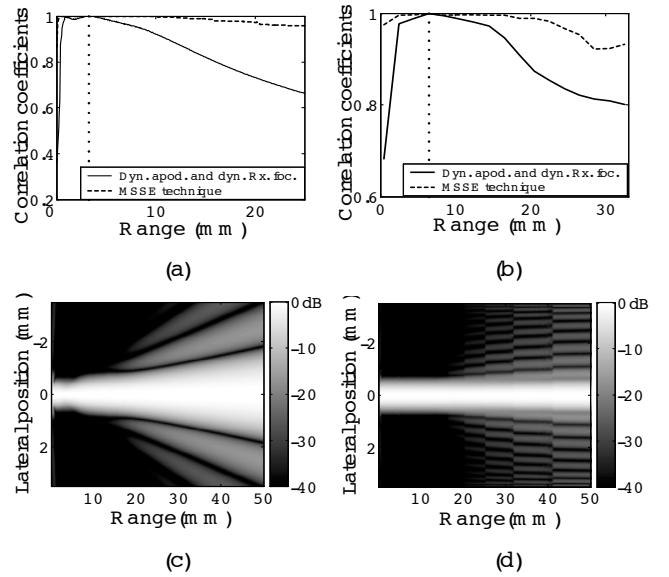


Figure 4. Application of the MSSE technique for enhanced depth of field (DOF): 4(a) shows CW correlation coefficients, 4(b) shows broadband correlation coefficients, and 4(c) and 4(d) depict images of the control and MSSE technique designed CW psfs.

IV. DISCUSSION

Figure 1 shows the results obtained in the one-way broadband design example. It can be seen from figures 1(a) and 1(b) that the goal and system psfs are very similar. Note that this goal psf is quite challenging since it lacks the normal wavefront curvature. Despite the flat wavefront of the goal psf, we were still able to approximate it well.

The effects of varying the design window size are shown in figure 2. It can be seen that when a $\pm 15^\circ$ window was used, the ultrasonic field outside the window had large grating lobes that occurred just outside the design window (shown by dotted lines). However, the magnitude of the grating lobes decreased dramatically when the window size was progressively increased to $\pm 45^\circ$. Therefore, it can be seen that the size of the design window significantly impacts the obtained ultrasonic field, and must be carefully chosen to suit the application. Ideally it would always cover $\pm 90^\circ$, although computational and memory requirements may limit the practical range.

The effect of errors in the assumed speed of sound are displayed in figure 3. It can be seen that the designed psf was not significantly altered from the psf observed with the correct speed (1540 m/s). Therefore, the M SSE algorithm is stable in the sense that small errors in the assumed wave propagation speed do not appear to result in a significant degradation of performance.

The ability of the M SSE technique to improve the depth of field (DOF) is shown in figure 4. The DOF was defined in terms of correlation coefficient as the axial region over which the coefficient was above 0.99. In CW and broadband simulations, the DOF increased by 249% and 325% respectively over control DOF on application of the M SSE technique. A qualitative assessment of the efficacy of the M SSE technique can be made using figures 4(c) and 4(d). It can be seen that applying the M SSE technique dramatically reduces the broadening of the psf mainlobe with range seen in the control simulation. This improvement, though, comes at the cost of slightly higher sidelobe levels. However, as described in [1], we can use a weighting function to selectively emphasize sidelobes in the M SSE design process.

V. CONCLUSIONS

The minimum sum squared error (M SSE) technique has been shown to be stable and useful in designing ultrasound systems with arbitrary system responses. It is efficient, since there is no iteration, and requires very little design time. One-way and two-way CW and broadband simulations demonstrate that it is easy to implement and can be applied to a wide range of applications. The M SSE technique has therefore been shown to have significant potential to improve ultrasound beam forming and can be implemented in any ultrasound application in which better control of beam parameters is desired.

V. ACKNOWLEDGEMENTS

This work was supported by Susan G. Komen Breast Cancer Foundation Imaging Grant No. 99-3021 and United States Army Congressionally Directed Medical Research Program Grant No. DAMD 17-01-10443. Inspiration for this work stems from National Science Foundation Major Research Instrumentation Grant 0079639.

V. REFERENCES

- [1] K. Ranganathan and W. F. Walker, "A novel beam former design method for medical ultrasound: Part I (Theory)," *IEEE Trans. Ultrason. Ferroelectr., Freq. Contr.*, in press.
- [2] K. Ranganathan and W. F. Walker, "A novel beam former design method for medical ultrasound: Part II (Simulation results)," *IEEE Trans. Ultrason. Ferroelectr., Freq. Contr.*, in press.
- [3] L. L. Scharf, *Statistical Signal Processing: Detection, Estimation, and Time Series Analysis*, Addison-Wesley Publishing Company, 1991.
- [4] J. W. Goodman, *Introduction to Fourier Optics*, Second Edition, McGraw-Hill, 1988.
- [5] J. A. Jensen and N. B. Svendsen, "Calculation of pressure fields from arbitrarily shaped apodized and excited ultrasound transducers," *IEEE Trans. Ultrason. Ferroelectr., Freq. Contr.*, vol. 39, no. 2, pp. 262-267, 1992.

Author's email—kr6u@virginia.edu

A CONSTRAINED ADAPTIVE BEAMFORMER FOR MEDICAL ULTRASOUND: INITIAL RESULTS

J.A. Mann and W.F. Walker

Department of Biomedical Engineering
University of Virginia, Charlottesville, VA

ABSTRACT

Adaptive beamforming has been widely used as a way to improve image quality in medical ultrasound applications by correcting phase and amplitude aberration errors resulting from tissue inhomogeneity. A less-studied concern in ultrasound beamforming is the deleterious contribution of bright off-axis targets. This paper describes a new approach, the constrained adaptive beamformer (CAB), which builds on classic array processing methods from radar and sonar. Given a desired frequency response for the mainlobe beam, the CAB reduces off-axis signals by imposing an optimal set of weights on the receive aperture. A linearly constrained adaptive filter dynamically adjusts the aperture weights in response to the incoming data. Initial results show a factor of two improvement in point target resolution and a 60% contrast improvement for low echogenicity cysts. The CAB could considerably improve cardiac and abdominal image quality. We address implementation issues and discuss future work.

1. INTRODUCTION

The ability of commercial ultrasound systems to image desired targets is often hindered by the presence of strong off-axis scattering. Echoes from such off-axis targets generate broad clutter which can overshadow the signal from desired targets, greatly reducing image contrast. In cardiac imaging, the ribs act as highly echoic undesired targets. In the abdomen strong echoes from the bladder reduce image contrast. A method to reduce side lobe levels and suppress clutter would improve diagnostic imaging in these situations.

Most adaptive imaging techniques used in medical ultrasound operate by correcting phase and amplitude aberration errors to improve image contrast and resolution [1,2]. We introduce a new approach to image

enhancement, the Constrained Adaptive Beamformer (CAB). Unlike other adaptive beamformers, the CAB calculates beamformer coefficients to minimize the impact of bright off-axis targets, not to correct for inhomogeneities in the propagation path. Adaptive beamforming has been used in radar and sonar applications to reduce noise in beam side lobes [3], but this generally is done using recursive methods to converge upon a single ideal set of aperture weights for narrowband sources in the aperture far-field [3,4]. For diagnostic ultrasound, the ideal aperture weighting changes constantly because of the poor shift invariance in the aperture near-field. The CAB therefore calculates new weights dynamically for each receive focus.

A typical beamformer for diagnostic ultrasound receives an RF line from each channel of a transducer array and applies appropriate delays to each channel to focus the signal for a given number of focal ranges. Preset system apodization is often used to weight the RF lines coming from the center of the aperture more heavily than those from the edges. Finally, the channels are summed and envelope detected to yield a B-Mode image.

The CAB begins with the focal delays already applied, but replaces the system apodization with an adaptive set of aperture weights that are determined from incoming RF lines. The weights are selected to reduce the power coming from off-axis noise sources, which can be accomplished by modifying a classical constrained least mean squares (CLMS) algorithm [5].

2. THEORY

The CLMS problem optimal weights are found by

$$\min_w w^T R w \quad (1)$$

constrained subject to

$$C^T w = f \quad (2)$$

where w is the set of weights imposed on the aperture, R is the autocorrelation matrix for the input data, C is the constraint matrix, and f is the vector of coefficients which constrain the problem.

The CAB technique uses the ideal system frequency response as the constraint f to preserve the desired signal. This is specified using a finite impulse response (FIR) filter of length L . The aperture weights for each range are calculated from a window of input data L samples long, so the filter length strongly influences computation time for the CAB. Accordingly, choosing an appropriate filter is a tradeoff between computation time and precise frequency response. All results presented in this paper were obtained using a tenth-order FIR filter with the same center frequency as the transducer.

The input data vector for each set of aperture weight calculations, denoted X , is a concatenation of L values for the N input channels (i.e. the first sample for all channels, followed by the second sample for all channels, etc.). The constraint matrix C serves as an index for the application of the constraint filter and is defined as

$$C^T = \begin{bmatrix} 1 & 0 & \dots & 0 \\ \vdots & \vdots & & \vdots \\ 1 & 0 & \dots & 0 \\ 0 & 1 & \dots & 0 \\ \vdots & \vdots & & \vdots \\ 0 & 1 & \dots & 0 \\ \vdots & \vdots & & \vdots \\ 0 & 0 & \dots & 1 \\ \vdots & \vdots & & \vdots \\ 0 & 0 & \dots & 1 \end{bmatrix} \quad \left. \vphantom{\begin{bmatrix} 1 & 0 & \dots & 0 \\ \vdots & \vdots & & \vdots \\ 1 & 0 & \dots & 0 \\ 0 & 1 & \dots & 0 \\ \vdots & \vdots & & \vdots \\ 0 & 1 & \dots & 0 \\ \vdots & \vdots & & \vdots \\ 0 & 0 & \dots & 1 \\ \vdots & \vdots & & \vdots \\ 0 & 0 & \dots & 1 \end{bmatrix}} \right\} \text{N rows} \quad (3)$$

Each column of the $M \times L$ matrix C has N rows of L nonzero entries corresponding to the N input channels. The dimension M is thus the product of N and the number of filter coefficients, L . This approach assures that a plane wave resulting from a focused target is subjected to the frequency response of the FIR filter.

Equations 1 and 2 can be solved using Lagrange multipliers in the manner described in [6] to yield the following equation for the optimal weight vector \tilde{w} :

$$\tilde{w} = R^{-1} C [C^T R^{-1} C]^{-1} f. \quad (4)$$

The $M \times M$ matrix R is approximated by

$$R = X^T X + \delta I, \quad (5)$$

where δ scales an identity matrix to approximately 100 dB below the mean of the magnitude of X . This ensures a well conditioned matrix for the inversion in Equation 4.

Finally, the weights are applied to the input data as follows:

$$y = \tilde{w}^T X. \quad (6)$$

Equation 6 yields the processed data for one range of the image. The CAB replaces the summing of channel data required in conventional ultrasound beamforming. Optimal weights and the resulting data are calculated for each range and each line of the input data to produce the processed image.

3. EXPERIMENTAL METHODS

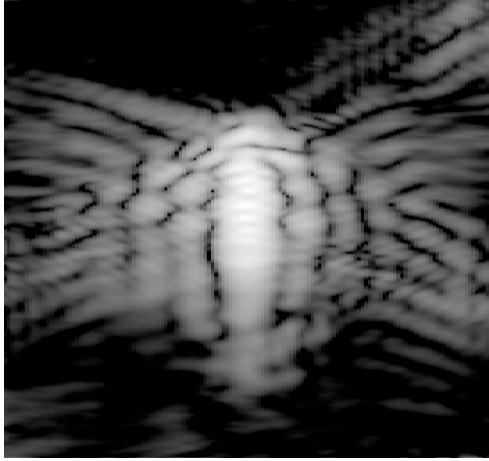
All experiments were performed using a Philips SONOS 5500 imaging system operating with a 10 MHz linear array. Conventional transmit focusing was employed, though system apodization was turned off for transmit. A single focal range (coinciding with the depth of the imaged target) was selected for receive data. Aperture growth was disabled on receive to maintain constant aperture size throughout all ranges. Data was obtained from each of 128 channels in succession by controlling system apodization and using custom software developed by McKee Poland of Philips Medical Systems.

For wire target lateral resolution experiments, a 100 μm steel wire was imaged in a water tank at 20°C. The target was placed at a depth of 4 cm. Reverberation in the tank was reduced using sheets of NPL Aptflex F28 acoustic absorbing rubber from Precision Acoustics, Ltd.

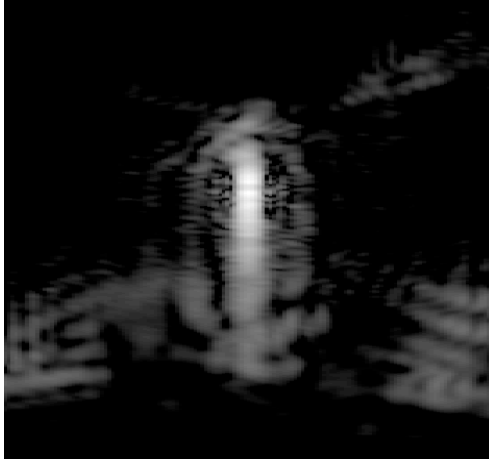
Contrast improvement experiments were performed using a Gammex RMI 404 grayscale tissue mimicking phantom with graphite scatterers and low echogenicity cysts approximately 4 mm in diameter. To improve acoustic coupling, a water standoff was used between the transducer array and phantom surface.

4. EXPERIMENTS: POINT RESOLUTION

A conventional B-mode image of a 100 μm wire target is presented in Figure 1a; Figure 1b shows the image formed using the CAB. The control image is noisy with pronounced tails only slightly lower in intensity than the target itself. As Figure 2a demonstrates, the full width beamwidth at half maximum (FWHM) for the control data is nearly 1 mm, with side lobes impinging on the main lobe and less than 10 dB below the main lobe. The beam



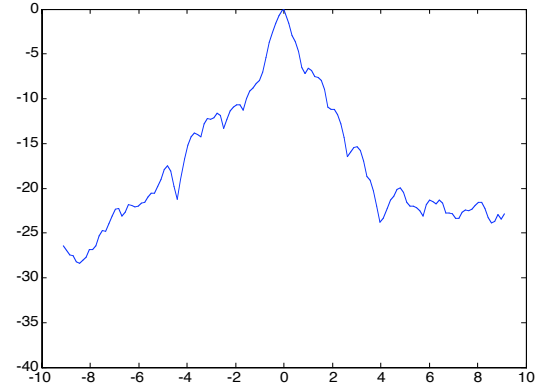
(a)



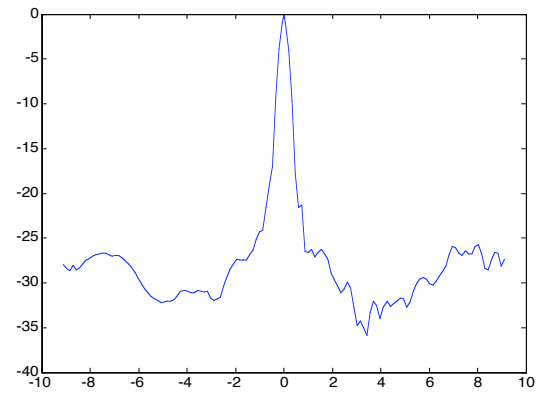
(b)

Figure 1. Images of 100 μm wire targets log compressed with a dynamic range of 40 dB. (a) Conventionally beamformed image; (b) CAB image.

profile for the CAB data given in Figure 2b, however, reveals a FWHM beamwidth of only 400 μm . The processed data also has easily distinguishable side lobes which are suppressed below 25 dB. The actual size and features of the wire target are much more clearly depicted in the CAB image of Figure 1b than in the control image.



(a)



(b)

Figure 2. Lateral beam profiles obtained from a 100 μm wire at a depth of 4 cm. (a) Conventional beamforming image; (b) CAB image.

5. EXPERIMENTS: CONTRAST RESOLUTION

The magnitude of contrast between tissue features and background speckle has a profound impact on the utility of medical ultrasound images. By reducing the contribution of noise from directions other than the focal direction, the CAB greatly improves image contrast for regions lying in the focal direction. Figure 3 shows images of a 4 mm low echogenicity cyst phantom. The cyst is apparent in the center of the control image (Figure 3a), but the image is noisy and the contrast between background and cyst is poor. The CAB image of Figure 3b shows the cyst more clearly and is far less noisy. The contrast ratio for the unprocessed image, calculated as the ratio of average pixel values between the background speckle and the cyst, is 1.82. The processed image yields a contrast ratio of 2.94, a 62% improvement in contrast.

Use of the FIR filter alone (without the CAB algorithm) also improves cyst contrast, but only by 20%.

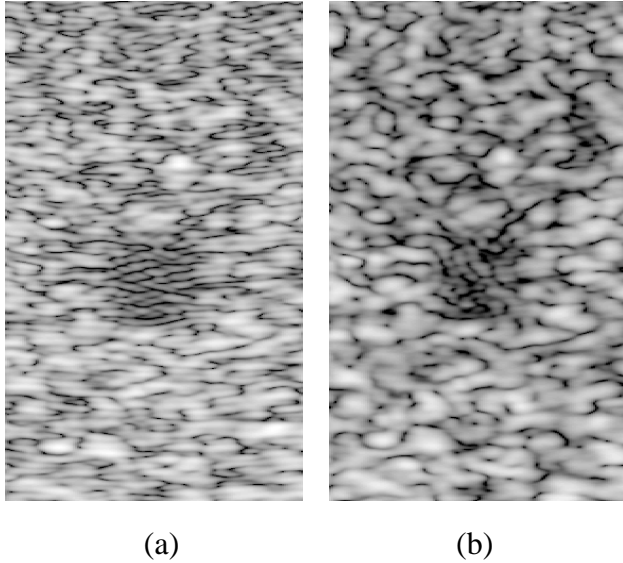


Figure 3. Images of low echogenicity cyst mimicking phantom, log compressed with a dynamic range of 40 dB.
(a) Unprocessed image; (b) CAB-processed image.

6. FUTURE WORK

The CAB technique may have broad applications. Further experiments will include bovine and porcine tissue imaging and additional point resolution work. We are currently working to modify the SONOS 5500 to enable simultaneous capture of all 128 beamformer channels over a period of 1.6 seconds. Once this modification is in place, the CAB will be applied to human cardiac and abdominal imaging. A major constraint of the CAB is the high computational cost associated with its application. We are exploring ways to speed its execution.

The methods presented in this paper could be effectively paired with other beamforming and image-enhancing techniques such as phase aberration correction and angular scatter imaging [7,8].

7. CONCLUSION

Through reduction of off-axis noise, the Constrained Adaptive Beamformer substantially improves both target resolution and image contrast for wire targets and low echogenicity cyst phantoms.

8. ACKNOWLEDGEMENTS

We received technical and equipment support from Philips Medical Systems and stipend support from a U.S. Department of Education GAANN grant. We would especially like to thank McKee Poland of Philips Medical Systems for his technical support on this project. This work was further supported by U.S. Army Congressionally Directed Medical Research Program Grant No. DAMD 17-01-10443. Inspiration from this work stems from National Science Foundation Major Research Instrumentation Grant 0079639.

9. REFERENCES

- [1] D. Zhao, L.N. Bohs, and G.E. Trahey, "Phase aberration correction using echo signals from moving targets. I: Description and theory," *Ultrasonic Imaging*, vol. 14 (2), pp. 97-110, 1992.
- [2] S. Krishnan, K.W. Rigby, and M. O'Donnell, "Adaptive Aberration Correction of Abdominal Images Using PARCA," *Ultrasonic Imaging*, vol. 19 (3), pp. 169-179, 1997.
- [3] O.L. Frost, III, "An Algorithm for Linearly Constrained Adaptive Array Processing," *Proc. IEEE*, vol. 60 (8), pp. 926-935, 1972.
- [4] Widrow, B., and Stearns, S.D., *Adaptive Signal Processing*, Prentice Hall, Upper River, New Jersey, 1985.
- [5] Scharf, L.L., *Statistical Signal Processing: Detection, Estimation, and Time Series Analysis*, Addison-Wesley, Reading, Massachusetts, 1991.
- [6] Haykin, S.S., *Adaptive Filter Theory*, 4th ed., Prentice Hall, Upper Saddle River, New Jersey, 2002.
- [7] W.F. Walker, "C- and D-Weighted Ultrasonic Imaging Using the Translating Apertures Algorithm," *IEEE Trans. Ultrason., Ferroelect., Freq. Contr.*, vol. 48 (2), pp. 452-461, 2001.
- [8] M.J. McAllister and W.F. Walker, "Evaluation of Translating Apertures Based Angular Scattering Imaging on a Clinical Imaging System," *Proc. 2001 IEEE Ultrasonics Symposium*.

Angular Scatter Imaging: Clinical Results and Novel Processing

William F. Walker and M. Jason McAllister

Department of Biomedical Engineering
University of Virginia, Charlottesville, VA.

Human tissues exhibit variation in scattering magnitude as the angle between transmission and reception is changed. These angular scatter variations result from intrinsic acoustic properties and sub-resolution structure. We have developed a clinical imaging system that uses the translating apertures algorithm to obtain statistically reliable, local angular scatter measurements. The obtained data can be processed to yield novel images.

A significant problem with angular scatter imaging is limited depth of field (DOF). We describe a new method to improve DOF by applying shift variant filters to the data obtained at each angle. We show that this approach is optimal in a minimum sum squared error sense. The filter coefficients used in the technique can be determined via experiment or simulation. Unlike prior methods, this approach does not assume a model for the source of decorrelation, rather it includes all sources of decorrelation implicitly. We present simulation results showing the improvements in DOF obtained using this technique.

We present experimental angular scatter data from phantoms and human subjects. In one phantom, designed to mimic microcalcifications in soft tissue, experimental data shows the angular scatter from 500 μm glass spheres falling off by 50% over a 20 degree range of interrogation angles. In the same phantom the angular scatter from 50 μm sephadex spheres fell off by only 10% over the same range. In the human calf muscle, brightness fell off by 60% over 20 degrees, while tendon brightness dropped by only 20%. Interestingly, the brightest target in the phantom (glass spheres) exhibited the greatest angular scatter variation, while the brightest target in the calf (tendon) exhibited the least angular scatter variation. These results provide compelling evidence that angular scatter properties are uncorrelated to b-mode image brightness.

Introduction:

As early as the mid 1980's, experimental data indicated that human tissues exhibit an intrinsic variation in angular scatter properties. (Note that the term angular scatter refers to the variations in scatter with the angle between the transmit incidence and received emission, not anisotropic scattering.) While angular scatter was extensively explored in *ex vivo* experiments, techniques used at the time were unable to make meaningful angular scatter measurements *in vivo*. We have recently described the use of the Translating Apertures Algorithm (TAA) for the acquisition of spatially localized, statistically robust angular scatter profiles [1].

We present initial results in phantoms and *in vivo*, showing that angular scatter variations are significant and are independent of b-mode image brightness. We also describe shift variant filters designed to improve depth of field (DOF) in angular scatter images. We present simulation results indicating the potential of these filters. Finally, we discuss directions for future work.

Experimental Methods:

The TAA was implemented on a General Electric Logiq 700MR Ultrasound system by developing custom scan software and employing a set of system software tools developed at the GE Global Research Center. Acquisition angle was varied for sequential transmit events by simulating system focal zone updates. The focal range was held steady for each focal zone while the transmit and receive apodization were modified to implement the TAA. The experiments presented here utilize an 8 element active aperture on both transmit and receive. Apodization and dynamic receive focusing were disabled for these experiments. Imaging was performed at roughly 6.9 MHz using a linear array probe with 205 μm element spacing. An active aperture of 8 elements was employed with shifts ranging from 0 to 9 elements (each way) over the range of

conditions explored. The system was focused at a range of 1.2 cm and at ~3.0 cm in elevation.

A tissue mimicking phantom was constructed to explore the potential contrast of angular scatter images. The phantom consisted of a background region of gelatin with 50 μm Sephadex added as a source of backscatter contrast. Glass spheres with 500 μm diameter were placed within the phantom to mimic the presence of microcalcifications. The glass spheres were suspended by placing them on the interface formed after one phantom layer had hardened, but before a second had been poured.

The myotendinous junction of a healthy adult female volunteer was also imaged to characterize its angular scatter properties.

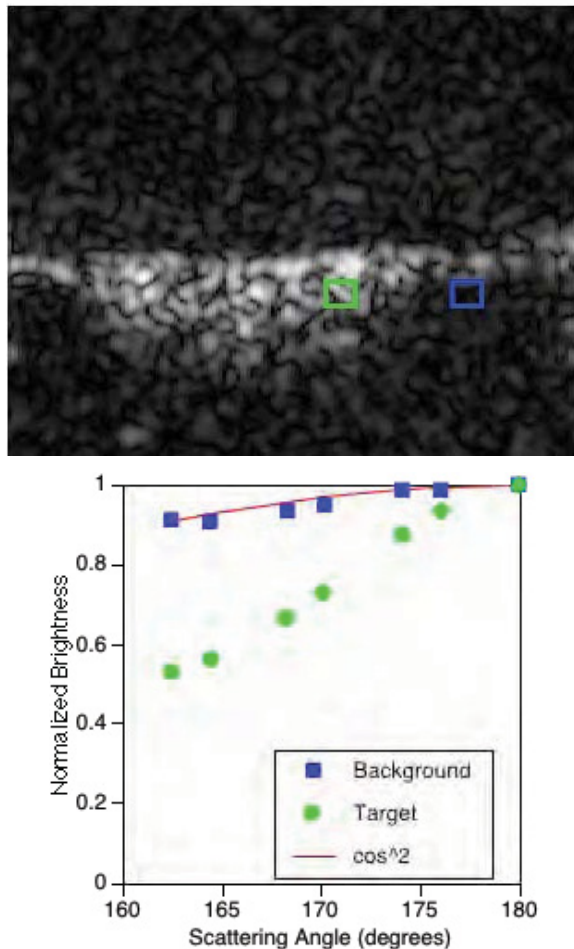


Figure 1: B-Mode image and accompanying angular scatter plot from glass sphere phantom. Note that the brighter glass sphere region exhibits a more pronounced reduction in scatter with angle.

Experimental Results:

Results from the glass sphere phantom are shown in figure 1. The left panel depicts B-Mode image and accompanying angular scatter plot from glass sphere phantom. Background region consists of 50 μm sephadex particles within a gelatin matrix. Highly echogenic 500 μm glass spheres are visible to the left of center. B-mode image shows boxed regions that were used to determine image brightness with acquisition angle

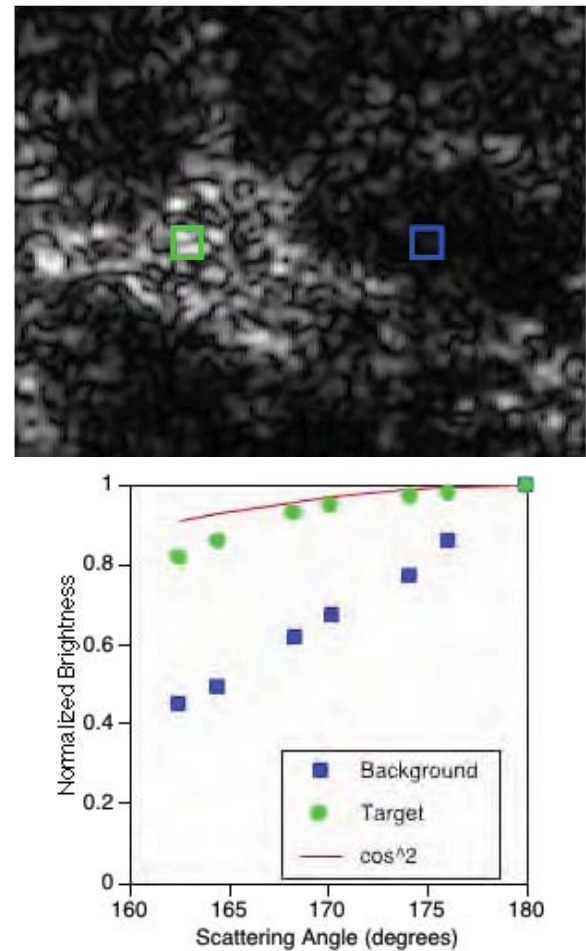


Figure 2: B-Mode image and accompanying angular scatter plot from the myotendinous junction of the gastrocnemius muscle of a healthy female volunteer.

Figure 2 depicts results from the myotendinous junction of the gastrocnemius muscle. The background region consists of skeletal muscle with the target region consisting of connective tissue. Data was acquired with the image plane perpendicular to the muscle/tendon fibers. These results

indicate that angular scatter properties vary among soft tissues. Furthermore, when compared with the results of figure 1, these results clearly indicate that angular scatter properties are independent of backscatter.

Our current experimental system obtains data over seven interrogation angles. While this data may be processed in a variety of ways, we have begun our investigations by examining difference-weighted images computed by envelope detecting the difference between the IQ data set obtained at angle θ_s and the IQ data set obtained at backscatter. An example d-weighted image for the previously described glass sphere phantom is shown below in figure 3. A control B-Mode image is provided for comparison. Both images are log compressed to 40 dB. Quantitative analysis shows that the glass sphere region appears with ~ 15 dB greater contrast in the d-weighted image.

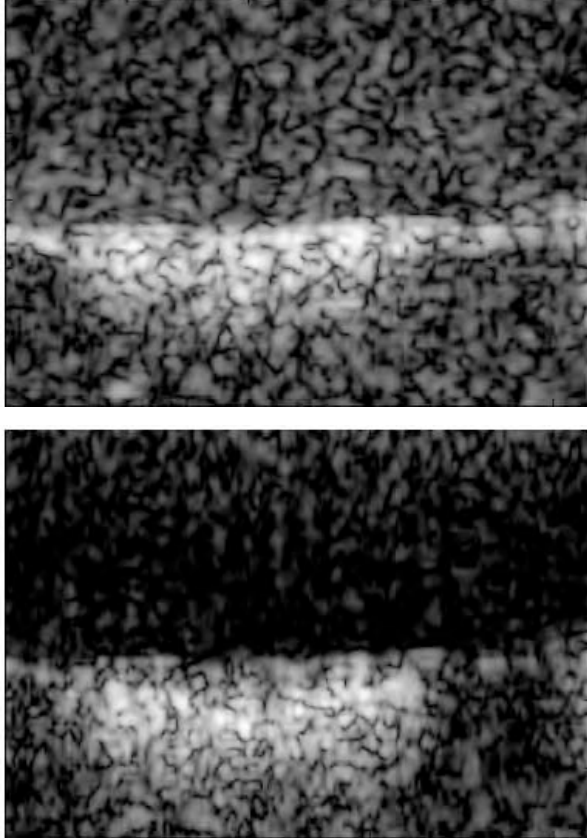


Figure 3: B-Mode image (top) and accompanying d-weighted image (bottom) from glass sphere phantom. Both are log compressed to 40 dB. The d-weighted image exhibits ~ 15 dB higher contrast.

Shift Variant Filtering:

While the TAA maintains a highly uniform system response with angle, it is subject to variations (especially at ranges far from the focus) that limit depth of field and reduce image quality. As we show below, the impact of these variations can be reduced by applying a shift variant filter.

We begin by considering two T sample temporal signals, r_1 and r_2 , received using different aperture geometries. These signals will be most useful for differentiating angular scatter information if they are identical for a medium with no angular scatter variations. We represent the signals received from such omnidirectional targets as \tilde{r}_1 and \tilde{r}_2 . We quantify the similarity of these signals using the mean squared error between them. Representing the signals \tilde{r}_1 and \tilde{r}_2 as column vectors, the expected value of the sum squared error between them is:

$$SSE = \langle (\tilde{r}_1 - \tilde{r}_2)' (\tilde{r}_1 - \tilde{r}_2) \rangle$$

We consider the signals to be the result of the interaction between a shift variant imaging system and a field of scatterers. This can be represented as the multiplication of a propagation matrix and a scattering vector:

$$\begin{aligned} \tilde{r}_1 &= Ps \\ \tilde{r}_2 &= Qs \end{aligned}$$

Where s is the scattering vector of X samples and P and Q are T by X propagation matrices. The vector s contains the amplitude of the scattering function throughout space. The matrices P and Q represent the system sensitivity to scatterers at specific locations in space as a function of time. The product yields a time dependent received signal. To maximize the similarity between the signals we would like to design a shift-variant filter which can be applied to \tilde{r}_2 to minimize the sum squared error between \tilde{r}_1 and \tilde{r}_2 . We represent this filter as a compensating matrix C , of dimensions T by T . Thus the compensated sum squared error is:

$$SSE_C = \langle (\tilde{r}_1 - C\tilde{r}_2)' (\tilde{r}_1 - C\tilde{r}_2) \rangle$$

substituting the definitions of \tilde{r}_1 and \tilde{r}_2 into this expression and regrouping terms yields:

$$SSE_C = \langle s^t (P - CQ)^t (P - CQ) s \rangle$$

To simplify intermediate steps we let $A = (P - CQ)^t (P - CQ)$ so that:

$$SSE_C = \langle s^t A s \rangle$$

Changing this expression from matrix notation to summation notation yields:

$$SSE_C = \left\langle \sum_{i=1}^X \sum_{j=1}^X s_i s_j A_{ij} \right\rangle$$

Since A is deterministic, the expected value operator can be brought inside the summation to yield:

$$SSE_C = \sum_{i=1}^X \sum_{j=1}^X \langle s_i s_j \rangle A_{ij}$$

If we assume that the scattering function s is a white noise process then $\langle ss^t \rangle = \sigma_s^2 I$. Substituting this result in and assuming that $\sigma_s^2 = 1$ yields:

$$SSE_C = \sum_{i=1}^X A_{ii}$$

If we represent A as $B^t B$ then the sum squared error is:

$$SSE_C = \sum_{i=1}^X \left(\sum_{j=1}^T B_{ji} B_{ji} \right)$$

If we reshape B into a column vector b such that $B_{ij} = b_{j+T(i-1)}$ then the sum squared error is simply:

$$SSE_C = b^t b$$

Following our earlier definition of B , $b_{j+T(i-1)} = P_{ij} - \sum_{k=1}^T C_{ik} Q_{kj}$. Thus the sum squared error can be represented as:

$$SSE_C = \left(p - \begin{bmatrix} Q^t & 0 & 0 \\ 0 & Q^t & 0 \\ 0 & 0 & 0 & Q^t \end{bmatrix} c \right)^t \left(p - \begin{bmatrix} Q^t & 0 & 0 \\ 0 & Q^t & 0 \\ 0 & 0 & 0 & Q^t \end{bmatrix} c \right)$$

where $c_{T(i-1)+j} = C_{ij}$ and $p_{T(i-1)+j} = P_{ij}$. This equation is a standard least squares problem and can be readily solved for the compensating weights, expressed as the vector c .

This problem can be further simplified by dividing it into a set of T independent least squares problems. We begin by considering the vectors p and c to be block vectors, each consisting of T column vectors denoted p_1 through p_T and c_1 through c_T respectively. Using this formalism the above expression can be rewritten as:

$$SSE_C = \left(\begin{bmatrix} p_1 \\ p_2 \\ \vdots \\ p_T \end{bmatrix} - \begin{bmatrix} Q^t & 0 & 0 \\ 0 & Q^t & 0 \\ & & \ddots & 0 \\ 0 & 0 & 0 & Q^t \end{bmatrix} \begin{bmatrix} c_1 \\ c_2 \\ \vdots \\ c_T \end{bmatrix} \right)^t \left(\begin{bmatrix} p_1 \\ p_2 \\ \vdots \\ p_T \end{bmatrix} - \begin{bmatrix} Q^t & 0 & 0 \\ 0 & Q^t & 0 \\ & & \ddots & 0 \\ 0 & 0 & 0 & Q^t \end{bmatrix} \begin{bmatrix} c_1 \\ c_2 \\ \vdots \\ c_T \end{bmatrix} \right)$$

From this expression it is clear that the sum squared error between p_1 and $Q^t c_1$ does not depend upon the other p_n or the other c_n . Thus the sum squared error for any individual compensating vector c_n is given by:

$$SSE_{c_n} = (p_n - Q^t c_n)^t (p_n - Q^t c_n)$$

Determination of the weights needed to minimize this sum squared error is a well known problem with the solution equal to:

$$\hat{c}_n = (Q Q^t)^{-1} Q p_n = (Q^t)^{\#} p_n$$

where $(Q^t)^{\#}$ is the pseudoinverse of the transposed propagation matrix Q^t . Using this method it is possible to determine the required filter coefficients to be used for each receive time of interest. Since this formalism has allowed for shift variant filtering, the filter coefficients will need to be updated for each new output time.

Simulation:

The Field II program [2] was used to test the potential utility of the shift variant filtering method described above. We utilized

geometry and operating frequency matching that used in our experiments. We generated lateral-axial system responses at each time range by resampling the normal Field space-time output.

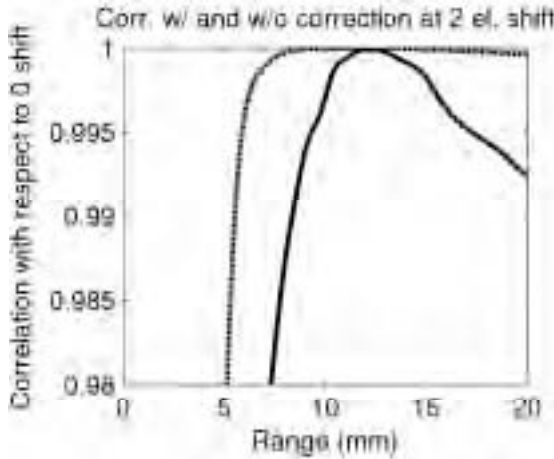


Figure 4: Solid line depicts the correlation between the backscatter data and the angular interrogation with a shift of 2 elements. The dashed line indicates the correlation resulting from application of shift variant filters.

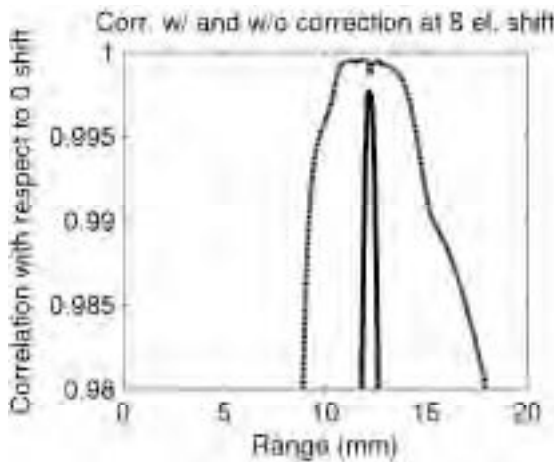


Figure 5: Solid line depicts the correlation between the backscatter data and the angular interrogation with a shift of 8 elements. The dashed line indicates the correlation resulting from application of shift variant filters.

Results of the application of the shift variant filters are shown with control curves in figures 4 and 5. The application of shift variant filters dramatically improves the depth of field of angular scatter imaging without the large computational cost associated with the advanced beamforming methods we have previously described [3, 4].

Conclusion:

The TAA can be successfully applied to the measurement of tissue and phantom angular scatter properties. Such properties provide a new source of image contrast. Shift variant filters should improve image depth of field and reduce artifacts.

Acknowledgements:

We would like to thank K. Wayne Rigby, Carl Chalek, Anne Hall, and Kai Thomenius of GE Medical Systems for their technical support on this project. We would also like to acknowledge the financial support of the Susan G. Komen Foundation for Breast Cancer Research and the US Army Congressionally Directed Medical Research Program.

REFERENCES

- [1] W. F. Walker and M. J. McAllister, "C- and D-Weighted Imaging Using the Translating Apertures Algorithm," *IEEE Transactions on Ultrasonics, Ferroelectrics, and Frequency Control*, vol. 48, pp. 452-461, 2001.
- [2] J. A. Jensen and N. B. Svendsen, "Calculation of pressure fields from arbitrarily shaped, apodized, and excited ultrasound transducers," *IEEE Transactions on Ultrasonics, Ferroelectrics, and Frequency Control*, vol. 39, pp. 262-267, 1992.
- [3] K. Ranganathan and W. F. Walker, "A Novel Beamformer Design Method for Medical Ultrasound: Part II (Simulation)," *IEEE Transactions on Ultrasonics Ferroelectrics & Frequency Control*, accepted.
- [4] K. Ranganathan and W. F. Walker, "A Novel Beamformer Design Method for Medical Ultrasound: Part I (Theory)," *IEEE Transactions on Ultrasonics Ferroelectrics & Frequency Control*, accepted.

Angular Scatter Imaging in Medical Ultrasound

William F. Walker and M. Jason McAllister
Department of Biomedical Engineering
University of Virginia, Charlottesville VA

Abstract

Ultrasonic imaging plays a critical diagnostic role in a broad range of medical specialties; however, there continue to be areas of clinical medicine where the advantages of ultrasound cannot be brought to bear because the targets of most interest do not exhibit sufficient image contrast.

We have invented a novel imaging method that utilizes modified ultrasonic imaging equipment to interrogate a previously unexploited source of image contrast, namely ultrasonic angular scatter variations. This technique takes advantage of the fact that the ultrasonic scattering from tissue changes with the angle between the incident (transmitted) ultrasonic wave and the observed (received) ultrasonic wave. Angular scatter variations result from spatial variations in the intrinsic material properties of density and compressibility, as well as the geometry of the tissue microstructure.

We present experimental results from tissue mimicking phantoms and in vivo human tissues indicating that angular scatter differentiates targets that are indistinguishable in conventional ultrasound images. We also present cases where angular scatter images improve the contrast of interesting targets relative to conventional images. Early in vivo results from the myotendinous junction of the human gastrocnemius muscle indicate that different soft tissues have different angular scatter profiles and that these profiles can be used to discern between tissues.

1. Background:

1.1 Theory:

Medical ultrasound, like other coherent imaging modalities such as RADAR and SONAR, relies primarily on backscatter for image contrast. That is, ultrasound images depict the echoes returned to the ultrasonic transmitter, while neglecting echoes propagating in other directions. Although conventional ultrasound images have incredible diagnostic utility, there are numerous clinically relevant targets for which ultrasonic backscatter fails to provide adequate image

contrast. In these cases it may be helpful to consider angular scatter.

Angular scatter refers to the variations in echogenicity that occur as the angle between the transmit and receive beams is altered. The standard geometry used for discussion of angular scatter is shown below in figure 1.

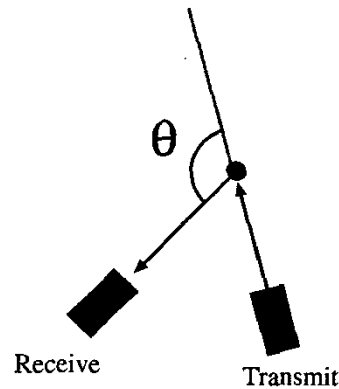


Figure 1: Angular scatter geometry. The angle θ is known as the scattering angle. Backscatter occurs at a scattering angle of 180° .

Angular scatter variations are intrinsic to acoustic scattering, even for targets in the Rayleigh scattering regime. This occurs because the acoustic wave equation, unlike the electromagnetic wave equation, includes two material properties, the material density and compressibility. The impact of these properties can be seen clearly in the acoustic Rayleigh scattering equation [1]:

$$p(r, \theta) = A \frac{e^{ikr}}{r} \frac{1}{3} k^2 a^3 \left(\frac{\kappa_e - \kappa}{\kappa} + \frac{3\rho_e - 3\rho}{2\rho_e + \rho} \cos \theta \right) \quad (1)$$

where $p(r, \theta)$ is the pressure at a distance r and a scattering angle θ relative to the target. In this expression k is the wavenumber ($k = 2\pi/\lambda$), a is the scatterer radius, κ and κ_e are the background and target compressibilities, ρ and ρ_e are the background and

target densities, and A is an arbitrary constant. This expression shows that a target consisting of only a compressibility difference with respect to the background medium will exhibit no variation in angular scatter. Alternatively, a target varying only in density will exhibit an angular scatter profile following the cosine of the scattering angle.

As the size of the scatterer grows beyond the Rayleigh regime, the variations in angular scatter become much more significant. Known as the Faran scattering regime in acoustics, this realm is analogous to Mie scattering in electromagnetics. Although scattering in this size range is extremely difficult to predict analytically, targets in this range include microcalcifications, small calcium crystals associated with cancer and atherosclerotic plaques. Because these targets exhibit densities that are significantly different from soft tissue, we expect that they will exhibit strong variations in angular scatter. Such variations may prove to be a useful source of image contrast as these clinically important targets are generally poorly visualized in backscatter ultrasound images.

1.2 Prior Work:

The potential diagnostic utility of angular scatter has been recognized for some time. Beginning in the mid-1980s a number of researchers performed experiments with the goal of quantifying the intrinsic angular scatter properties of human tissues. To support this goal, these researchers measured the average angular scatter over a large area, at a single frequency [2, 3]. These systems rotated piston transducers about a target to interrogate different scattering angles. This approach was subject to rapid signal decorrelation with angle, even when interrogating omnidirectional scatterers [4]. This instability made the angular scatter profile measured at any given location highly variable, requiring averaging over many samples and spatial locations to obtain meaningful profiles. The high degree of required averaging, narrow bandwidth, and awkward construction of these systems make them unsuitable for clinical application.

Recognizing the diagnostic potential of angular scatter, other researchers developed clinical systems able to image at a single scattering angle other than backscatter [5, 6]. These approaches used one or more phased array transducers with the transmit aperture displaced physically from the receive aperture. By applying electronic focusing and beam steering, these systems were able to interrogate a 2-D region at high spatial resolution and with broad bandwidth. Once configured, the transmit and receive aperture locations were fixed, making it impossible to acquire angular scatter data at more than two angles (angular scatter and backscatter) in any given location. Acquired angular

scatter images were displayed next to corresponding B-mode images, however direct comparison was difficult because each image presented a different speckle pattern. While these systems have yielded interesting results, their failure to coherently process data acquired at different scattering angles limits their sensitivity to angular scatter variations.

We have developed a new approach to angular scatter imaging that has the advantages of both prior approaches, without their significant limitations. Our method uses a clinical phased array imaging system to acquire angular scatter profiles throughout a plane, in real time [4]. By using broadband excitation and focusing we are able to maintain the high spatial resolution typical of standard B-mode images. The use of novel software and a phased array transducer allows us to acquire data at multiple scattering angles without physically moving the transducer. The key to acquiring stable angular scatter profiles is the translating apertures algorithm.

2 Methods:

2.1 The Translating Apertures Algorithm:

The translating apertures algorithm (TAA) is a method of data acquisition that allows interrogation at multiple angles without changing the system's response to an omnidirectional scatterer. Such an approach is critical if one wishes to acquire angular scatter profiles with high fidelity. The TAA is implemented by maintaining a constant focal location while displacing the transmit and receive apertures by equal and opposite amounts. In its standard implementation the TAA utilizes a phased array so that all steering, focusing, and aperture translation can be performed electronically.

The performance of the TAA can be explained by examining figure 2. The first row depicts data acquisition using conventional backscatter geometry. The point spread function exhibits a flat phase front, which is consistent with the centered lateral frequency response of this geometry, shown in the third column. Traditional angular scatter geometry uses a shifted receive aperture, as shown in the second row. In this case the phase front of the point spread function is tilted and the lateral frequency response is shifted off center. This change in the system response would tend to overwhelm intrinsic variations in target angular scatter. Finally, in the third row we see the TAA. By shifting the transmit and receive apertures in equal and opposite directions the TAA maintains a flat phase response and a centered lateral frequency response, enabling angular scatter measurement with high fidelity.

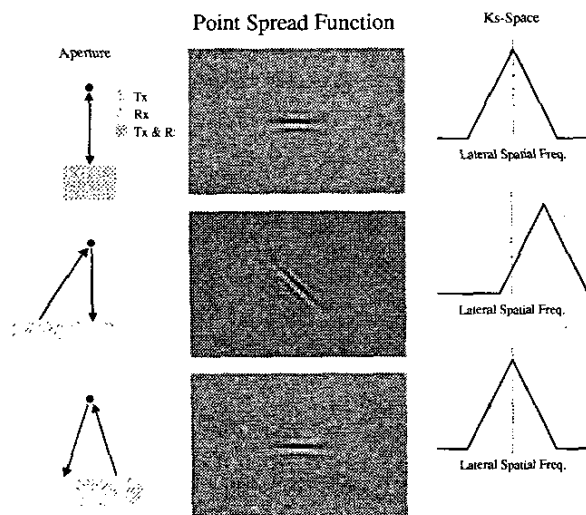


Figure 2: Aperture geometries, point spread functions, and k-space representations for angular scatter data acquisition. The first row depicts conventional backscatter acquisition, the second depicts traditional angular scatter acquisition, and the third depicts angular scatter acquisition with the Translating Apertures Algorithm.

2.2 The Experimental System:

The TAA was implemented on a General Electric Logiq 700MR Ultrasound system by developing custom scan software and employing a set of system software tools developed at the GE Global Research Center. The acquisition angle was varied for sequential transmit events by simulating system focal zone updates. The focal range was held steady for each focal zone while the transmit and receive apodization were modified to implement the TAA. The experiments presented here utilize an 8 element active aperture on both transmit and receive. Apodization and dynamic receive focusing were disabled for these experiments. Imaging was performed at roughly 6.9 MHz using a linear array probe with 205 μm element spacing. An active aperture of 8 elements was employed with shifts ranging from 0 to 9 elements (each way) over the range of conditions explored. The system was focused at a range of 1.2 cm and at ~ 3.0 cm in elevation.

2.3 Phantoms:

Tissue mimicking phantoms were constructed to explore the contrast of angular scatter images. The first phantom, referred to here as the glass sphere phantom, consisted of a background region of gelatin with 50 μm Sephadex added as a source of backscatter contrast. Glass spheres with 500 μm diameter were placed within the phantom to mimic the presence of microcalcifications. The glass spheres were suspended

by placing them on the interface formed after one phantom layer had hardened, but before a second had been poured.

The second phantom, referred to here as the three wire phantom, consisted of the same Sephadex/gelatin background with three 100 μm diameter wires suspended perpendicular to the image plane. The wires were steel wire, nylon monofilament, and a cotton/polyester thread. Each target was degassed prior to phantom construction to eliminate trapped gas.

2.4 Human Subjects:

The myotendinous junction of a healthy adult female volunteer was also imaged to characterize its angular scatter properties. Images were obtained perpendicular to the fiber orientation. This experiment was performed under a human investigations protocol approved by both the university Human Investigations Committee and the research sponsor.

2.5 D-Weighted Images:

A broad variety of angular scatter images may be formed using the local angular scatter profiles acquired by the TAA. One of the simplest image types, which we term difference-weighted (d-weighted) images, are formed by envelope detecting the complex data found by subtracting the echo data obtained at some scattering angle (other than backscatter) from the echo data obtained at backscatter. Prior to taking the difference between data sets we applied a range dependent phase rotation to compensate for path length differences between the backscatter and angular scatter aperture geometries. We expect that d-weighted images will highlight targets with significant variations in angular scatter, while suppressing targets with uniform angular scatter.

3 Results:

3.1 Angular Scatter Profiles:

Figure 3 shows a B-mode image and accompanying normalized angular scatter profiles obtained from the glass sphere phantom. The bright region slightly to the left of the image center is the location of a cluster of glass spheres. Note that the angular scatter profile from this region falls rapidly as the angle of interrogation decreases. This is as expected since these scatterers have a significantly different density from the surrounding gelatin medium. The angular scatter profile from the corresponding speckle generating region shows a much slower change with angle. While the glass and speckle regions can be easily differentiated by their brightnesses at backscatter, the

different angular scatter behaviors of these targets could be used to differentiate them even if they had identical backscatter magnitudes.

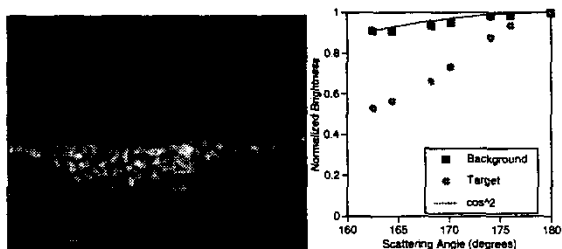


Figure 3: B-Mode image and accompanying angular scatter plots from the glass sphere phantom. Note that the target region (500 μ m glass spheres) exhibits rapid changes in scatter with angle while the background (50 μ m Sephadex in gelatin) exhibits little change in scattering with angle. The cosine squared curve represents a possible bias due to the transducer's limited angular response.

Figure 4 depicts a B-mode image and accompanying angular scatter plot from the myotendinous junction of the human gastrocnemius (calf) muscle. We hypothesize that the different protein concentrations and structure of the muscle and connective tissues should cause them to have different angular scatter profiles. The bright region to the left of center is a region of tendon within the muscle. The darker surrounding regions are skeletal muscle. The angular scatter plots on the right clearly indicate different angular scatter properties for these two tissue types.

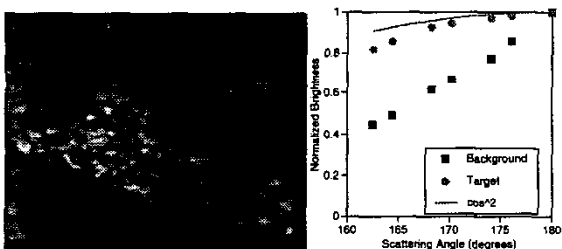


Figure 4: B-Mode image and accompanying angular scatter plots from the *in vivo* human gastrocnemius muscle. The more echogenic tendon region exhibits a nearly flat angular scatter profile while the less echogenic skeletal muscle shows a rapid reduction in angular scatter. Note that this is the opposite of the behavior seen for the glass sphere phantom.

3.2 D-Weighted Images:

Figure 4 depicts a b-mode and accompanying d-weighted image from the glass sphere phantom. Both images were log compressed to a 40 dB dynamic range. In the b-mode image the glass sphere region is clearly visible in the left side of the image, however a membrane, formed during phantom construction, is also visible over the full width of the phantom. This

environment may mimic the presence of connective tissue near a calcified tissue region. In the d-weighted image the contrast of the glass sphere region is significantly improved with respect to both the background and the membrane between layers.

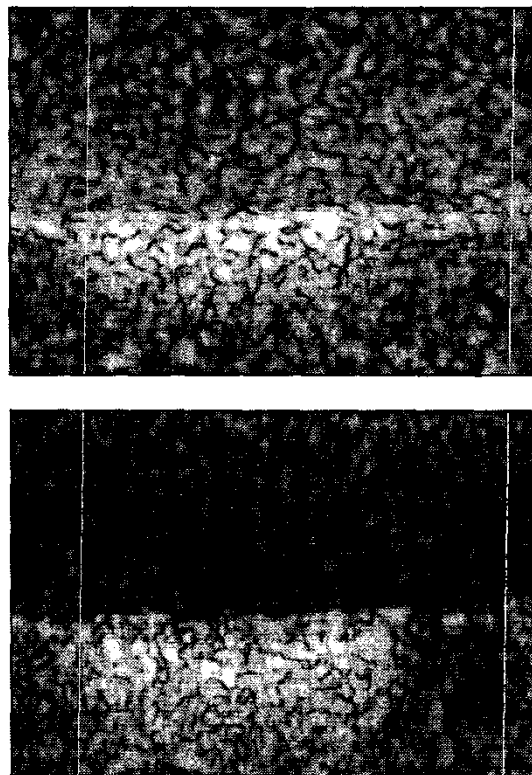


Figure 5: B-Mode (upper panel) and d-weighted (lower panel) images of the glass sphere phantom. The contrast of the glass sphere region is increased by 15 dB in the d-weighted image when compared to a background region at the same range.

Figure 6 depicts a b-mode and accompanying d-weighted image from the three wire phantom. In the b-mode image the contrast of all three wire targets is roughly identical, making differentiation of these targets practically impossible. In the d-weighted image however the steel wire exhibits significantly greater contrast relative to the background, the cotton/polyester thread exhibits significantly lower contrast, and the nylon monofilament exhibits approximately the same contrast relative to the b-mode image. These results are summarized quantitatively in table 1. These results indicate clearly that angular scatter differentiates targets that are indistinguishable in conventional backscatter images.

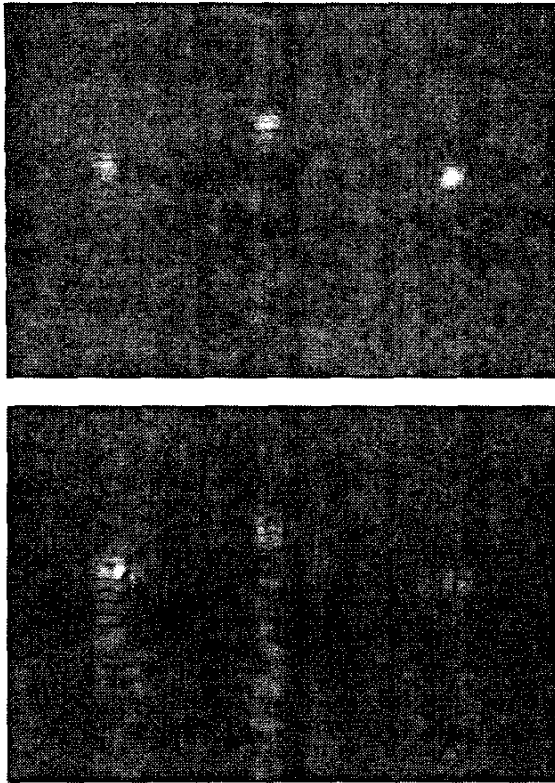


Figure 6: B-Mode (upper panel) and d-weighted (lower panel) images of the three wire phantom. The steel, nylon, and cotton/polyester threads (from left to right) which are indistinguishable in the b-mode image can be easily differentiated in the d-weighted image.

	Steel	Nylon	Cotton/Poly
B-mode	21.3 dB	21.9 dB	23.8 dB
D-weighted	27.9 dB	22.5 dB	17.1 dB

Table 1: Target contrast in the three wire phantom. All contrast measurements are relative to a range matched background region. These results clearly show that d-weighted images differentiate targets which cannot be differentiated in conventional backscatter images.

4 Conclusions:

The experimental results presented here indicate that angular scatter imaging offers new, potentially valuable information in both human tissues and in tissue mimicking phantoms. The techniques employed here might be readily adapted to other coherent imaging modalities such as RADAR and SONAR, where angular scatter may offer a new means of target classification.

5 Acknowledgements:

We would like to thank K. Wayne Rigby, Carl Chalek, Anne Hall, and Kai Thomenius of GE Medical Systems for their technical support on this project. We would also like to acknowledge the financial support of the Susan G. Komen Foundation for Breast Cancer Research and the US Army Congressionally Directed Medical Research Program.

6 References:

- [1] P. M. Morse and K. U. Ingard, *Theoretical Acoustics*. Princeton, NJ: Princeton University Press, 1968.
- [2] W. J. Davros, J. A. Zagzebski, and E. L. Madsen, "Frequency-dependent angular scattering of ultrasound by tissue-mimicking materials and excised tissue," *Journal of the Acoustical Society of America*, vol. 80, pp. 229-237, 1986.
- [3] J. A. Campbell and R. C. Waag, "Measurements of calf liver ultrasonic differential and total scattering cross sections," *J. Acoust. Soc. Am.*, vol. 75, pp. 603-611, 1984.
- [4] W. F. Walker and M. J. McAllister, "C- and D-Weighted Imaging Using the Translating Apertures Algorithm," *IEEE Transactions on Ultrasonics, Ferroelectrics, and Frequency Control*, vol. 48, pp. 452-461, 2001.
- [5] J. C. Lacefield, "Angular Scatter Ultrasound Imaging using Separated Arrays," Duke University, 1999.
- [6] M. T. Robinson and O. T. V. Ramm, "Real-Time Angular Scatter Imaging System for Improved Tissue Contrast in Diagnostic Ultrasound Images," *IEEE Transactions on Ultrasonics, Ferroelectrics, and Frequency Control*, vol. 41, pp. 44-52, 1994.

Constrained adaptive beamforming: point and contrast resolution

Jake A. Mann and William F. Walker

Biomedical Engineering, University of Virginia, Charlottesville, VA 22908

ABSTRACT

Adaptive beamforming has been widely used as a way to correct phase and amplitude aberration errors in medical ultrasound. A less-studied concern in ultrasound beamforming is the deleterious contribution of off-axis bright targets. We describe a new approach, the constrained adaptive beamformer (CAB), which builds on classic array processing methods. Given a desired frequency response in the focal direction, the CAB dynamically imposes an optimal set of time-dependent weights on the receive aperture, reducing signals from directions other than the focal direction. Two implementations of the CAB are presented which differ in their use of calculated weights to form an output image: the Single Iteration CAB and Multiple Iteration CAB.

We present results from experiments performed on a Philips SONOS 5500 imaging system operating with an 8.7 MHz linear array and contrast the performance of the two CAB implementations. Data was acquired from wire targets in a water tank and low echogenicity cysts in a grayscale tissue mimicking phantom. The desired system frequency response was specified by a FIR filter with the same center frequency as the transducer. Improvements in lateral resolution for wire targets and contrast for low echogenicity cysts are shown. Simulations are used to demonstrate limitations of the CAB.

Keywords: ultrasound, beamforming, resolution, constrained adaptive beamformer, CAB, CLMS

1. INTRODUCTION

The ability of commercial ultrasound systems to image desired targets is often hindered by the presence of strong off-axis scattering. Echoes from such off-axis targets generate broad clutter which can overshadow the signal from desired targets, greatly reducing image contrast. In cardiac imaging, the ribs act as highly echoic undesired targets. In the abdomen strong echoes from the bladder and from bowel gas reduce image contrast. An effective method to reduce side lobe levels and suppress clutter would improve diagnostic imaging in these situations.

Most adaptive imaging techniques used in medical ultrasound operate by correcting phase and amplitude aberration errors to improve image contrast and resolution [1,2]. We introduce a new approach to image enhancement, the Constrained Adaptive Beamformer (CAB). Unlike other adaptive beamformers, the CAB calculates beamformer coefficients to minimize the impact of bright off-axis targets, not to correct for inhomogeneities in the propagation path. Adaptive beamforming of this sort has been used in radar and sonar applications to reduce noise in beam side lobes [3], but this generally is done using recursive methods to converge upon a single ideal set of aperture weights for narrowband sources in the aperture far-field [3,4]. For diagnostic ultrasound, the ideal aperture weighting changes constantly because of the poor shift invariance in the aperture near-field. The CAB therefore calculates new weights dynamically for each receive focus.

A typical receive beamformer for diagnostic ultrasound (shown in Figure 1a) obtains an RF line from each channel of a transducer array and applies appropriate delays to each channel to focus the signal for a given number of focal ranges. Preset system apodization is often used to reduce sidelobe levels by weighting the RF lines coming from the center of the aperture more heavily than those from the edges. Finally, the channels are summed and envelope detected to yield a B-Mode image.

The CAB (Figure 1b) begins with the focal delays already applied, but replaces the system apodization with an adaptive set of aperture weights that are determined from incoming RF data. The weights are selected to reduce the power

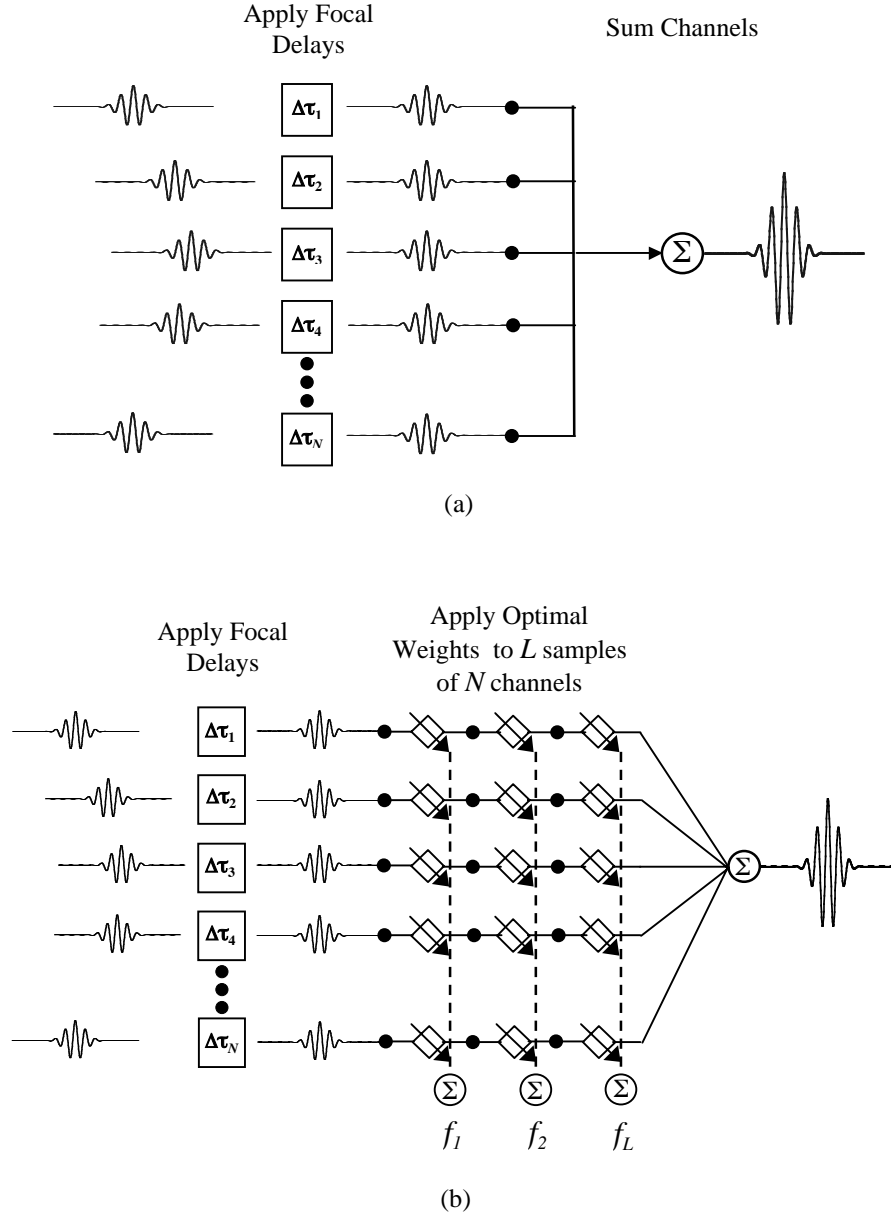


Figure 1. Schematic diagrams of (a) conventional delay-and-sum receive beamformer and (b) constrained adaptive beamformer. Time delays $\Delta\tau_n$ are precalculated for each sample.

coming from off-axis noise sources, which can be accomplished by modifying a classical constrained least mean squares (CLMS) algorithm [5].

2. THEORY

2.1 Algorithm

The general CLMS approach minimizes the mean output power in a signal given a linear constraint. This is done through calculation of optimal weights found by

$$\min_w w^T R w \quad (1)$$

constrained subject to

$$C^T w = f \quad (2)$$

where w is a set of weights imposed on the input array, R is the estimated autocorrelation matrix for the input data, C is the constraint matrix, and f is the vector of coefficients which constrain the problem. The CAB technique uses the ideal system frequency response as the constraint f to preserve the desired signal received by channels of an ultrasound transducer array. This frequency specification is delineated by a finite impulse response (FIR) filter of length L .

The aperture weights for each range r are calculated for a window of input data L samples long (r to $r + L - 1$), so the filter length strongly influences computation time for the CAB. Accordingly, choosing an appropriate filter is a tradeoff between computation time and precise frequency response. All results presented in this paper were obtained using a tenth-order FIR filter with the same center frequency and bandwidth as the transducer. Shorter filter lengths were unable to effectively approximate the desired frequency response, and higher orders filters significantly increased computation time without noticeable improvement in CAB output.

The input data vector for each set of aperture weight calculations, denoted X , is a concatenation of L values for the N input channels (i.e. sample r for all channels, followed by sample $r + 1$ for all channels, etc.). The constraint matrix C serves as an index for the application of the constraint filter. Figure 2 shows a simple case of the matrix formulation in Equation 2. Each column of the $NL \times L$ matrix C has N nonzero entries which align the aperture weights for one range sample to the corresponding filter coefficient. This approach ensures that a plane wave resulting from a focused target is subjected to the frequency response of the FIR filter, while noise signals arriving incoherently at the beamformer input are minimized.

$$\begin{bmatrix} 1 & 0 & 0 \\ 1 & 0 & 0 \\ 0 & 1 & 0 \\ 0 & 1 & 0 \\ 0 & 0 & 1 \\ 0 & 0 & 1 \end{bmatrix}^T \begin{bmatrix} w_{11} \\ w_{21} \\ w_{12} \\ w_{22} \\ w_{13} \\ w_{23} \end{bmatrix} = \begin{bmatrix} f_1 \\ f_2 \\ f_3 \end{bmatrix}$$

Figure 2. Matrix formulation of $C^T w = f$ for the case of $N = 2$ channels and filter length $L = 3$. Subscripts of w denote channel number and filter coefficient number, respectively.

Equations 1 and 2 can be solved using Lagrange multipliers in the manner described in [6] to yield the following equation for the optimal weight vector \tilde{w} :

$$\tilde{w} = R^{-1} C [C^T R^{-1} C]^{-1} f. \quad (3)$$

The $NL \times NL$ matrix R is approximated by

$$R = X^T X + \delta I, \quad (4)$$

where δ scales an identity matrix to a desired level. This regularization ensures a well conditioned matrix for the inversion in Equation 3. Large values of δ can reduce output side lobe levels slightly [7], but also reduce the dependence of R on the input samples and therefore decrease the effectiveness of the CAB. Though the use of δ values as high as 20 dB below the root mean squared of X does not noticeably affect the beamformer output, the results presented in this paper were obtained using the smallest δ which allowed a well conditioned matrix, approximately 100 dB below the

mean of X . For Equation 4 to be a valid representation of the autocorrelation of input data, it is assumed that the input signals can be modeled effectively as zero-mean random processes.

2.2 Single Iteration CAB

$$y = \tilde{w}^T X. \quad (5)$$

2.3 Multiple Iteration CAB

$$y_l = \sum_{n=1}^N \tilde{w}_{nl} \cdot X_{nl}, \quad (6)$$

$[y_{1,1} \quad y_{1,2} \quad \cdots \quad y_{1,L}]$	Weighted samples for 1st iteration
$[y_{2,1} \quad y_{2,2} \quad \cdots \quad y_{2,L}]$	Weighted samples for 2nd iteration
$[y_{3,1} \quad y_{3,2} \quad \cdots \quad y_{3,L}]$	Weighted samples for 3rd iteration
\vdots	\vdots
$+$	\vdots
$[y_{M,1} \quad y_{M,2} \quad \cdots \quad y_{M,L}]$	Weighted samples for Mth iteration
<hr/>	
$[Y_1 \quad Y_2 \quad Y_3 \quad \cdots \quad Y_{M-1} \quad Y_M]$	Final output sum for all M ranges

Because every output pixel depends on L iterations of the algorithm, this new approach is called the Multiple Iteration CAB, denoted MI-CAB in the remainder of the paper.

2.4 Frequency Space Considerations

The constraint specified in Equation 2 is designed to yield a desired frequency response in the focal direction. Exploration of the Fourier domain characteristics of the CAB imparts intuition about its performance. By forcing the sum of calculated aperture weights for each range to equal the FIR filter coefficients, the constraint forces the central axis frequency content of the weights to match the Fourier transform of the FIR filter. Consider the weights for a single iteration of the CAB before summing, given by

$$\tilde{W} = \begin{bmatrix} \tilde{w}_{11} & \tilde{w}_{12} & \cdots & \tilde{w}_{1L} \\ \tilde{w}_{21} & \tilde{w}_{22} & \cdots & \tilde{w}_{2L} \\ \vdots & \vdots & \ddots & \vdots \\ \tilde{w}_{N1} & \tilde{w}_{N2} & \cdots & \tilde{w}_{NL} \end{bmatrix}, \quad (6)$$

where \tilde{W} denotes the ideal aperture weights reshaped into an $N \times L$ matrix, and subscripts indicate channel number and range/filter coefficient number, respectively.

The center row of the 2D Fourier transform of \tilde{W} corresponds to a signal with constant lateral frequency, i.e. a plane wave. Comparison of this center row to the Fourier transform of the FIR filter f shows them to be equal. As a result, any portion of the output signal resulting from a plane wave input will have the same frequency content as the specified FIR filter. Noise signals arriving from off-axis are not retained by the CAB, and the overall frequency content of the final image will be nearly as desired. The extent to which this is true depends on the CAB implementation used. Since the pixels of an SI-CAB output image are calculated independently, the spectrum of the image is not guaranteed to be bandlimited. The MI-CAB, however, does consistently produce a bandlimited (in range) image due to the spatial-averaging characteristic of each output Y .

3. POINT RESOLUTION

3.1 Experimental methods

All experiments were performed using a Philips SONOS 5500 imaging system operating with a 50% fractional bandwidth 8.7 MHz linear array. 128 channels were used for transmit with no system apodization on either transmit or receive. A single transmit focal range (coinciding with the depth of the imaged target) was selected. Conventional dynamic receive focusing was employed, though aperture growth was disabled to maintain constant aperture size throughout all ranges. Data was obtained at a sampling rate of 40 MHz from each of 128 channels in succession by controlling system apodization and using custom software developed by McKee Poland of Philips Medical Systems.

For point target lateral resolution experiments, a 20 μm steel wire was imaged in a water tank at 20°C. The target was placed at a depth of 4 cm. Sheets of NPL Aptflex F28 acoustic absorbing rubber from Precision Acoustics, Ltd. were used to limit reflection from the sides of the tank, but no other efforts were made to reduce reverberation.

3.2 Results

A conventional B-mode image (obtained by simple summing across all 128 channels) of a 20 μm wire is presented in Figure 4a, log compressed with a dynamic range of 40 dB. The background is noisy due to reverberation, and the point target is accompanied by pronounced tails only slightly lower in intensity than the target itself. Figure 4b shows the image formed for the same data using the SI-CAB implementation. The MI-CAB is less effective for wire target experiments and results using it are not presented here.

As Figure 4c illustrates, the full width beamwidth at half maximum (FWHM) for the control data is nearly 2 mm, with sidelobes less than 5 dB below the main lobe and hardly distinguishable from the main lobe. The beam profile for the SI-CAB data given in Figure 4d, however, reveals a FWHM beamwidth of less than 500 μm . The processed data also has more easily distinguishable side lobes which are suppressed to about 9 dB below the main lobe. The actual size and features of the wire target are more clearly depicted in the SI-CAB image of Figure 4b than in the control image. It is also interesting to note that the greatest reduction in clutter intensity occurs in the sidelobe tails of the point target, a

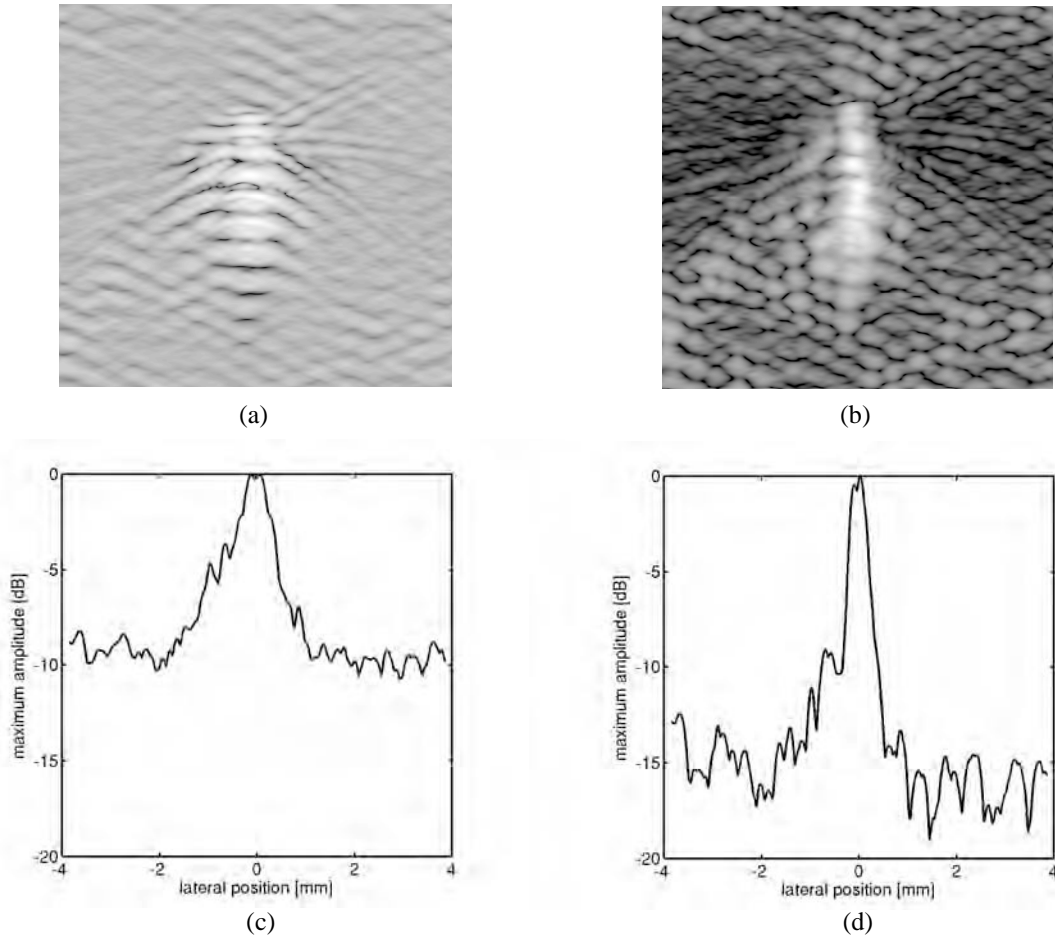


Figure 4. Results for 20 μm point target imaged at a depth of 4 cm using 128 channels. (a) Conventionally beamformed image; (b) SI-CAB image; (c) Lateral beam profile for conventional beamforming; (d) Beam profile for SI-CAB.

consistent feature of images produced with the SI-CAB. The wire was slightly angled from perpendicular to the transducer during imaging, which likely explains the asymmetry of the beam plots.

3.3 Effect of fewer input channels

While most commercial ultrasound systems can receive echoes on a maximum of 128 channels, certain transducers or modes of operation do not allow data to be acquired on all channels. In other cases, a smaller aperture size is desired (e.g. some elements obstructed by discontinuous acoustic windows [9]) or necessary (e.g. imaging between the ribs in cardiac applications). Differences in required image acquisition time and hard drive storage space also make the use of fewer channels an attractive option in certain experimental circumstances.

The behavior of the SI-CAB was investigated for input channel numbers $N = 64$ and $N = 32$. The same experimental data was used as in the above images, with RF samples from unused channels discarded. Figures 5a and 5b show point target images for standard beamforming and the SI-CAB, respectively, obtained from only the center 64 channels of the array. Figures 5c and 5d show the lateral beam profiles for each image. Using the center 32 channels for beamforming yields Figures 6a – 6d.

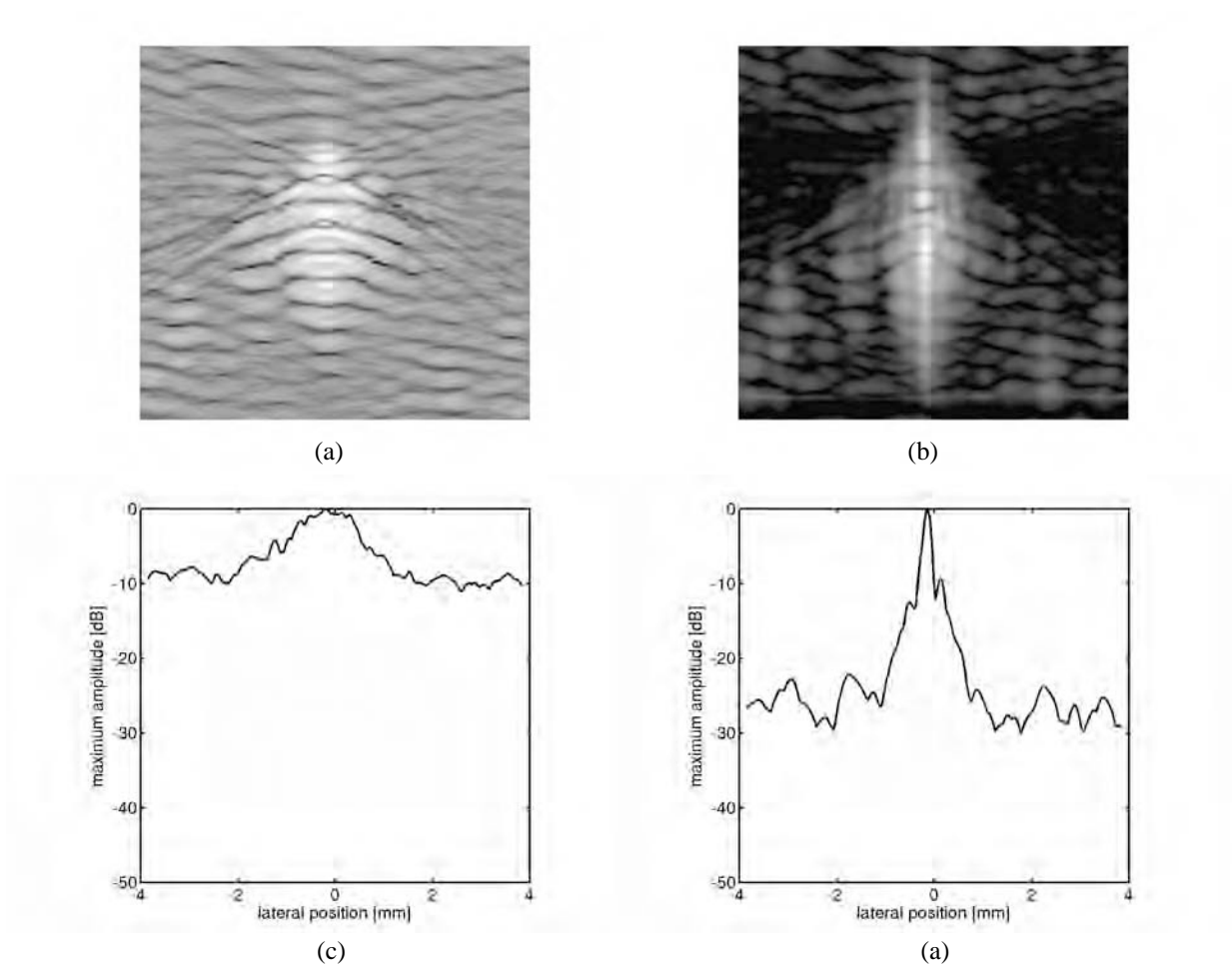


Figure 5. Results for 20 μm point target imaged at a depth of 4 cm using 64 channels. (a) Conventionally beamformed image; (b) SI-CAB image; (c) Lateral beam profile for conventional beamforming; (d) Beam profile for SI-CAB.

Comparison of the images in Figures 4-6 clearly shows that while using fewer channels degrades the control images, it greatly improves the SI-CAB processed images. Table 1 summarizes the lateral beamwidths for standard beamformer and SI-CAB processing of 128, 64, and 32 channel data.

	Full Width at Half Maximum [μm]		
	<i>128 channels</i>	<i>64 channels</i>	<i>32 channels</i>
Conventional Beamformer	1570	2160	3360
Single Iteration CAB	480	230	220

Table 1. Lateral maximum amplitude beamwidths (in microns) for processed point target data.

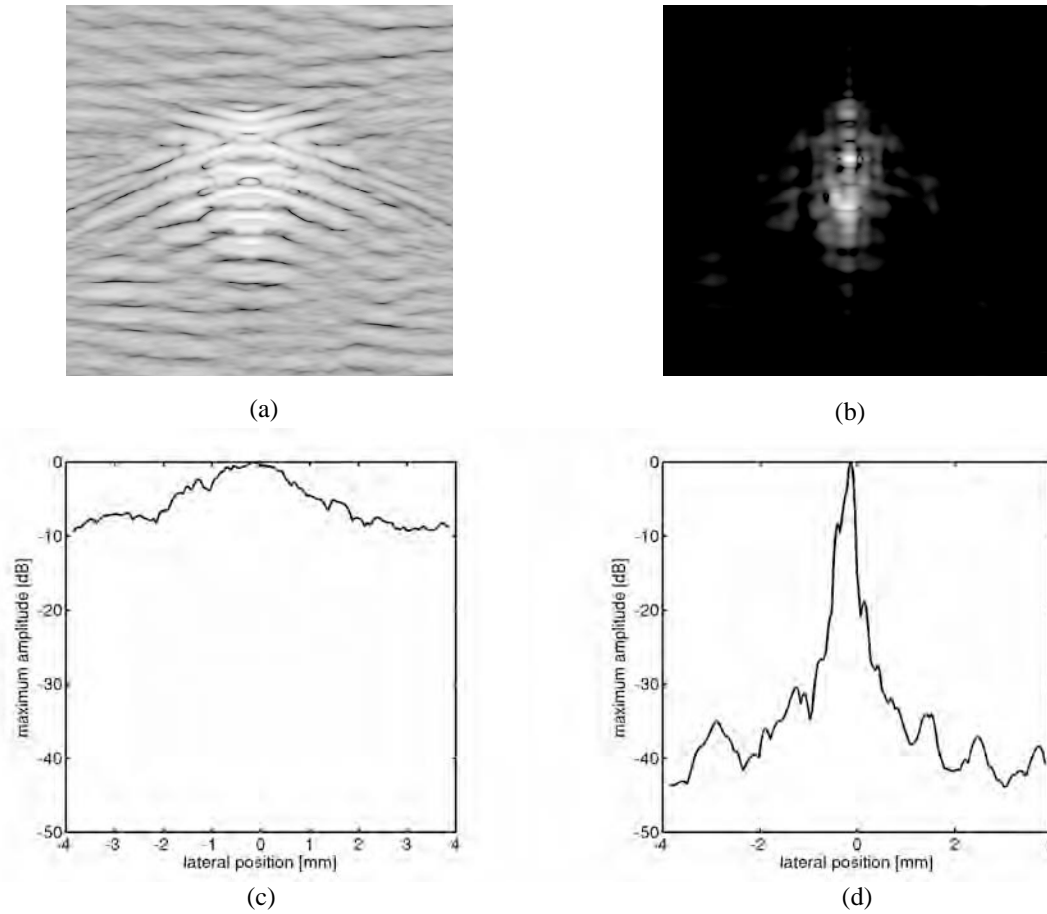


Figure 6. Results for 20 μm point target imaged at a depth of 4 cm using 32 channels. (a) Conventionally beamformed image; (b) SI-CAB image; (c) Lateral beam profile for conventional beamforming; (d) Beam profile for SI-CAB.

4. CONTRAST RESOLUTION

4.1 Experimental methods

Contrast improvement experiments were performed using a Gammex RMI 404 grayscale tissue mimicking phantom with graphite scatterers and low echogenicity cysts approximately 4 mm in diameter. To improve acoustic coupling, a small amount of water was used between the transducer array and phantom surface.

4.2 Experiments

The magnitude of contrast between tissue features and background speckle has a profound impact on the utility of medical ultrasound images. By reducing the contribution of noise from directions other than the focal direction, the CAB should improve image contrast for regions lying in the focal direction. Figure 7 shows images of a 4 mm low echogenicity cyst phantom. The cyst is apparent in the center of the control image (Figure 7a), but the image is cluttered and the contrast between background and cyst is poor. The SI-CAB image of Figure 7b shows the cyst more clearly and is far less noisy. Figure 7c displays the image obtained with the MI-CAB approach, which exhibits an even greater improvement in contrast. Though the number of channels used for processing does affect the beamformer output, the difference is not as obvious as for the point resolution experiments; the results are thus omitted from this paper.

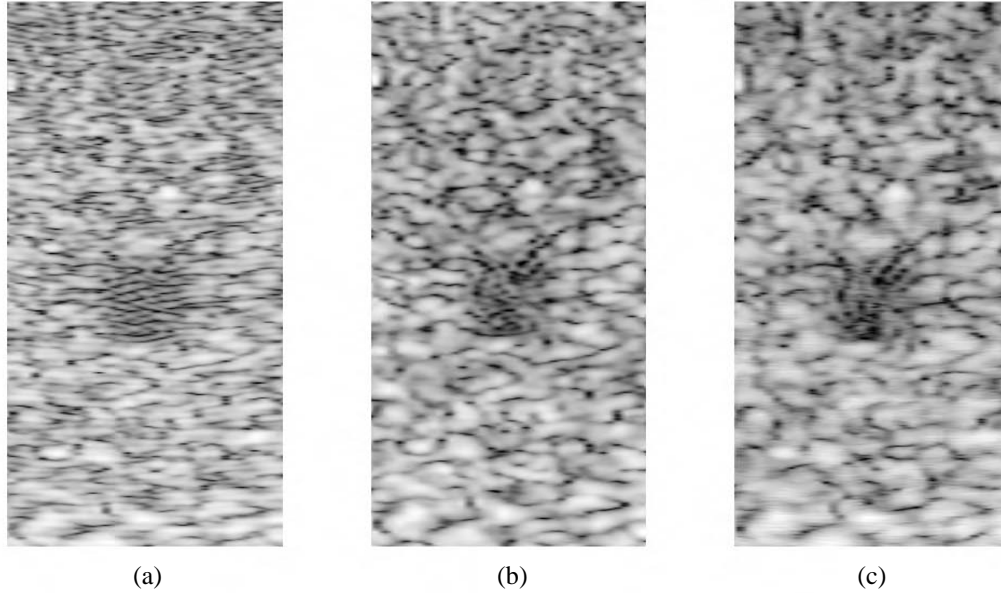


Figure 7. Images of low echogenicity cyst mimicking phantom, log compressed with a dynamic range of 40 dB. (a) Unprocessed image; (b) SI-CAB processed image; (c) MI-CAB processed image.

The contrast ratio for the unprocessed image, calculated as the ratio of average pixel values between the background speckle and the cyst, is 1.82. The SI-CAB processed image yields a contrast ratio of 2.94, a 62% improvement in contrast. Processing the data by MI-CAB produces a 73% improvement in with a contrast ratio of 3.15. Visual inspection may suggest that the images in Figures 7b and 7c could be obtained strictly by applying the FIR filter alone (without the CAB algorithm), but this is not the case. Use of the filter alone does improve cyst contrast, but only by 20%. Close examination of the images also reveals that the CAB has a selective effect on the features in the control image, eliminating some bright speckles while better defining others. We suspect that speckles exhibiting improved definition are actually single bright scatterers. Further experiments using spherical scatterers such as Sephadex beads will be performed.

5. DISCUSSION

5.1 CAB performance

The implementations of the beamformer considered in this paper each have strengths and weaknesses. As mentioned earlier, the MI-CAB offers a more stable bandwidth for output images due to the smoothing effect of multiple algorithm iterations. In fact, this approach is generally more robust. We believe that this explains its superior performance in contrast experiments, where features of interest are considerably larger than the resolution volume of the transducer. For point resolution, however, desired targets are small and produce echoes of much greater amplitude than their surroundings. Each SI-CAB output pixel's relative independence allows it greater dynamic range in improving the resolution of such targets.

5.2 Limitations

The Constrained Adaptive Beamformer shows the potential to dramatically improve image resolution and contrast in many important applications. Unfortunately, even for the types of ultrasound data presented in this paper, the CAB is not entirely reliable. The SI-CAB is extremely effective for improving resolution, but is also sensitive to array imperfections. The MI-CAB responds well to individual element gain aberrations, but is not as powerful at reducing side lobe levels under ideal conditions as the SI-CAB.

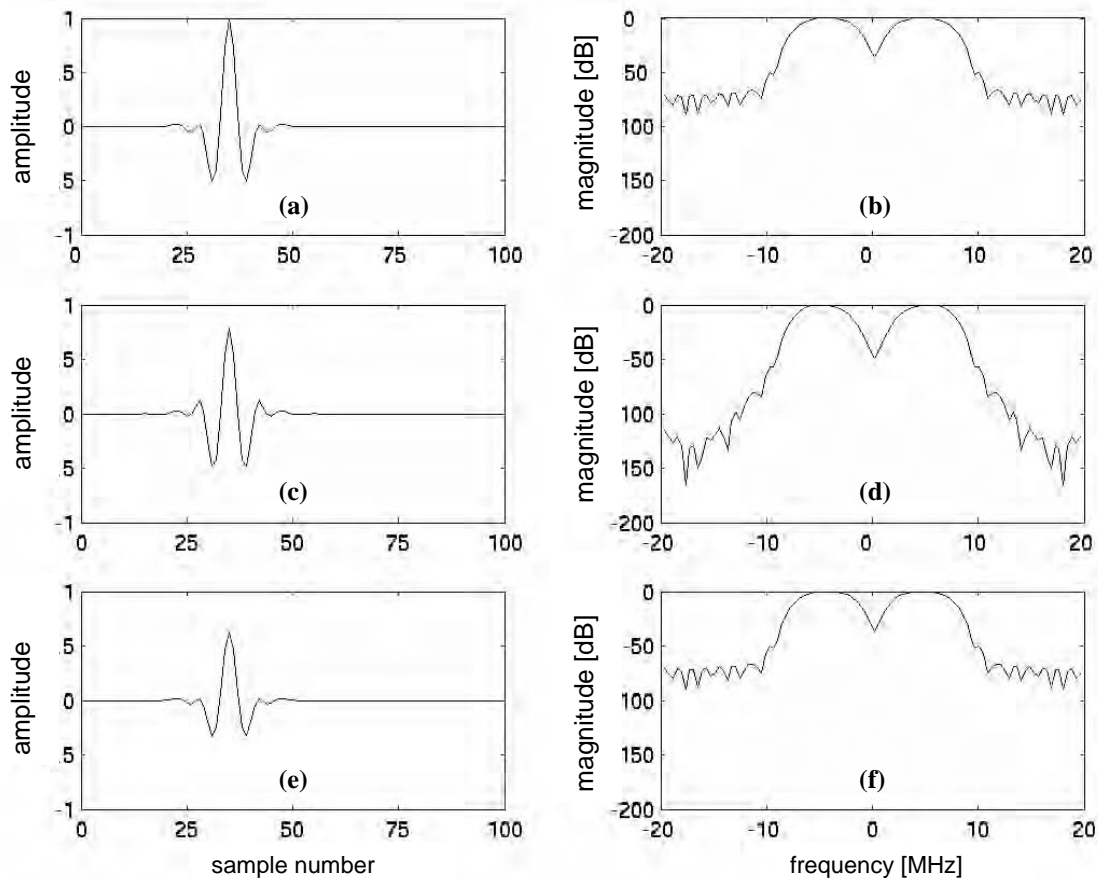


Figure 8. Simulation results for processing of a zero-mean Gaussian plane wave echo. The left panel shows time domain signals for (a) one channel of the input signal; (c) SI-CAB output signal; (e) MI-CAB output signal. The x-axis is sample number and the y-axis indicates amplitude. The right panel shows the frequency content of the signals, where (b), (d), and (f), correspond to the Fourier transform of (a), (c), and (e), respectively. The x-axis is frequency in MHz, while the y-axis gives amplitude in dB.

To illustrate this, we constructed a zero-mean Gaussian plane wave echo with the same center frequency as the FIR filter (and therefore the transducer used to obtain experimental data) to simulate the echo from a focused point target. The input signal was specified as the broadband constructed pulse (shown in Figure 8a) duplicated across seven input channels. Figure 8c displays the time domain output signal from beamforming with the SI-CAB, and Figure 8e displays the MI-CAB output. The right panel of the figure shows the same signals in the Fourier domain.

The MI-CAB output signal in Figure 8f retains almost the same frequency content as the input signal. The time domain amplitude for Figure 8e is slightly lower than the input signal, but this can be corrected through simple scaling and is not believed to indicate poor performance. The SI-CAB output signal shown in Figure 8c is closer to maintaining the input amplitude, and the high frequency components of the input signal (above 10 MHz) are reduced significantly.

For the next simulation, one channel of the input array was scaled to 10% higher than the others, approximating an array gain imperfection. Figure 9a shows the input signal for one of the unaltered channels, and the right panel again presents Fourier domain signals. In this trial, the CAB performance is substantially degraded. The SI-CAB time domain output given in Figure 9c is a strongly modulated version of the input signal. The signal amplitude is orders of magnitude lower than that of the input signal (note the different scale of Figure 9c), which indicates a failure of the algorithm to retain the

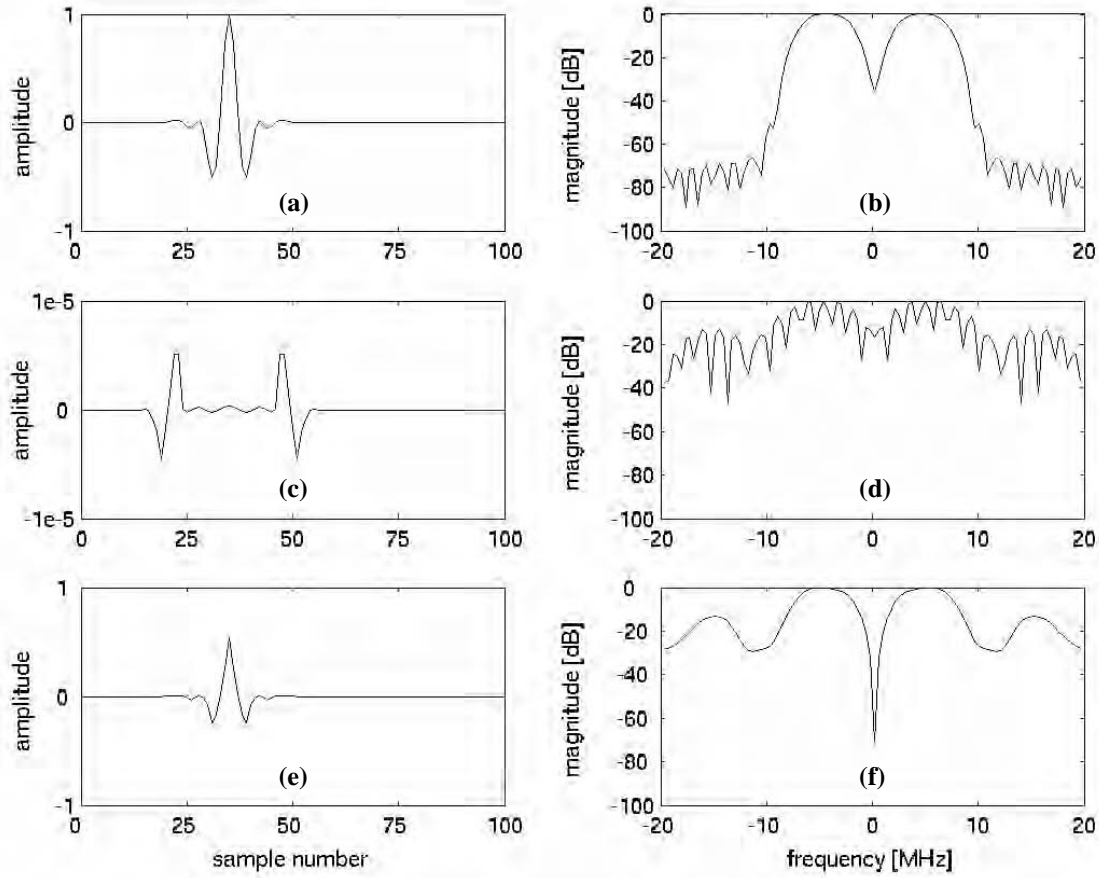


Figure 9. Simulation results for processing of a plane wave echo with one aberrated channel. The left panel shows time domain signals for (a) one unaltered channel of the input signal; (c) SI-CAB output signal; (e) MI-CAB output signal. The x-axis is sample number and the y-axis indicates amplitude. The right panel shows the frequency content of the signals, where (b), (d), and (f), correspond to the Fourier transform of (a), (c), and (e), respectively. The x-axis is frequency in MHz, while the y-axis gives amplitude in dB.

input plane wave effectively. The Fourier domain SI-CAB output of Figure 9d shows modulated frequency content as well as amplified high frequency noise. This result is certainly problematic, as a 10% difference in amplitude on a single channel of experimental data could be expected from electronic noise. To explain this undesirable behavior, the method in which optimal weights are calculated must be revisited. When the SI-CAB receives a signal with large amplitude on one channel, it minimizes the output power while meeting the constraint by imposing a strong negative weight on that channel. This allows the weights across all channels to sum to the required filter coefficient, but does not allow the output sample to adequately reflect the presence of a plane wave signal.

The MI-CAB is more robust to this problem through the smoothing capability of its multiple iterations. Figure 9e shows that the time domain output of the beamformer retains the same general shape as the input signal. High frequency noise is added (see Figure 9f), but the Fourier domain signal remains smooth and unmodulated in the frequency band of interest. This result is encouraging, though future work with the CAB will be directed at further reducing its sensitivity to array imperfections and single channel noise. Initial results in which a constraint is placed on the maximum magnitude of any given weight have been promising.

6. CONCLUSION

Through reduction of off-axis noise, the Constrained Adaptive Beamformer substantially improves both target resolution and image contrast for wire targets and low echogenicity cyst phantoms. The Single Iteration CAB performs best for point resolution and has excellent dynamic capability. The SI-CAB is especially effective for RF data sets using fewer than 128 channels. The Multiple Iteration CAB is more robust than the SI-CAB and has proved to be most appropriate for enhancing contrast resolution.

ACKNOWLEDGEMENTS

We received technical and equipment support from Philips Medical Systems and stipend support from a U.S. Department of Education GAANN grant. We would especially like to thank McKee Poland of Philips Medical Systems for his technical support on this project. This work was further supported by U.S. Army Congressionally Directed Medical Research Program Grant No. DAMD 17-01-10443. Inspiration from this work stems from National Science Foundation Major Research Instrumentation Grant 0079639.

REFERENCES

- [1] D. Zhao, L.N. Bohs, and G.E. Trahey, "Phase aberration correction using echo signals from moving targets. I: Description and theory," *Ultrasonic Imaging*, vol. 14 (2), pp. 97-110, 1992.
- [2] S. Krishnan, K.W. Rigby, and M. O'Donnell, "Adaptive Aberration Correction of Abdominal Images Using PARCA," *Ultrasonic Imaging*, vol. 19 (3), pp. 169-179, 1997.
- [3] O.L. Frost, III, "An Algorithm for Linearly Constrained Adaptive Array Processing," *Proc. IEEE*, vol. 60 (8), pp. 926-935, 1972.
- [4] Widrow, B., and Stearns, S.D., *Adaptive Signal Processing*, Prentice Hall, Upper Saddle River, NJ, 1985.
- [5] Scharf, L.L., *Statistical Signal Processing: Detection, Estimation, and Time Series Analysis*, Addison-Wesley, Reading, Massachusetts, 1991.
- [6] Haykin, S.S., *Adaptive Filter Theory*, 4th ed., Prentice Hall, Upper Saddle River, NJ, 2002.
- [7] Johnson, D.H. and Dudgeon, D.E., *Array Signal Processing*, Prentice Hall, Englewood Cliffs, NJ, 1993.
- [8] J.A. Mann and W.F. Walker, "Constrained Adaptive Beamformer: Initial Results," *Proc. 2002 IEEE Ultrason. Symp.* (in press).
- [9] P.-C. Li, S. W. Flax, E. S. Ebbini, and M. O'Donnell, "Blocked element compensation in phased array imaging," *IEEE Trans. Ultrason. Ferroelectr., Freq. Contr.*, vol. 40 (4), pp. 283-292, 1993.

Synthetic Aperture Methods for Angular Scatter Imaging

D. A. Guenther¹, K. Ranganathan¹, M.J. McAllister¹, K.W. Rigby², and W.F. Walker¹

¹ - Dept. of Biomedical Engineering, University of Virginia, Charlottesville, VA

² - GE Global Research

Abstract – Angular scatter offers a new source of tissue contrast and an opportunity for tissue characterization in ultrasound imaging. We have previously described the application of the translating apertures algorithm (TAA) to coherently acquire angular scatter data over a range of scattering angles. While this approach works well at the focus, it suffers from poor depth of field (DOF) due to a finite aperture size. Furthermore, application of the TAA with large focused apertures entails a tradeoff between spatial resolution and scattering angle resolution. While large multielement apertures improve spatial resolution, they encompass many permutations of transmit/receive element pairs. This results in the simultaneous interrogation of multiple scattering angles, limiting angular resolution.

We propose a synthetic aperture imaging scheme that achieves both high spatial resolution and high angular resolution. In backscatter acquisition mode, we transmit successively from single transducer elements, while receiving on the same element. Other scattering angles are interrogated by successively transmitting and receiving on different single elements chosen with the appropriate spatial separation between them. Thus any given image is formed using only transmit/receive element pairs at a single separation. This synthetic aperture approach minimizes averaging across scattering angles, and yields excellent angular resolution. Likewise, synthetic aperture methods allow us to build large effective apertures to maintain a high spatial resolution. Synthetic dynamic focusing and dynamic apodization are applied to further improve spatial resolution and DOF.

We present simulation results and experimental results obtained using a GE Logiq 700MR system modified to obtain synthetic aperture TAA data. Images of wire targets exhibit high DOF and spatial resolution. We also present a novel approach for combining angular scatter data to effectively reduce grating lobes. With this approach we have been able to push the grating lobes below –50 dB in simulation and effectively eliminate their presence in the experimental wire target images.

Keywords: ultrasound, beamforming, synthetic aperture, angular scatter, K-Space

I. Introduction

Conventional ultrasound imaging systems form B-mode images by combining a series of A-lines that map the acoustic impedance differences present in the interrogated tissue. These images are composed primarily of acoustic backscatter, or those pressure waves that are reflected directly back towards the transmitting aperture. This acoustic backscatter comprises only a fraction of the scattered sound field available. Obviously, pressure waves are scattered at multiple angles in the tissue. Angular scatter imaging attempts to form images from the scattered echoes at angles other than the 180° backscattered path.

Angular scatter is defined using the aperture geometry depicted in Fig. 1. Typically, we refer to acoustic backscatter as being a scattering angle of 180° and angular scattered data occurring at angles less than 180° . The scattering angle, Φ , is measured as the angle between the transmit wave propagation path and the receive wave propagation path.

Although angular scatter has been a topic of research for well over a decade, previous measurements were marred by large fluctuations in the received data. Furthermore, prior measurement systems required piston transducers to be mechanically rotated around the target [1], [2]. While these studies gave great insight into the potential of angular scatter for tissue characterization, their methods cannot be applied to clinical imaging.

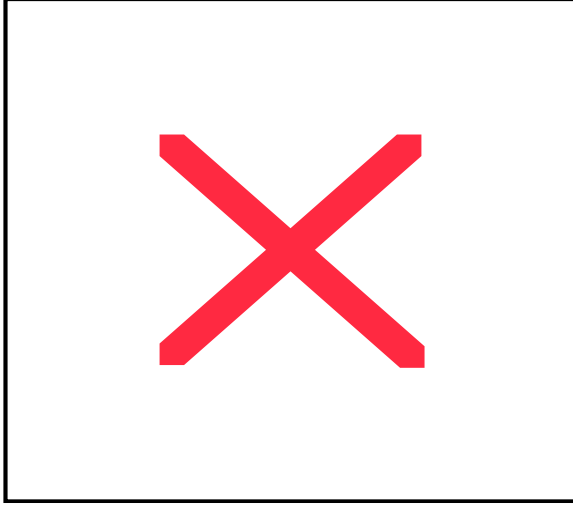


Figure 1: Angular Scatter Geometry

Experiments performed by Robinson [3] and Lacefield [4] used phased array transducers that were either mechanically displaced or divided into subapertures in order to acquire scattered sound field information at angles other than 180° . The phased array transducers maintained high spatial resolution and broad bandwidths. However, the lateral displacement of the receive apertures and the electronic focusing and beamsteering applied resulted in a varying system response with scattering angle. This, in turn, caused rapid speckle decorrelation, making comparison of backscattered B-mode images and angular scatter images extremely difficult. Although these studies yielded many useful insights, failure to coherently acquire the scattered sound field across angles greatly limited their impact.

This paper describes a new method for coherently acquiring backscatter and angular scatter information using a synthetic aperture based approach on a 1D linear array. This novel technique draws upon previous research on the translating apertures algorithm (TAA) [5] and the application of K-space to develop optimal transmit and receive aperture geometries [6]. Synthetic aperture methods allow us to maintain a large effective aperture size for high spatial resolution, utilize a large DOF, and implement the TAA using a single element geometry. The TAA is advantageous because it maintains a constant system PSF with angle, coherently forming images at multiple scattering angles, and thereby making it easier to identify the angular scatter properties of tissue. Previous studies applying the TAA with large apertures to angular scatter imaging found very intriguing outcomes, but images were degraded by very limited DOF. This paper describes a new synthetic aperture method that yields high spatial resolution, high angular resolution, and excellent DOF. While synthetic aperture methods can yield excellent DOF, they also require high spatial sampling rates in the transducer which may not be practical experimentally. The performance of this new algorithm and sample images will be evaluated and presented.

II. Single Element Transmit & Receive Synthetic Aperture

Synthetic aperture methods offer many theoretical advantages, however application in clinical ultrasound has been very limited due to relatively slow acquisition times, computationally expensive image reconstruction, and the potential for motion artifacts. With the advent of faster processors and new ultrasonic research platforms, many of the earlier hardware roadblocks have been overcome. Because technology has improved, synthetic aperture imaging is showing increasing clinical potential [7].

Our method of angular scatter imaging uses a single element synthetic aperture approach to acquire reflected acoustic data at multiple scattering angles. For collecting backscatter data, one specific element is designated for transmit and receive, and that active element is successively translated across the array to synthetically produce an effective aperture. For acquiring angular scattered data, a transmit and receive element pair are identified which define a certain scattering angle. The lateral separation, indicative to this scattering angle, is kept constant as the active elements are translated across the array. In this manner we acquire data at one specific angle for the entire effective aperture; therefore, we avoid the averaging across multiple scattering angles that results from large, focused apertures.

One of the many advantages of synthetic aperture imaging is the ability to dynamically focus received data anywhere with the application of previously calculated time delays. A simple single element synthetic aperture scheme is depicted in Fig. 2. The lateral positions of the transmit element and receive element are denoted x_t and x_r , respectively. The point (x_p, z_p) is the position of the focal point. We can calculate the

one way propagation time for both the transmit and receive pathlengths from geometry. Given these propagation times we can create delay profiles in order to focus the received synthetic aperture RF data. This process is repeated at every point in the resultant image, yielding exquisite spatial resolution and DOF at low f-numbers.

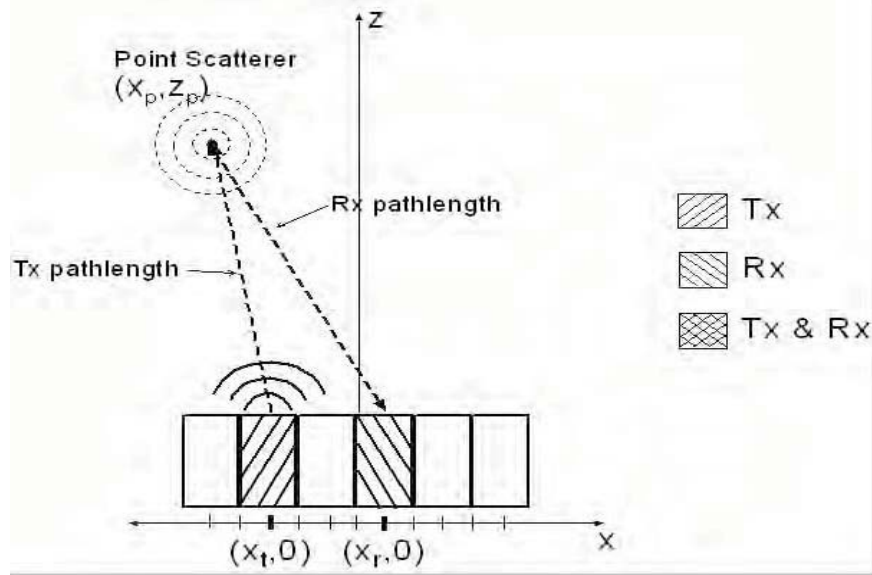


Figure 2: Calculation of propagation times for Single Element Angular Scatter. The transmit and receive pathlengths are calculated from Pythagorean geometry and divided by the assumed sound velocity through the medium. The lateral positions of the transmit element and receive element are denoted x_t and x_r , respectively. The point (x_p, z_p) is the point at which we focus the received data.

III. K-space with respect to Scattering Angle

Linear systems can be characterized by their frequency domain representation. In many cases, such an approach provides more intuitive analysis of particular problems. Signal analysis and filtering are regularly performed in the frequency domain because of this utile representation. K-space is a frequency domain depiction of ultrasonic imaging systems that is extremely useful in graphically demonstrating the spatial frequency response of transmit and receive apertures. Lerner and Waag used K-space to differentiate the scattering response of the target to the response of an aperture [8].

Ultrasonic image formation is inherently a multidimensional problem, and for our discussion here we simplify it to two dimensions, namely lateral spatial frequency and scattering angle. Using the synthetic aperture based approach described above we can see how different transmit/receive element geometries sample K-space with respect to scattering angle. In order to determine the lateral spatial frequency, θ , that a given transmit/receive aperture pair interrogates, we perform the convolution of the scaled and reversed transmit aperture with the scaled and reversed receive aperture [6]. The scattering angle, ϕ , is calculated as the angle between the transmit wave propagation path and the receive wave propagation path. Fig. 3 below depicts a 1D linear transducer array and the simple case of single element synthetic aperture for acquiring acoustic backscatter. The set of axes to right of the array plots K-space and scattering angle. The Θ axis is the lateral spatial frequency axis and it intersects the Φ -axis (scattering angle) at 180° . Translation of this Tx/Rx aperture to the left would sample a more positive lateral spatial frequency and a scattering angle, Φ , still on the Φ axis. Fig. 4 depicts a transmit and receive aperture pair where the receive element is shifted one element to the right of the transmit element. This is a special case of the TAA where we keep the transmit aperture fixed and translate the receive aperture. We refer to this case as a TAA half element step. Notice that this geometry samples a different lateral spatial frequency than the backscattered case (hollow diamond). It also collects angular scattered data at an angle less than 180° .

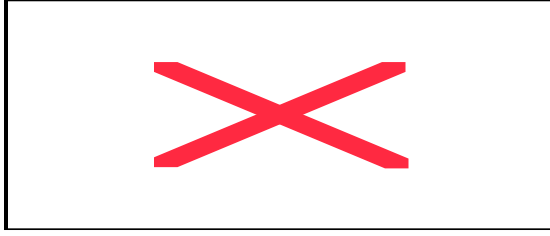


Figure 3: Synthetic Aperture based approach for acquiring acoustic backscatter. The Θ axis intersects the Φ axis at 180° .

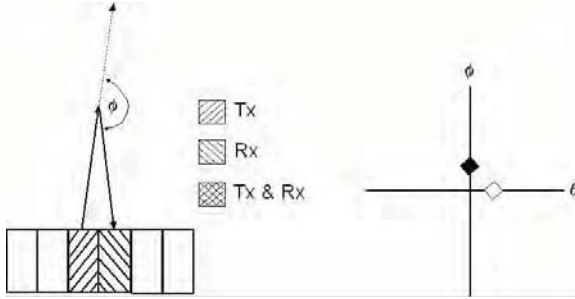


Figure 4: Synthetic Aperture Angular Scatter depicting the half element TAA where the receive aperture has been translated to the right. Notice that this particular geometry samples a different lateral spatial frequency than backscatter (hollow diamond) as well as a scattering angle less than 180° degrees.

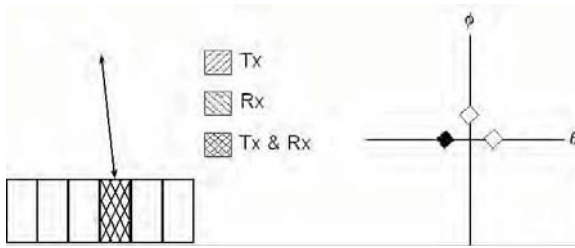


Figure 5: Translation of the acoustic backscatter geometry depicted in Fig. 3. Notice that this setup samples the opposite lateral spatial frequency, but the same scattering angle.

We can sample a full line of K-space at a particular scattering angle by translating our transmit/receive aperture geometry across the array. If we translate the backscattered geometry depicted in Fig. 3 we arrive at the situation shown. This geometry samples the opposite lateral spatial frequency of that shown in Fig. 3 when both apertures are dynamically focused at the same point in space. We can continue translating this aperture across the rest of the array and acquire backscattered data at increasingly negative lateral spatial frequencies. For the sake of completeness, consider the case of the half element TAA where the receive aperture is translated to the **left** of the transmit aperture as shown in Fig. 6. This setup samples the same lateral spatial frequency as the earlier half element TAA scheme yet acquires information at the negative scattering angle with respect to that in Fig. 4. It is also important to note that the lateral spatial frequencies sampled by the half element TAA geometries fall in between those sampled by the backscattered case. Therefore, combining the backscattered data with the half element TAA data allows an increase in K-space sampling rate.

Fig. 7 applies the full element TAA relative to the backscattered case depicted in Fig. 3. Both geometries sample the same lateral spatial frequency; however, the full element TAA geometry acquires information at a scattering angle that is smaller than both 180° and the half element TAA scattering angle.

As stated before, we can acquire multiple lines of K-space at a single scattering angle by translating backscatter, half element and full element TAA aperture geometries across the full linear array. It should be clear that a well designed pulse sequence can fully populate K-space across scattering angles and spatial frequencies.

The fully populated K-space diagram depicted in Fig. 8 shows how we can effectively sample lateral spatial frequencies at multiple scattering angles by implementing backscatter, half element TAA and full element TAA geometries. The black diamonds designate those samples acquired with



Figure 6: Half element TAA geometry where the receive aperture has been translated to the left of the transmit aperture. This geometry samples the same lateral spatial frequency as the previous half element TAA scheme depicted in Fig. 4 and acquires the corresponding negative scattering angle.

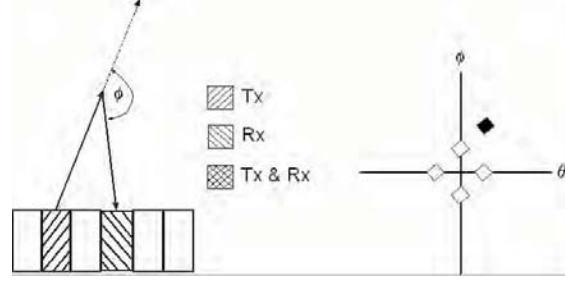


Figure 7: Full element TAA geometry where the algorithm has been applied relative to the backscattered case depicted in Fig. 3. Notice how this setup samples the same lateral spatial frequency as the backscattered case but at a scattering angle that is less than 180° and less than the half element TAA scattering angle.

backscatter and half element TAA with translation of the receive element to the right of the transmit element. If we combine these two data sets we can increase our lateral spatial frequency sampling with a minor loss in angular resolution. Increasing our lateral spatial frequency sampling will reduce or effectively eliminate the grating lobe artifacts, which result from inadequate K-space sampling. The degree to which we can reduce grating lobes is explored in the simulation and wire target experiments shown below.

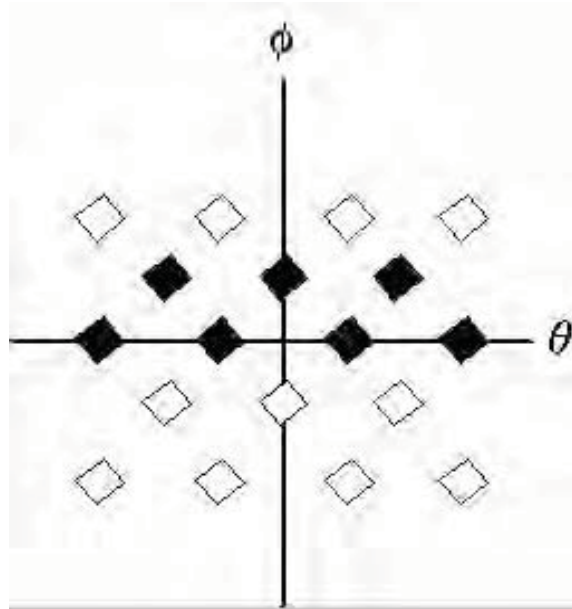


Figure 8: Fully populated K-space is acquired by translating the backscatter, half and full element TAA aperture geometries across the array. The black diamonds designate backscattered samples and the samples acquired with the half element TAA with the receive aperture translated to the right of the transmit element.

IV. Simulation Methods

Synthetic Aperture Angular Scatter (SAAS) simulations were performed in FIELD II [9] by modeling a 192 element linear array with a center frequency of 6 MHz and a Gaussian enveloped, sinusoidal impulse response. The array was curved in elevation to mimic the effect of an acoustic lens in this dimension. The

data was dynamically focused over a range from 2 mm to 3.2 cm. Apodization schemes were applied to acquire angular scatter information ranging from 180° to 156° . The goal of these simulations was to test the ability of our algorithm to reduce grating lobe artifacts. Beamplots were formed and graphed on a dB scale to determine the magnitude of the grating lobes. For the backscattered case in Fig. 9 the grating lobes appear at the level of -23 dB. By summing the backscatter information with the half element TAA data (179°) we reduce the grating lobes to -67 dB. This 44 dB decrease corresponds to a reduction of the grating lobe magnitudes by a factor greater than 100. The scattering angles of 178° , 176° , and 168° correspond to TAA transmit and receive element shifts of 1, 2, and 6 elements, respectively. The scattering angles of 177° , 175° , and 167° correspond to the half element TAA where the Rx aperture is translated one more element to the right. It should be emphasized that at higher scattering angles we see a monotonic increase of the grating lobes (168° grating lobes at -47 dB). This likely results from the plane wave approximations inherent in our K-space analysis, however this is a phenomenon we are continuing to explore.

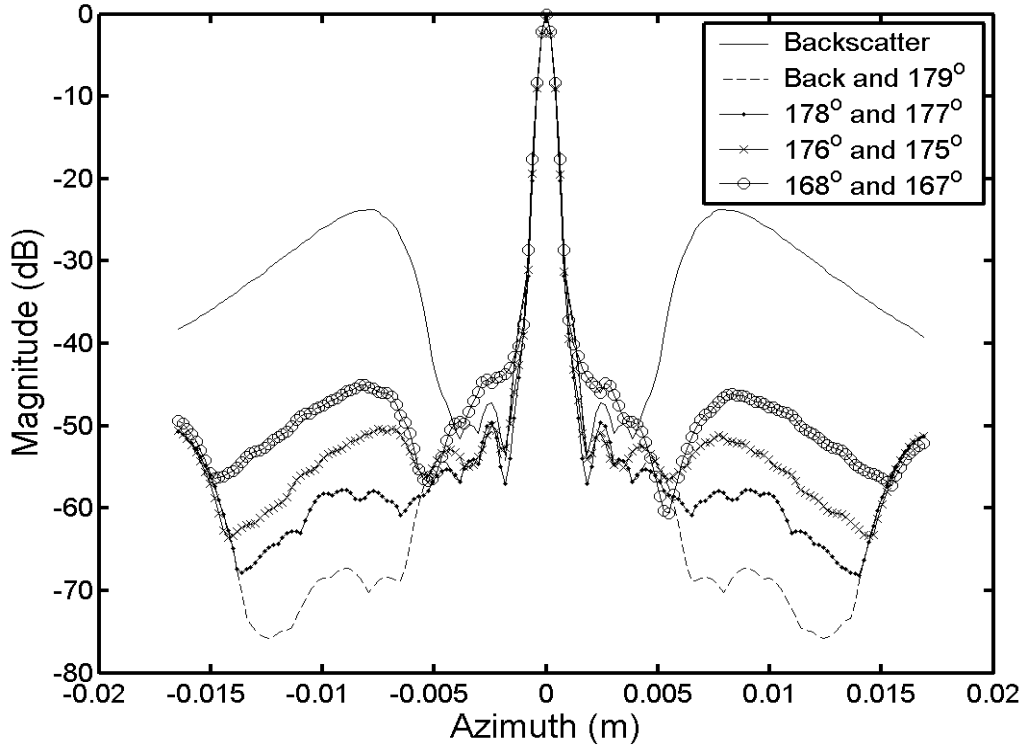


Figure 9: Simulation Beamplots showing the reduction in grating lobes by applying the TAA half element step algorithm. Grating lobes in the backscattered case were reduced in magnitude by a factor of over 100.

V. Experimental Methods

Wire target experiments with a $20\mu\text{m}$ steel wire phantom placed in a water tank were conducted to validate the simulation results. A GE Logiq 700MR system with the 739-L 192 element linear probe was used in these experiments. The same SAAS transmit and receive geometries described above were carried out to acquire data over a range of scattering angles. Beamforming was accomplished by applying a precalculated set of focal delays and using dynamic transmit and receive apodization. The resulting experimental beamplots are graphed with the simulation results. In Fig. 10 we see that the backscattered beamplots for the simulation and wire target experiments show evidence of grating lobes around the -23 dB level. Applying the half element TAA strategies reduced the experimental grating lobes to at least -50 dB. We believe they were actually lower, but were obscured by the system noise floor at approximately -50 dB.

The half element SAAS scheme greatly reduced the grating lobes. This result is also shown in the log compressed wire target images (Fig. 11).

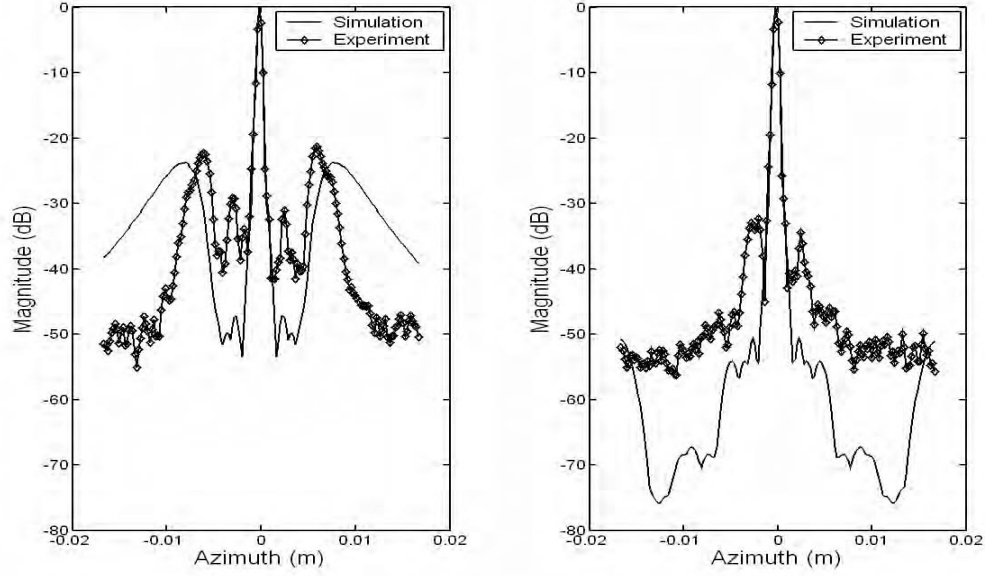


Figure 10: Lateral beamplots for simulation and experimental data showing the reduction of grating lobes achieved when applying the TAA half element step. Acoustic backscatter (left) is combined with the TAA half element step to produce the beamplots on the right.

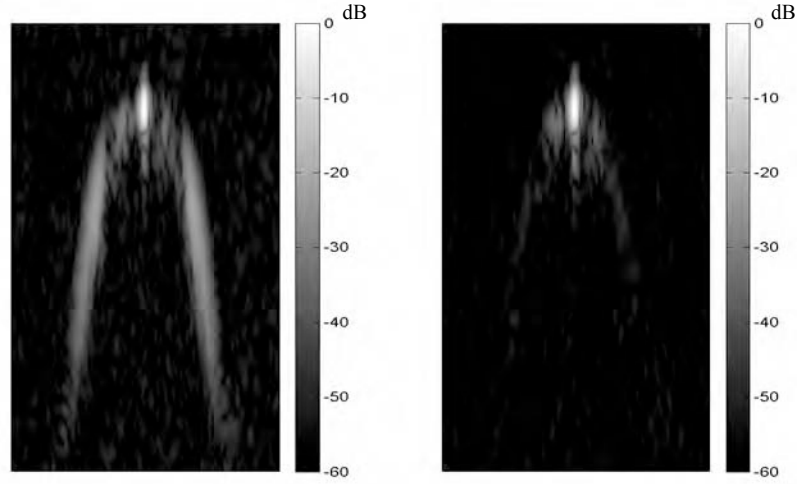


Figure 11: Log compressed envelope detected data for experimental wire targets: Backscatter (left) and Backscatter plus TAA half element step (right). Notice the absence of the grating lobes in the image on the right.

VI. Discussion

Because we transmit and receive on a single transducer element, we essentially sonicate and acquire information from all space with an unfocused sound wave. Superposition allows us to synthetically increase our effective Tx/Rx aperture sizes to yield excellent spatial resolution. For our experiments we

synthesized a 165 element array corresponding to an effective aperture width of 33.5 mm. The applied synthetic dynamic focusing maintains exquisite DOF. It should be noted that due to data acquisition limitations on our GE system, our synthetic aperture approach requires 165 transmissions in order to form one B-mode image at a single scattering angle. However, a system that could acquire the RF data in parallel on multiple channels could collect **all** the scattering angles with the same 165 transmissions. Therefore the potential exists to maintain high frame rates.

The synthetic aperture based approach for acquiring angular scatter information described in this paper is an effective way of reducing the grating lobe artifacts. Oftentimes in linear arrays the element pitch is insufficient in regards to the $\lambda/2$ spacing requirement, and grating lobes appear in the image. The SAAS imaging approach using the TAA half element step samples K-space in between the backscatter and full element TAA K-space samples. Therefore, we can theoretically mitigate the effects of a poorly sampled linear array with the superposition of two scattering angles. The oversampling of K-space in the spatial frequency domain dissipates the grating lobes in the image domain.

The performance of our angular scatter algorithm will ultimately be influenced by the angular sensitivity of the individual elements. With our synthetic 165 element effective aperture we are inherently limited to a max scattering angle of 156° (-24°) which is well within the bounds of angular sensitivity for the elements in our array. The fall off in signal magnitude due to element angular response is something that will have to be accounted for when comparing images. The fall off in signal magnitude due to tissue angular response may serve as a simple metric for tissue characterization. Distinguishing between these two effects is an area of continuing research.

With decreased grating lobes, we expect to gain useful results when forming angular scatter images. Assuming Rayleigh scattering in the interrogated medium, angular scatter imaging will detect fundamental material property information. A Rayleigh scatterer has a monopolar omnidirectional scattering component and a dipolar angle dependent scattering component [5]. Therefore angular scatter images can be formed that highlight these different scattering components and present a natural source of contrast for tissue differentiation in terms of compressibility (angle independent) and density (angle dependent). And since the TAA reasonably maintains the system PSF we should strictly be imaging the response to scattering angle and observe little or no speckle decorrelation. In contrast, previous studies compared angular scatter images that did not maintain the system PSF and thus were comparing incoherent images of the same target rather than detecting the true angular response of the interrogated medium [3], [4].

Robinson showed that the -45° angular scatter lateral beamplots exhibited a significant improvement in lateral resolution compared to the backscattered beamplots. In this study with SAAS imaging using the TAA we do not notice any major improvements in lateral resolution. One possible explanation for this is that our system interrogates smaller scattering angles. Furthermore, the TAA maintains a similar PSF across scattering angles; whereas, the Robinson angular scatter PSF would have a planar tilt due to the receive aperture geometry, which would in turn improve lateral resolution. Although we do not see any observable improvement in lateral resolution, the acquisition of coherent angular scatter information should lead to improved comparison between angular scatter image sets.

VII. Conclusion and Future Work

A synthetic aperture based imaging approach for acquiring angular scatter data was described and methods for reducing grating lobe artifacts were investigated. By applying a novel K-space motivated algorithm that results in optimal transmit/receive aperture displacements, we can increase our lateral spatial frequency sampling on an otherwise undersampled linear array. The beamplots show that for the backscattered case the grating lobes rise to a level around -23 dB but can be reduced by a factor greater than 100 (-67 dB) when applying our method.

Since the parasitic grating lobes are no longer an issue in the SAAS images we expect to reap great benefits in contrast when forming angular scatter images. The *in vivo* potential of angular scatter is significant. Contrast improvements are possible for microcalcifications, atherosclerotic plaques, thyroid diseases, and cysts. Improved contrast from angular scatter imaging would yield better diagnosis.

Acknowledgements

We would like to acknowledge the support of the Susan G. Komen Breast Cancer Foundation and the United States Army Congressionally Directed Medical Research Program.

References

- [1] W. J. Davros, J. A. Zagzebski, and E. L. Madsen, "Frequency-dependent angular scattering of ultrasound by tissue-mimicking materials and excised tissue," *J. Acoust. Soc. Amer.*, vol. 80, pp. 229-237, 1986.
- [2] J. A. Campbell and R.C. Waag, "Measurements of calf liver ultrasonic differential and total scattering cross sections," *J. Acoust. Soc. Amer.*, vol. 75, pp. 603-611, 1984.
- [3] M. T. Robinson and O. T. Von Ramm, "Real-time angular scatter imaging system for improved tissue contrast in diagnostic ultrasound images," *IEEE Trans. Ultrason., Ferroelect., Freq. Contr.*, vol. 41, 1994.
- [4] J. C. Lacefield, "Angular scatter ultrasound imaging using separated arrays," Ph.D. dissertation, Duke University, 1999.
- [5] W. F. Walker, "C- and D-Weighted Ultrasonic Imaging Using the Translating Apertures Algorithm," *IEEE Trans. Ultrason., Ferroelect., Freq. Contr.*, vol. 48, 2001.
- [6] W. F. Walker and G. E. Trahey, "The Application of K-Space in Pulse Echo Ultrasound," *IEEE Trans. Ultrason., Ferroelect., Freq. Contr.*, vol. 45, 1998.
- [7] J. A. Jensen et al., "Experimental ultrasound system for real time synthetic imaging," *Proc. IEEE Ultrason. Symp.*, vol. 2, pp. 1595-1599, 1999.
- [8] R. M. Lerner and R. C. Waag, "Wave space interpretation of scattered ultrasound," *Ultrasound Med. Biol.*, vol. 14, pp. 97-102, 1988.
- [9] J. A. Jensen. "Field: A program for simulating ultrasound systems," *Med. Biol. Eng. Comp.*, col. 10th Nordic-Baltic Conference on Biomedical Imaging., 4(1): 351-353, 1996.

Synthetic Aperture Angular Scatter Imaging: System Refinement

D. A. Guenther, K. Ranganathan, M. J. McAllister,
and W. F. Walker
Department of Biomedical Engineering
University of Virginia
Charlottesville, VA 22908
dag2m@virginia.edu

K.W. Rigby
GE Global Research
Niskayuna, NY 12309

Abstract—Angular scatter imaging has been proposed as a new source of image contrast in medical ultrasound and as a parameter for tissue characterization. We describe a new method of acquiring angular scatter data that combines the Translating Apertures Algorithm (TAA) with synthetic aperture methods to coherently obtain angular scatter information with high resolution in both space and scattering angle. This method, which we term Synthetic Aperture Angular Scatter (SAAS) imaging effectively applies the TAA to single array elements and then focuses the data synthetically to form high resolution images at precisely defined scattering angles.

In this paper, we present experimental results implementing SAAS on a GE Logiq 700MR system. We applied the SAAS method to form angular scatter images of a 5-wire depth of field (DOF) phantom, a tissue mimicking 3-wire phantom (steel, nylon, and cotton) and *in vivo* human thyroid. We present results from this data and discuss the degree of uniformity necessary in element response for successful SAAS imaging. Results from these experiments show new image information previously unavailable in conventional B-mode images and suggest that angular scatter imaging may have applications in the breast, thyroid, and peripheral vasculature.

Keywords—beamforming; synthetic aperture; angular scatter

I. INTRODUCTION

Human tissues exhibit variation in scattering response when the angle between transmission and reception is changed. These differences result from intrinsic acoustic properties and tissue microstructure, both of which might provide valuable information for tissue characterization and to aid in diagnosis [1]. Conventional ultrasound B-mode images are formed primarily of acoustic backscatter; and thus fail to take advantage of the prodigious amount of information that has been scattered away from the transducer. Angular scatter imaging attempts to form images from the scattered echoes available at angles other than the 180° backscattered path.

An ideal angular scatter system should have but is not limited to the following characteristics:

- collect data with high angular and spatial resolution
- easily access an acoustic window on the patient
- acquire angular scatter data coherently

This paper describes a new method for coherently acquiring backscatter and angular scatter information using a synthetic aperture approach on a 1D linear array. Utilizing k-space techniques and the TAA, our method allows us to maintain high spatial resolution, high angular resolution, and large DOF using simple single element geometries. Problems encountered in previous systems (a varying system response with scattering angle) are minimized with the TAA, and the limited DOF of previous TAA measurements with multielement focused apertures are overcome with synthetic aperture dynamic focusing techniques. Although many favorable system characteristics are offered by SAAS, this method requires fine element spacing in the transducer and demands a high degree of element response uniformity, both of which are less critical for conventional beamforming.

II. THEORY

A. SAAS geometry and k-space

Our angular scatter system approach is intuitively understood and described in k-space. K-space is a frequency domain depiction of ultrasonic imaging systems that is extremely useful in graphically demonstrating the spatial frequency response of transmit and receive apertures. We refer the reader to previous work in [2]–[4] for a complete analysis of our k-space method and provide an abbreviated synopsis here.

Although full analysis is a multidimensional problem, we simplify our k-space analysis to two dimensions: lateral spatial frequency, θ , and scattering angle, ϕ . The scattering angle k-space response of a linear array applying conventional beamforming methods where a subset of elements is used on transmit and receive is depicted in Fig. 1. The axes to the right of the transducer show how this method samples our k-space domain. The θ -axis intersects the ϕ -axis at $\phi=180^\circ$. We see that conventional beamforming acquires a range of lateral spatial frequencies and multiple scattering angles. Applying the TAA to the conventional case in Fig. 1 results in the response depicted in Fig. 2. We notice that the footprint of the TAA response is the same, interrogating identical lateral spatial frequencies, and it samples some new scattering angles. However, the use of the TAA and multielement apertures is not ideal because these methods interrogate multiple scattering angles, blurring system resolution in this dimension.

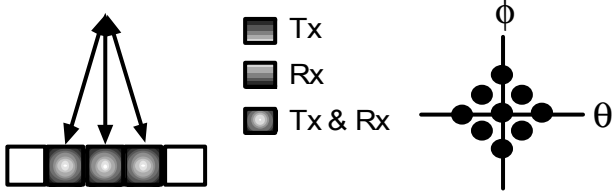


Figure 1. Angular scatter k-space response using conventional beamforming methods with multielement, focused apertures.

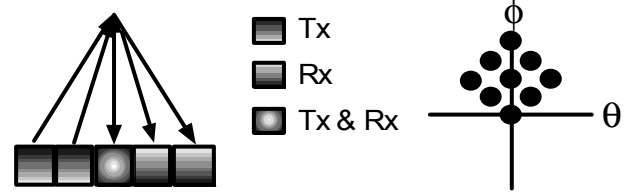


Figure 2. Angular scatter k-space response for a 1D array utilizing multielement apertures and the TAA to maintain system psf.

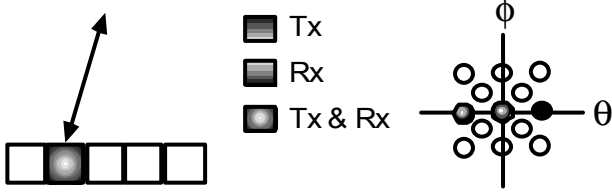


Figure 3. SAAS 180° pure backscatter geometry. We can acquire k-space data at a specific scattering angle (shaded circles) by translating the active element across the array.

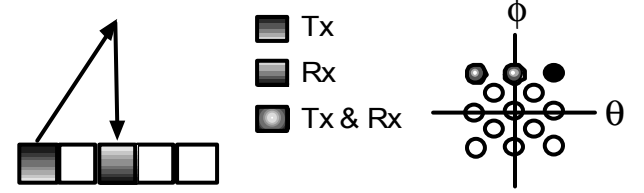


Figure 4. SAAS TAA geometry. We can acquire k-space data at the same lateral spatial frequencies as the backscatter case but at scattering angles less than 180°.

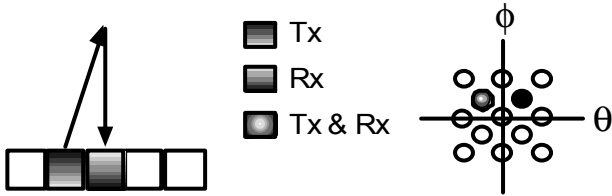


Figure 5. SAAS TAA half step geometry. We can acquire angular scatter data that improves our lateral spatial frequency sampling when summed with the backscatter or TAA full step data.

We can sample precise scattering angles in k-space at varying lateral spatial frequencies by translating active transmit and receive synthetic aperture geometries across the array. Using the SAAS 180° backscatter geometry depicted in Fig. 3, we notice that we can acquire data at a specific scattering angle (black circle). Translating the active element to the right samples increasingly negative lateral spatial frequencies (shaded circles). Likewise, we can apply the TAA to our SAAS 180° case as shown in Fig. 4. This geometry samples the same lateral spatial frequency as the backscatter case but acquires data at a scattering angle that is less than 180°. The modified TAA half step (Fig. 5) allows us to improve our lateral spatial frequency sampling thereby suppressing grating lobes. This improvement comes with a minor reduction in scattering angle resolution. It is clear from this discussion that our SAAS scheme can achieve excellent angular resolution and collect angular scatter data coherently. The geometries discussed were used in simulations and experiments in order to acquire and analyze SAAS data at varying angles with axial range.

B. Beamforming to improve psf uniformity

Angular scatter data can be processed in a multitude of ways. Currently we have focused on forming D-weighted images, a process outlined in [5], which highlight intrinsic density differences between the target and the background. Although graphically useful, formation of D-weighted images requires subtracting two sets of data acquired at different

scattering angles. This process amplifies the noise in the image and is extremely susceptible to slight variations in system psf.

Acquiring angular scatter data coherently is arguably the most important angular scatter system characteristic. The degree of psf uniformity across scattering angles required is rigorously investigated in this paper. We have refined and adjusted our system to maintain a well correlated psf across scattering angles ($\bar{\rho} = .9979 \pm .0014$). Refinements included the modified TAA half step previously mentioned and accounting for variations in individual element responses. As shown later, element nonuniformities adversely affect our ability to form D-weighted images.

III. EXPERIMENTS

We performed two sets of wire target experiments using our GE Logiq 700MR system modified to acquire SAAS data. The 739-L 192 element linear probe was used in these experiments. The first utilized a 10% Acrylamide ($c \approx 1545$ m/s) phantom with five 20 μ m steel wire targets ranging axially every centimeter from 1.7 cm to 5.5 cm and spaced laterally every 0.7 cm. Apodization schemes were applied to acquire angular scatter data ranging from 180° to 170° at 3.0 cm. The goal of these experiments was to quantify the grating lobe suppression capabilities of the modified SAAS algorithm and to observe the increased DOF. The data was apodized and dynamically focused on transmit and receive over a range from 1.5 cm to 6.7 cm.

The second set of wire target experiments conducted utilized a 3-wire (steel, nylon, and cotton) 10% Acrylamide phantom with enough Sephadex® to elicit fully developed speckle. The 3 wires were set at a depth of 3 cm after being degassed for 5 hours. Angular scatter data was acquired ranging from 180° to 170°. Difference weighted (D-weighted) images were formed from the resulting 10 different scattering angle data sets. Note that one angular scatter data set is the summation of two independent angles in order to improve spatial sampling. The stainless steel type 304 wire has a

published density, ρ_s , of 7.9 g/cm^3 and a diameter of $20 \text{ }\mu\text{m}$. The diameters of the nylon suture and cotton thread were $150 \text{ }\mu\text{m}$ and $100 \text{ }\mu\text{m}$, respectively. The steel's density is much higher than the assumed density of cotton ($\rho_c = 1.5 \text{ g/cm}^3$) and ophthalmic nylon suture ($\rho_n = 1.1 \text{ g/cm}^3$). The density of the Acrylamide phantom was assumed to be 1.02 g/cm^3 [6]. Given these density values, we expect to see no discernible differences between the wires in conventional ultrasound B-mode images but expect that the steel (most dense) will show up the brightest in the D-weighted image. Since the nylon and Acrylamide have similar densities, the nylon wire should "disappear" in the D-weighted image. Finally, preliminary angular scatter data of *in vivo* human thyroid was collected and sample images are presented.

IV. RESULTS AND DISCUSSION

Fig. 6 below shows log compressed B-mode images of the 5-wire phantom. The image on the left is of pure backscatter data and the image on the right is backscatter plus TAA half step data highlighting the suppression of the grating lobes.

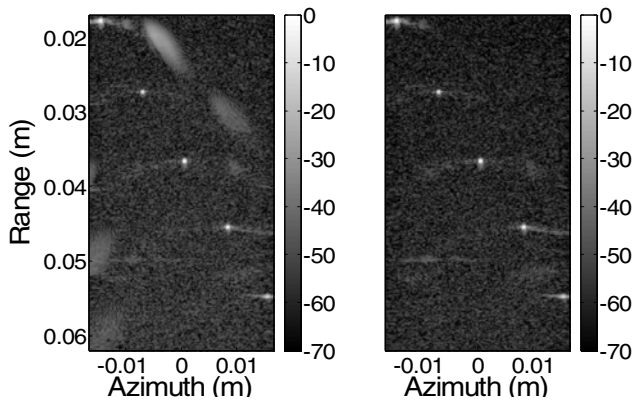


Figure 6. 5-Wire log compressed B-mode images of backscatter (left) and backscatter plus TAA half step (right).

The -6dB resolution for each of the wires in the backscatter plus TAA half step image from top to bottom were: $486 \text{ }\mu\text{m}$, $406 \text{ }\mu\text{m}$, $411 \text{ }\mu\text{m}$, $435 \text{ }\mu\text{m}$ and $645 \text{ }\mu\text{m}$. These values highlight the excellent DOF with the synthetic aperture focusing technique. The deviation in the top and bottom wires is presumably due to the wires' lateral position and the apodization function falling off the side of the aperture.

It was empirically observed that element nonuniformities in the experimental system were degrading psf uniformity across scattering angles. These element nonuniformities were manifesting themselves as small time delays ($\sim 2.2 \text{ ns rms}$) and amplitude variations ($\sim 15\%$ deviation about the mean). The element delays could be determined empirically and were noted to be constant across trials and acquisitions; therefore, they could be corrected. The amplitude variations across the aperture on the other hand did not have any consistency with range, trial, or scattering medium; thus they could not be accounted for. This anomalous behavior is an area of ongoing investigation.

In order to fully appreciate the effects of the various system nonuniformities note the following figures which demonstrate

how these deviations affect sidelobe level and position. In Fig. 7 the pure backscatter B-mode image acquired from a wire target is shown and to the right is the beamplot taken as the maximum value down each A-line. The next figure (Fig. 8) is backscatter plus the TAA half angle data, which was added to suppress the grating lobes. The associated beamplot is shown along with the pure backscatter beamplot (dashed line). The grating lobes are suppressed below the noise floor (-50 dB).

Assuming that our point target radiates spherical waves upon insonification, we can theoretically fit an amplitude profile that follows $\cos(\psi)/R$ to the received channel rf data, where ψ is the angle between an element on the aperture plane to the point source on the measurement plane, and R is the distance between these two points [7]. Pulse-echo image formation requires this amplitude obliquity term to be squared. Given this profile we can account for the element amplitude variations across the aperture and observe the effects on sidelobe level once these deviations are corrected for. The image in Fig. 9 shows the result of element time delay and amplitude compensation. The sidelobes in the beamplot have been reduced to below -40 dB . However, as mentioned earlier the amplitude variations were not deterministic and could not be compensated for in speckle targets.

To further investigate the effects of amplitude variation on psf uniformity, FIELD II [8] simulations were conducted that mimicked our experimental system. The control rf amplitude profile was set to the previously mentioned spherical wave formulation and then amplitude variations were applied with a normal distribution and maximum deviation of 2.5% , 5% , 10% , and 20% about the mean. 180° backscatter and the TAA half element step data were summed to reduce grating lobes. Lateral beamplots were made to observe the effects of these variations on sidelobe level and position.

The simulation beamplots in Fig. 10 show that amplitude variations have dramatic effects on sidelobe level and position. These sidelobe variations will likely dominate useful scattering information in D-weighted images. It is evident that element response amplitude variations across the aperture should deviate no more than 5% about the mean in order to effectively form angular scatter images. We empirically observe amplitude variations on the order of 15% deviation about the mean in our current system, and although these variations are masked by redundancy in conventional beamforming they accumulate and propagate through synthetic aperture techniques. We are currently exploring methods to compensate for these effects.

Regardless of the aforementioned system nonuniformities, we have been able to successfully form D-weighted images with some scattering angle data sets. Fig. 11 depicts three images of the 3-wire phantom. The steel, nylon and cotton wires are laterally spaced left to right, respectively. The top image of pure backscatter with associated half angle shows that the cotton wire is the brightest target followed by steel and then nylon. The middle image is a D-weighted image between a backscatter data set and 176° . The brightest target in this image is the **sidelobe** of the steel wire. This D-weighted image is being dominated by the sidelobe noise due to the psf nonuniformities arising from varying element responses. The

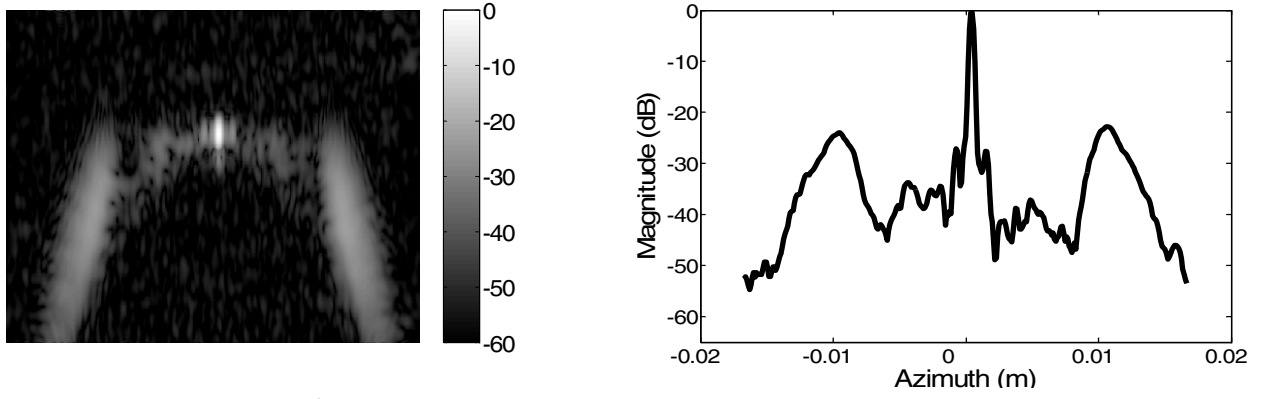


Figure 7. Log compressed 180° SAAS image of a wire target (left) and associated beamplot (right). Sidelobe levels are around -27 dB.

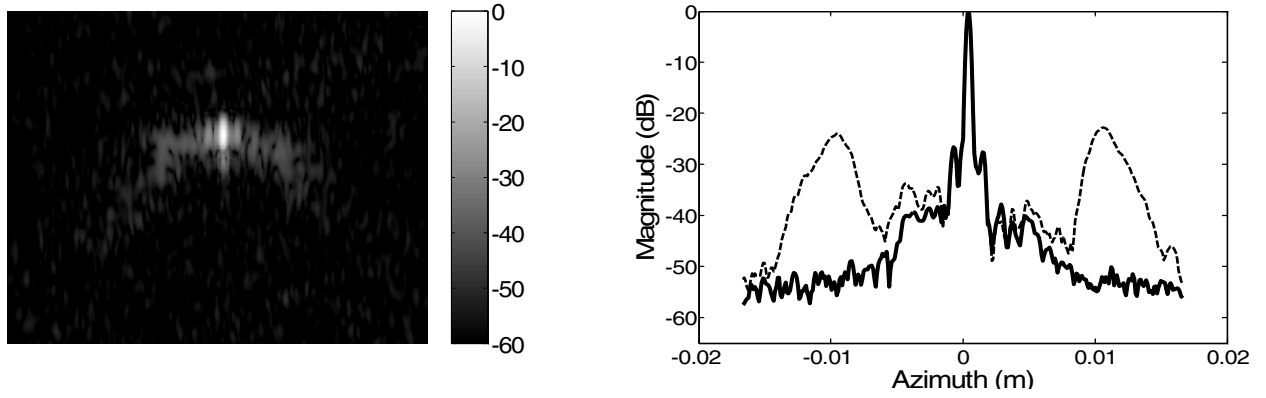


Figure 8. Log compressed pure backscatter plus TAA half angle image of a wire target (left) and the associated beamplot (right). The original beamplot from Fig. 7 is the dashed line. Notice the reduction of the grating lobes below the noise floor (-50 dB).

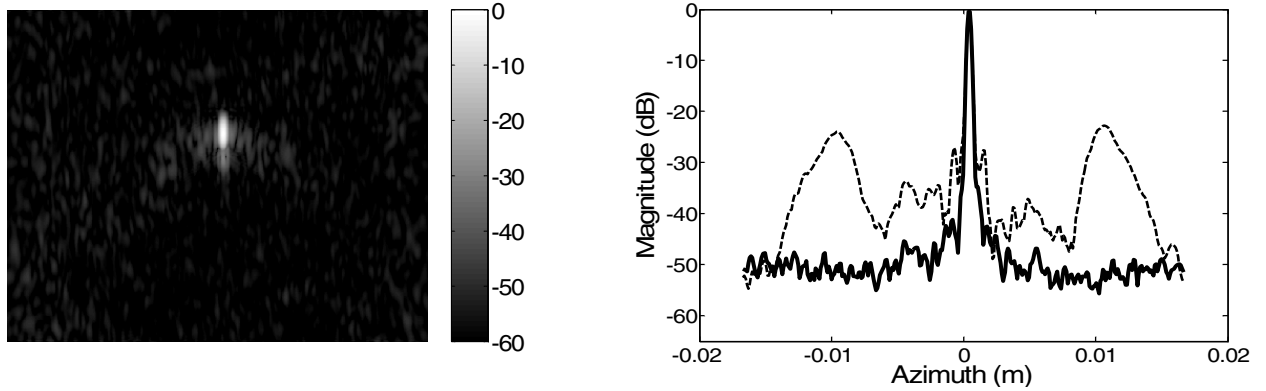


Figure 9. Log compressed B-mode image of wire target after element delay and amplitude compensation (left) and the associated beamplot (right). The original beamplot from Fig. 7 is the dashed line. Notice the reduction of the sidelobes to -41 dB.

bottom image is a successful D-weighted image where the steel wire is the brightest target. Also notice that the nylon wire has essentially “vanished” since its density is nearly identical to the Acrylamide background. The cotton wire intensity has also decreased. The steel wire’s intensity increased 10 dB over the cotton wire between the original B-mode and successful D-weighted images, highlighting the contrast available in angular scatter imaging.

Fig. 12 depicts *in vivo* human thyroid images from a male volunteer. The carotid artery can be seen in the bottom left and

the trachea in the bottom right. The thyroid is the gray mass superficial to the trachea. The top image is a conventional log compressed B-mode image of 180° backscatter and the associated TAA half angle. The bottom image is a D-weighted image between 180° and 176°. Although these images suffer from poor SNR, notice the suppression of the bright scatterer lying in the ring of D-weighted image. Although intriguing, this “bright scatterer” could be a specular reflection returning from a muscular interface. Clearly we need to improve our SNR in SAAS imaging *in vivo*. This is an area of continuing research.

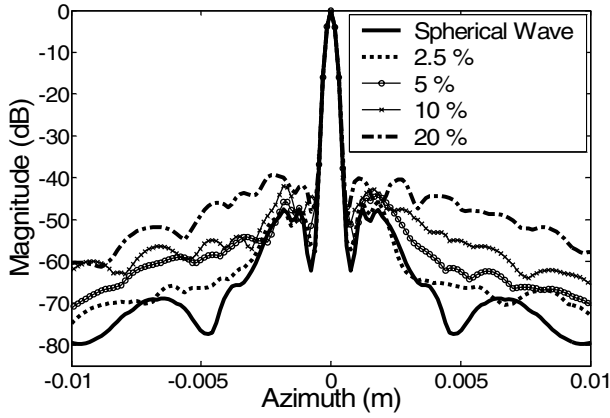


Figure 10. Simulation beamplots investigating amplitude variations.

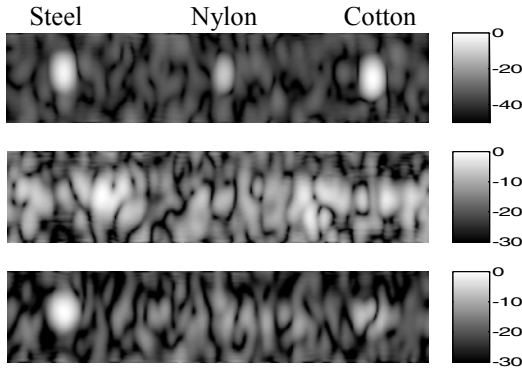


Figure 11. SAAS 180° B-mode image of a 3-wire phantom (top). The middle image is an unsuccessful D-weighted image that is being dominated by the steel wire sidelobes due to psf nonuniformity. The bottom image is a successful D-weighted image highlighting the contrast available in angular scatter imaging.

V. CONCLUSIONS

SAAS imaging proves to be an effective method for coherently acquiring angular scatter data with high angular and spatial resolution. In order to successfully form angular scatter images, individual element response uniformity is critical for sidelobe suppression. Further work must be performed in order to compensate for element amplitude variations and increase SNR *in vivo*. Angular scatter imaging does present a latent source of image contrast that could have dramatic applications *in vivo*.

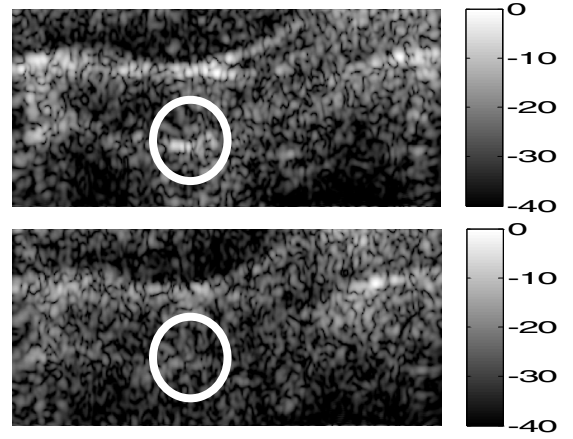


Figure 12. SAAS 180° pure backscatter B-mode image of *in vivo* human thyroid (top) and a D-weighted image of human thyroid (bottom) between 180° and 176°. Notice the dissipation of the bright scatterer inside the white ring in the D-weighted image.

ACKNOWLEDGMENT

The authors acknowledge technical support from GE Global Research and grant support from the U.S. Army CDMRP in Breast Cancer. We would also like to thank Matthew Oberhardt for the construction of the phantoms.

REFERENCES

- [1] K. K. Shung and G. A. Thieme, *Ultrasonic Scattering in Biological Tissues*. Boca Raton, Florida: CRC Press Inc., 1993.
- [2] W. F. Walker and G. E. Trahey, "The application of k-space in pulse echo ultrasound," *IEEE Trans., Ultrason., Ferroelect., Freq. Contr.*, vol. 45, 1998.
- [3] J. A. Campbell and R.C. Waag, "Measurements of calf liver ultrasonic differential and total scattering cross sections," *J. Acoust. Soc. Amer.*, vol. 75, 1984, pp. 1879-1886.
- [4] D. A. Guenther, K. Ranganathan, M.J. McAllister, K.W. Rigby and W. F. Walker, "Synthetic aperture methods for angular scatter imaging," *Proc. SPIE* vol. 5373, 2004, pp. 52-60.
- [5] W. F. Walker, "C- and D- weighted ultrasonic imaging using the translating apertures algorithm," *IEEE Trans., Ultrason., Ferroelect., Freq. Contr.*, vol. 48, 2001.
- [6] A. Prokop et al, "A polyacrylamide gel acoustic coupling medium for therapy applications of high intensity focused ultrasound," *Ultrasound Med Biol.* 29(9), Sept. 2003, pp. 1351-8.
- [7] J. Gaskill, *Linear Systems, Fourier Transforms, and Optics*. New York: John Wiley and Sons, 1978.
- [8] J. A. Jensen, "Field: A program for simulating ultrasound systems," *Med. Biol. Eng. Comp.*, col. 10th Nordic-Baltic Conference on Biomedical Imaging., 4(1), 1996, pp. 351-353.

Ultrasonic Synthetic Aperture Angular Scatter Imaging

D. A. Guenther, K. Ranganathan, M. J. McAllister,
and W. F. Walker

Department of Biomedical Engineering
University of Virginia
Charlottesville, VA 22908
dag2m@virginia.edu

K.W. Rigby

GE Global Research
Niskayuna, NY 12309

Abstract—Conventional coherent imaging systems map the energy which is reflected directly back towards the transducer. While extremely useful, these systems fail to utilize information in the energy field which has been scattered at other angles. Angular scatter imaging attempts to form images from the scattered energy field at angles other than the 180° backscattered path.

We propose a synthetic aperture based imaging scheme for acquiring angular scatter data in medical ultrasound. We describe this technique in k-space and provide an intuitive explanation of the imaging system's behavior. This method, which we term Synthetic Aperture Angular Scatter (SAAS) imaging effectively uses single element geometries to acquire data at a range of scattering angles.

In this paper, we present experimental results implementing SAAS on a GE Logiq 700MR system. We applied the SAAS method to form angular scatter images of a 5-wire depth of field (DOF) phantom and a tissue mimicking 3-wire phantom (steel, nylon, and cotton). We present results from this data and discuss the degree of uniformity necessary in element response for successful SAAS imaging. Results from these experiments show new image information previously unavailable in conventional B-mode images and suggest that angular scatter imaging may have applications in the breast, thyroid, and peripheral vasculature.

Keywords—beamforming; synthetic aperture; angular scatter

I. INTRODUCTION

Coherent imaging systems such as RADAR, SONAR, medical ultrasound, and optical imaging, do not conventionally detect the energy field that has been scattered at angles other than directly back towards the source. While bi-static RADAR and similar techniques do obtain limited information about angular scatter, they are unable to coherently process data obtained at multiple scattering angles. In medical ultrasound there has been significant research performed in an attempt to measure angular scatter data from tissue. This research is motivated by observations that human tissues exhibit variation in scattering response when the angle between transmission and reception is changed. These differences result from intrinsic acoustic properties and tissue microstructure, both of which might provide valuable information for tissue characterization and to aid in diagnosis [1]. Conventional ultrasound B-mode images are formed primarily of acoustic backscatter; and thus fail to take advantage of the prodigious

amount of information that has been scattered away from the transducer. Angular scatter imaging acquires the scattered echoes available at angles other than the 180° backscattered path and utilizes the variations in scattering response as a new source of image contrast.

This paper describes a new method for coherently acquiring backscatter and angular scatter information using a synthetic aperture approach on a 1D linear array. Utilizing k-space techniques and the Translating Apertures Algorithm (TAA), our method allows us to maintain high spatial resolution, high angular resolution, and large DOF using simple single element geometries. Problems encountered in previous systems (a varying system response with scattering angle) are minimized with the TAA, and the limited DOF of previous TAA measurements with multielement focused apertures are overcome with synthetic aperture dynamic focusing techniques. Although many favorable system characteristics are offered by SAAS, this method requires fine element spacing in the transducer and demands a high degree of element response uniformity, both of which are less critical for conventional beamforming.

II. THEORY

A. Transmit/Receive aperture geometries and k-space

Linear systems can be characterized by their frequency domain representation. In many cases, such an approach provides an easier analysis of particular problems. Signal analysis and filtering are regularly performed in the frequency domain because of this utile representation. Our angular scatter system approach is intuitively understood and described in k-space. K-space is a frequency domain depiction of ultrasonic imaging systems that is extremely useful in graphically demonstrating the spatial frequency response of transmit and receive apertures. Lerner and Waag used k-space to differentiate the scattering response of the target to the response of an aperture in ultrasound [2].

A typical angular scatter system is shown in Fig. 1, where the scattering angle, ϕ , is measured as the angle between the transmit wave propagation path and the receive wave propagation path. In order to acquire acoustic backscatter data, the transmitter and receiver must be the same transducer. Angular scatter data is then acquired at angles less than 180° . Although full analysis is a multidimensional problem, we

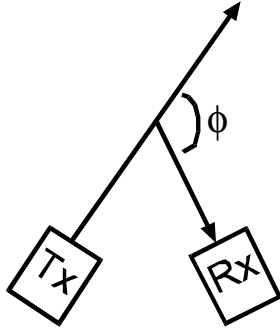


Figure 1. Angular scatter system geometry. The scattering angle, ϕ , is calculated as the angle between the transmit wave propagation path and the receive wave propagation path.

simplify our k-space analysis to two dimensions: lateral spatial frequency, θ , and scattering angle, ϕ . In order to determine the lateral spatial frequency that a given transmit/receive aperture pair interrogates, we perform the convolution of the scaled and reversed transmit aperture with the scaled and reversed receive aperture [3].

Fig. 2 depicts a 1D linear transducer array and the simple case of single element synthetic aperture for acquiring acoustic backscatter. The set of axes to the right of the array show how this method samples our k-space domain. The θ -axis intersects the ϕ -axis at $\phi=180^\circ$. This particular geometry samples a specific lateral spatial frequency at a scattering angle of 180° . Translation of this particular Tx/Rx aperture to the left would acquire a more positive lateral spatial frequency and a scattering angle still on the θ axis. Fig. 3 depicts a transmit and receive aperture pair where the receive element is shifted one element to the right of the transmit element. Notice that this geometry samples a different lateral spatial frequency than the backscattered case (hollow circle). It also collects angular scatter data at an angle less than 180° . If we switch the transmit and receive apertures of this previous case, we arrive at the geometry depicted in Fig. 4. We see that in reference to Fig. 3 this transmit and receive aperture pair sample the identical lateral spatial frequency but at the corresponding negative scattering angle. Because the transmit and receive acoustic paths are the same in the last two cases, we expect the received signal to also be the same due to acoustic reciprocity.

B. Conventional vs. SAAS aperture geometries and k-space

The scattering angle k-space response of a linear array applying conventional beamforming methods where a subset of elements is used on transmit and receive is depicted in Fig. 5. We see that conventional beamforming samples a range of lateral spatial frequencies and multiple scattering angles. The three circles on the θ -axis correspond to each element receiving its own backscattered signal.

Previous attempts at acquiring angular scatter data kept the transmit aperture fixed and translated the receive aperture [4]-[5]. Such an approach is depicted in Fig. 6.

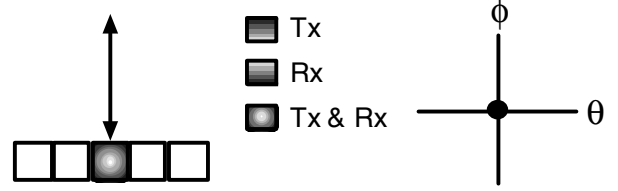


Figure 2. Angular scatter k-space response of a single element designated on transmit and receive.

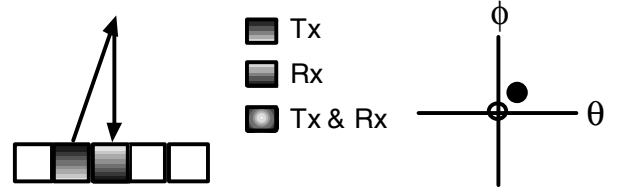


Figure 3. Angular scatter k-space response where the transmit and receive elements are different.

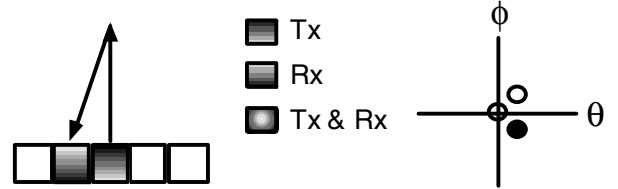


Figure 4. Angular scatter k-space response where the transmit and receive elements are switched in reference to Fig. 3.

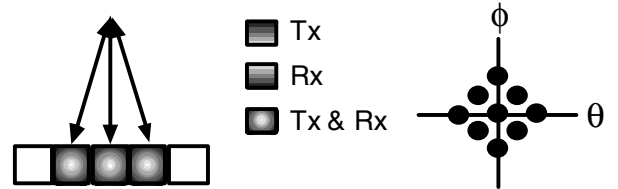


Figure 5. Angular scatter k-space response using conventional beamforming methods with multielement, focused apertures.

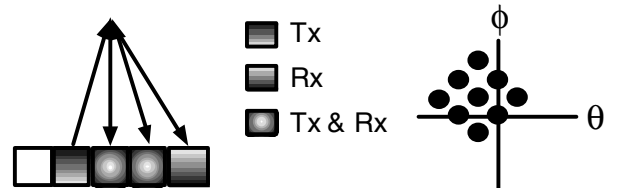


Figure 6. Angular scatter k-space response for a 1D array utilizing multielement apertures that acquires angular scatter data incoherently with respect to scattering angle compared to Fig. 5.

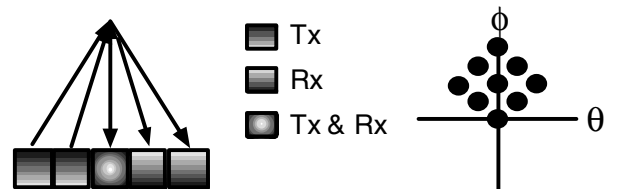


Figure 7. Angular scatter k-space response for a 1D array utilizing multielement apertures and the TAA to maintain system psf.

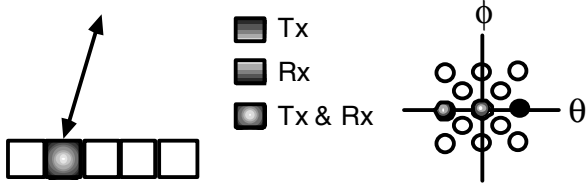


Figure 8. SAAS 180° pure backscatter geometry. We can acquire k-space data at a specific scattering angle (shaded circles) by translating the active element across the array.

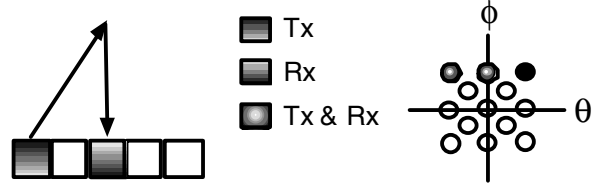


Figure 9. SAAS TAA geometry. We can acquire k-space data at the same lateral spatial frequencies as the backscatter case but at scattering angles less than 180°.

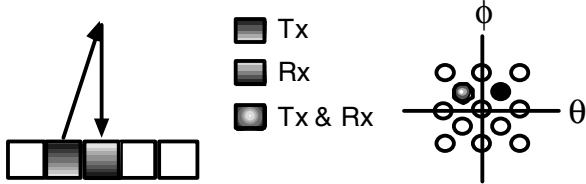


Figure 10. SAAS TAA half step geometry. We can acquire angular scatter data that improves our lateral spatial frequency sampling when summed with the backscatter or TAA full step data.

Notice that the footprint of the k-space response is the same as the previous geometry but some different lateral spatial frequencies and scattering angles are interrogated. Because different lateral spatial frequencies are interrogated, spatial coherence is not maintained with respect to scattering angle. As an objectionable result, the angular scatter data is not being acquired coherently and thus the two data sets cannot be compared most effectively.

Spatial coherence, and therefore system response, with respect to scattering angle can be maintained by applying the Translating Apertures Algorithm (TAA). The TAA was previously outlined in [6] as a way to maintain system response by translating the transmit and receive apertures in equal and opposite directions. Applying the TAA to the conventional case in Fig. 5 results in the response depicted in Fig. 7. We notice the TAA response interrogates identical lateral spatial frequencies, and it samples some new scattering angles. Unfortunately, the use of the TAA and multielement apertures is not ideal because these methods interrogate multiple scattering angles, blurring system resolution in this dimension.

Synthetic aperture techniques will allow us to improve angular resolution as well as to dynamically focus received data anywhere with the application of previously calculated geometric focal delays. To acquire SAAS data, a transmit and receive element pair are identified which define a certain scattering angle. The lateral separation, indicative to this scattering angle, is kept constant as the active elements are translated across the array. In this manner we acquire data at one specific angle for the entire effective aperture; therefore, we avoid the averaging across multiple scattering angles that results from the use of multielement, focused apertures.

Using the SAAS 180° backscatter geometry depicted in Fig. 8, we notice that we can acquire data at a specific scattering angle (black circle). Translating the active element to the right samples increasingly negative lateral spatial frequencies (shaded circles). Likewise, we can apply the TAA to our SAAS 180° case as shown in Fig. 9. This geometry samples the same lateral spatial frequency as the backscatter case but acquires data at a scattering angle that is less than 180°. The modified TAA half step (Fig. 10), where only one aperture is translated while the other remains fixed, allows us to sample different lateral spatial frequencies. By combining two angular scatter data sets, we can improve our lateral spatial frequency sampling thereby suppressing grating lobes that would otherwise be present due to a poorly sampled aperture. This improvement comes with a minor reduction in scattering angle resolution. It is clear from this discussion that our SAAS scheme can achieve excellent angular resolution and collect angular scatter data coherently. The geometries discussed were used in experiments in order to acquire and analyze SAAS data at varying angles with axial range.

C. Angular scatter and psf uniformity

Angular scatter data can be processed in a multitude of ways. Currently we have focused on forming D-weighted images, a process outlined in [6], which highlights intrinsic density differences between the target and the background. Although graphically useful, formation of D-weighted images requires subtracting two sets of data acquired at different scattering angles. This process amplifies the noise in the image and is extremely susceptible to slight variations in system psf.

Acquiring angular scatter data coherently is arguably the most important angular scatter system characteristic. Maintaining a high degree of psf uniformity across scattering angles is paramount for D-weighted image formation. We have refined and adjusted our system to maintain a well correlated psf across scattering angles ($\bar{\rho} = .9979 \pm .0014$). Refinements included the modified TAA half step previously mentioned and accounting for variations in individual element responses. As shown later, element nonuniformities adversely affect our ability to form D-weighted images.

III. EXPERIMENTS

We performed two sets of wire target experiments using our GE Logiq 700MR system modified to acquire SAAS data. The 739-L 192 element linear probe was used in these experiments.

The first utilized a 10% Acrylamide ($c \approx 1545$ m/s) phantom with five 20 μm steel wire targets ranging axially every centimeter from 1.7 cm to 5.5 cm and spaced laterally every 0.7 cm. Apodization schemes were applied to acquire angular scatter data ranging from 180° to 170° at 3.0 cm. The goal of these experiments was to quantify the grating lobe suppression capabilities of the modified SAAS algorithm and to observe the increased DOF. The data was apodized and dynamically focused on transmit and receive over a range from 1.5 cm to 6.7 cm.

The second set of wire target experiments conducted utilized a 3-wire (steel, nylon, and cotton) 10% Acrylamide phantom with enough Sephadex® to elicit fully developed speckle. The 3 wires were set at a depth of 3 cm after being degassed for 5 hours. Angular scatter data was acquired ranging from 180° to 170° . Difference weighted (D-weighted) images were formed from the resulting 10 different scattering angle data sets. Note that one angular scatter data set is the summation of two independent angles in order to improve spatial sampling. The stainless steel type 304 wire has a published density, ρ_s , of 7.9 g/cm³ and a diameter of 20 μm . The diameters of the nylon suture and cotton thread were 150 μm and 100 μm , respectively. The steel's density is much higher than the assumed density of cotton ($\rho_c = 1.5$ g/cm³) and ophthalmic nylon suture ($\rho_n = 1.1$ g/cm³). The density of the Acrylamide phantom was assumed to be 1.02 g/cm³ [7]. Given these density values, we expect to see no discernible differences between the wires in conventional ultrasound B-mode images but expect that the steel (most dense) will show up the brightest in the D-weighted image. Since nylon and Acrylamide have similar densities, the nylon wire should "disappear" in the D-weighted image.

IV. RESULTS AND DISCUSSION

Fig. 11 below shows log compressed B-mode images of the 5-wire phantom. The image on the left is of pure backscatter data and the image on the right is backscatter plus TAA half step data highlighting the suppression of the grating lobes.

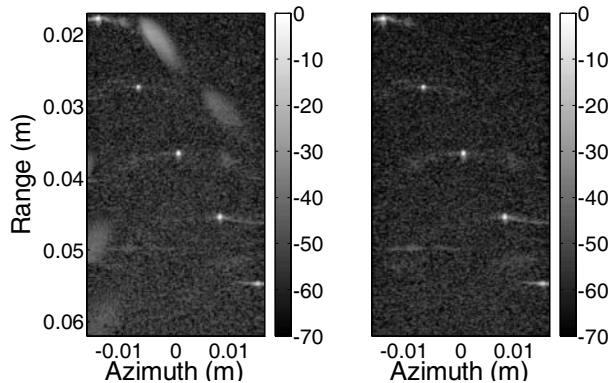


Figure 11. 5-Wire log compressed B-mode images of backscatter (left) and backscatter plus TAA half step (right).

The -6dB resolution for each of the wires in the backscatter plus TAA half step image from top to bottom were: 486 μm , 406 μm , 411 μm , 435 μm and 645 μm . These values highlight the excellent DOF with the synthetic aperture focusing technique. The deviation in the top and bottom wires is presumably due to the wires' lateral position and the apodization function falling off the side of the aperture.

It was empirically observed that element nonuniformities in the experimental system were degrading psf uniformity across scattering angles. These element nonuniformities were manifesting themselves as small time delays (~ 2.2 ns rms) and amplitude variations ($\sim 15\%$ deviation about the mean). The element delays could be determined empirically and were noted to be constant across trials and acquisitions; therefore, they could be corrected. The amplitude variations across the aperture on the other hand did not have any consistency with range, trial, or scattering medium; thus they could not be accounted for. As a result of these element nonuniformities, the intensity and spatial location of the psf sidelobes varied across scattering angle. Sidelobe variations will adversely affect the ability to form successful D-weighted images. This anomalous behavior is an area of ongoing investigation.

Regardless of the aforementioned system nonuniformities, we have been able to successfully form D-weighted images with some scattering angle data sets. Fig. 12 depicts three images of the 3-wire phantom. The steel, nylon and cotton wires are laterally spaced left to right, respectively. The top image of pure backscatter with associated half angle shows that the cotton wire is the brightest target followed by steel and then nylon. The middle image is a D-weighted image between a backscatter data set and 176° . The brightest target in this image is the **sidelobe** of the steel wire. This D-weighted image is being dominated by the sidelobe noise due to the psf nonuniformities arising from varying element responses. The bottom image is a successful D-weighted image where the steel wire is the brightest target. Also notice that the nylon wire has essentially "vanished" since its density is nearly identical to the Acrylamide background. The cotton wire intensity has also decreased. The steel wire's intensity increased 10 dB over the cotton wire between the original B-mode and successful D-weighted images, highlighting the contrast available in angular scatter imaging.

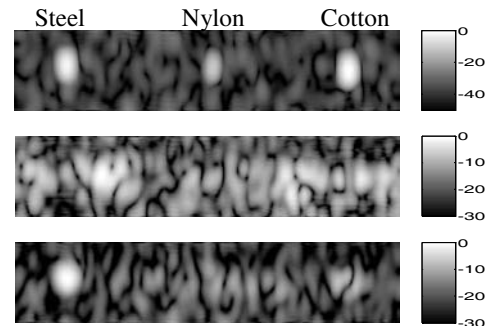


Figure 12. SAAS 180° B-mode image of a 3-wire phantom (top). The middle image is an unsuccessful D-weighted image that is being dominated by the steel wire sidelobes due to psf nonuniformity. The bottom image is a successful D-weighted image highlighting the contrast available in angular scatter imaging.

V. CONCLUSIONS

SAAS imaging proves to be an effective method for coherently acquiring angular scatter data with high angular and spatial resolution. In order to successfully form angular scatter images, individual element response uniformity is critical for sidelobe suppression. Further work must be performed in order to compensate for element amplitude variations in order to maintain a constant system psf. Angular scatter imaging does present a latent source of image contrast that could have dramatic applications *in vivo*.

ACKNOWLEDGMENT

The authors acknowledge technical support from GE Global Research and grant support from the U.S. Army CDMRP in Breast Cancer. We would also like to thank Matthew Oberhardt for the construction of the phantoms.

REFERENCES

- [1] K. K. Shung and G. A. Thieme, *Ultrasonic Scattering in Biological Tissues*. Boca Raton, Florida: CRC Press Inc., 1993.
- [2] R. M. Lerner and R. C. Waag, "Wave space interpretation of scattered ultrasound," *Ultrasound Med. Biol.*, vol. 14, pp. 97-102, 1988.
- [3] W. F. Walker and G. E. Trahey, "The application of k-space in pulse echo ultrasound," *IEEE Trans., Ultrason., Ferroelect., Freq. Contr.*, vol. 45, 1998.
- [4] J. C. Lacefield, "Angular scatter ultrasound imaging using separated arrays," Ph.D. dissertation, Duke University, 1999.
- [5] M. T. Robinson and O. T. Von Ramm, "Real-time angular scatter imaging system for improved tissue contrast in diagnostic ultrasound images," *IEEE Trans. Ultrason., Ferroelect., Freq. Contr.*, vol. 41, 1994.
- [6] W. F. Walker, "C- and D- weighted ultrasonic imaging using the translating apertures algorithm," *IEEE Trans., Ultrason., Ferroelect., Freq. Contr.*, vol. 48, 2001.
- [7] A. Prokop et al, "A polyacrylamide gel acoustic coupling medium for therapy applications of high intensity focused ultrasound," *Ultrasound Med Biol.* 29(9), Sept. 2003, pp. 1351-8.

A New Performance Analysis Metric for Medical Ultrasound

Karthik Ranganathan and William F. Walker

Department of Biomedical Engineering
University of Virginia
Charlottesville, VA
kr6u@virginia.edu

Abstract— The resolution of medical ultrasound systems is usually characterized by the width of the mainlobe, typically the full width at half maximum (FWHM), in beamplots. The FWHM has, however, been shown to sometimes provide misleading information about systems. The concept of “cystic resolution”, in which performance is quantified as the size of the void that produces a specified contrast, has been previously introduced to medical ultrasound. We extend the concept and develop a general metric to analyze the 3D broadband performance of arbitrary ultrasound systems. We provide an example of application in which we compare the performance of a conventional system using a 1D array and time delay beamforming of radio frequency (RF) data to that of a system based on a 2D array that focuses solely via phase rotation of complex I/Q data formed by directly sampling the received RF signal.

Keywords - ultrasound; beamformer; resolution; contrast

I. INTRODUCTION

The characterization of imaging performance of ultrasound systems is a critical part of the system development process. System resolution is most often described using a combination of the full width at half maximum (FWHM) or -6 dB beamwidth and the beamwidth at other levels, a metric that has been adapted from RADAR. However, Vilkomerson *et al* [1] demonstrated that the FWHM criterion sometimes provides misleading information about performance in ultrasound systems. Targets in medical ultrasound are usually weakly reflecting tissues in a scattering medium, unlike RADAR targets that are highly reflective and in a non-scattering background. Therefore, there may be scenarios in which the FWHM criterion indicates excellent performance, but actual images of tissue do not reveal important details. In addition, it is difficult to be certain about the best levels at which to characterize and optimize the beamplot. Actual system performance may be determined by imaging phantoms; however, this does not provide a way to theoretically assess the performance of proposed or hypothetical imaging systems.

Vilkomerson *et al* addressed the above problem and proposed the concept of “cystic resolution” [1] in which performance was quantified as the size of the void that produced a given contrast. The analysis, while novel and useful, was limited to narrowband circular apertures and neglected the axial dimension. A general 3D broadband metric is therefore needed to theoretically quantify the performance of an ultrasound imaging system.

II. THEORY

Our goal, as in [1], is to derive an expression for the contrast of a cyst and use it to characterize performance as the radius of the cyst that yields a given contrast.

Let the point spread function (psf) of the ultrasound system be $P(\vec{x}, t)$, a function of 3D space (\vec{x}) and time (t). The medium scattering function is modeled as a white noise process $N(\vec{x})$, assuming no tissue motion and therefore being constant with time. The received signal as a function of time is therefore,

$$S_b(t) = \int_{-\infty}^{\infty} P(\vec{x}, t) N(\vec{x}) d\vec{x}. \quad (1)$$

We consider the received signal at a single instant in time t_o ,

$$Sb_{t_o} = \int_{-\infty}^{\infty} P_{t_o}(\vec{x}) N(\vec{x}) d\vec{x}. \quad (2)$$

Consider the mean squared quantity $\langle Sb_{t_o}^2 \rangle$,

$$\langle Sb_{t_o}^2 \rangle = \left\langle \int_{-\infty}^{\infty} P_{t_o}(\vec{x}_1) N(\vec{x}_1) d\vec{x}_1 \int_{-\infty}^{\infty} P_{t_o}(\vec{x}_2) N(\vec{x}_2) d\vec{x}_2 \right\rangle \quad (3)$$

where $\langle \rangle$ is the expected value operator. Since the psfs are deterministic,

$$\langle Sb_{t_o}^2 \rangle = \int_{-\infty}^{\infty} \int_{-\infty}^{\infty} P_{t_o}(\vec{x}_1) P_{t_o}(\vec{x}_2) \langle N(\vec{x}_1) N(\vec{x}_2) \rangle d\vec{x}_1 d\vec{x}_2 \quad (4)$$

Since $N(\vec{x})$ is a white noise process,

$$\langle Sb_{t_o}^2 \rangle = \int_{-\infty}^{\infty} \int_{-\infty}^{\infty} P_{t_o}(\vec{x}_1) P_{t_o}(\vec{x}_2) a \delta(\vec{x}_1 - \vec{x}_2) d\vec{x}_1 d\vec{x}_2, \quad (5)$$

where a is a scaling factor. Therefore,

$$\langle Sb_{t_o}^2 \rangle = a \int_{-\infty}^{\infty} P_{t_o}^2(\vec{x}) d\vec{x}. \quad (6)$$

The mean squared received signal is therefore purely a function of the 3D psf. We can now describe a mask that defines the location and size of a spherical cyst centered at the focus,

$$M(\vec{x}) = 0, |\vec{x}| \leq R$$

$$= 1, |\vec{x}| > R, \quad (7)$$

where R is the radius of the cyst and the focus is at the origin of the coordinate system. $M(\vec{x})$ is also independent of time since we assume no tissue motion.

The scattering medium can then be represented as $N(\vec{x})M(\vec{x})$. The received signal is minimum when the beam axis coincides with the center of the void. The signal at time t_o can be written as,

$$Sc_{t_o} = \int_{-\infty}^{\infty} P_{t_o}(\vec{x}) N(\vec{x}) M(\vec{x}) d\vec{x}. \quad (8)$$

$$\langle Sc_{t_o}^2 \rangle = \left\langle \int_{-\infty}^{\infty} P_{t_o}(\vec{x}_1) N(\vec{x}_1) M(\vec{x}_1) d\vec{x}_1 \right. \\ \left. \cdot \int_{-\infty}^{\infty} P_{t_o}(\vec{x}_2) N(\vec{x}_2) M(\vec{x}_2) d\vec{x}_2 \right\rangle. \quad (9)$$

Since the psf and the mask are both deterministic,

$$\langle Sc_{t_o}^2 \rangle = \int_{-\infty}^{\infty} \int_{-\infty}^{\infty} P_{t_o}(\vec{x}_1) P_{t_o}(\vec{x}_2) M(\vec{x}_1) M(\vec{x}_2) \\ \cdot \langle N(\vec{x}_1) N(\vec{x}_2) \rangle d\vec{x}_1 d\vec{x}_2 \quad (10)$$

Once again, since $N(\vec{x})$ is a white noise process

$$\langle Sc_{t_o}^2 \rangle = \int_{-\infty}^{\infty} \int_{-\infty}^{\infty} P_{t_o}(\vec{x}_1) P_{t_o}(\vec{x}_2) M(\vec{x}_1) M(\vec{x}_2) \\ \cdot a \delta(\vec{x}_1 - \vec{x}_2) d\vec{x}_1 d\vec{x}_2. \quad (11)$$

Therefore,

$$\langle Sc_{t_o}^2 \rangle = a \int_{-\infty}^{\infty} P_{t_o}^2(\vec{x}) M^2(\vec{x}) d\vec{x}. \quad (12)$$

The contrast of the cyst can then be defined as,

$$Contrast = \frac{\sqrt{\langle Sc_{t_o}^2 \rangle}}{\sqrt{\langle Sb_{t_o}^2 \rangle}} = \sqrt{\frac{\int_{-\infty}^{\infty} P_{t_o}^2(\vec{x}) M^2(\vec{x}) d\vec{x}}{\int_{-\infty}^{\infty} P_{t_o}^2(\vec{x}) d\vec{x}}} \quad (13)$$

Note that the expression for contrast in (13) only requires knowledge of the psf and the size of the cyst.

III. SIMULATIONS

We have previously detailed [2, 3] the development of a small, low-cost, portable, and hand-held ultrasound system. We chose to implement a narrowband beamforming scheme, direct sampled I/Q (DSIQ) beamforming [4], in our system. We implement focusing by phase rotation of complex I/Q data that are acquired by directly sampling the received radio frequency (RF) signal on each channel. Our strategy sacrifices some image quality in exchange for significant size and cost benefits [4]. However, the results in [4] were obtained by performing a 2D analysis using a 1D array on a Philips SONOS 5500. Our system is based on a fully sampled 2D array, made possible in large part by our compact and inexpensive beamforming scheme.

We performed simulations to further explore the potential of our system design, in which we used the expression for the contrast of a cyst in (13) to compare conventional time delay beamforming on a 1D array to DSIQ beamforming on a 2D array. We evaluated beamformer performance using the radius of the cyst required to produce a specified level of contrast. We believe that this is a more relevant resolution metric for medical ultrasound than those based on beamplots because it takes into account the full 3D problem of detecting targets in a speckle generating background.

TABLE I. SIMULATION PARAMETERS

Parameter	Conventional	Sonic Window
Array type	1D linear array	2D array (circular aperture)
F/#	1.5	1.5 (receive only)
Apodization	Hann window	2D Hann window (receive only)
Pitch	135 μ m	635 μ m
Center frequency	3.5 MHz	3.5 MHz
Fractional -6 dB bandwidth	75%	75%
Beamforming	Time delays	DSIQ beamforming (receive only)
Spatial extent of psf computation	2.1 x 2.1 x 0.6 cm	2.1 x 2.1 x 0.6 cm
Spatial sampling intervals	150 x 150 x 50 μ m	150 x 150 x 50 μ m
Radii of cysts investigated	0.05 cm - 1.65 cm	0.05 cm - 1.65 cm

Table 1 lists relevant simulation parameters. In simulations for the conventional geometry, we used Field II [5] to compute the pulse-echo field $P(\vec{x}, t)$ at each location in the 3D spatial grid defined in table 1 as a function of time. We then constructed the purely spatial psf $P_{t_o}(\vec{x})$ where t_o is the propagation time from the aperture to the focus and back. In the Sonic Window geometry simulations, we assumed symmetry in the plane of the transducer for reduced computational complexity. We computed individual spatial psfs for each receive element in the azimuth-range plane and rotated it about the beam axis to obtain the full 3D psf. We simulated two psfs, at times t_o and $t_o + \frac{1}{4f_o}$, where f_o was

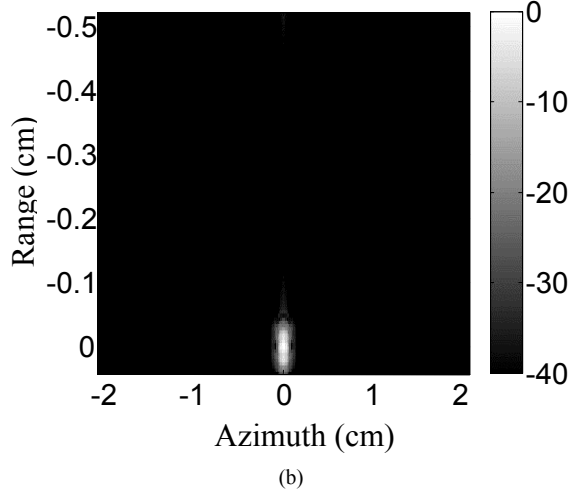
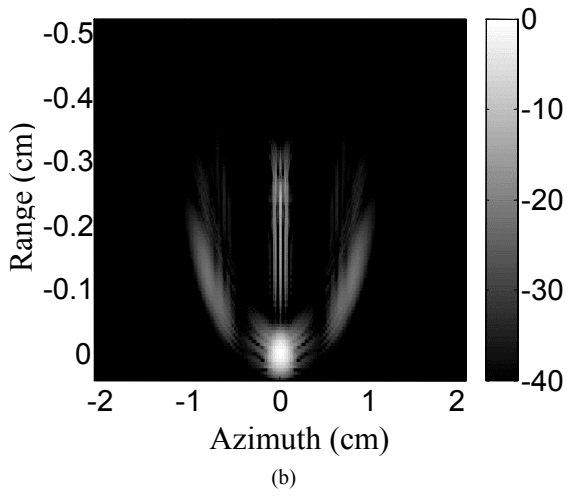
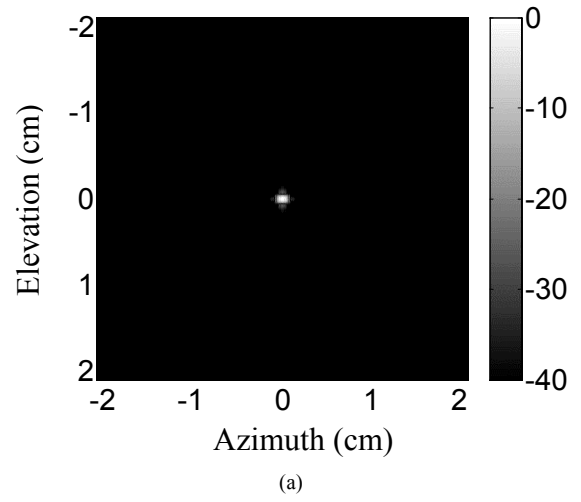
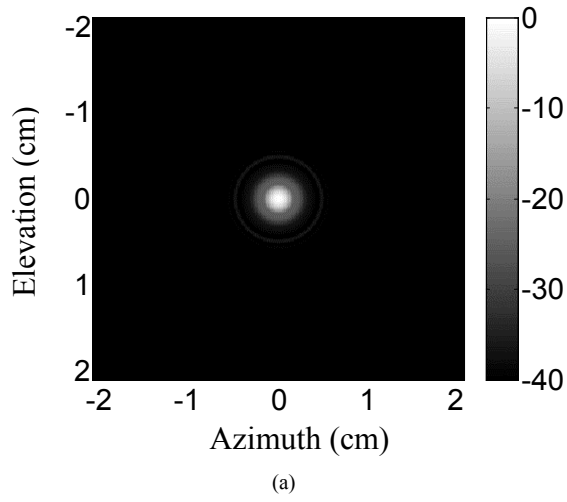


Figure 1. Slices of the envelope detected Sonic Window psf in (a) range and (b) elevation, computed using a 2D array and DSIQ beamforming.

Figure 2. Slices of the envelope detected conventional psf in (a) range and (b) elevation, computed using a 1D array and time delay beamforming.

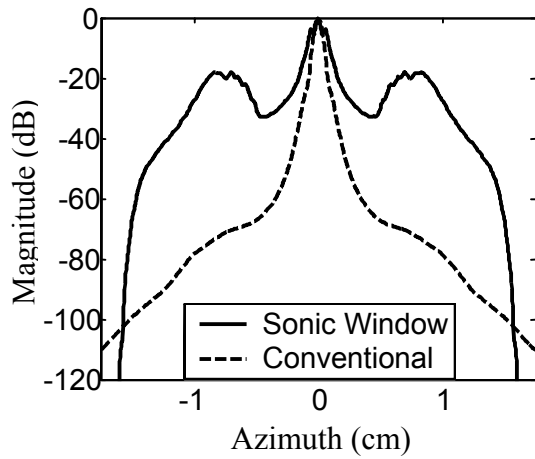


Figure 3. Beamplots derived from the psfs of the Sonic Window and conventional geometries.

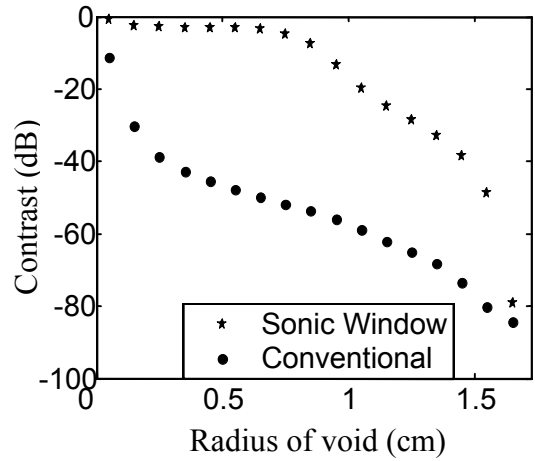


Figure 4. Contrasts as a function of cyst radius, determined using (13).

the center frequency, and then constructed a complex psf [4] for each receive element. These were focused by phase rotation and then summed to obtain the final psf. Note that the psf for the conventional geometry was also a complex function, constructed using the Hilbert transform of the computed psf, for accurate comparison with the Sonic Window. We then used (13) to determine the contrasts of voids of different sizes in both cases.

IV. RESULTS AND DISCUSSION

Fig. 1 depicts slices of the envelope detected psf computed using the geometry of the Sonic Window in range and elevation, while fig. 2 depicts slices of the envelope detected psf computed using the conventional geometry. Fig. 3 plots beamplots that were computed by integrating the psf in the range dimension at the center of the elevation plane. It can be seen that the Sonic Window psf is not only wider in all dimensions, but also has significant grating lobes. The -6 dB beamwidth of the Sonic Window beamplot is 1.8 times that of the conventional beamplot, suggesting that the resolution of the conventional geometry is 1.8 times better than that of the Sonic Window.

Fig. 4 plots contrast as a function of cyst radius, calculated using (13), for the two geometries. It can be seen that the difference in contrast is as much as 50 dB at certain radii. Our metric therefore indicates that the resolution of the Sonic Window is in fact much poorer than that of conventional systems.

While beamplots may provide an accurate estimate of resolution in the case of strongly scattering targets in a weak or non-scattering background, the above example shows that they can be misleading in characterizing the resolution of medical ultrasound systems. It is obvious that the resolution of the Sonic Window is poorer than that of conventional systems from the beamplots in fig. 3, and we can qualitatively include the effects of sidelobes and grating lobes in our estimate of resolution, but it is complicated to estimate exactly how much poorer the resolution is without our metric and the results depicted in fig. 4. It is, in addition, difficult to be certain about the best strategy to improve the beamplot to achieve the maximum attainable resolution. For example, it is unclear from fig. 3 if the resolution would be best improved by optimizing the -6 dB beamwidth, the -20 dB beamwidth, the -40 dB beamwidth, or the beamwidth at some other level. The metric described above eliminates any guesswork in the determination of resolution since it provides one value for resolution, given the desired contrast. The effect of any changes in the psf on resolution can be directly gauged. These simulation results indicate the usefulness of the described metric in determining imaging system resolution in a manner relevant to ultrasound imaging.

The primary reason for the poor resolution of the Sonic Window geometry is the appearance of grating lobes, as can be

seen in fig. 1 and fig. 3, due to our large element pitch (635 μ m). We intend to reduce our pitch in future versions of our system and hope to eliminate this problem. However, decreasing the pitch significantly would reduce the array size, since we can only accommodate a limited number of channels. Therefore, while reducing the pitch would limit the effect of grating lobes, the mainlobe width would increase and affect resolution. We will use our metric to find the pitch that strikes the best balance between minimizing grating lobes and maintaining a reasonable array size, and thus optimize performance.

Note that the elevation focus of the conventional 1D array was set to coincide with the azimuthal focus to attain the best possible resolution. The resolution of the conventional system will therefore become worse away from the elevation focus, unlike the Sonic Window, which uses a 2D array and can focus arbitrarily in elevation. A more thorough system analysis is therefore required.

V. CONCLUSION

We have developed a general 3D broadband resolution metric, adapted from [1], that can be used to characterize arbitrary ultrasound systems. We derived an expression for the contrast of a cyst in a speckle generating medium in terms of the 3D psf. Resolution is quantified as the radius of the cyst required to generate a specified contrast. Our metric is more relevant to medical ultrasound than metrics based on beamplots, and it eliminates any ambiguity in the determination of resolution.

ACKNOWLEDGEMENT

This work was supported by grant RO1 EB002348 from the National Institutes of Health.

REFERENCES

- [1] D. Vilkomerson, J. Greenleaf, and V. Dutt, "Towards a resolution metric for medical ultrasonic imaging," *Proc. IEEE Ultrason. Symp.*, vol. 2, pp. 1405-1410, 1995.
- [2] M. I. Fuller, T. N. Blalock, J. A. Hossack and W. F. Walker, "A Portable, Low-Cost, Highly Integrated, 3D Medical Ultrasound System," *Proc. IEEE Ultrason. Symp.*, vol. 1, pp. 38-41, 2003
- [3] K. Ranganathan, M. K. Santy, M. I. Fuller, S. Zhou, T. N. Blalock, J. A. Hossack, and W. F. Walker, "A prototype low-cost handheld ultrasound imaging system," *Proc. SPIE*, vol. 5373, pp. 24-32, Medical Imaging 2004: Ultrasonic Imaging and Signal Processing, 2004.
- [4] K. Ranganathan, M. K. Santy, J. A. Hossack, T. N. Blalock, and W. F. Walker, "Direct Sampled I/Q Beamforming: A Strategy for Very Low Cost Ultrasound," *Proc. IEEE Ultrason. Symp.*, vol.2, pp. 1863-1866, 2003.
- [5] J. A. Jensen and N. B. Svendsen, "Calculation of pressure fields from arbitrarily shaped apodized and excited ultrasound transducers," *IEEE Trans. Ultrason. Ferroelectr., Freq. Contr.*, vol. 39, no. 2, pp. 262-267, 1992.

Design of Apodization Profiles Using a Cystic Resolution Metric for Ultrasound

K. Ranganathan, D. A. Guenther, and W. F. Walker

Department of Biomedical Engineering

University of Virginia

Charlottesville, VA 22908

dag2m@virginia.edu

Abstract—We have previously described a metric that characterizes the 3D resolution of broadband ultrasound systems [1]. Resolution is expressed as the size of a spherical anechoic cyst, embedded in a speckle generating background, that is required to generate a specific contrast. The contrast of the cyst relative to the background depends on the ratio of the system point spread function (psf) energy outside the cyst to the total psf energy. In this work, we apply our formulation to guide the design of a low-cost, C-scan system being developed at the University of Virginia, demonstrating the utility of our metric in the optimization of system parameters. We simulated the impact of $f/\#$ and show that higher $f/\#$'s yield better cystic contrast for larger cysts, but lower contrast for smaller cysts. We also applied a constrained least squares (CLS) approach to design receive apodization profiles to optimize cystic contrast. We use a linear algebra formulation of the psf and minimize the psf's energy in regions outside a specified boundary. We show results that the CLS apodization profiles improve contrast around -10 dB compared to a flat apodization profile at a range of cyst sizes. Our results highlight the metric's utility in designing system parameters and our CLS apodization profiles improve cystic contrast.

I. INTRODUCTION

The ability to reliably estimate the imaging performance of ultrasound systems is critical, both to characterize the fundamental imaging limits of the system, and to optimize image quality. It is possible to estimate the performance of existing systems by imaging phantoms or human subjects, but it is necessary during system design to be able to determine imaging performance prior to system construction. The ability to accurately predict performance enables system optimization and quantitative consideration of engineering tradeoffs early in the design process and significantly reduces the time and cost investment in system development.

The most common metric used to estimate scanner performance is the beamplot [2], the use of which has been adapted from RADAR. The -6 dB beamwidth of the beamplot, the full width at half maximum (FWHM), and the beamwidth at other levels are used to estimate scanner resolution. Sidelobe and grating lobe levels are used to estimate eventual image contrast. Although widely used, there are disadvantages to using the beamplot to estimate the performance of ultrasound systems. Targets in medical ultrasound are usually weakly reflecting tissues in a scattering medium, unlike RADAR

targets that are more often highly reflective and in a non-scattering background. There may be scenarios in which the FWHM criterion indicates excellent performance, but actual images of tissue do not reveal important details. Vilkomerson *et al.* [3] demonstrated that the FWHM criterion sometimes provides misleading information about resolution in ultrasound systems. It is, in addition, difficult to decide whether to optimize the mainlobe width or sidelobe and grating lobe levels for an overall increase in image quality. Although imaging phantoms and repeated simulations may determine imaging performance, such approaches are time consuming and do not offer a simple method to guide system design. A theoretical metric that combines resolution and contrast in a relevant way to diagnostic ultrasound imaging is therefore required.

Vilkomerson *et al.* addressed the limitations of the beamplot and proposed the concept of “cystic resolution” [3] in which performance was quantified as the size of a void that produced a given contrast. The analysis, while novel and useful, was limited to narrowband circular apertures and neglected the axial dimension. Üstüner *et al.* [4] extended cystic resolution to a 3D broadband model that addressed the above problems, but did not describe its theoretical foundation, resulting in a limited understanding of the formulation and its utility and drawbacks. A general cystic resolution metric was previously derived by our group [1]; the metric accounts for the effect of electronic noise and, under certain assumptions, reduces to that described in [4].

This paper demonstrates the utility of the resolution metric to optimize system parameters. We have applied it to guide the design of a low-cost, C-scan system being developed at the University of Virginia. We also apply the metric in designing apodization windows for optimal cystic resolution on a 1D linear array. Using this metric, parameter optimization reduces to the straightforward task of picking the value that yields the maximum contrast at the cyst size of interest, or alternatively picking the value that yields the required contrast with the smallest cyst.

II. THEORY

A. Cystic Resolution Metric

The goal of the metric, as stated above, is to quantify the contrast resolution of an arbitrary broadband ultrasound system. We refer the reader to [1] for a more detailed

discussion of the derivation of the metric and provide a brief synopsis here. Let the point spread function (psf) of the ultrasound system be defined as $P(\vec{x}, t)$, a function of three-dimensional (3D) space (\vec{x}) and time (t). The medium scattering function is modeled as a zero-mean stochastic process $N(\vec{x})$ undergoing negligible tissue motion during reception of an individual echo line and therefore is constant with time. The effect of electronic noise during transmit is assumed to be negligible due to the high signal to noise ratio (SNR) on transmit, and the electronic noise on receive is modeled as another zero-mean stochastic process $E(t)$ which is purely additive. We define a mask that describes the location and size of a spherical anechoic void (cyst):

$$\begin{aligned} M(\vec{x}) &= 0, |\vec{x}| \leq R \\ &= 1, |\vec{x}| > R, \end{aligned} \quad (1)$$

where R is the radius of the cyst and the cyst center is at the origin of the coordinate system. $M(\vec{x})$ is also independent of time since tissue motion during the acquisition is assumed to be negligible. The cyst embedded in a scattering background is therefore represented as $N(\vec{x})M(\vec{x})$. The received signal energy is expected to be at a minimum when the beam axis coincides with the center of the void. The received signal in this circumstance can be written as:

$$S_c(t) = \int_{-\infty}^{\infty} P(\vec{x}, t) N(\vec{x}) M(\vec{x}) d\vec{x} + E(t) \quad (2)$$

The electronic SNR can be defined as a function of time:

$$SNR(t) = \frac{\sigma_{signal}(t)}{\sigma_{noise}(t)} = \sqrt{\frac{a \int_{-\infty}^{\infty} P^2(\vec{x}, t) d\vec{x}}{\langle E^2(t) \rangle}} \quad (3)$$

where $\sigma_{signal}(t)$ and $\sigma_{noise}(t)$ are the standard deviations of the signal and noise components respectively and a is a scaling factor. Note that the standard deviations are defined over an ensemble of signal and noise realizations and not over time.

While the metric can completely characterize system performance for a given cyst, analysis at the instant in time when the received signal is minimum (i.e. when as much of the psf energy as possible lies within the cyst) is usually sufficient. At this single instant in time t_o , the psf can be expressed as a function of only 3D space at the time of interest $P_{t_o}(\vec{x})$, and the SNR is also defined at the time of interest SNR_{t_o} . The contrast of the cyst relative to the background is defined as the ratio of the rms signal received with the cyst to the rms signal received from the background [1]:

$$C_{t_o} = \sqrt{\frac{1 + SNR_{t_o}^2 \frac{E_{t_o}^{out}}{E_{t_o}^{tot}}}{1 + SNR_{t_o}^2}} \quad (4)$$

where $E_{t_o}^{out}$ is the psf energy outside the cyst and $E_{t_o}^{tot}$ is the total psf energy, both at time t_o . Equation (4) describes the contrast of an anechoic cyst, whose size and location are described by the mask $M(\vec{x})$, relative to background speckle obtained by an imaging system with the psf $P(\vec{x})$ and electronic SNR defined statistically by SNR_{t_o} . Neglecting electronic noise, SNR_{t_o} becomes infinite and (4) can be modified to the equation for contrast presented in [4], which is simply the square root of the ratio of the psf energy outside the cyst and the total psf energy:

$$C_{t_o} = \sqrt{\frac{E_{t_o}^{out}}{E_{t_o}^{tot}}} \quad (5)$$

The contrast for cysts of different sizes can be computed using the above expressions for cystic contrast, and system performance can be characterized as a function of cyst size as in [3] and [4]. This metric can be used for 4D spatiotemporal analysis of broadband ultrasound systems, but 3D spatial analysis using (4) or (5) is adequate to characterize scanner performance as temporal analysis does not provide critical information. Note that in certain cases, it is valuable to compute the metric with cysts at different locations to quantify the depth of field, the effect of dynamic focusing, and other factors pertaining to the shift variance of the imaging system. Note also that while the metric can be used to determine cystic resolution, it can also be used to optimize system parameters by computing contrast as a function of cyst size and determining parameter values that maximize the contrast at the cyst sizes of interest.

B. Constrained Least Squares (CLS) Apodization Design

One conspicuous result of the above metric is that cystic contrast is a function of the spatiotemporal psf energy. In fact, contrast would be maximum if all the energy of the psf lies inside the void of the cyst. Whereas the beamplot can be misleading about overall image quality, our new metric specifically defines the portions of the psf that affect cystic contrast most dramatically. Contrast will improve when any region of the psf outside the cyst boundary contains less energy or there is more energy of the psf inside the cyst.

Cystic contrast is degraded due to psf energy outside the cyst. We minimize this energy by solving for the set of receive aperture weights that, when applied to the synthetic receive element responses, will yield a psf with minimum energy outside the cyst boundary. The acoustic field during pulse echo propagation at a point in space at a single time point can be expressed as a function of a propagation matrix, S , and a set of aperture weightings, w . The propagation matrix uses superposition to describe the contribution of each element at each field point as a function of time. S is a function of the transmit aperture weights, the excitation pulse, and the individual element impulse responses of the transmit and receive apertures [5].

The two way pulse echo propagation matrix, S , for a fixed transmit aperture and n element receive aperture at a total number of p points in three dimensional space is:

$$S = \begin{bmatrix} s_{1,1} & s_{1,2} & \cdots & s_{1,n} \\ s_{2,1} & . & \cdots & . \\ \vdots & \vdots & \ddots & \vdots \\ s_{p,1} & . & \cdots & s_{p,n} \end{bmatrix}, \quad (6)$$

where $S_{i,j}$ is the contribution of the j th element at the i th point in space. The receive aperture weighting function, w_i^T , for each of the n elements used on receive can be written in vector form as:

$$w_i^T = [w_1 \quad w_2 \quad w_3 \quad \cdots \quad w_n]^T, \quad (7)$$

where T denotes the vector transpose operation. Using (6) and (7), we can now write the complete two-way pulse echo system psf, P_z , as follows:

$$P_z = S w^T \quad (8)$$

the propagation matrix multiplied by the receive weighting vector. Note that this results in the one dimensional column vector, P_z , where $z = [1, 2, \dots, p]$ the total number of points where the system psf is measured in three dimensional space.

Adequate spatial sampling of the three dimensional psf yields huge propagation matrices, and therefore for this paper we have limited our analysis to two dimensions, azimuth and range. Clearly the elevation dimension matters in planar ultrasonic B-mode images, even with acoustic lenses on linear arrays. However, restricting our analysis to two dimensions eases visualization of the algorithm while still providing meaningful results.

Assuming the psf is focused at the center of the cyst, our problem becomes minimizing the energy outside the cyst boundary. The algorithm is initialized by selecting the spatial points of the psf which lie outside the cyst. We form the associated propagation matrix, S , which has as many rows as the number of points outside the cyst region and as many columns as elements in the active receive aperture. The algorithm calculates the weights which minimize the energy in the sidelobe regions while simultaneously maintaining a peak gain at the center of the cyst. These weights are determined from the constrained least squares problem:

$$\min_{w^T} \|S w^T\|^2 \quad \text{subject to the linear constraint } C w^T = 1 \quad (9)$$

In this expression $\|\bullet\|^2$ denotes the square of the ℓ^2 -norm and the row vector C has elements corresponding to the amplitude of each synthetic receive response at the center of the cyst. The equation in (9) is common in the signal processing literature and drawing upon [6] the optimal receive aperture weightings are given by:

$$w_{opt}^T = \frac{(S^T S)^{-1} C}{C^T (S^T S)^{-1} C} \quad (10)$$

where $(\bullet)^{-1}$ denotes the matrix inverse operation. Equation (10) provides a simple method to calculate the receive weightings that will minimize the energy in the psf outside a specified mainlobe region while simultaneously achieving peak gain inside the mainlobe region. The optimal receive weights minimize E_o^{out} in (5) above, so we expect to see improved cystic contrast using the CLS apodization windows over commonly used windows such as the flat, Hamming and the Nuttall [7] window.

III. SIMULATIONS

The cystic resolution metric is useful in guiding the design and optimization of ultrasound systems. In our group's efforts to develop a low cost, handheld, C-scan ultrasound system, the metric was used to quantify the impact of system parameters such as $f/\#$, electronic noise, quantization in the analog to digital converter, crosstalk, and apodization. The new system utilizes a fully sampled 2D array interfaced to a custom integrated circuit [8]. Our beamforming strategy, direct sampled IQ (DSIQ) beamforming [9], reduces system complexity and cost but suffers from poorer image quality than might be obtained using time delays. The system transmits an unfocused plane wave and apodizes and focuses on receive.

We simulated our system using DELFI [10], a custom ultrasound simulation package that efficiently calculates the spatial response of a given aperture. Spatial pulse-echo responses were computed by transmitting a plane wave on all elements and synthetically receiving on each individual element. The psfs were computed in a 3D cylindrical volume, focused using DSIQ beamforming and apodized with a 2D Nuttall [7] window on receive.

One of the system parameters investigated was the choice of $f/\#$ during reception. This is an important design parameter for our system because the DSIQ focusing scheme is limited by larger apertures [9]. In addition the elements in the 2D array are highly directive due to a large pitch (635 μm) and thus larger apertures will suffer from higher grating lobes. We explored the impact of $f/\#$ by computing cystic contrast curves as a function of cyst radius for varying $f/\#$'s.

Another system parameter investigated was receive apodization profiles. We calculated receive weights for a linear array operating at 6.5 MHz and a 50% fractional bandwidth with a fixed transmit focus at 2cm. Using DELFI [10] 2D spatial psfs were computed for the linear array by synthetically receiving on each element at the transmit focus. The 2D psfs were then used to calculate the optimal receive weights according to the CLS approach outlined above. Corresponding cystic contrast curves as a function of cyst radius were calculated for the CLS windows and compared to the flat, Hamming and the Nuttall [7] window.

IV. RESULTS AND DISCUSSION

Figure 1 below shows the cystic contrast curves for the $f/\#$ simulations.

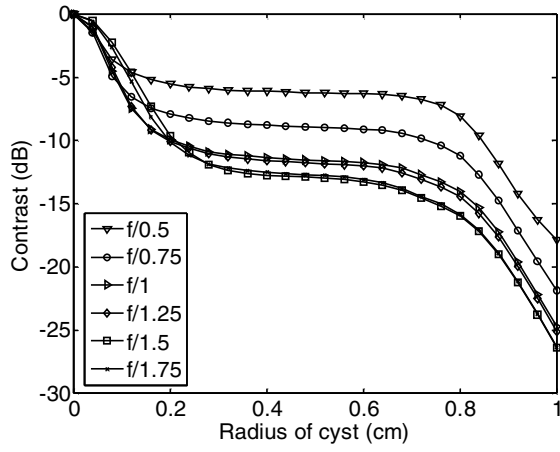


Figure 1. Effect of receive $f/\#$. Contrasts were computed using equation (6) and are plotted as a function of cyst size for varying $f/\#$'s.

It is apparent that contrast increases with increasing $f/\#$ for large cysts. This is due to highly directive elements that generate large grating lobes when larger apertures are used. However, higher $f/\#$'s ($>f/1.5$) result in a broad mainlobe and reduce contrast when imaging small cysts. Figure 1 suggests that an $f/1$ for the low cost system would be a good compromise for imaging cysts of all sizes. This analysis ignores the effect of aperture size on system sensitivity. Sensitivity increases with increasing aperture size. Considering the impact of SNR and $f/\#$ simultaneously may be necessary.

Optimal receive apodization profiles were computed for a linear 1D array according to the CLS formulation discussed above. For every cyst radius from 0.1mm to 2cm the CLS apodization profiles resulted in psfs that had the lowest energy in the sidelobe region compared to other windows. In conventional systems, scanning through apodization profiles for each cyst radii would be unrealistic. Therefore, it is interesting to see how a profile designed for a specific cyst size performs across a range of sizes. We chose the profile corresponding to a cyst radius of 0.4mm and then computed the cystic contrast curve. Figure 2 shows the contrast curves for this particular CLS profile compared to the flat, Hamming, and Nuttall windows. Although the CLS window does not produce the best contrasts for smaller cysts (<0.2 mm) or for larger cysts (>0.8 mm), it performs well over the entire range, with -10dB improvement in contrast over the flat apodization and -2dB improvement over the Hamming profile for cysts around 0.4mm in radius. The Nuttall window does a poor job for the small cysts due to a relatively large mainlobe. All the curves plateau as the cyst encompasses more of the psf energy.

We attempted to maximize cystic contrast through our least squares formulation by minimizing the energy in the psf outside the cyst region. Although the apodization profiles did minimize this energy they also reduced sensitivity in the mainlobe region. For larger cyst sizes the CLS apodization profiles do not produce "optimal" cystic contrast due to decreased psf energy inside the cyst compared to the other apodization windows. We are currently addressing this shortcoming by adjusting the constraints. It may be necessary to consider the impact of SNR and apodization simultaneously.

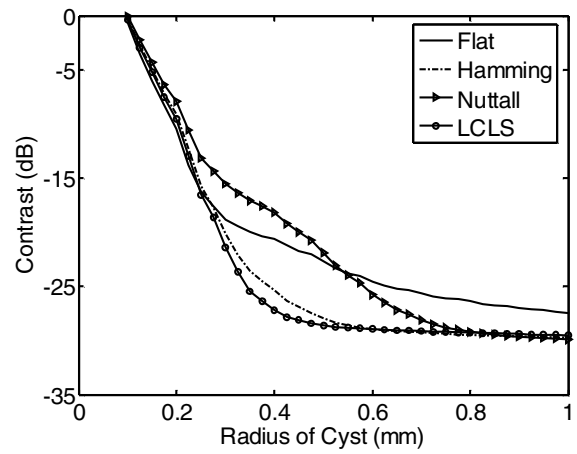


Figure 2. Effect of apodization. The CLS window performs well across the range of cyst sizes.

V. CONCLUSIONS

Our cystic contrast resolution metric is extremely useful in guiding system design of 3D broadband coherent imaging systems including the effects of electronic noise. The metric was used in the design of a portable, low cost ultrasound system currently under development. The metric also stimulated the design of optimal apodization profiles to maximize cystic contrast for a 1D linear array. The results presented in this paper demonstrate the utility of the metric in designing ultrasound systems and show that it enables optimization of any parameter that affects image quality.

REFERENCES

- [1] K. Ranganathan and W. F. Walker, "A General Cystic Resolution Metric for Medical Ultrasound," submitted to the IEEE Transactions on Ultrasonics, Ferroelectrics, and Frequency Control.
- [2] B. D. Steinberg, *Principles of Aperture and Array System Design*, John Wiley & Sons, 1976, pp. 40-52.
- [3] D. Vilkomerson, J. Greenleaf, and V. Dutt, "Towards a resolution metric for medical ultrasonic imaging," *Proc. IEEE Ultrason. Symp.*, vol. 2, pp. 1405-1410, 1995.
- [4] K. F. Üstüner and G. L. Holley, "Ultrasound Imaging System Performance Assessment," presented at the 2003 AAPM Annual Meeting.
- [5] K. Ranganathan and W. F. Walker, "A novel beamformer design method for medical ultrasound. Part I: Theory," *IEEE Trans. Ultrason., Ferroelect., and Freq. Contr.*, vol. 50, no. 1, pp. 15-24, 2003.
- [6] L. L. Scharf, *Statistical Signal Processing: Detection, Estimation, and Time Series Analysis*, Addison-Wesley Publishing Company, 1991, p.365.
- [7] A. H. Nuttall, "Some Windows with Very Good Sidelobe Behavior," *IEEE Trans. Acoust. Speech Signal Process.*, vol. 29, no. 1, pp. 84-91, 1981.
- [8] M. Fuller, T. Blalock, W. Walker, and J. Hossack, "A Portable, Low-cost, Highly Integrated 3D Medical Ultrasound System," *Proc. IEEE Ultrason. Symp.*, pp. 38-41, 2003.
- [9] K. Ranganathan, M. K. Santy, T. N. Blalock, J. A. Hossack., and W. F. Walker, "Direct Sampled I/Q Beamforming for Compact and Very Low Cost Ultrasound Imaging," *IEEE Trans. Ultrason. Ferroelectr., Freq. Contr.*, vol. 51, no. 9, pp. 1082-1094, 2004.
- [10] W. F. Walker, "A Spline Based Approach for Computing Spatial Impulse Responses," submitted to the IEEE Transactions on Ultrasonics, Ferroelectrics, and Frequency Control.

Adaptive Signal Processing in Medical Ultrasound Beamforming

Francesco Viola and William F. Walker

Department of Biomedical Engineering
University of Virginia
Charlottesville, VA 22908

Abstract— For over thirty years adaptive beamforming (AB) algorithms have been applied in RADAR and SONAR signal processing. Higher resolution and contrast is attainable using those algorithms at the price of an increased computational load. In this paper we consider four beamformers (BFs): Frost BF, Duvall BF, SSB, and SPOC. These algorithms are well known in the RADAR/SONAR literature. We have performed a series of simulations using ultrasound data to test the performance of those algorithms and compare them to the conventional, data independent, beamforming. Every algorithm was applied on single channel ultrasonic data that was generated using Field II. For a 32 element linear array operating at 5 MHz, beamplot results show that while the Duvall and SSB beamformers reduce sidelobes by roughly 20 dB, the sidelobes using the Frost algorithm rise by 23dB. The -6 dB resolution is improved by 38%, 83%, and 43% in the case of Duvall, Frost, and SSB algorithms, respectively. In the case of SPOC, the beamplot shows a super-resolution peak with noise floor at -110 dB. Similar results were obtained for an array consisting of 64 elements.

I. INTRODUCTION

The application of Wiener filter theory to RADAR and SONAR signal processing led to the development of adaptive beamforming (AB) [1, 2]. In AB, the information associated with the data received by an array of sensors is used to determine a set of weights that optimize the beamformer output [2]. The weights are determined by minimizing the energy in the beamsum signal, subject to the constraint that the beamformer must exhibit a given response in the look-direction. The second order statistics of the data are used to generate the weights. These algorithms are able to achieve resolutions far superior to those predicted by diffraction theory, while attaining excellent side lobe reduction. In parallel, a series of adaptive algorithms has also been developed which do not rely on statistical properties of the data and thus can be used on a single realization (or snapshot). In the past fifty years a plethora of algorithms have been developed, each exploiting specific properties of the received data.

In medical ultrasound, bright off-axis targets can seriously degrade image quality by introducing broad image clutter, which reduces image contrast and resolution. Figure 1 shows single channel radio frequency (RF) echo data obtained from calcifications in the thyroid of a human subject at Duke University. At least three clear waveforms are visible in this

data set. Although summation across channels to form an RF image line would amplify the echo coming from directly in front of the array, it would not entirely eliminate the two other visible targets. These non-focal targets would appear in this image line as clutter, reducing image contrast.

The application of AB can reduce the effects of bright off-axis targets, thus improving the overall image quality. In our laboratory we are exploring the application of these AB algorithms to medical ultrasonic imaging. We have examined statistical AB algorithms such as the Duvall and Frost beamformers [3,4], as well as deterministic AB algorithms such as the Adaptive Single Snapshot Beamformer (SSB) and the Spatial Processing Optimized and Constrained (SPOC) algorithm [5,6]. These algorithms are well known and recognized in the RADAR/SONAR literature.

We briefly describe some AB algorithms and present simulation results obtained applying the algorithms to medical ultrasound data.

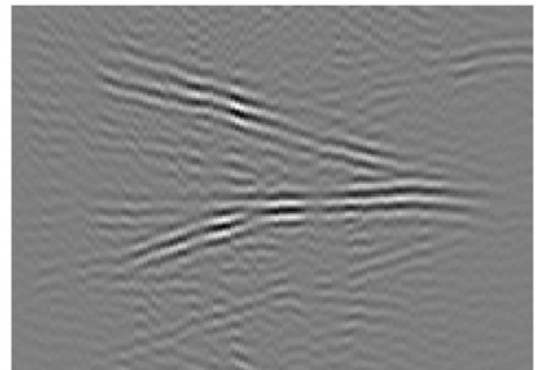


Figure 1. *In vivo* single channel thyroid data. The data clearly show the presence of bright off-axis scatterers as evidenced by the tilted plane wave visible in the top half of the image. Courtesy of G. E. Trahey.

II. ADAPTIVE BEAMFORMING ALGORITHMS

Adaptive beamformers can be divided in two broad categories: statistical and deterministic. While many algorithms have been developed in the past years, we consider two statistical and two deterministic beamformers (BF).

A. Statistical Beamformers

1) Frost Beamformer [3]

A weight vector is chosen to minimize the output energy given a linear constraint on the weights. Mathematically:

$$\min_w w^T R w \quad \text{subject to} \quad C^T w = f \quad (1)$$

$$w_{opt} = \frac{R^{-1}C}{C^T R^{-1}C} f, \quad y_{opt} = w_{opt}^T x$$

where R is the covariance matrix, C is the constraint matrix, and f is the desired frequency response. w_{opt} in (1) represents the optimal weight solution. The Frost BF uses K taps in time, therefore allowing the use of broadband signals. This algorithm requires knowledge of the second order statistics of the signal of interest and interference. Significant problems occur if the signal of interest and noise (off-axis signal) are correlated (i.e., they have the same spectral response). A schematic representation of the Frost BF is shown in figure 2.

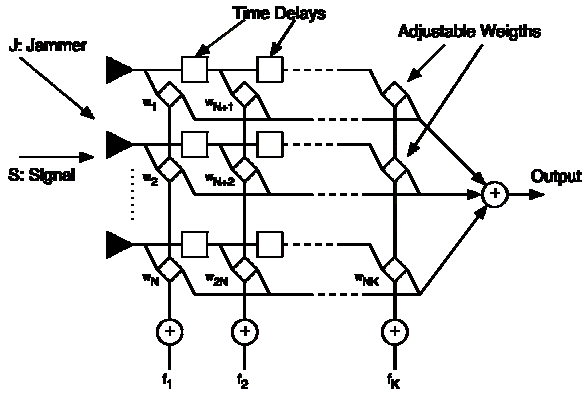


Figure 2. Schematic representation of the Frost beamformer.

2) Duvall Beamformer [4]

The Duvall BF is equivalent to the Frost BF in its formulation and assumptions. This algorithm, however, is designed to get around the problem arising when signal and noise are correlated. It uses two BFs; the first one is a slave BF, whereas the second is connected to the array elements through a subtractive process. The weights calculated in the latter BF are then copied in the slave BF to generate an output. A schematic representation of the Duvall BF is shown in figure 3.

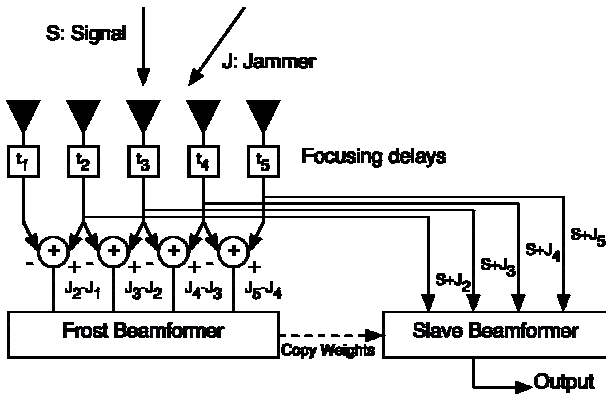


Figure 3. Schematic representation of the Duvall beamformer.

B. Deterministic Beamformers

The following BFs do not make use of any statistics, therefore are suitable to use with only a single snapshot of data.

1) Adaptive Single Snapshot Beamformer (SSB) [5]

This algorithm subdivides the array into G groups of K elements (the groups can overlap), and rearranges the data into a $G \times K$ matrix X . For every steering direction, this beamforming scheme solves the right- and left-hand side generalized eigenvalue problem given by:

$$(X - (a_1 g_1^T) y) v = 0, \quad u^T (X - (a_1 g_1^T) y) = 0^T \quad (2)$$

$$u^T = \frac{g_1^T X^{-1}}{g_1^T X^{-1} a_1}, \quad v = \frac{X^{-1} a_1}{g_1^T X^{-1} a_1}, \quad y_{opt} = u^T X v$$

where a_1 and g_1 are the group and sub-group (respectively) on-axis steering vector, whereas u and v are the beamforming weights. The SSB BF is designed for narrowband, far field signals. However, it can also be implemented in the frequency domain for broadband data. A schematic representation of the SSB BF is given in figure 4.

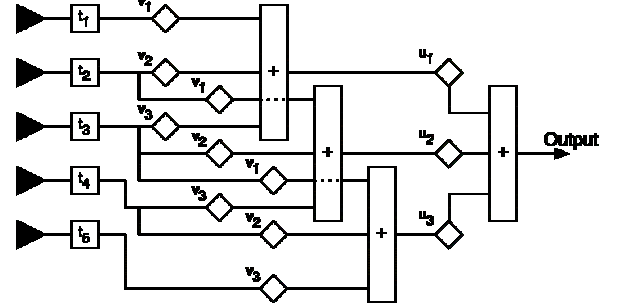


Figure 4. Schematic representation of the SSB beamformer.

2) SPOC [6]

This algorithm takes a completely different approach. A signal model is first generated of the field produced by a series of hypothetical sources. The sensors' output is matched to the signal model to solve for the position and intensity of the real sources. Statistics are not required and both near-field/far-field and broad/narrow band cases can be modeled.

The algorithm:

- The region of interest (ROI) is subdivided in a grid of hypothetical sources at arbitrary positions, as shown in figure 5. Finer grid sampling yields finer final resolution.
- For each point in the ROI, we calculate the hypothetical field received by the array for that specific point. These responses are included into the array manifold matrix V of dimensions $L \times P$, where L and P are the numbers of hypothetical sources in the range and lateral dimensions, respectively.
- The data vector $x = [x_1 \ x_2 \ \dots \ x_N]$ is received by the N -element linear array. This vector can be modeled as $x = V^* f$. In this expression, f is the $L \times 1$ signal vector,

whose elements are the amplitudes of sources located in the ROI.

- Given x and V , SPOC recursively estimates the signal vector f .

The main problems with this algorithm are the high computational cost, and the derivation of an accurate signal model. SPOC is shown schematically in figure 5.

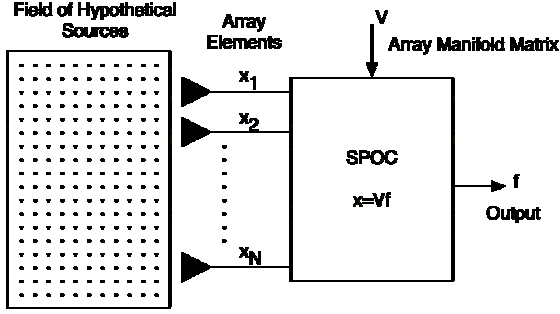


Figure 5. Schematic representation of SPOC.

III. SIMULATION METHODS AND RESULTS

A. Beamplots

For this and the successive section, single channel data was generated with Field II. We modeled a linear array operating at 5MHz with roughly 70% fractional bandwidth (BW). The final sampling rate was 40MHz. While the Frost, Duvall, and SSB BFs were applied on RF data, SPOC was applied on complex demodulated IQ signals. Another important difference is that with SPOC the transmit pulse is a plane wave. This allows a more efficient and compact description of the ROI.

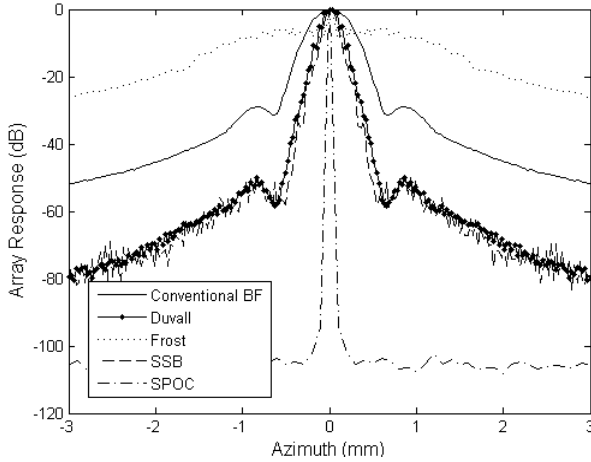


Figure 6. Beamplots for a 32 element linear array operating at 5MHz with 70% bandwidth. No apodization was used for the conventional BF.

Figure 6 shows beamplots obtained from a 32 element linear array. The four adaptive BFs are compared to the conventional, data independent BF. No apodization was used in the conventional BF. In the case of Frost and Duvall BFs, the constraint vector f is chosen to match the signal BW. For the SSB BF, the array is divided in sub-apertures of 16 elements

each. Finally, in the case of SPOC, hypothetical sources are placed every $20\mu\text{m}$ in range and every $100\mu\text{m}$ in azimuth.

The results presented in figure 6 clearly show that SPOC outperform other adaptive BFs both in terms of resolution and contrast. For this reason and because of limited space, in the following sections we present simulation results that compare only conventional BF and SPOC.

B. Wire Targets

In this case, we simulated a 33 element linear array. A plane wave was used in transmit. A series of wire targets were distributed within a $4\times 5\text{mm}$ region in range and azimuth, respectively. The receive data was sampled at 40MHz and the conventional BF was applied on RF data using dynamic focusing. In the case of SPOC, we discretized the image region in a series of hypothetical sources separated $20\mu\text{m}$ in range and $120\mu\text{m}$ in azimuth. As before, complex demodulated IQ signals were used with SPOC. The results of this set of simulations are presented in figure 7 and 8. The figures are in linear scale. Note that the wires are placed in spatial positions which do not correspond to the positions of hypothetical sources.

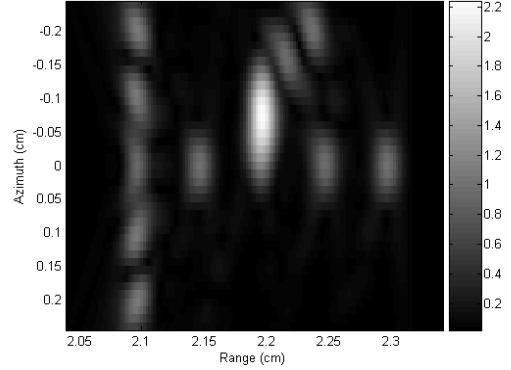


Figure 7. Conventional delay-and-sum beamforming. No apodization.

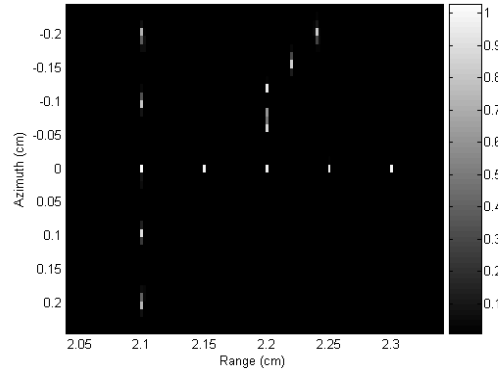


Figure 8. SPOC beamformer output.

C. Anechoic Cyst

An anechoic cyst was placed in front of the array and surrounded by ultrasonic scatterers. The cyst is round with a 1mm radius. Simulation methods are the same of those described in the previous section, except that the hypothetical source sampling was now reduced to $100\mu\text{m}$ in azimuth. The

results of this set of simulations are presented in figure 9 and 10. The figures are in linear scale. The scatterers are placed in random positions within the image region.

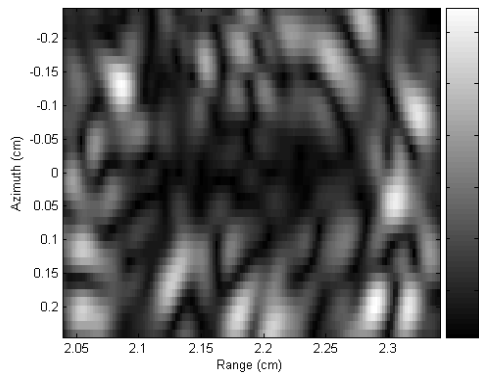


Figure 9. Conventional delay-and-sum beamforming. No apodization.

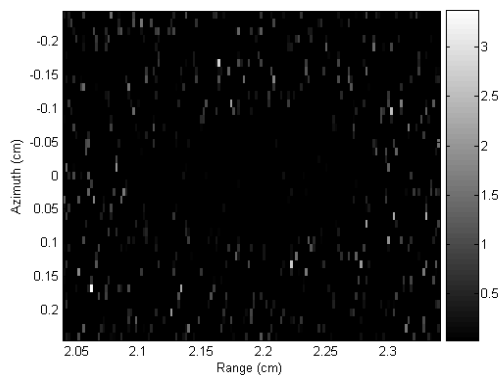


Figure 10. SPOC beamformer output.

IV. DISCUSSION

A series of AB algorithms have been presented in this paper and their performances were compared to the conventional, data independent beamforming technique.

As shown in figure 6, all the adaptive BFs achieve resolutions that are significantly better than that obtained by conventional BF. Furthermore, except for the Frost BF, we can observe a significant reduction in side lobe level. This figure also reveals that the SPOC significantly outperforms every other algorithms with a noise floor level of roughly -110 dB. Also note that the super-resolution peak obtained with SPOC is a function of the hypothetical sources sampling; the finer the sources' grid, the better the final resolution. The performance of the Frost algorithm is significantly limited in medical ultrasound. Unlike SONAR and RADAR, we operate in a limited statistics scenario where on-axis and off-axis signals are highly correlated. These factors conspire to reduce the performance of this algorithm. The Duvall BF, instead, takes into account the correlation between signal of interest and off-axis signals using a subtractive process, as shown schematically in figure 3. From figure 6 it can be observed that

the Duvall BF performs significantly better than the Frost BF, with a reduction of side lobe levels of roughly 20dB when compared to conventional BF. Finally, figure 6 shows that the SSB BF has similar performance to that of the Duvall BF. The main limitation of this algorithm is that narrow-band signals are originated from far-field. Obviously this is not a good assumption for medical ultrasound. Note that we have also performed additional simulations using a 64 elements array and found similar trends to those presented in figure 6.

It is clear at this point that most of the AB algorithms previously described, tend to fail when applied to medical ultrasound data. This can be attributed to some or all of the following factors: we are operating in a near-field scenario, our signals are broadband, and we have limited statistical information available. However, SPOC is well suited for medical ultrasound since it requires neither a far-field/narrow-band assumption nor second order statistics of the signals. Figures 7-10 compare the SPOC algorithm with the conventional BF on synthetic data depicting wires and anechoic cyst phantoms. The superiority of SPOC is clearly evident from those figures. Although not presented, we have performed additional simulations analyzing the stability of SPOC with respect to additive noise. We have found that down to a 10 dB/channel SNR the performance of SPOC remains excellent. The main limitation of this algorithm is the high computational complexity associated with it. We are currently investigating how to maintain the same performance with more efficient implementation.

V. CONCLUSIONS

Adaptive beamforming could help reduce clutter and yield super-resolution in medical ultrasound imaging. Simulation results show that SPOC significantly outperforms other AB algorithms. Additional work is required, however, to reduce the computational costs associated with SPOC.

REFERENCES

- [1] S. Haykin, "Adaptive Filter Theory," 4th ed., Prentice-Hall, Upper Saddle River, New Jersey, 2002.
- [2] B. D. Van Veen and K. M. Buckley, "Beamforming: A Versatile Approach to Spatial Filtering," *IEEE ASSP Magazine*, pp. 4-24, 1988.
- [3] O. L. Frost III, "An Algorithm for Linearly Constrained Adaptive Array Processing," *Proc. IEEE*, vol. 60, no. 8, pp. 926-935, 1972.
- [4] B. Widrow, K. M. Duvall, R. P. Gooch, and W. C. Newman, "Signal Cancellation Phenomena in Adaptive Antennas: Causes and Cures," *IEEE Trans. Antennas Propagat.*, vol. AP-30, no. 3, pp. 469-478, 1982.
- [5] M. E. Ali and F. Schreib, "Adaptive Single Snapshot Beamforming: A New Concept for the Rejection of Nonstationary and Coherent Interferers," *IEEE Trans. Signal Processing*, vol. 40, no. 12, pp. 3055-3058, 1992.
- [6] R. Bethel, B. Shapo, and H. L. Van Trees, "Single Snapshot Spatial Processing: Optimized and Constrained," *Sensor Array and Multichannel Signal Processing Workshop Proceedings*, pp. 508-512, 2002.